



# **D-Band Filtering Six-Port Junction**

by

**Chen, Xun**

A thesis submitted to the University of Birmingham for the degree of Doctor of  
Philosophy

College of Engineering and  
Physical Sciences  
University of Birmingham  
August 2022

UNIVERSITY OF  
BIRMINGHAM

**University of Birmingham Research Archive**

**e-theses repository**

This unpublished thesis/dissertation is copyright of the author and/or third parties. The intellectual property rights of the author or third parties in respect of this work are as defined by The Copyright Designs and Patents Act 1988 or as modified by any successor legislation.

Any use made of information contained in this thesis/dissertation must be in accordance with that legislation and must be properly acknowledged. Further distribution or reproduction in any format is prohibited without the permission of the copyright holder.

# Abstract

Featured with low cost, simple structure, high phase accuracy, calibration convenience and algorithm transparentness (Four outputs provide flexibility for algorithm), six port junctions (SPJs) have found their application in microwave measurements, receivers, and angle-of-arrival (AoA) measurements. This thesis aims to demonstrate a novel filtering SPJ working in the D-band (150 GHz, a radar band) with minimum magnitude imbalance. One circuit synthesis technique and five designs will be presented.

The technique is a general and systematic way to incorporate non-resonant circuits (NRCs) into a single coupling matrix (CM). With the matrix, a compound circuit with resonant and non-resonant circuits can be designed as a whole. The CM technique also allows combining ideal circuits with practical circuits. In this way, the influence of the impairment from the practical circuits can be investigated without computationally intensive simulations.

The five case designs include three filtering couplers (named Coupler-A, -B and -C) and two filtering SPJs (named SPJ-A and -B). Coupler-A is an amplitude-balance enhanced  $180^\circ$  filtering coupler. The influence of physical configuration on the amplitude balance has been investigated. This amplitude balancing approach ran through the coupler and SPJ designs in this thesis.

SPJ-A is an E-plane X-band filtering SPJ. The bandwidth is from 9.8 GHz to 10.2 GHz. The measured minimum return loss is 15 dB and the phase error is  $10^\circ$ . Thanks to the E-plane configuration, the measured insertion-loss is only 0.4 dB.

As a prototype prior to the D-band filtering SPJ, this work verified the theory and the proposed topology.

Coupler-B is an E-plane D-band  $180^\circ$  filtering coupler while Coupler-C is an E-plane D-band  $90^\circ$  filtering coupler. Fan-shaped resonators were proposed in the Coupler-B design. E-plane configuration is feasible using the proposed resonator. The measurement showed less than 0.46 dB insertion loss in the working band of 148 to 152 GHz. SPJ-B is an E-plane D-band filtering SPJ. It combined the design in Coupler-B and Coupler-C. Silicon chips based absorbers were used in SPJ-B for compactness. The measurement showed a minimum 11-dB return loss and a maximum 2-dB insertion loss at D-band. The phase error is  $15^\circ$ .

There are two appendixes. Appendix I gives the settings in simulation and optimization when using the commercial simulation software. Appendix II gives the design of an H-plane filtering SPJ working at 10 GHz. Coupler A was used in the implementation. This SPJ was not fabricated due to the potential large insertion loss H-plane configuration brings. Only simulated response will be presented in Appendix II.



# Acknowledgement

As a student of the Joint PhD Training Program offered by the University of Birmingham (UoB) and Southern University of Science and Technology (SUSTech), I would like to express my heartfelt gratitude to my supervisors, Yi Wang, Michael Lancaster in UoB and Qingfeng Zhang in SUSTech, for their supervision as well as to UoB and SUSTech for their support for my studies in both universities. It all started from the day I landed at Birmingham Airport, Professor Yi Wang picked me up and drove me where I live. In the first few months, the research concept in the UK clashed with my old mindset, making the beginning of the study not smooth. After a long-talk with Professor Yi Wang, I finally managed to walk in the right direction. Besides, the conversation with Professor Michael Lancaster every month inspired me a lot, letting me know a research itself is as important as publications.

I appreciate Dr. Milan Salek, who accompanied me in the lab despite sweating in the hot weather, and sent me silicon chips from overseas. I also appreciate Dr. Talal Skaik and Dr. Qiang Shao, who helped me with device measurement. Without the help from you, I could not have finished my work. On the last day in Birmingham, I met Dr. Milan Salek in the gym working hard. Hope you have achieved your goal. I also express my appreciation to my progress report assessor Dr. Stephen Hanham for his time and useful advice.

My thanks also goes to Professors Sheng Sun and Yifan Chen, who made the journey happen.

At last I would like to express my gratitude to my parents, who always back me up.

# Table of Contents

<b>Publication List .....</b>	<b>8</b>
Journals: .....	8
Conferences: .....	8
<b>List of Acronyms .....</b>	<b>9</b>
<b>Chapter 1. Introduction .....</b>	<b>10</b>
1.1 Overview of SPJ .....	10
1.1.1 SPJ Criteria in Receivers & AoA Measurement .....	10
1.1.2 Design Challenge in SPJs .....	12
1.2 Motivation .....	13
1.3 Novelty and Contribution .....	15
1.4 Thesis Organization .....	17
Reference .....	17
<b>Chapter 2 Literature Review .....</b>	<b>20</b>
2.1 SPJ Based Microwave Measurement .....	20
2.2 SPJ Based Homodyne Receivers .....	24
2.3 SPJ based AoA Measurement .....	27
2.4 SPJ designs .....	30
2.5 Summary .....	31
Reference .....	32
<b>Chapter 3. Theory of Filtering SPJ Designs .....</b>	<b>35</b>
3.1 Synthesis of Cascaded Bandpass Filters .....	36
3.1.1 Resonators .....	36
3.1.2 Lowpass to Bandpass Filters .....	38
3.1.3 $J/K$ Inverters in Filters .....	42
3.2 Coupling Matrix .....	45
3.2.1 $N \times N$ Coupling Matrix .....	47
3.2.2 $N+2$ Coupling Matrix .....	51
3.2.3 $N+X$ Coupling Matrix .....	53
3.3 Waveguide Circuit Realization .....	55
3.3.1 Rectangular Waveguide .....	55
3.3.2 Rectangular Waveguide Resonators/ Cavities .....	58
3.3.3 Irises and Coupling Realization .....	59
3.4 CM of Non-Resonant Circuits .....	64

35	Design Procedure .....	68
36	Summary.....	69
	Reference: .....	70
<b>Chapter 4.</b>	<b>Amplitude-Balance Enhanced Filtering Coupler .....</b>	<b>71</b>
41	Amplitude Imbalance in Filtering Coupler .....	72
42	Effect of Aperture Position on Amplitude Balance .....	76
43	Modified Balanced Coupler .....	78
44	Fabrication and Measurement .....	80
4.5	Summary .....	82
	Reference .....	83
<b>Chapter 5.</b>	<b>E-plane X-band Filtering SPJ.....</b>	<b>84</b>
5.1	Topology of the SPJ .....	84
5.2	Theoretical response of the SPJ.....	86
5.3	Implementation of the E-plane SPJ .....	93
5.3.1	Implementation of the Branch-Line Couplers.....	93
5.3.2	Hybrid CM of the E-plane SPJ .....	96
5.3.3	Design of the E-plane filtering coupler .....	99
5.4	SPJ Simulation and Measurement.....	104
5.5	Summary.....	113
	Reference .....	114
<b>Chapter 6.</b>	<b>Ring-Shaped D-Band 180° Filtering Coupler.....</b>	<b>115</b>
6.1	Fan-Shaped Resonator .....	115
6.2	Implementation and Simulation .....	118
6.3	Fabrication and Measurement .....	125
6.4	Summary.....	127
	Reference .....	128
<b>Chapter 7.</b>	<b>E-plane D-band Filtering SPJ.....</b>	<b>129</b>
7.1	E-Plane D-Band 90° filtering coupler.....	130
7.1.1	Challenge of 90° Filtering Couplers.....	130
7.1.2	Solution for 90° Filtering Coupler.....	132
7.1.3	Realization of the 90° Filtering Coupler.....	133
7.2	Topology of the Filtering SPJ .....	136
7.3	Simulation of the Filtering SPJ.....	139
7.4	SPJ Fabrication and Measurement .....	145
7.5	Summary.....	150
	Reference .....	150

<b>Chapter 8. Conclusion and Future Work.....</b>	<b>152</b>
8.1 Summary and conclusion.....	152
8.2 Future Works .....	154
<b>Appendix I: Simulation and Optimization Settings.....</b>	<b>156</b>
<b>Appendix II: H-Plane X-band Filtering SPJ.....</b>	<b>159</b>
II.1. Topology of the SPJ .....	159
II.2. Theoretical Response of the SPJ.....	160
II.3. Implementation of the H-plane SPJ .....	166

# Publication List

## Journals:

1. X. Chen, Y. Wang, and Q. Zhang, "Ring-Shaped D-Band E-Plane Filtering Coupler," IEEE Microwave and Wireless Components Letters, vol. 31, no. 8, pp. 953-956, 2021.
2. X. Chen, Y. Wang, T. Skaik, and Q. Zhang, "E-Plane Waveguide Filtering Six-Port Junction," IEEE Transactions on Microwave Theory and Techniques, vol. 69, no. 12, pp. 5360-5370, 2021.
3. X. Chen, Y. Wang, M. Salek, and Q. Zhang, " Sub-Terahertz Filtering Six-Port Junction," IEEE Transactions on Microwave Theory and Techniques, vol. 70, no. 8, pp. 3877-3885, 2022.

## Conferences:

4. X. Chen, Y. Wang, Q. Shao, T. Skaik, and Q. Zhang, " Filtering Waveguide Cavity Couplers with Tight Amplitude Balance," European Microwave Week 2022, accepted.

# List of Acronyms

AoA	Angle of Arrival
BER	bit error rate
BiCMOS	Bipolar Complementary Metal-Oxide-Semiconductor
CAD	Computer Aided Design
CM	Coupling Matrix
CNC	Computer Numerical Control
DSP	Digital Signal Processing
DUT	Device Under Test
EVM	Error Vector Magnitude
FBW	Fractional Bandwidth
I-Q	In-phase and quadrature
LNA	Low Noise Amplifier
LO	Local Oscillator
MHMIC	Miniaturized Hybrid Microwave Integrated Circuit
NRC	Non-Resonant Circuit
PSK	Phase Shift Keying
QAM	Quadrature Amplitude Modulation
QPSK	Quadrature Phase Shift Keying
SiGe	Silicon Germanium
SNR	signal-to-noise ratio
SIW	Substrate Integrated Waveguide
SLA	Stereolithography
SPJ	Six-Port Junction
VNA	Vector Network Analyzer

# Chapter 1. Introduction

## 1.1 Overview of SPJ

Six-port junctions (SPJs), with two inputs and four outputs, first appeared in microwave measurement systems (e.g., vector network analyzer) [1, 2]. Then, it was spread to receivers and angle-of-arrival (AoA) measurements (e.g., to detect the incident angle of a signal in a radar system) [3]. The criteria of the SPJs for microwave measurement are different from those for receivers and AoA measurement. This section provides the criteria of the SPJ employed by receivers and AoA measurement at first, since this thesis is based on these criteria. A brief introduction of an issue that SPJs are facing is also discussed in this chapter. The criteria of the SPJs in microwave measurement will be given in Chapter 2.

### 1.1.1 SPJ Criteria in Receivers & AoA Measurement

In receivers and AoA measurement systems, the most popular form of the SPJ is illustrated in Fig. 1.1, which is also the focus of this thesis. It has two inputs

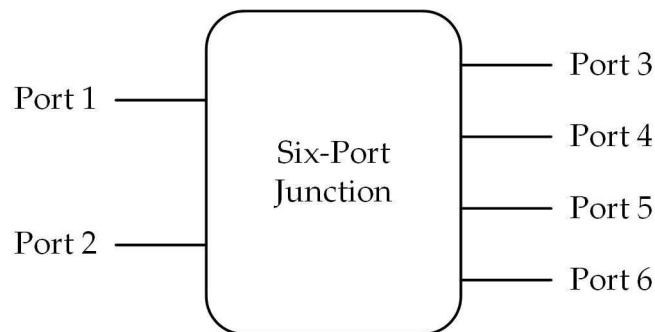


Fig. 1.1. SPJ concept in receivers and AoA measurement.

and four outputs. The four outputs divide the magnitude of one input to a quarter while doing the same to the other input but adding four different phase shifts ( $0^\circ$ ,  $90^\circ$ ,  $180^\circ$  and  $270^\circ$ ). Given the schematic in Fig. 1.1, the corresponding S-parameters are given in (1.1) [4].

$$[S] = \frac{1}{2} \begin{bmatrix} 0 & 0 & e^{j\theta} & -je^{j\theta} & e^{j\theta} & -je^{j\theta} \\ 0 & 0 & e^{j\theta} & je^{j\theta} & je^{j\theta} & -e^{j\theta} \\ e^{j\theta} & e^{j\theta} & 0 & 0 & 0 & 0 \\ -je^{j\theta} & je^{j\theta} & 0 & 0 & 0 & 0 \\ e^{j\theta} & je^{j\theta} & 0 & 0 & 0 & 0 \\ -je^{j\theta} & -e^{j\theta} & 0 & 0 & 0 & 0 \end{bmatrix} \quad (1.1)$$

where  $\theta$  represents the phase shift caused by the connections in an SPJ. The output magnitudes at the four outputs are the same, while the phase responses can be written as:

$$\begin{cases} \angle S_{31} - \angle S_{32} = 0^\circ \\ \angle S_{41} - \angle S_{42} = 180^\circ \\ \angle S_{51} - \angle S_{52} = 90^\circ \\ \angle S_{61} - \angle S_{62} = 270^\circ \end{cases} \quad (1.2)$$

There is no particular order of these phase responses, provided that the phase responses are  $0^\circ$ ,  $90^\circ$ ,  $180^\circ$  and  $270^\circ$ .

If the power of the two inputs is similar (at same frequency), depending on the phase and magnitude difference, constructive and destructive interaction take place at the four outputs [3]. Demodulation and AoA calibration using SPJs are based on this characteristic, which will be detailed in Chapter 2. The following section introduces the issue SPJs are facing in these two applications.



### 1.1.2 Design Challenge in SPJs

The main issue the SPJs are facing is imbalanced amplitude. Conventionally, SPJs for receivers and AoA measurement are constructed by three  $90^\circ$  3-dB

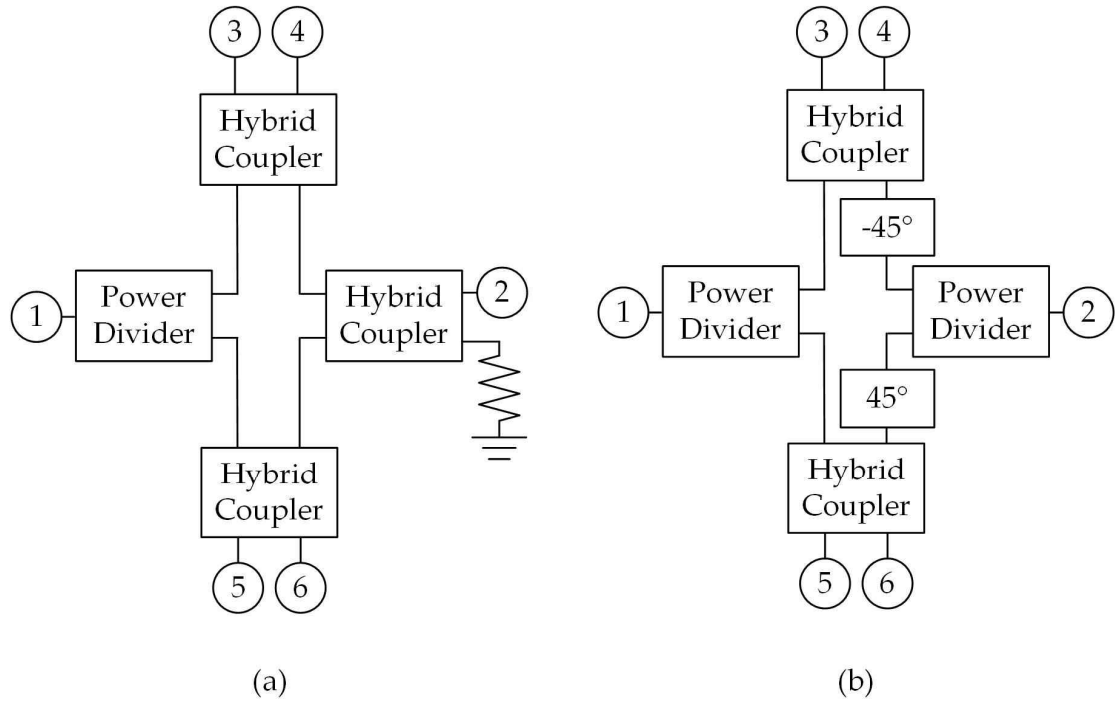


Fig. 1.2. Two typical topologies of conventional SPJs. (a) Three hybrid couplers and one power divider. (b) Two hybrid couplers and two power dividers. The hybrids are all  $90^\circ$  couplers.

hybrid couplers and one 3-dB power divider, as shown in Fig. 1.2 (a), or by two  $90^\circ$  3-dB hybrid couplers and two 3-dB power dividers with additional  $\pm 45^\circ$  phase shifters (see Fig. 1.2 (b)). Port 1 and Port 2 are the two inputs, Port 3 to 6 are four outputs. The two output signals from the power dividers are in-phase while the hybrid couplers add a  $90^\circ$  phase shift. The additional phase shifters in Fig. 1.2 (b) realize the  $90^\circ$  phase shift. SPJs often suffer from amplitude

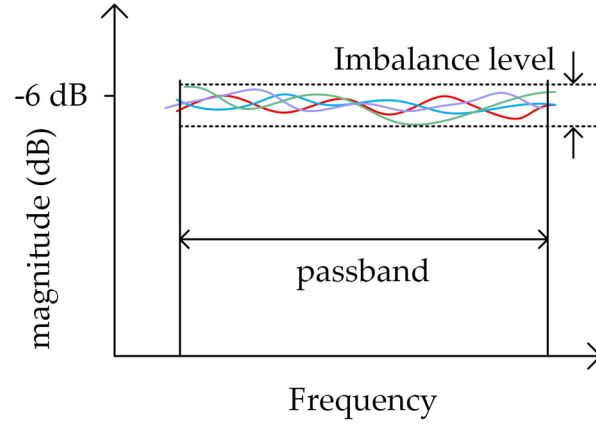


Fig. 1.3. Illustration of amplitude imbalance in an SPJ. The colored lines depict output amplitudes.

imbalance. Fig. 1.3 illustrates the issue of amplitude imbalance. If the SPJ is perfectly balanced, the magnitudes of the outputs are equal within the working band (-6 dB in the case of SPJs). In practice, the output magnitudes vary in a range due to the loss and asymmetrical configuration. The work in [5] demonstrated a 6.67% fractional bandwidth (FBW) around 30 GHz with a 6-dB amplitude imbalance. Another work in [6] reported an SPJ working around 40 GHz with 10.0% FBW. The amplitude imbalance at the center frequency is 2.2 dB, whereas the amplitude fluctuates significantly in the range of -5 to -12 dB in the working band. Even with a narrow frequency span of 2%, the imbalance is still noticeable from the provided response in these works. Poor response of SPJs adds extra noise to the system and deteriorates the robustness and reliability of the receivers.

## 1.2 Motivation

With the development of wireless communication, more and more wireless

components are designed in sub-terahertz and even terahertz since they provide us with more available bands and compact circuit footprint. D-band (110-170 GHz) has been given much focus in digital communication, radar and imaging applications since fog, dust and fabrics can be easily penetrated within it [7]. There are many radar systems working in the D-band presented in the literature [8-11]. For transceivers, SPJs have advantages over conventional in-phase and quadrature (I-Q) mixers in simple structure, calibration convenience and algorithm transparentness [3]. The principle of employing an SPJ to a receiver is well studied in the literature [5, 6, 12-17]. However, amplitude imbalance often prevents a SPJ to realise its full performance potential. Besides, the merits of SPJ receivers manifest along with higher operating frequencies (to tens or even hundreds of gigahertz). Under same fractional bandwidth (FBW), higher frequency provides wider available working band that promises higher speed. Also, in AoA and distance measurements, higher frequency means shorter wavelength that provides high resolution and higher accuracy. The main challenge with SPJs lies in the implementation above 100 GHz with minimum imbalance. From substrate integrated waveguide (SIW) based SPJs [12] to double ridge gap waveguide based SPJs [6], there has been tremendous literature on SPJs. However, SPJs working at higher than 100 GHz are rarely reported. [18] reported an SPJ-based up-conversion mixer fabricated in a SiGe BiCMOS process. It works at 120 GHz. Embedding filtering function to circuit components also facilitates high frequency application. From couplers [19] to

antennas [20], integration of filtering function into other passive or even active circuits saves the footprint of the circuit and provides lower insertion loss with the absence of the interconnection between components. The embedded filter function also offers balanced and flat amplitude and phase response to the SPJ. Only one work of SPJ with filtering function was found in [21], but the lack of detail makes the design procedure unclear.

## 1.3 Novelty and Contribution

Motivated by the demand for high frequency SPJs with minimum amplitude imbalance, and by the advantages of filter integration, this thesis aims at designing a filtering SPJ working in the D-band (150 GHz) with amplitude-balance enhanced response. The study cases in this thesis include:

- **Formulation of CM with non-resonant circuits (NRCs).**

Contribution: As the proposed filtering SPJ consists of filtering couplers (resonant circuits) and branch-line couplers (non-resonant circuits), a systematic and simple method was given to include resonant circuits and NRCs into a single coupling matrix (CM). The CM provides accurate theoretical response of the filtering SPJ, which makes the synthesis more efficient. In addition, this CM can be built partially by theoretical values and simulated values, from which the imperfection brought by the simulated values can be analyzed.

- **An amplitude-balance enhanced filtering coupler (180°) (Coupler-A).**

Contribution: The relationship between physical configuration and amplitude balance was suggested. It shows under the same topology, optimal physical configuration brings improved amplitude balance. This concept was also applied in the filtering SPJ designs.

- **An E-plane X-band filtering SPJ (SPJ-A).**

Contribution: E-plane configuration was implemented in this waveguide-based SPJ for minimum insertion loss. The SPJ was fabricated and measured. The design provides a systematic way for filtering SPJ design for the first time.

- **A ring-shaped D-band 180° filtering coupler (Coupler-B).**

Contribution: This work proposed a ring-shaped filtering coupler that fulfilled E-plane configuration while eliminated capacitive iris with small aperture at 150 GHz. This ring-shaped structure was further used in the D-band filtering SPJ. This design is the first work of the filtering coupler in the D-band.

- **An E-plane D-band 90° filtering coupler (Coupler-C).**

Contribution: This coupler also was used in the design of SPJ-B, to avoid inner circuitry ports in SPJ-A. This is the first report of a 90° filtering coupler.

- **An E-plane D-band filtering SPJ (SPJ-B).**

Contribution: Waveguide-based SPJ-B combines the outcomes of Coupler-B and Coupler-C, provided a topology of a filtering SPJ that can be

implemented in the D-band. In addition, absorbers made of silicon chips were given for compactness. Measurement shows the SPJ have a maximum 2 dB insertion loss at 150 GHz and the maximum phase error is 15°.

## 1.4 Thesis Organization

There are eight chapters in this thesis. The first chapter is *Introduction*, in which the criteria of SPJs for receivers and AoA measurement are presented, since the thesis is based on these criteria. The second chapter is *literature review*. It details the application of SPJs and the state-of-the-art on SPJ designs. The applications include microwave measurement, receivers and AoA measurement. The criteria of SPJs for microwave measurement are also detailed in this chapter. The third chapter is about the theoretical background of designing a filtering SPJ. The proposed CM with NRCs is given in this chapter. Chapter 4 to Chapter 7 are the works having been done during the Ph.D. period. It includes three couplers and two filtering SPJs, they are: amplitude-balance enhanced filtering coupler, E-plane X-band filtering SPJ, ring-shaped D-band 180° filtering coupler, E-plane D-band 90° filtering coupler and E-plane D-band filtering SPJ. The last chapter is on conclusion and future work.

## Reference

- [1] G. F. Engen and C. A. Hoer, "Application of an arbitrary 6-port junction to power-measurement problems," *IEEE transactions on Instrumentation and Measurement*, vol. 21, no. 4, pp. 470-474, 1972.
- [2] G. F. Engen, "The six-port reflectometer: An alternative network analyzer," *IEEE Transactions on microwave theory and techniques*, vol. 25, no. 12, pp. 1075-

1080, 1977.

- [3] A. Koelpin, G. Vinci, B. Laemmle, D. Kissinger, and R. Weigel, "The six-port in modern society," *IEEE Microwave Magazine*, vol. 11, no. 7, pp. 35-43, 2010.
- [4] S. O. Tatu, E. Moldovan, K. Wu, R. G. Bosisio, and T. A. Denidni, "Ka-band analog front-end for software-defined direct conversion receiver," *IEEE Transactions on microwave theory and techniques*, vol. 53, no. 9, pp. 2768-2776, 2005.
- [5] A. A. Sakr, W. M. Dyab, and K. Wu, "A dually polarized six-port junction based on polarization-selective coupling for polarization-inclusive remote sensing," *IEEE Transactions on microwave theory and techniques*, vol. 66, no. 8, pp. 3817-3827, 2018.
- [6] X. Jiang *et al.*, "Millimeter-Wave Double Ridge Gap Waveguide Six-Port Network Based on Multi-Via Mushroom," *IEEE Transactions on Plasma Science*, vol. 49, no. 12, pp. 3778-3785, 2021.
- [7] Z. Xu *et al.*, "D-band CMOS transmitter and receiver for multi-giga-bit/sec wireless data link," in *IEEE Custom Integrated Circuits Conference 2010*, 2010, pp. 1-4: IEEE.
- [8] T. Jaeschke, C. Bredendiek, S. Küppers, and N. Pohl, "High-precision D-band FMCW-radar sensor based on a wideband SiGe-transceiver MMIC," *IEEE Transactions on Microwave Theory and Techniques*, vol. 62, no. 12, pp. 3582-3597, 2014.
- [9] M. Furqan, F. Ahmed, K. Aufinger, and A. Stelzer, "A D-band fully-differential quadrature FMCW radar transceiver with 11 dBm output power and a 3-dB 30-GHz bandwidth in SiGe BiCMOS," in *2017 IEEE MTT-S International Microwave Symposium (IMS)*, 2017, pp. 1404-1407: IEEE.
- [10] V. Issakov, A. Bilato, V. Kurz, D. Englisch, and A. Geiselbrechtinger, "A highly integrated D-band multi-channel transceiver chip for radar applications," in *2019 IEEE BiCMOS and Compound semiconductor Integrated Circuits and Technology Symposium (BCICTS)*, 2019, pp. 1-4: IEEE.
- [11] W. A. Ahmad *et al.*, "Multimode W-band and D-band MIMO scalable radar platform," *IEEE Transactions on Microwave Theory and Techniques*, vol. 69, no. 1, pp. 1036-1047, 2020.
- [12] X. Xu, R. G. Bosisio, and K. Wu, "A new six-port junction based on substrate integrated waveguide technology," *IEEE Transactions on microwave theory and techniques*, vol. 53, no. 7, pp. 2267-2273, 2005.
- [13] J. Chen, W. Hong, P. Yan, B. Liu, Y. Wang, and K. Wu, "Design of a six-port junction using half-mode substrate integrated waveguide," in *2007 Asia-Pacific Microwave Conference*, 2007, pp. 1-4: IEEE.
- [14] T. Djerafi, M. Daigle, H. Boutayeb, X. Zhang, and K. Wu, "Substrate integrated waveguide six-port broadband front-end circuit for millimeter-wave radio and radar systems," in *2009 European Microwave Conference (EuMC)*, 2009, pp. 77-80: IEEE.
- [15] A. Moscoso-Martir and I. Molina-Fernandez, "Six-port junction with complete UWB band coverage in multilayer technology," in *2011 41st European Microwave Conference*, 2011, pp. 655-658: IEEE.

- [16] B. Laemmle, G. Vinci, L. Maurer, R. Weigel, and A. Koelpin, "A 77-GHz SiGe integrated six-port receiver front-end for angle-of-arrival detection," *IEEE Journal of Solid-State Circuits*, vol. 47, no. 9, pp. 1966-1973, 2012.
- [17] J. L. Cano, E. Villa, A. Mediavilla, and E. Artal, "A wideband correlation and detection module based on substrate-integrated waveguide technology for radio astronomy applications," *IEEE Transactions on microwave theory and techniques*, vol. 66, no. 6, pp. 3145-3152, 2018.
- [18] B. Laemmle *et al.*, "A fully integrated 120-GHz six-port receiver front-end in a 130-nm SiGe BiCMOS technology," in *2013 IEEE 13th Topical meeting on silicon monolithic integrated circuits in RF systems*, 2013, pp. 129-131: IEEE.
- [19] K.-X. Wang, X. Y. Zhang, S. Y. Zheng, and Q. Xue, "Compact filtering rat-race hybrid with wide stopband," *IEEE Transactions on Microwave Theory and Techniques*, vol. 63, no. 8, pp. 2550-2560, 2015.
- [20] W.-J. Wu, Y.-Z. Yin, S.-L. Zuo, Z.-Y. Zhang, and J.-J. Xie, "A new compact filter-antenna for modern wireless communication systems," *IEEE Antennas and Wireless propagation letters*, vol. 10, pp. 1131-1134, 2011.
- [21] Y. Cheng and Y. Fan, "Compact substrate-integrated waveguide bandpass rat-race coupler and its microwave applications," *IET microwaves, antennas and propagation*, vol. 6, no. 9, pp. 1000-1006, 2012.



## Chapter 2. Literature Review

This chapter will first review the application of six-port junctions (SPJs) in microwave measurements, receivers and angle-of-arrival (AoA) measurements. Then the SPJ design in the literature will be presented.

### 2.1 SPJ Based Microwave Measurement

In microwave device measurement, the measurands of interest are the power delivered to the device-under-test (DUT) and the reflection coefficient to the DUT. This scenario is described in Fig. 2.1. In Fig. 2.1,  $P$  represents the delivered power to the DUT from the measurement instrument, and  $\Gamma$  is the reflection

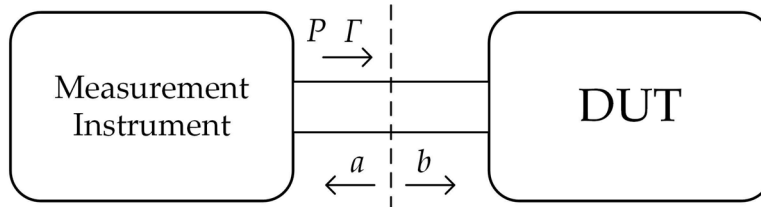


Fig. 2.1. Measurement setup.  $\Gamma$  is the reflection coefficient at the connection point and  $P$  is the power delivered to the DUT.  $a$  and  $b$  are the amplitude of the reflected and transmitted waves, respectively.

coefficient, which is obtained through:

$$\Gamma = \frac{a}{b} \quad (2.1)$$

$a$  is the magnitude of the reflected wave from the DUT, and  $b$  is the magnitude of the transmitted wave to the DUT. The delivered power can be written as:

$$P = |b|^2 - |a|^2 = |b|^2 (1 - |\Gamma|^2) \quad (2.2)$$

However, it is impossible to measure  $a$  and  $b$  directly, as probes introduced to the position of interest will disturb the existing fields [1]. Metrologists use indirect methods to infer  $a$  and  $b$ , for example, coupling out the signal for measurement. This can be achieved by using SPJs in microwave measurement. The scenario of using an SPJ in microwave measurement is detailed in [2] and shown in Fig. 2.2. One port of the SPJ is connected to the source while another

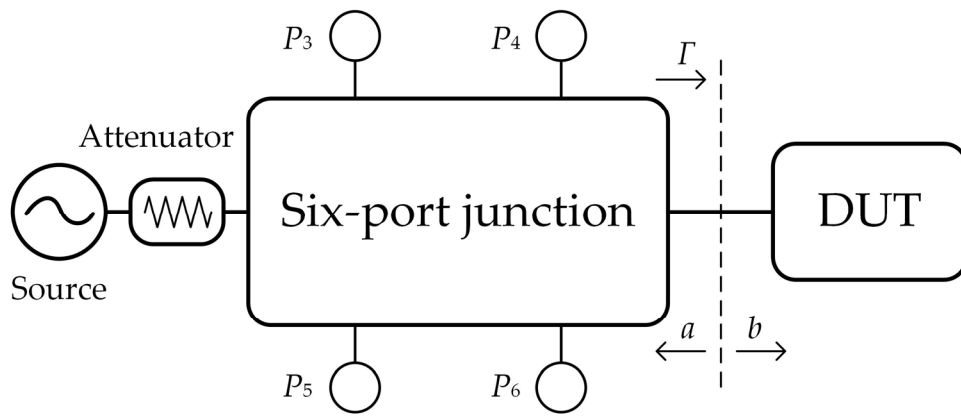


Fig. 2.2. SPJ in a measurement setup.

is to the DUT. The remaining four ports are connected to four power detectors, respectively. The SPJ introduces a function group that links the measured powers with the measurands of the DUT. The function group is:

$$P_3 = |Aa + Bb|^2 \quad (2.3a)$$

$$P_4 = |Ca + Db|^2 \quad (2.3b)$$

$$P_5 = |Ea + Fb|^2 \quad (2.3c)$$

$$P_6 = |Ga + Hb|^2 \quad (2.3d)$$

$P_3$  to  $P_6$  are the measured power by the power detectors.  $A$  to  $H$  are the intrinsic parameters of the SPJ, which are determined by calibration. The measurands of

interest are  $P$  and  $\Gamma$ . Since  $P$  is real and  $\Gamma$  is complex, there are three numbers to be determined. This indicates (2.3) is overdetermined. In practice, the overdetermination is necessary as it helps minimise the error and sensitivity brought by the imperfection of the instrument. This characteristic makes six-port outperform five-port in microwave measurement [1]. In addition, the power at detectors needs to be maintained in an optimal region when the test frequency varies. This is achieved by sampling the power  $|b|^2$  and making a feedback loop to the attenuator, which locates between the source and the SPJ, controlling the incident power [2]. This task is generally done by designing an SPJ with  $C$  in (2.3b) equals zero. Then, one can rewrite (2.3) into:

$$P_3 = |A|^2 |b|^2 |\Gamma - q_3|^2 \quad (2.4a)$$

$$P_4 = |D|^2 |b|^2 \quad (2.4b)$$

$$P_5 = |E|^2 |b|^2 |\Gamma - q_5|^2 \quad (2.4c)$$

$$P_6 = |G|^2 |b|^2 |\Gamma - q_6|^2 \quad (2.4d)$$

where  $q_3 = -B/A$ ,  $q_5 = -F/E$ , and  $q_6 = -H/G$ .

In (2.4b),  $P_4$  is proportional to  $|b|^2$  and sampled for the feedback loop to the attenuator. By substituting (2.4b) to (2.4a), (2.4c) and (2.4d), forming a function group,  $|b|^2$  can be further eliminated and the complex  $\Gamma$  can be deduced:

$$|\Gamma - q_3|^2 = \left| \frac{D}{A} \right|^2 \frac{P_3}{P_4} \quad (2.5a)$$

$$|\Gamma - q_5|^2 = \left| \frac{D}{E} \right|^2 \frac{P_5}{P_4} \quad (2.5b)$$

$$|\Gamma - q_6|^2 = \left| \frac{D}{G} \right|^2 \frac{P_6}{P_4} \quad (2.5c)$$

These three equations represent three circles in a  $\Gamma$  plane (complex plane), where  $q_3$ ,  $q_5$  and  $q_6$  are the centres. When the DUT is passive,  $\Gamma$  falls in the unit circle (origin as the centre and one as the radius). Ideally, passive  $\Gamma$  can be determined in the unit circle by the intersection of two of the circles in (2.5), shown in Fig. 2.3. However, the imperfection of the system brings error to the

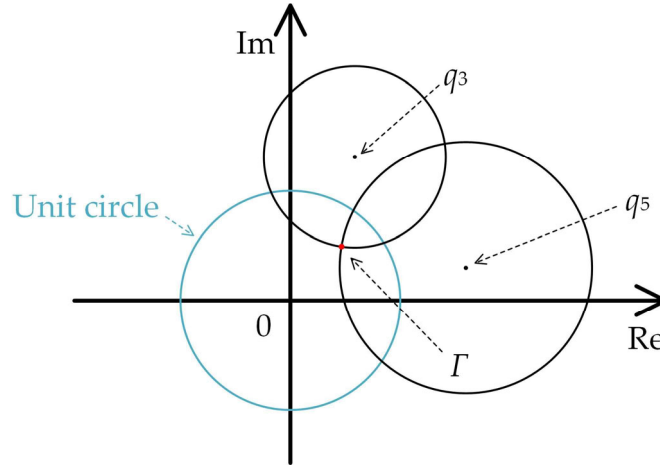


Fig. 2.3.  $\Gamma$  determined by the intersection of the two circles.

circles, degrading the accuracy of  $\Gamma$ . As stated, the equation group for  $P$  and  $\Gamma$  is overdetermined, and the redundant equation helps minimize the error. This scenario is depicted in Fig. 2.4. Because of the system error, the three circles in Fig. 2.4 do not intersect at the same point, the redundant equation (2.5c) helps locate  $\Gamma$  in a small area (depicted in red).

Ideally, when SPJs are used in microwave measurement, the topologies can be arbitrary [3]. However, different circles result in different sensitivity. The desired distribution of the three circle centres are  $120^\circ$  apart with respect to the

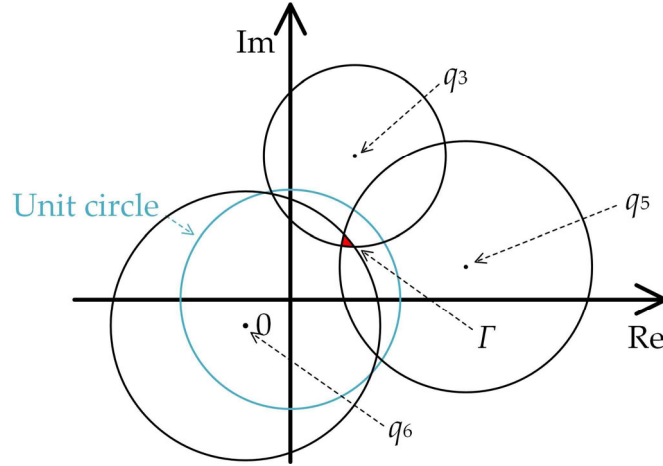


Fig. 2.4.  $\Gamma$  determined by the intersections of the three circles.

origin [4]. Nevertheless, the criteria of the SPJs for receivers and AoA measurement are different, which has been provided in Section 1.1. The detail of these two applications is given below.

## 2.2 SPJ Based Homodyne Receivers

Homodyne is one of the most popular architectures among radio frequency (RF) receiver systems because of its low cost, simple structure (with no image reject

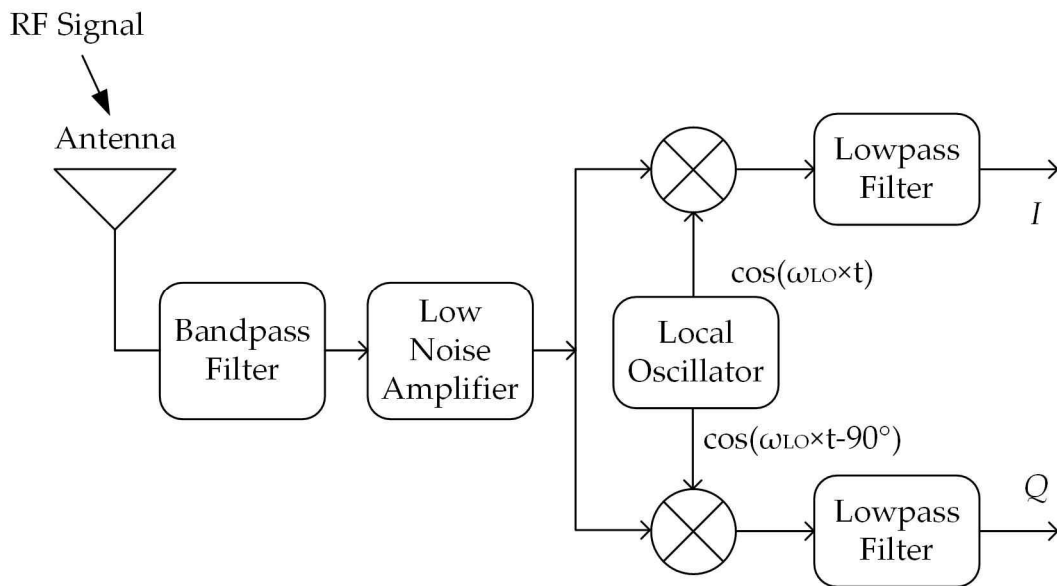


Fig. 2.5. Block diagram of a homodyne receiver.

filter) and ease of integration [5]. Fig. 2.5 gives a block diagram of a homodyne receiver with an I-Q mixer. The RF signal passing through the bandpass filter and the low noise amplifier (LNA) is divided into two paths, and mixed with the signal from a local oscillator (LO) with  $90^\circ$  phase difference. The two output signals  $I$  and  $Q$  can be used to reconstruct the original signal. Amplitude and phase imbalance brought by the hardware imperfection of the I-Q mixers degrades the performance. It was reported that the phase imbalance of  $5^\circ$ ,  $10^\circ$ ,  $15^\circ$ ,  $20^\circ$  can cause equivalent 1.5, 2.1, 2.9 and 3.7-dB of loss in signal-to-noise ratio (SNR) under a QPSK modulation with a 10 Mb/s data rate at  $10^{-4}$  bit error rate (BER) threshold [6]. Modulation methods with more points on the constellation diagram (e.g. 8PSK and QAM) are more sensitive to the imbalance. Moreover, the higher the operating frequency is, more sensitive to fabrication error the circuit can be, leading to the larger imbalance. This is undesired and should be addressed.

The first report of using a six-port junction (SPJ) in a direct digital receiver is in [7]. SPJs may be the best solution in homodyne receivers working in millimeter-wave frequencies, for its simple structure, calibration convenience and algorithm transparentness [8]. Calibration procedure in SPJ can dramatically reduce the imbalance brought by the hardware imperfection. For example, for a conventional I-Q demodulator, the imbalance of 1 dB/ $25^\circ$  resulted in 2-dB/ $25^\circ$  amplitude and phase error [6]. For an SPJ with 1-dB amplitude and maximum  $40^\circ$  phase imbalance, the residual amplitude and phase imbalance can be

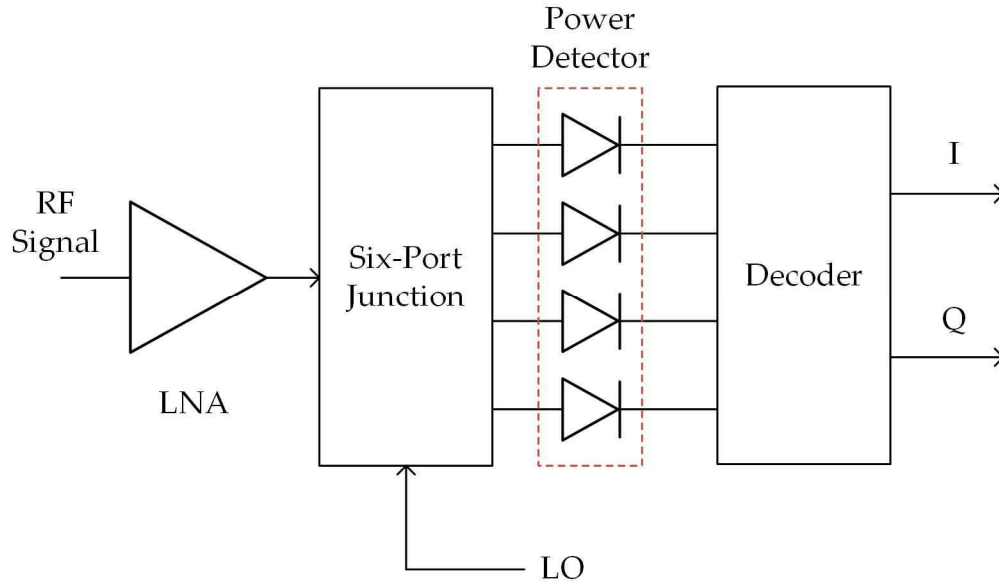


Fig. 2.6. Schematic of a direct receiver using an SPJ.

reduced to 0.1 dB and  $0.7^\circ$  after calibration [6].

Fig. 2.6 shows the schematic of an SPJ-based receiver. The RF signal is superpositioned by the LO signal in the SPJ with four different phase shifts ( $0^\circ$ ,  $90^\circ$ ,  $180^\circ$  and  $270^\circ$ ). The power detector at the four outputs feed the decoder with the status of the four magnitudes. For digital demodulation, algorithm is embedded in the decoder. Different output magnitude responses represent different I-Q signals. [9] illustrated a possible transformation between the magnitude status and I-Q signals, as given in Table 2.1. Although the situation in [9] is in a transmitter, the principle is the same. For analog modulation, the

TABLE 2.1

ILLUSTRATION OF THE RELATIONSHIP BETWEEN AMPLITUDE STATUS AND THE CORRESPONDING I-Q SIGNAL. O STANDS FOR OPEN AND S STANDS FOR SHORT.

Modulation State	Port 3	Port 4	Port 5	Port 6	I	Q
0	O	O	O	O	0	0
1	O	S	O	S	0	1
2	S	O	S	O	1	0
3	S	S	S	S	1	1

setup of the SPJ with comparators can be found in [10].

There are many receiver designs based on SPJs. An SPJ-based receiver was designed using miniaturized hybrid microwave integrated circuit (MHMIC) in [11]. QPSK demodulation was achieved and the maximum data rate is 58 Mb/s. The SPJ based digital receiver was further extended to 8PSK, 16PSK and QAM in [10]. For a higher speed, 16-QAM was realized in [12] with data rate of 1.67 Gbit/s. It also claimed that the limit in performance was from the amplifiers not the SPJ itself. Despite the promise of high speed, limitation brought by the imperfection of the SPJs still need attention. [14] introduced a calibration approach with which the error vector magnitude (EVM) can be improved from 7.9 % to 1.6 % for a 64-QAM signal. The imperfection of SPJ-based receivers listed in [14] include: *a*) Non-flat frequency response of the SPJ. *b*) Imbalanced power division. *c*) Memory effects (amplitude or phase of the distortion component is influenced by the modulation frequency [15]) and *d*) Nonlinearities of the power detectors. This thesis is aiming to address *a* and *b*.

## 2.3 SPJ based AoA Measurement

In angle of arrival (AoA) measurement, the SPJ features with low cost, high phase accuracy and robustness [16, 17]. Fig. 2.7 depicts an SPJ-based AoA measurement in long-range radar sensor calibration for autonomous driving technology [8]. Fig. 2.7 illustrates two lanes with a width  $w$  of 3.75 m. The



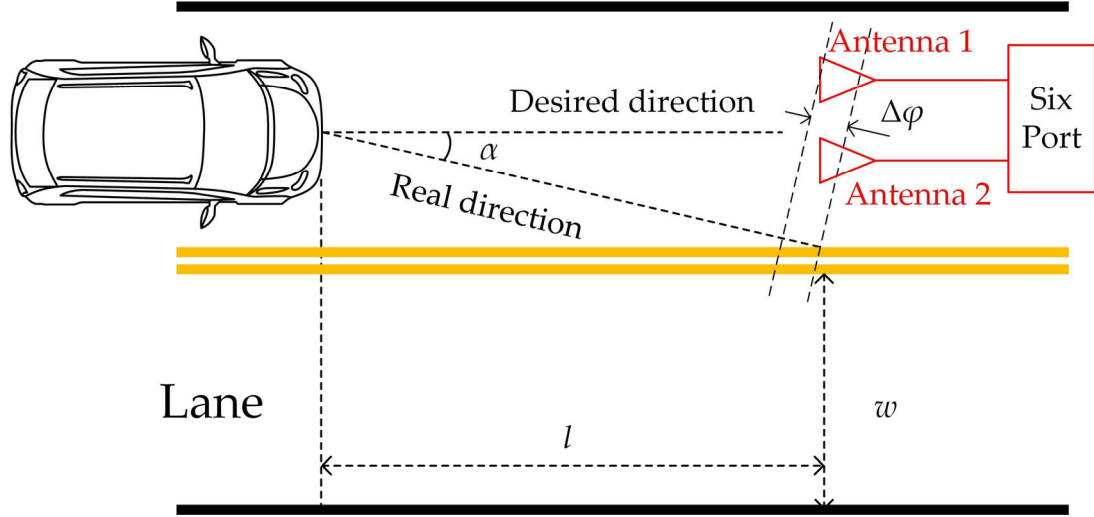


Fig. 2.7. Concept of radar-sensor calibration using an SPJ.

operating distance  $l$  of the sensor mounted to the car is 250 m. When the sensor does not point to the desired direction (as same as the car's direction), the object in the adjacent lane will be detected as being in the car's lane (which is a mistake). In this situation, the maximum misalignment angle  $\alpha$  is only  $0.4^\circ$ . In the real situation, when the sensor is not loaded at the center of the car and the car is always driven near to one side, the tolerance is always less. Thus, the direction of the radar sensor when mounting to the vehicle needs an accurate cablication. Fig. 2.7 also provides two antennas, connected to the two input ports of an SPJ, respectively. When there is a misalignment to the desired direction, phase difference  $\Delta\varphi$  exists between the two received signals at the two antennas. This  $\Delta\varphi$  can be deduced from the status of the four outputs. For a conventional SPJ, whose topology is given in Fig. 1.2 (a), [18] provided a formula (2.6) with which  $\Delta\varphi$  in Fig. 2.7 can be derived:

$$\Delta\varphi = \arctan\left(\frac{P_3 - P_4}{P_6 - P_5}\right) \quad (2.6)$$

$P_3, P_4, P_5$  and  $P_6$  are the output power of the SPJ topology in Fig. 1.2 (a). The SPJ-based AoA measurement was further extended to 77 GHz [19] in 2012. It also predicted that phase detection has the potential to work above 500 GHz. In the same year, Koelpin claimed while conventional magnitude based measurement proved a  $0.25^\circ$  phase resolution, the SPJ based AoA measurement gives a  $0.05^\circ$  minimum resolution [20]. SPJ can also be used in distance measurement. When a wave is incident to an object and reflected, the phase change detected by the SPJ can be transferred to the distance by multiplying the wavelength, given in (2.7).

$$d = \frac{1}{2} \cdot \frac{\Delta\sigma}{2\pi} \lambda_{RF} \quad (2.7)$$

$\Delta\sigma$  is the phase difference between the transmitted and received signal. Thus, in addition to AoA measurement, the high phase accuracy that SPJs can offer is also useful in vital-sign monitoring [21] by detecting the body vibration. However, periodic repetition of the detected angle will occur depending on the distance of the two receiving antennas. Distinguishing whether one input is shifted by one or more periods compared to the other input is impossible. This leads to ambiguity in SPJ-based AoA and distance measurement. For AoA measurement, larger than  $2\pi$  phase difference leads to ambiguity. For distance measurement, the ambiguity appears when the measured distance is larger than one wavelength; This can be solved by using dual SPJ systems, suggested in [20, 22]. This concept is illustrated in Fig. 2.8. There are two SPJs. The inputs are connected to two antenna arrays, which are placed parallel. The outputs of

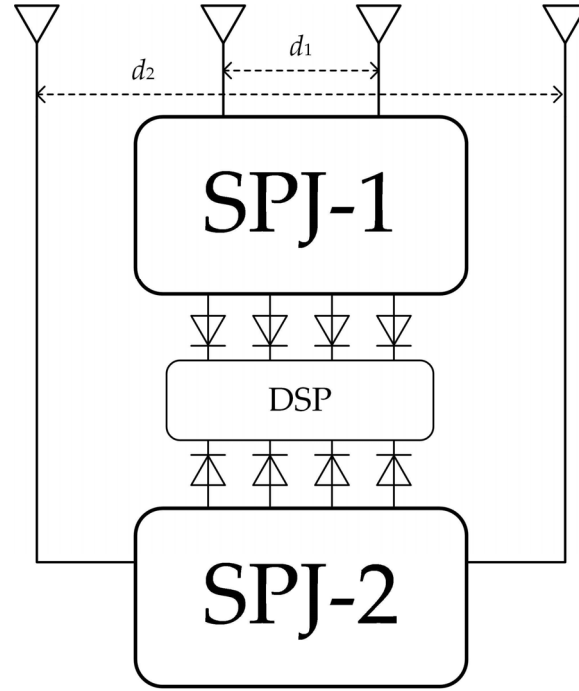


Fig. 2.8. Concept of dual SPJs to eliminate ambiguity.

the two SPJs are connected to a same digital signal processing (DSP) system. The distance between the antennas in SPJ-1 is  $d_1$  while in SPJ-2 is  $d_2$ . For an incident signal, two phase differences,  $\theta_1$  and  $\theta_2$ , will be detected by the two SPJs. The difference of the two detected angle,  $\Delta\theta$ , depends on the ratio between  $d_1$  and  $d_2$ . By choosing an appropriate ratio,  $\Delta\theta$  can be used to map the desired angle of incidence range with no ambiguity [22].

## 2.4 SPJ designs

As mentioned in Section 1.2, the main challenges in SPJs are balanced magnitude response at higher frequencies. The literature has seen many SPJ designs based on the two topologies provided in Fig. 1.2 and their variations for receivers. [23] is the first work that detailed SPJ design using substrate intergrated waveguide (SIW). The working frequency is 24 GHz with a

fractional bandwidth (FBW) of 16.67%. The measured magnitude response showed the outputs varies between -5 dB to -10 dB in the working band. Other SIW based SPJs can be found in [24-28]. Among these works, the widest achieved FBW is 40% [24, 27]. With respect to amplitude imbalance, [28] outperforms other papers, showing an SPJ working from 7.5 to 10 GHz, but still have an amplitude imbalance of 3 dB from simulation. Even when the band is narrowed to only 2%, amplitude imbalance is still around 3 dB from the measurement. Microstrip lines are used in SPJs at frequencies lower than 20 GHz [29-32]. Among them, [30, 31] depict ultra-wide band SPJ with less than 0.8-dB amplitude imbalance. At higher frequencies, the waveguide is one of the best choices [33, 34]. The FBWs of the two SPJs are 6.67% and 15%, with center frequency of 30 and 40 GHz, respectively. Although waveguides can provide less insertion loss, the magnitudes fluctuate in the working band. The variation of magnitudes is 6 dB in [33] and 7 dB in [34].

## **2.5 Summary**

This chapter reviewed SPJ based microwave measurement systems, receivers and AoA measurement systems at first. In microwave measurements, the SPJ brings a redundant equation for measurands of interest. This necessary overdetermination helps relieve system error and sensitivity. In receivers and AoA measurement, SPJ features with low cost, simple structure, high phase accuracy, calibration convenience and algorithm transparentness. This chapter

then reviewed the state-of-the art of SPJ designs. Although most of them can achieve FBW wider than 10%, the amplitude imbalance issue needs special concern. The aim of this thesis is to address this design challenge and design a filtering SPJ with minimum amplitude imbalance. [35] is the only work we found where a filtering SPJ was reported. However, it did not provide the design procedure that one can follow.

## Reference

- [1] G. F. Engen, *Microwave circuit theory and foundations of microwave metrology* (no. 9). IET, 1992.
- [2] G. F. Engen, "The six-port reflectometer: An alternative network analyzer," *IEEE Transactions on microwave theory and techniques*, vol. 25, no. 12, pp. 1075-1080, 1977.
- [3] G. F. Engen, "A (historical) review of the six-port measurement technique," *IEEE Transactions on Microwave Theory and Techniques*, vol. 45, no. 12, pp. 2414-2417, 1997.
- [4] G. F. Engen, "An improved circuit for implementing the six-port technique of microwave measurements," *IEEE Transactions on microwave theory and techniques*, vol. 25, no. 12, pp. 1080-1083, 1977.
- [5] B. Razavi and R. Behzad, *RF microelectronics*. Prentice hall New York, 2012.
- [6] J. Li, R. G. Bosisio, and K. Wu, "Computer and measurement simulation of a new digital receiver operating directly at millimeter-wave frequencies," *IEEE Transactions on Microwave Theory and Techniques*, vol. 43, no. 12, pp. 2766-2772, 1995.
- [7] J. Li, R. Bosisio, and K. Wu, "Performing PSK demodulation using six-ports," in *Symposium on Antenna Technology and Applied Electromagnetics [ANTEM 1994]*, 1994, pp. 15-18: IEEE.
- [8] A. Koelpin, G. Vinci, B. Laemmle, D. Kissinger, and R. Weigel, "The six-port in modern society," *IEEE Microwave Magazine*, vol. 11, no. 7, pp. 35-43, 2010.
- [9] R. Bosisio *et al.*, "New-wave radio," *IEEE Microwave Magazine*, vol. 9, no. 1, pp. 89-100, 2008.
- [10] S. O. Tatu, E. Moldovan, K. Wu, R. G. Bosisio, and T. A. Denidni, "Ka-band analog front-end for software-defined direct conversion receiver," *IEEE Transactions on microwave theory and techniques*, vol. 53, no. 9, pp. 2768-2776, 2005.
- [11] S. O. Tatu, E. Moldovan, K. Wu, and R. G. Bosisio, "A new direct millimeter-wave six-port receiver," *IEEE Transactions on microwave theory and techniques*, vol. 49, no. 12, pp. 2517-2522, 2001.

- [12] J. Östh, A. Serban, M. Karlsson, S. Gong, J. Haartsen, and P. Karlsson, "Six-port gigabit demodulator," *IEEE Transactions on microwave theory and techniques*, vol. 59, no. 1, pp. 125-131, 2010.
- [13] S. Gong and M. Karlsson, "Pushing the wireless data rate to the Internet speed," *IEEE Access*, vol. 4, pp. 8787-8792, 2016.
- [14] A. Hasan and M. Helaoui, "Novel modeling and calibration approach for multiport receivers mitigating system imperfections and hardware impairments," *IEEE Transactions on microwave theory and techniques*, vol. 60, no. 8, pp. 2644-2653, 2012.
- [15] J. H. Vuolevi, T. Rahkonen, and J. P. Manninen, "Measurement technique for characterizing memory effects in RF power amplifiers," *IEEE Transactions on microwave theory and techniques*, vol. 49, no. 8, pp. 1383-1389, 2001.
- [16] T. Yakabe, F. Xiao, K. Iwamoto, F. M. Ghannouchi, K. Fujii, and H. Yabe, "Six-port based wave-correlator with application to beam direction finding," *IEEE Transactions on instrumentation and Measurement*, vol. 50, no. 2, pp. 377-380, 2001.
- [17] G. Vinci, A. Koelpin, F. Barbon, and R. Weigel, "Six-port-based direction-of-arrival detection system," in *2010 Asia-Pacific Microwave Conference*, 2010, pp. 1817-1820: IEEE.
- [18] G. Vinci, A. Koelpin, and R. Weigel, "Employing six-port technology for phase-measurement-based calibration of automotive radar," in *2009 Asia Pacific Microwave Conference*, 2009, pp. 329-332: IEEE.
- [19] B. Laemmle, G. Vinci, L. Maurer, R. Weigel, and A. Koelpin, "A 77-GHz SiGe integrated six-port receiver front-end for angle-of-arrival detection," *IEEE Journal of Solid-State Circuits*, vol. 47, no. 9, pp. 1966-1973, 2012.
- [20] A. Koelpin, G. Vinci, B. Laemmle, S. Lindner, F. Barbon, and R. Weigel, "Six-port technology for traffic safety," *IEEE Microwave Magazine*, vol. 13, no. 3, pp. 118-127, 2012.
- [21] G. Vinci *et al.*, "Six-port radar sensor for remote respiration rate and heartbeat vital-sign monitoring," *IEEE Transactions on microwave theory and techniques*, vol. 61, no. 5, pp. 2093-2100, 2013.
- [22] G. Vinci, S. Lindner, F. Barbon, R. Weigel, and A. Koelpin, "Promise of a better position," *IEEE Microwave Magazine*, vol. 13, no. 7, pp. S41-S49, 2012.
- [23] X. Xu, R. G. Bosisio, and K. Wu, "A new six-port junction based on substrate integrated waveguide technology," *IEEE Transactions on microwave theory and techniques*, vol. 53, no. 7, pp. 2267-2273, 2005.
- [24] T. Djerafi, M. Daigle, H. Boutayeb, X. Zhang, and K. Wu, "Substrate integrated waveguide six-port broadband front-end circuit for millimeter-wave radio and radar systems," in *2009 European Microwave Conference (EuMC)*, 2009, pp. 77-80: IEEE.
- [25] A. Doghri, T. Djerafi, A. Ghiotto, and K. Wu, "Broadband substrate-integrated-waveguide six-port applied to the development of polarimetric imaging radiometer," in *2011 41st European Microwave Conference*, 2011, pp. 393-396: IEEE.
- [26] M. Dušek and J. Šebesta, "Design of substrate integrated waveguide six-port

- for 3.2 GHz modulator," in *2011 34th International Conference on Telecommunications and Signal Processing (TSP)*, 2011, pp. 274-278: IEEE.
- [27] J. L. Cano, E. Villa, A. Mediavilla, and E. Artal, "A wideband correlation and detection module based on substrate-integrated waveguide technology for radio astronomy applications," *IEEE Transactions on microwave theory and techniques*, vol. 66, no. 6, pp. 3145-3152, 2018.
  - [28] S. Liu and F. Xu, "Novel substrate-integrated waveguide phase shifter and its application to six-port junction," *IEEE Transactions on microwave theory and techniques*, vol. 67, no. 10, pp. 4167-4174, 2019.
  - [29] S. M. Winter, A. Koelpin, and R. Weigel, "Six-port receiver analog front-end: Multilayer design and system simulation," *IEEE Transactions on Circuits and Systems II: Express Briefs*, vol. 55, no. 3, pp. 254-258, 2008.
  - [30] A. Moscoso-Martir and I. Molina-Fernandez, "Six-port junction with complete UWB band coverage in multilayer technology," in *2011 41st European Microwave Conference*, 2011, pp. 655-658: IEEE.
  - [31] A. Moscoso-Martir, I. Molina-Fernandez, and J. Avila-Ruiz, "Ultra-wideband multilayer six-port junction with common phase error cancellation," in *2012 42nd European Microwave Conference*, 2012, pp. 17-20: IEEE.
  - [32] D. Ghosh and G. Kumar, "Six-port reflectometer using edge-coupled microstrip couplers," *IEEE Microwave and Wireless Components Letters*, vol. 27, no. 3, pp. 245-247, 2017.
  - [33] A. A. Sakr, W. M. Dyab, and K. Wu, "A dually polarized six-port junction based on polarization-selective coupling for polarization-inclusive remote sensing," *IEEE Transactions on microwave theory and techniques*, vol. 66, no. 8, pp. 3817-3827, 2018.
  - [34] X. Jiang *et al.*, "Millimeter-Wave Double Ridge Gap Waveguide Six-Port Network Based on Multi-Via Mushroom," *IEEE Transactions on Plasma Science*, vol. 49, no. 12, pp. 3778-3785, 2021.
  - [35] Y. Cheng and Y. Fan, "Compact substrate-integrated waveguide bandpass rat-race coupler and its microwave applications," *IET microwaves, antennas and propagation*, vol. 6, no. 9, pp. 1000-1006, 2012.

# Chapter 3. Theory of Filtering SPJ Designs

This chapter presents the theoretical background involved in the filtering six-port junction (SPJ) designs. While the theories about filters, coupling matrix (CM) and waveguides are mostly from the literature, the formulation of the CM incorporating non-resonant circuits (NRCs) is original and has been published in [1].

Section 3.1 starts from the definition of resonators, which are the bricks of a filter. Then, the synthesis of cascaded bandpass filters will be detailed.  $J/K$  inverters link the section of filters to CM. CM is a widely used methodology in resonant circuit (filters, duplexers, etc.) synthesis. It provides maximum topological flexibility (compared with lowpass prototype, which only supports cascaded topologies). The third section is about waveguides, which were adopted in the implementation of the couplers and SPJs. The fourth section is extracted from the author's published paper [1]. It extends the usage of the CM technique to non-resonant circuits. As the filtering SPJ contains both resonant and non-resonant circuits, this extended CM technique facilitates the filtering SPJ synthesis. The last section gives a flowchart about the procedure of filtering SPJ design. A clear usage of the background knowledge mentioned in this chapter will be detailed along with the flowchart.



## 3.1 Synthesis of Cascaded Bandpass Filters

This section gives the synthesis of cascaded bandpass filters. It starts from the introduction of resonators, followed by the synthesis method based on lowpass prototype filters. It ends with the concept of  $J/K$  inverters, which link the conventional cascaded bandpass filter to CM technique.

### 3.1.1 Resonators

Categorized by the selected frequency span, there are three types of filters, shown in Fig. 3.1. The conventional definition of the cutoff frequency is where the magnitude is 3 dB lower than the maximum magnitude. Bandpass filters only allow the signal in between the two cutoff frequencies to pass. This thesis integrates the bandpass filtering function (Fig. 3.1 (b)) into the couplers and SPJs.

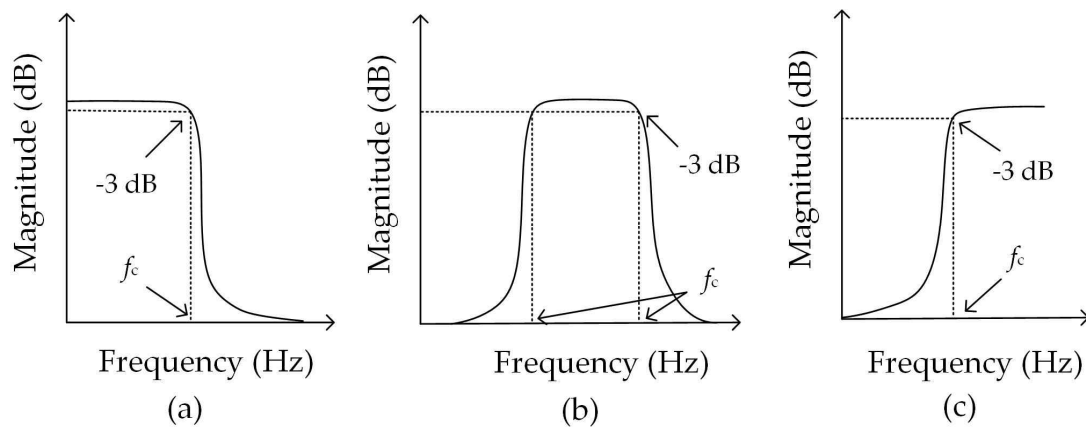


Fig. 3.1. Three types of filters. (a) Lowpass. (b) Bandpass. (c) Highpass.  $f_c$  stands for cut-off frequency.

The fundamental components of bandpass filters are resonators. Conventional LC resonators are formed by one inductor ( $L$ ), one capacitor ( $C$ ) and one resistor

( $R$ ) if the resonator is lossy. There are two types of LC resonators. One is series and the other is parallel, given in Fig. 3.2 [2].  $Z_{in}$  is the input impedance, which can be calculated by (3.1).

$$Z_{in}^{series} = R + j\omega L - \frac{j}{\omega C} \quad (3.1a)$$

$$Z_{in}^{parallel} = \left( \frac{1}{R} + \frac{1}{j\omega L} + j\omega C \right)^{-1} \quad (3.1b)$$

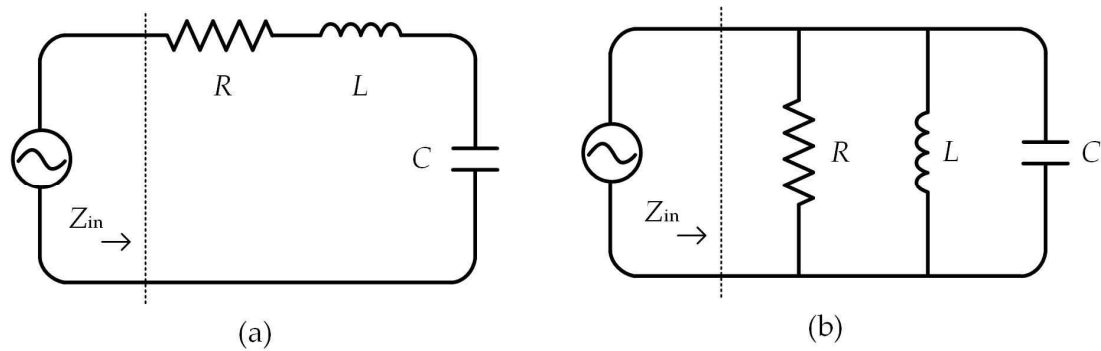


Fig. 3.2. Concept of the basic LC resonators. (a) Series LC resonator. (b) Parallel LC resonator.

(3.1) reveals that the input impedance is not only related to the value of the elements, but also to the angular frequency, which is represented by  $\omega$ .  $\omega = 2\pi \times f$ . The graph of input impedance versus frequency is plotted in Fig. 3.3. The

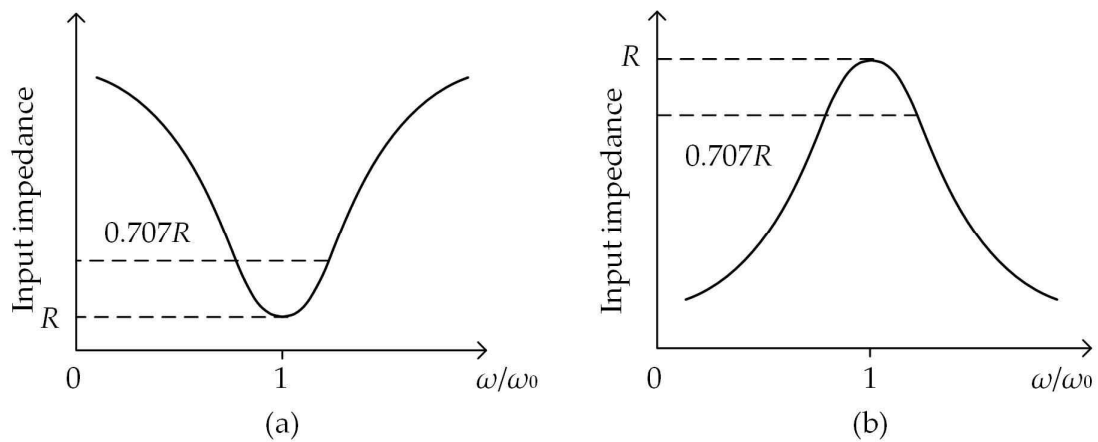


Fig. 3.3. Relationship between input impedance and frequency of series resonators and parallel resonators. (a) Series resonators. (b) Parallel resonators.

energy stored in the inductor is magnetic, while in the capacitor is electric. When the two restored powers are equal, resonance happens. In this situation, the input impedance hits its valley (in a series resonator) or the peak (in a parallel resonator), and  $\omega = 1 / \sqrt{LC}$ ,  $Z_{in} = R$ .

### 3.1.2 Lowpass to Bandpass Filters

Generally, a cascaded bandpass filter is synthesized from a lowpass prototype. The first procedure is using transfer function to describe the magnitude response of the filter. The transfer function is defined as:

$$|S_{21}(j\Omega)|^2 = \frac{1}{1 + \varepsilon^2 F_n^2(\Omega)} \quad (3.2)$$

$\varepsilon$  is the ripple constant,  $F_n(\Omega)$  is a function of the filter characteristic. Different from  $\omega$ , which is positive real angular frequency for practical situation.  $\Omega$  is angular frequency exclusively for prototype filter (centred at 0 Rad/s). According to the transfer function, filters are conventionally categorized into (1) Maximally flat, (2) Equal ripple (Chebyshev), and (3) Elliptic function. Only Chebyshev will be detailed here since it was adopted in this thesis. The transfer function of the Chebyshev filter is:

$$|S_{21}(j\Omega)|^2 = \frac{1}{1 + \varepsilon^2 T_n^2(\Omega)} \quad (3.3)$$

$\varepsilon$  is the ripple constant, written as:

$$\varepsilon = \sqrt{10^{\frac{L_{Ar}}{10}} - 1} \quad (3.4)$$

$L_{Ar}$  is a given passband ripple in dB.  $T_n(\Omega)$  is the first kind of Chebyshev

function with order  $n$ , which is:

$$T_n(\Omega) = \begin{cases} \cos(n \cos^{-1} \Omega) & |\Omega| \leq 1 \\ \cosh(n \cosh^{-1} \Omega) & |\Omega| \geq 1 \end{cases} \quad (3.5)$$

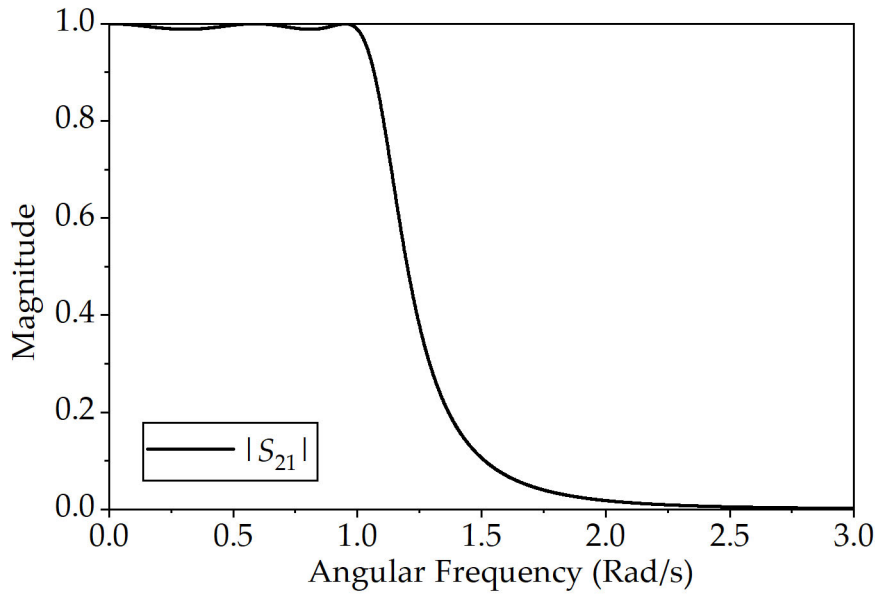


Fig. 3.4.  $|S_{21}|$  of a fifth-order Chebyshev lowpass filter.

By applying (3.3), the magnitude response of a fifth-order Chebyshev lowpass filter with 0.1-dB ripple is given as an example, shown in Fig. 3.4. It can be noticed that there are ripples in the passband.

Keeping the transfer function in mind, the next step is finding the component values in a lowpass prototype, as given in Fig. 3.5. Serial inductor and parallel capacitor are placed alternatively in the prototype. There are dual prototype filters with same responses. Which type to use depends on whether the circuit is led by an inductor or a capacitor. The last components are also different according to different orders.  $g_0$  to  $g_{n+1}$  represent the element values of the lowpass topology filter. For Chebyshev lowpass prototype filters, they are:

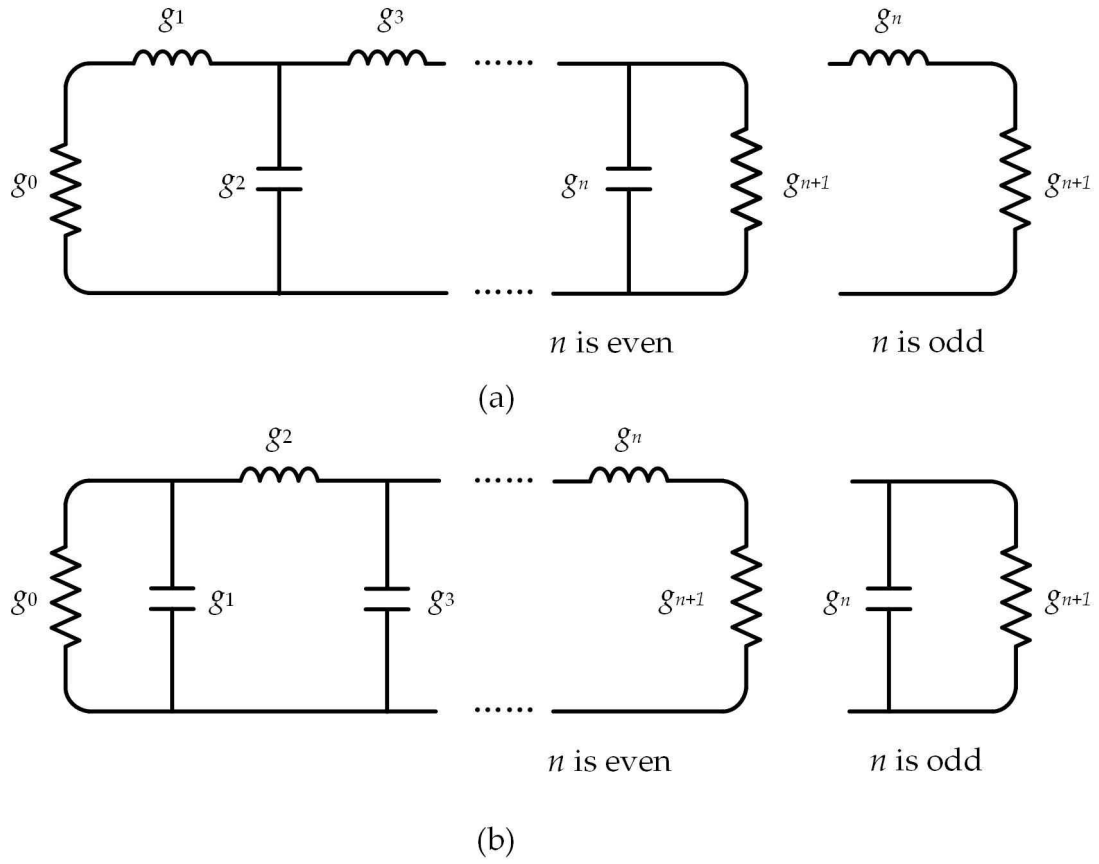


Fig. 3.5. Two types of  $N^{\text{th}}$ -order lowpass prototype filter. The two types are dual.

$$\begin{aligned}
 g_0 &= 1.0 \\
 g_1 &= \frac{2}{\gamma_0} \sin\left(\frac{\pi}{2n}\right) \\
 g_i &= \frac{1}{g_{i-1}} \times \frac{4 \sin\left[\frac{(2i-1)\pi}{2n}\right] \sin\left[\frac{(2i-3)\pi}{2n}\right]}{\gamma_0^2 + \sin^2\left[\frac{(i-1)\pi}{n}\right]} \text{ for } i = 2, 3, \dots, n \\
 g_{n+1} &= \begin{cases} 1.0 & \text{for } n \text{ is odd} \\ \coth^2\left(\frac{\beta}{4}\right) & \text{for } n \text{ is even} \end{cases}
 \end{aligned} \tag{3.6}$$

where:

$$\begin{cases} \beta = \ln \left[ \coth \left( \frac{L_{Ar}}{17.37} \right) \right] \\ \gamma = \sinh \left( \frac{\beta}{2n} \right) \end{cases} \tag{3.7}$$

$$\gamma_0 = \begin{cases} Z_0 / g_0 & \text{for } g_0 \text{ being the resistance} \\ g_0 / Y_0 & \text{for } g_0 \text{ being the conductance} \end{cases} \quad (3.8)$$

$Z_0$  and  $Y_0$  are the terminating impedance or admittance, respectively.

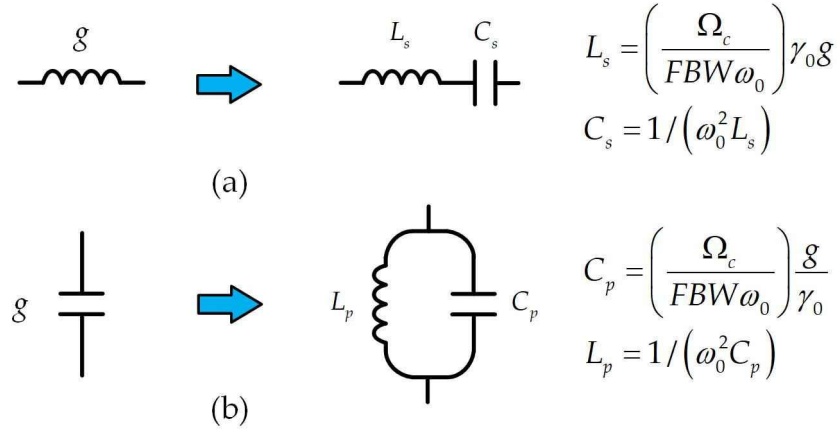


Fig. 3.6. Lowpass prototype to band pass transform. (a) Inductor to series resonator. (b) Capacitor to parallel resonator.

Now the construction of the bandpass filter is transforming the lowpass prototype into the bandpass filter. In [3], a transform method was introduced, given in Fig. 3.6. A series inductor in a lowpass prototype can be transformed into a series resonator, and a parallel capacitor can be transformed into a parallel resonator. The values of the transformed elements are also given in Fig.

3.6. Note  $FBW$  represents the fractional bandwidth, which is:

$$FBW = \frac{\omega_2 - \omega_1}{\omega_0} \quad (3.9)$$

$\omega_2$  and  $\omega_1$  is the higher and lower cutoff angular frequency of the passband (practical circuits),  $\omega_0$  is the center angular frequency.  $\Omega_c$  is the cutoff angular frequency in prototype filter, which is 1 Rad/s. The transformed bandpass filters also have two types, given in Fig. 3.7.

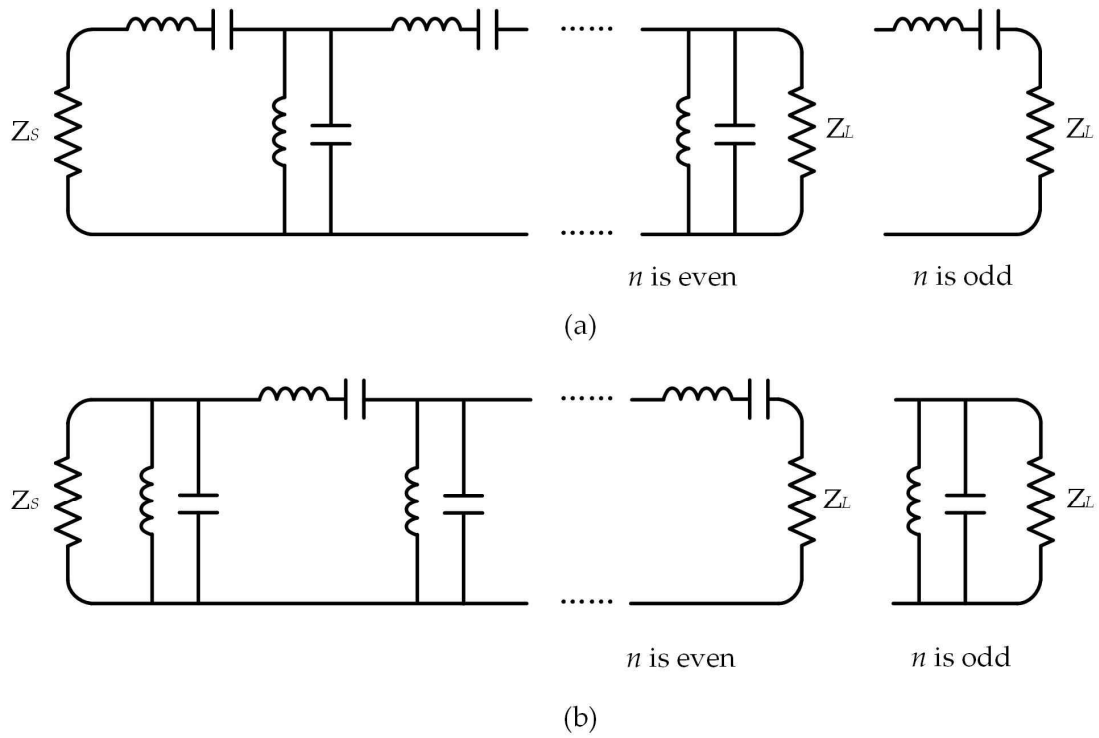


Fig. 3.7. Bandpass filter (a) and its dual (b).

### 3.1.3 $J/K$ Inverters in Filters

The preceding section gave the basic concept of building a cascaded bandpass filter from a lowpass prototype. The bandpass filter is formed by series resonators and parallel resonators placed alternately. In realization, the same resonator type is preferred for simple implementation.  $J/K$  inverters are used to transform a series/parallel resonator into a parallel/series resonator, making the

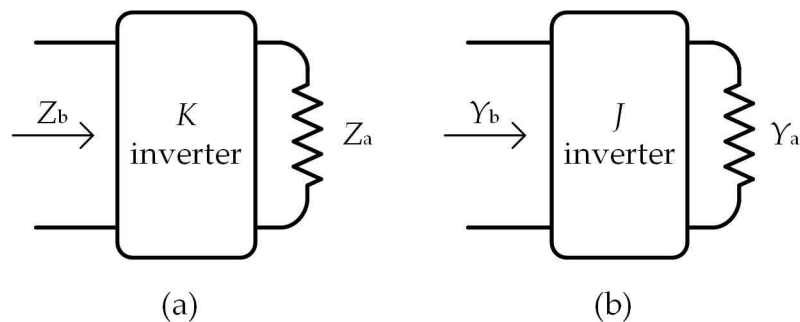


Fig. 3.8.  $J/K$  inverters. (a) A  $K$  inverter terminated by a resistor with impedance  $Z_a$  and (b) A  $J$  inverter terminated by a resistor with admittance  $Y_a$ .

resonators the same type.  $J/K$  inverters are two-port frequency-invariant devices, shown in Fig. 3.8. A resistor with impedance  $Z_a$  is in Fig. 3.8 (a), and a resistor with admittance  $Y_a$  is in Fig. 3.8 (b). A  $K$  inverter and a  $J$  inverter are placed in Fig. 3.8 (a) and (b), respectively.  $Z_b$  is the input impedance,  $Y_b$  is the input admittance. The transformation by the inverters is:

$$\begin{cases} Z_b = \frac{K^2}{Z_a} \\ Y_b = \frac{J^2}{Y_a} \end{cases} \quad (3.10)$$

From (3.10), a  $K$  inverter converts a series resistor into parallel resistor, and a  $J$  inverter converts a parallel resistor into a series resistor. Similarly, in filter design,  $K$  inverters convert series elements into parallel ones,  $J$  inverters convert parallel elements into series ones, illustrated in Fig. 3.9. The ABCD matrix of  $J/K$  inverters is given by (3.11) and (3.12).

$$\begin{bmatrix} A & B \\ C & D \end{bmatrix}_{K\text{-inverter}} = \begin{bmatrix} 0 & \mp jK \\ \pm \frac{1}{jK} & 0 \end{bmatrix} \quad (3.11)$$

$$\begin{bmatrix} A & B \\ C & D \end{bmatrix}_{J\text{-inverter}} = \begin{bmatrix} 0 & \pm \frac{1}{jJ} \\ \mp jJ & 0 \end{bmatrix} \quad (3.12)$$

In practice, this can be realized by a one-quarter-wavelength transmission line with impedance  $K$  or admittance  $J$ .



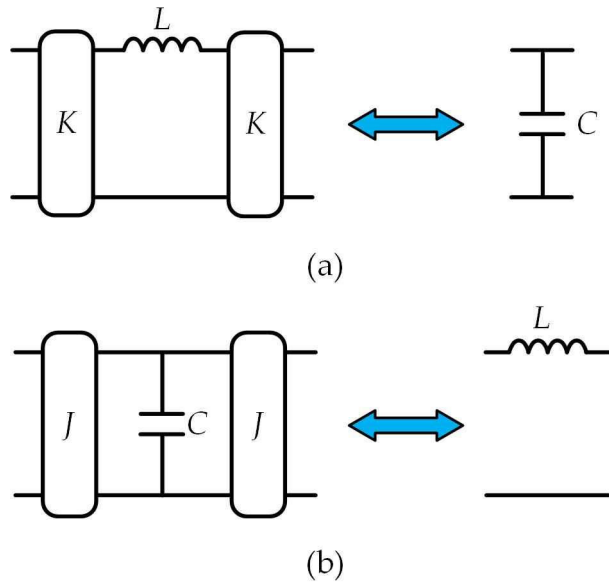


Fig. 3.9.  $J/K$  inverters that transfers an element into its dual. (a) Two  $K$  inverters transfer a series inductor to a parallel capacitor. (b) Two  $J$  inverters transfer a parallel capacitor into a series inductor.

With the inverters, the bandpass filter given in Fig. 3.7 can be transformed into the one in Fig. 3.10. The inverters separate the resonators and transform the

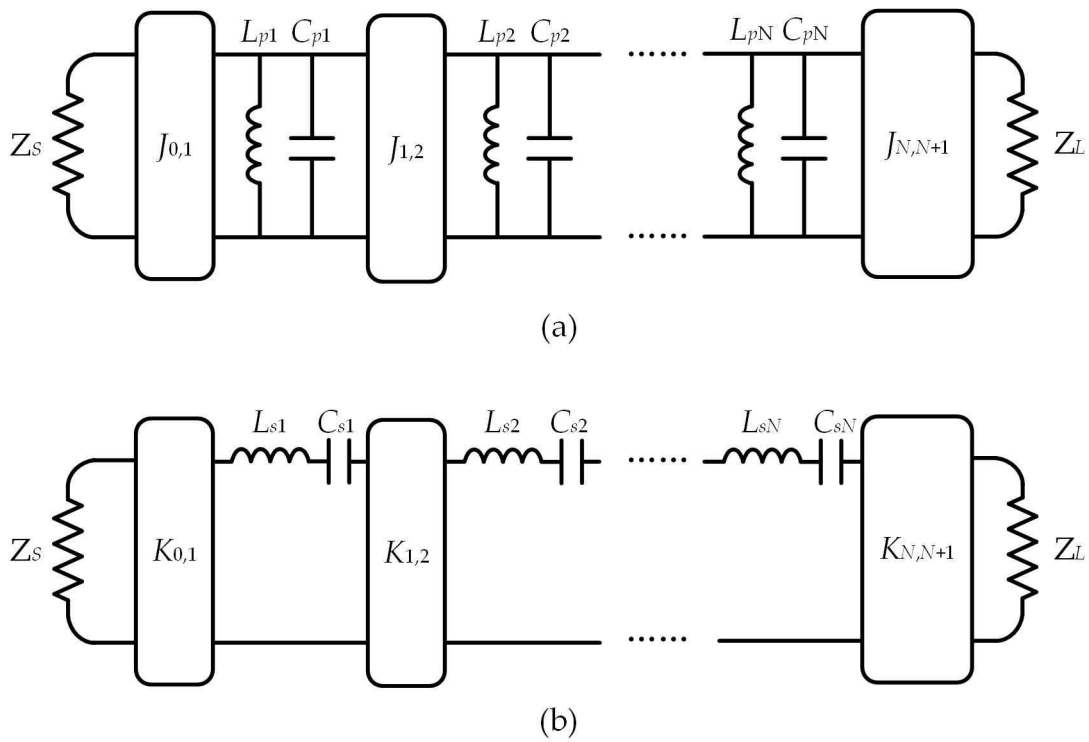


Fig. 3.10.  $N^{\text{th}}$ -order bandpass filter. (a) Parallel resonators with  $J$  inverters. (b) Series resonators with  $K$  inverters.

dual resonators into one type. The values of the inverters depend on the working frequency and the values of the adjacent components, which are [3]:

$$\begin{cases} J_{0,1} = \sqrt{\frac{Y_0 FBW \omega_0 C_{p1}}{\Omega_c g_0 g_1}} \\ J_{i,i+1} = \frac{FBW \omega_0}{\Omega_c} \sqrt{\frac{C_{pi} C_{p(i+1)}}{g_i g_{i+1}}} \\ J_{N,N+1} = \sqrt{\frac{Y_L FBW \omega_0 C_{pn}}{\Omega_c g_N g_{N+1}}} \end{cases} \quad \begin{matrix} \\ i=1 \text{ to } N-1 \\ \end{matrix} \quad (3.13)$$

$$\begin{cases} K_{0,1} = \sqrt{\frac{Z_0 FBW \omega_0 L_{s1}}{\Omega_c g_0 g_1}} \\ K_{i,i+1} = \frac{FBW \omega_0}{\Omega_c} \sqrt{\frac{L_{si} L_{s(i+1)}}{g_i g_{i+1}}} \\ K_{N,N+1} = \sqrt{\frac{Z_L FBW \omega_0 L_{sN}}{\Omega_c g_N g_{N+1}}} \end{cases} \quad \begin{matrix} \\ i=1 \text{ to } N-1 \\ \end{matrix} \quad (3.14)$$

It can be noticed that the values of  $J/K$  inverters are related to the LC values of the resonators. The LC values are arbitrary, provided  $\omega_0 = 1 / \sqrt{L_{pi} C_{pi}}$ ,  $i = 1$  to  $N$  in parallel resonators and  $\omega_0 = 1 / \sqrt{L_{si} C_{si}}$ ,  $i = 1$  to  $N$  in series resonators.  $FBW$  is fractional bandwidth defined in (3.9),

The conventional way of synthesizing a cascaded LC bandpass filter is introduced above. Filters can have many other topologies other than the cascaded. The CM technique is a powerful tool to synthesize all possibilities of filters. This is detailed in the next section.

## 3.2 Coupling Matrix

The above section gave the information on the synthesis of cascaded bandpass

filters based on the lowpass prototypes. This conventional method has limitation as it can only be applied to cascaded filter synthesis. Coupling matrix (CM), as a powerful filter synthesis method, has been widely used in modeling filtering circuits since the first report in [4]. Unlike in the cascaded filter topology, where the resonators only form a line through  $J/K$  inverters, the resonators can couple with each other, leading to various topologies. Under the concept of CM, the  $J/K$  inverters can be regarded as couplings. As the name suggests, CM represents a filtering circuit using a matrix. All the resonators and couplings in the circuit can be represented in one square matrix. The diagonal entries of the matrix are related to the resonant frequencies of the resonators, while the other entries represent the couplings.

Generally, there are two forms of CMs for a two port circuit. One is  $N \times N$  [5], the other is  $N+2$  [6]. The  $N \times N$  CM is primary. Each port in  $N \times N$  CM is bounded with only one resonator. The  $N+2$  is advanced as one port can couple to multiple resonators and even the other port. It also can be expanded to multi-port situations. The  $N \times N$  CM is to be introduced first for the understanding of the concept. The  $N+2$  CM will also be detailed. The  $N+X$  CM is an extension from the  $N+2$  CM as it expands the port number to  $X$  ( $X > 3$ ). The CM applied in this thesis is  $N+X$  one.

### 3.2.1 $N \times N$ Coupling Matrix

Unlike the cascaded filter, a filter that applies a CM has more flexibility. Fig. 3.11 shows an equivalent circuit of a filter with  $n$  LC resonators. The resonators are coupled through mutual inductances in Fig. 3.11.  $e_s$  on the left side is the

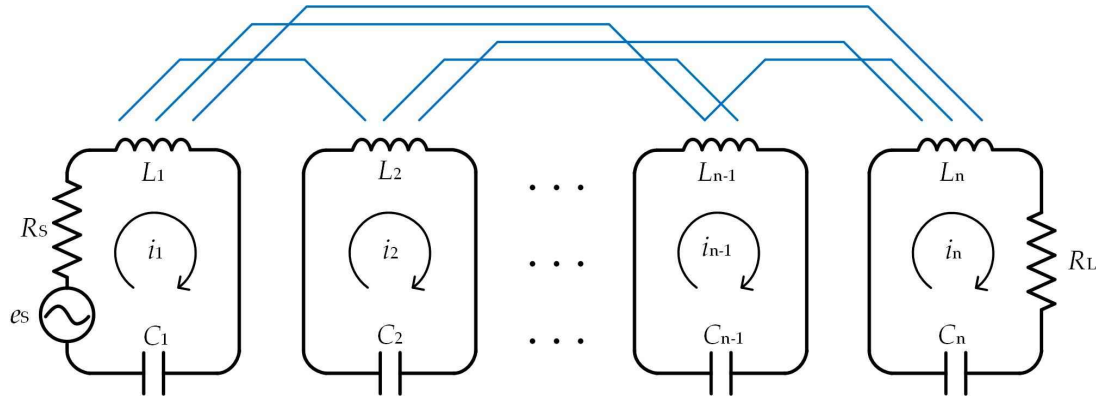


Fig. 3.11. Equivalent circuits of a filter with  $n$  resonators. The resonators are coupled by inductances.

source, and  $R_s$  is the impedance of the source.  $R_L$  on the right represents the load. The LC resonators with capacitors ( $C_1$  to  $C_n$ ) and inductors ( $L_1$  to  $L_n$ ) represent Resonator 1, 2, ...  $n-1$  and  $n$ . The loop current in the resonator is marked as  $i_n$ . Resonators in Fig. 3.11 are coupled through mutual inductances (depicts by blue lines), which means the loop current in one resonator will be influenced by other LC resonators. For instance, for Resonator 1, the mutual inductances are  $L_{(1,2)}$ ,  $L_{(1,3)}$ , ...,  $L_{(1,n)}$ .

Apply Kirchhoff's voltage law to every LC loop gives:

$$\left\{ \begin{array}{l} \left( R_s + \frac{1}{j\omega C_1} + j\omega L_1 \right) i_1 - j\omega L_{1,2} i_2 \cdots - j\omega L_{1,n-1} i_{n-1} - j\omega L_{1,n} i_n = e_s \\ -j\omega L_{1,2} i_1 + \left( \frac{1}{j\omega C_2} + j\omega L_2 \right) i_2 \cdots - j\omega L_{2,n-1} i_{n-1} - j\omega L_{2,n} i_n = 0 \\ \vdots \\ -j\omega L_{1,n-1} i_1 - j\omega L_{2,n-1} i_2 \cdots + \left( \frac{1}{j\omega C_{n-1}} + j\omega L_{n-1} \right) i_{n-1} - j\omega L_{n-1,n} i_n = 0 \\ -j\omega L_{1,n} i_1 - j\omega L_{2,n} i_2 \cdots - j\omega L_{n-1,n} i_{n-1} + \left( R_L + \frac{1}{j\omega C_n} + j\omega L_n \right) i_n = 0 \end{array} \right. \quad (3.15)$$

This equation set can be rewritten in matrix form:

$$\left[ \begin{array}{cccc} \left( R_s + \frac{1}{j\omega C_1} + j\omega L_1 \right) & -j\omega L_{1,2} & \cdots & -j\omega L_{1,n} \\ -j\omega L_{1,2} i_1 & \left( \frac{1}{j\omega C_2} + j\omega L_2 \right) & \cdots & -j\omega L_{2,n} \\ \vdots & \vdots & \vdots & \vdots \\ -j\omega L_{1,n} & -j\omega L_{2,n} & \cdots & \left( R_L + \frac{1}{j\omega C_n} + j\omega L_n \right) \end{array} \right] \begin{bmatrix} i_1 \\ i_2 \\ \vdots \\ i_n \end{bmatrix} = \begin{bmatrix} e_s \\ 0 \\ \vdots \\ 0 \end{bmatrix} \quad (3.16)$$

or:

$$[Z][i] = [e] \quad (3.17)$$

To simplify the analysis, all the resonators are assumed synchronous, which

means they resonate at the same frequency  $\omega_0 = 1/\sqrt{LC}$ , and:

$$\begin{cases} L_1 = L_2 = \cdots = L_n = L \\ C_1 = C_2 = \cdots = C_n = C \end{cases} \quad (3.18)$$

Also, assuming the bandwidth is narrow, which means  $\omega \approx \omega_0$ . Then,  $[Z]$

can be normalized into:

$$[Z] = \omega_0 L \cdot FBW \cdot [\bar{Z}] \quad (3.19)$$

where  $\omega_0 = 2\pi f_0$ .  $f_0$  is the resonant frequency of the resonators. Now  $[\bar{Z}]$  can

be finally represented by:

$$\left[\bar{Z}\right] = \begin{bmatrix} \frac{1}{q_{e_s}} & 0 & \cdots & 0 \\ 0 & 0 & \cdots & 0 \\ \vdots & \vdots & \vdots & \vdots \\ 0 & 0 & \cdots & \frac{1}{q_{e_L}} \end{bmatrix} + p \begin{bmatrix} 1 & 0 & \cdots & 0 \\ 0 & 0 & \cdots & 0 \\ \vdots & \vdots & \vdots & \vdots \\ 0 & 0 & \cdots & 1 \end{bmatrix} - j \begin{bmatrix} m_{1,1} & m_{1,2} & \cdots & m_{1,n} \\ m_{2,1} & m_{2,2} & \cdots & m_{2,n} \\ \vdots & \vdots & \vdots & \vdots \\ m_{n,1} & m_{n,2} & \cdots & m_{n,n} \end{bmatrix} \quad (3.20)$$

in which:

$$p = j \frac{1}{FBW} \left( \frac{\omega}{\omega_0} - \frac{\omega_0}{\omega} \right) \quad (3.21)$$

$$q_{e_i} = \frac{\omega_0 L}{R_i} FBW \quad \text{for } i = S, L \quad (3.22)$$

$$m_{i,j} = \frac{L_{i,j}}{L} \cdot \frac{1}{FBW} \quad (3.23)$$

In (3.21)  $\omega$  is the resonant angular frequency, which is assumed to vary in a small range. In (3.22) and (3.23),  $q_{ei}$  is the scaled external quality factor, and  $m_{ij}$  is the normalized coupling coefficient between Resonator  $i$  and  $j$ . They can be obtained through:

$$\begin{cases} q_{e_i} = Q_{e_i} \cdot FBW \\ m_{i,j} = \frac{M_{i,j}}{FBW} \end{cases} \quad (3.24)$$

$Q_{ei}$  is the external quality factor;  $M$  is the coupling coefficient.

For the case of filters coupled by mutual capacitances, shown in Fig. 3.12, the normalized  $[Y]$  can be represented by (3.25).

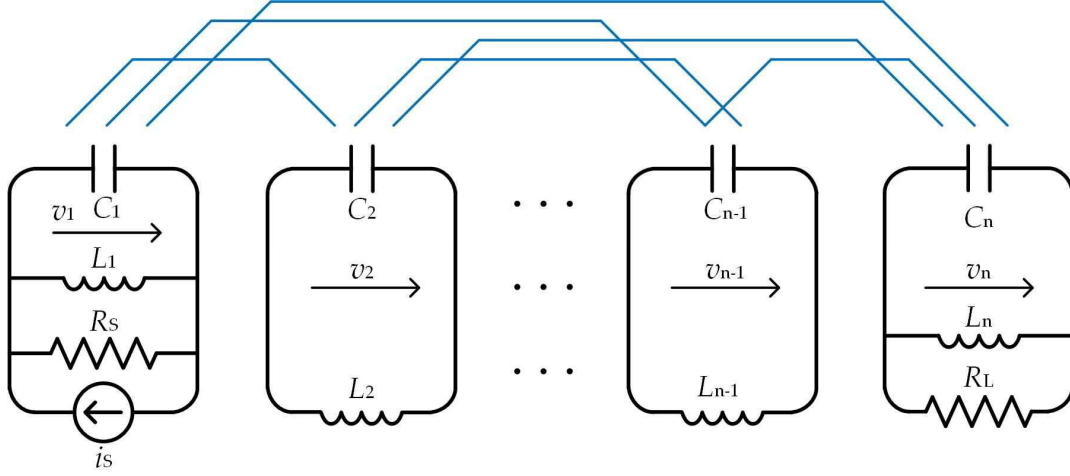


Fig. 3.12. Equivalent circuits of a filter with  $n$  resonators. The resonators are coupled by capacitances.

$$[\bar{Y}] = \begin{bmatrix} \frac{1}{q_{e_s}} & 0 & \cdots & 0 \\ 0 & 0 & \cdots & 0 \\ \vdots & \vdots & \vdots & \vdots \\ 0 & 0 & \cdots & \frac{1}{q_{e_L}} \end{bmatrix} + p \begin{bmatrix} 1 & 0 & \cdots & 0 \\ 0 & 0 & \cdots & 0 \\ \vdots & \vdots & \vdots & \vdots \\ 0 & 0 & \cdots & 1 \end{bmatrix} - j \begin{bmatrix} m_{1,1} & m_{1,2} & \cdots & m_{1,n} \\ m_{2,1} & m_{2,2} & \cdots & m_{2,n} \\ \vdots & \vdots & \vdots & \vdots \\ m_{n,1} & m_{n,2} & \cdots & m_{n,n} \end{bmatrix} \quad (3.25)$$

$[\bar{Z}]$  and  $[\bar{Y}]$  share the same form and same parameters. Thus, they can be replaced by  $[\bar{A}]$ . The  $S$ -parameters of the filter can be derived from  $[\bar{A}]$  [5]:

$$S_{21} = \frac{2}{\sqrt{q_{e_s} \cdot q_{e_L}}} [\bar{A}]_{n,1}^{-1} \quad (3.26)$$

$$S_{11} = 1 - \frac{2}{q_{e_s}} [\bar{A}]_{1,1}^{-1}$$

where:

$$[\bar{A}] = \begin{bmatrix} \frac{1}{q_{e_s}} & 0 & \cdots & 0 \\ 0 & 0 & \cdots & 0 \\ \vdots & \vdots & \vdots & \vdots \\ 0 & 0 & \cdots & \frac{1}{q_{e_L}} \end{bmatrix} + p \begin{bmatrix} 1 & 0 & \cdots & 0 \\ 0 & 0 & \cdots & 0 \\ \vdots & \vdots & \vdots & \vdots \\ 0 & 0 & \cdots & 1 \end{bmatrix} - j \begin{bmatrix} m_{1,1} & m_{1,2} & \cdots & m_{1,n} \\ m_{2,1} & m_{2,2} & \cdots & m_{2,n} \\ \vdots & \vdots & \vdots & \vdots \\ m_{n,1} & m_{n,2} & \cdots & m_{n,n} \end{bmatrix} \quad (3.27)$$

The third term in (3.27) is called  $N \times N$  CM.  $q$ ,  $p$ , and  $m$  are defined as soon as

the filter's magnitude response is specified. For a cascaded Chebyshev filter,  $q$ ,  $p$ , and  $m$  can be derived from the lumped-element low-pass prototype elements  $g_0, g_1, \dots, g_{n+1}$  in (3.28).

$$q_{e_s} = g_0 \cdot g_1 \quad (3.28a)$$

$$q_{e_L} = g_n \cdot g_{n+1} \quad (3.28b)$$

$$m_{i,i+1} = \frac{1}{\sqrt{g_i g_{i+1}}}, \quad i = 1 \text{ to } n-1 \quad (3.28c)$$

This form of CM can be applied in the synthesis where the number of ports is two and each port is bounded to only one resonator. For filters with more complexity,  $N+2$  CM is normally used. The “2” in the name means “2 ports”. This matrix also can be extended to a multi-port situation.

### 3.2.2 $N+2$ Coupling Matrix

The previous section gives the detail of the  $N \times N$  CM. For a filter with couplings between ports and resonators, it needs an  $N+2$  coupling matrix for

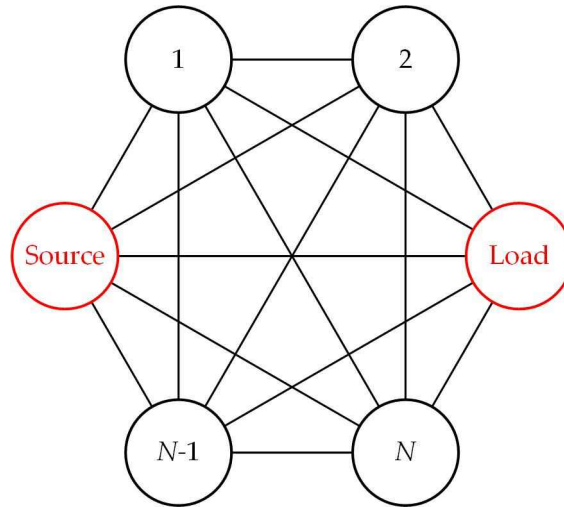


Fig. 3.13. Topology with  $N$  resonators and two ports. It contains all possible couplings between the nodes, depicted by solid lines.



synthesizing. Fig. 3.13 gives a generalised two-port topology with all the possible couplings. The solid lines indicate the couplings. These extra couplings add two extra rows and columns to the original  $N \times N$  CM, shown in Fig. 3.14. The center  $N \times N$  square matrix, highlighted in deep blue, is the same as in (3.27). The periphery of the CM is the couplings related to the ports, which are shown in light blue. The couplings to ports are represented by external  $Q$ , and the relationships between external  $Q$  and couplings are:

$$Q_{e,S,i} = \frac{1}{m_{S,i}^2 FBW} \quad (3.29a)$$

$$Q_{e,L,i} = \frac{1}{m_{L,i}^2 FBW} \quad (3.29b)$$

$i = 1, 2, \dots, N$ . The  $S$ -parameters of the filter can be deduced from (3.30) [3].

$$S_{11} = 1 - 2[A]_{11}^{-1} \quad (3.30a)$$

$$S_{21} = 2[A]_{21}^{-1} \quad (3.30b)$$

	Source	1	2	...	$N$	Load
Source	0	$m_{S,1}$	$m_{S,2}$	$m_{S,\dots}$	$m_{S,N}$	$m_{S,L}$
1	$m_{1,S}$	$m_{1,1}$	$m_{1,2}$	$m_{1,\dots}$	$m_{1,N}$	$m_{1,L}$
2	$m_{2,S}$	$m_{2,1}$	$m_{2,2}$	$m_{2,\dots}$	$m_{2,N}$	$m_{2,L}$
...	$m_{\dots,S}$	$m_{\dots,1}$	$m_{\dots,2}$	$m_{\dots,\dots}$	$m_{\dots,N}$	$m_{\dots,L}$
$N$	$m_{N,S}$	$m_{N,1}$	$m_{N,2}$	$m_{N,\dots}$	$m_{N,N}$	$m_{N,L}$
Load	$m_{L,S}$	$m_{L,1}$	$m_{L,2}$	$m_{L,\dots}$	$m_{L,N}$	0

Fig. 3.14.  $N+2 \times N+2$  coupling matrix of an  $N^{\text{th}}$ -order bandpass filter.

$$[A] = [X] + j \times \Omega [U] - j[m] \quad (3.30c)$$

Similarly,  $[A]$  is composed of three matrices.  $[m]$  is the  $N+2$  CM shown in Fig. 3.14.  $[X]$  is related to normalized nodes impedance and  $[U]$  is related to node resonant frequency, detailed in Fig. 3.15, both are  $N+2$  squares.  $[X]$  is a zero matrix except for the entries at  $m_{S,S}$  and  $m_{L,L}$ , which are 1.  $[U]$  is a unit

$$[X] = \begin{bmatrix} 1 & 0 & \cdots & 0 & 0 \\ 0 & 0 & \cdots & 0 & 0 \\ \vdots & \vdots & \ddots & \vdots & \vdots \\ 0 & 0 & \cdots & 0 & 0 \\ 0 & 0 & \cdots & 0 & 1 \end{bmatrix} \quad [U] = \begin{bmatrix} 0 & 0 & \cdots & 0 & 0 \\ 0 & 1 & \cdots & 0 & 0 \\ \vdots & \vdots & \ddots & \vdots & \vdots \\ 0 & 0 & \cdots & 1 & 0 \\ 0 & 0 & \cdots & 0 & 0 \end{bmatrix}$$

$\underbrace{\hspace{10em}}_{N \text{ columns}} \quad \underbrace{\hspace{10em}}_{N \text{ columns}}$

Fig. 3.15.  $[X]$  and  $[U]$  matrix.

matrix except for the entries at  $m_{S,S}$  and  $m_{L,L}$ , which are 0.  $\Omega$  is the normalized angular frequency, which is:

$$\Omega = \frac{1}{FBW} \left( \frac{\omega}{\omega_0} - \frac{\omega_0}{\omega} \right) \quad (3.31)$$

### 3.2.3 $N+X$ Coupling Matrix

The  $N+2$  matrix can be expanded to a multi-port scenario. A computer-aided diplexer design was reported in [7], where the CM applied has three ports. The  $N+X$  CM is the same as the  $N+2$  CM but has more than two ports. The representation is given in Fig. 3.16. There are  $X$  ports and  $N$  resonators. The

	Port 1	Port 2	...	Port X	1	2	...	N
Port 1	0	0	0	0	$m_{P1,1}$	$m_{P1,2}$	...	$m_{P1,N}$
Port 2	0	0	0	0	$m_{P2,1}$	$m_{P2,2}$	...	$m_{P2,N}$
...	0	0	0	0	...	...	...	...
Port X	0	0	0	0	$m_{PX,1}$	$m_{PX,2}$	...	$m_{PX,N}$
1	$m_{1,P1}$	$m_{1,P2}$	...	$m_{1,PX}$	$m_{1,1}$	$m_{1,2}$	...	$m_{1,N}$
2	$m_{2,P1}$	$m_{2,P2}$	...	$m_{2,PX}$	$m_{2,1}$	$m_{2,2}$	...	$m_{2,N}$
...	...	...	...	...	...	...	...	...
N	$m_{N,P1}$	$m_{N,P2}$	...	$m_{N,PX}$	$m_{N,1}$	$m_{N,2}$	...	$m_{N,N}$

Fig. 3.16.  $N+X$  coupling matrix of an  $N^{\text{th}}$ -order bandpass filter.

couplings between the ports are noted in the upper left of the matrix (can be non zero). The deep blue at the lower right part representing the couplings between resonators is the same as in Fig. 3.14. The S-parameters deriving from the  $N+X$  CM are:

$$S_{X,X} = 1 - 2 \left[ A^{X-port} \right]_{X,X}^{-1} \quad (3.32a)$$

$$S_{i,j} = 2 \left[ A^{X-port} \right]_{i,j}^{-1} \quad i \neq j \quad (3.32b)$$

$$\left[ A^{X-port} \right] = \left[ X^{X-port} \right] + j \times \Omega \left[ U^{X-port} \right] - j \left[ m^{X-port} \right] \quad (3.32c)$$

$\left[ m^{X-port} \right]$  is the CM given in Fig. 3.16, and other components of  $\left[ A^{X-port} \right]$  are in Fig. 3.17. Both  $\left[ X^{X-port} \right]$  and  $\left[ U^{X-port} \right]$  are  $N+X$  square matrices. The first  $X$  diagonal entries in  $\left[ X^{X-port} \right]$  are 1 and the last  $N$  diagonal entries in  $\left[ U^{X-port} \right]$  are also 1. Other entries in the two matrices are zero.

This technique will be used in the design of the filtering couplers and filtering

$$\begin{aligned}
\left[ X^{X-port} \right] &= \begin{bmatrix} 1 & 0 & \dots & 0 & 0 & 0 & 0 & 0 \\ 0 & 1 & \dots & 0 & 0 & 0 & 0 & 0 \\ \vdots & \vdots & \ddots & \vdots & \vdots & \vdots & \vdots & \vdots \\ 0 & 0 & \dots & 1 & 0 & 0 & 0 & 0 \\ 0 & 0 & \dots & 0 & 0 & 0 & 0 & 0 \\ 0 & 0 & \dots & 0 & 0 & 0 & 0 & 0 \\ 0 & 0 & \dots & 0 & 0 & 0 & \ddots & \vdots \\ 0 & 0 & \dots & 0 & 0 & 0 & \dots & 0 \end{bmatrix} \quad \left[ U^{X-port} \right] = \begin{bmatrix} 0 & 0 & \dots & 0 & 0 & 0 & 0 & 0 \\ 0 & 0 & \dots & 0 & 0 & 0 & 0 & 0 \\ \vdots & \vdots & \ddots & \vdots & \vdots & \vdots & \vdots & \vdots \\ 0 & 0 & \dots & 0 & 0 & 0 & 0 & 0 \\ 0 & 0 & \dots & 0 & 1 & 0 & 0 & 0 \\ 0 & 0 & \dots & 0 & 0 & 1 & 0 & 0 \\ 0 & 0 & \dots & 0 & 0 & 0 & \ddots & \vdots \\ 0 & 0 & \dots & 0 & 0 & 0 & \dots & 1 \end{bmatrix} \\
&\quad \underbrace{\hspace{10em}}_{X \text{ columns}} \quad \underbrace{\hspace{10em}}_{N \text{ columns}} \quad \underbrace{\hspace{10em}}_{X \text{ columns}} \quad \underbrace{\hspace{10em}}_{N \text{ columns}}
\end{aligned}$$

Fig. 3.17.  $\left[ X^{X-port} \right]$  and  $\left[ U^{X-port} \right]$  matrices.

SPJs. Also, a novel CM technique that combines resonant and NRCs is proposed in the thesis and will be discussed in the last section of this chapter.

### 3.3 Waveguide Circuit Realization

Waveguides are one of the first practical structures invented to carry microwave transmission. Although it is often large in size compared with planar structures, the closed structure ensures the low radiation loss (caused by imperfect assembly) suitable for high-frequency application. In this thesis, waveguides are used to implement SPJs.

#### 3.3.1 Rectangular Waveguide

Rectangular waveguides are the simplest waveguide structures. They are used in a frequency range from 1 GHz to the terahertz domain. Fig. 3.18 shows a perspective view of a rectangular waveguide. It is hollow with perfect electric conductor (PEC) for walls. The main parameters are the width  $a$  and height  $b$ .

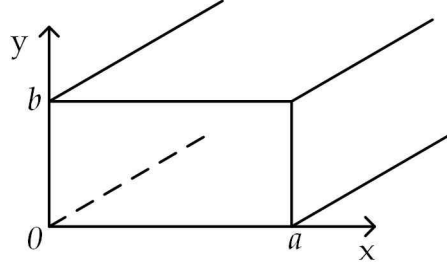


Fig. 3.18. Rectangular waveguide perspective view.

A rectangular waveguide supports two types of modes - TE mode and TM mode. Every mode in a rectangular waveguide has a cutoff frequency, which means that for a particular mode, only if the frequency is higher than the cutoff frequency can the mode propagate [2]. The cutoff frequency is defined as:

$$f_{cutoff(m,n)} = \frac{1}{2\pi\sqrt{\mu\epsilon}} \sqrt{\left(\frac{m\pi}{a}\right)^2 + \left(\frac{n\pi}{b}\right)^2} \quad (3.33)$$

$m$  and  $n$  in (3.33) depict mode  $TE_{m,n}$  or  $TM_{m,n}$ ,  $\mu$  and  $\epsilon$  are the permeability and the permittivity of the material inside the waveguide. As given in (3.33), the cutoff frequency is related to the width  $a$  and height  $b$ . The mode with the lowest cut-off frequency is called the fundamental mode. In a rectangular waveguide, the fundamental mode is  $TE_{10}$ , and its cutoff frequency is:

$$f_{cutoff(m,n)} = \frac{1}{2a\sqrt{\mu\epsilon}} \quad (3.34)$$

For a waveguide, working at the dominant mode is desired. This simplifies the response of the waveguide device as no influence of other modes occurs. The boundary condition only allows normal electric (E) field and transversal magnetic (H) field against conducting wall. The pattern of  $TE_{10}$  mode in a rectangular waveguide is shown in Fig. 3.19. Note the arrow length is not

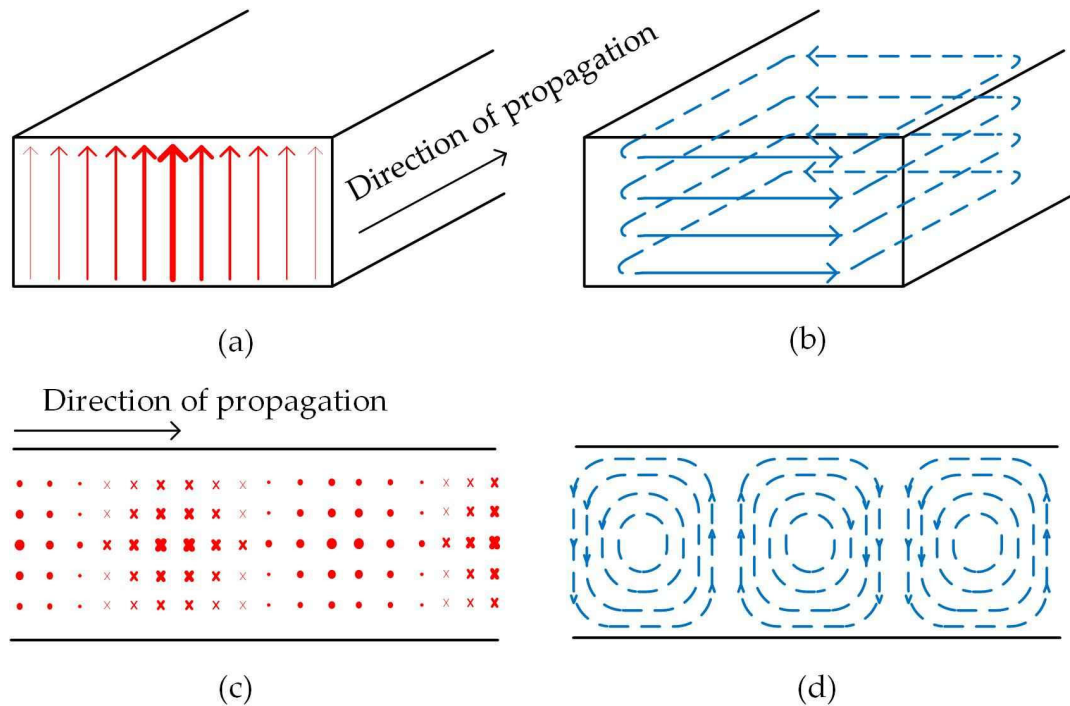


Fig. 3.19. TE<sub>10</sub> mode in a rectangular waveguide. (a) The perspective view of the E field. (b) The perspective view of the H field. (c) The top view of the E field and (d) The top view of the H field. Arrows indicate the direction of propagation.

related to the magnitude of the field.

Although ideally waveguide is closed and has no radiation loss, in practice, it is usually manufactured in a split-block fashion and assembly is required. The plane where it is split is vital for minimizing radiation loss. The radiation is caused by the interception of the surface current. The surface current is perpendicular to the H field. Fig. 3.20 gives the surface current when working at TE<sub>10</sub> mode. To split the waveguide along with z-axis, there are two directions. One is in plane “zoy” (E-plane) and the other is “zox” (H-plane). It can be noticed that at TE<sub>10</sub> mode, only when the waveguide is split in the center, through plane “zoy”, can the interception of surface current be avoided. Both

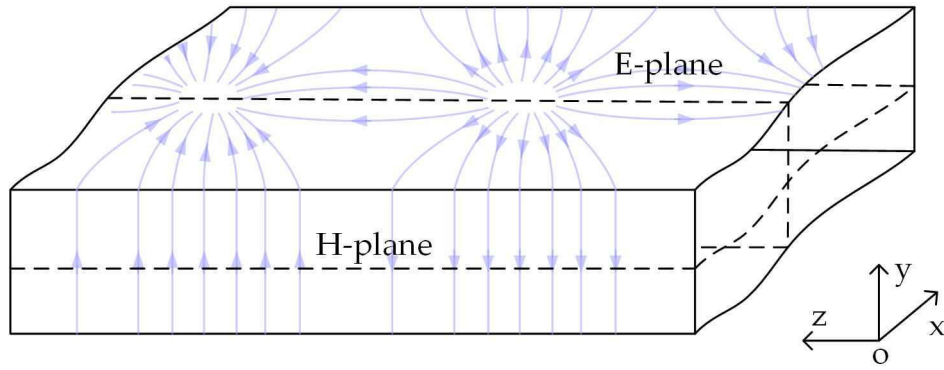


Fig. 3.20. Indication of surface current on a rectangular waveguide when working at TE<sub>10</sub> mode. The surface current is shown in light purple arrows. The black dash line depicts the E-plane and H-plane.

planes are depicted by dash lines in Fig. 3.20. This E-plane configuration was adopted in the SPJs for minimum radiation loss in this thesis.

### 3.3.2 Rectangular Waveguide Resonators/ Cavities

A chamber of rectangular waveguide (cavity) can support resonant modes. Fig. 3.21 gives a schematic of a cavity. The supported resonant frequencies for mode TE<sub>mnl</sub> or TM<sub>mnl</sub> in a cavity are related to the dimensions. The frequencies are:

$$f_{mnl} = \frac{c}{2\pi\sqrt{\mu\epsilon}} \sqrt{\left(\frac{m\pi}{a}\right)^2 + \left(\frac{n\pi}{b}\right)^2 + \left(\frac{l\pi}{d}\right)^2} \quad (3.35)$$

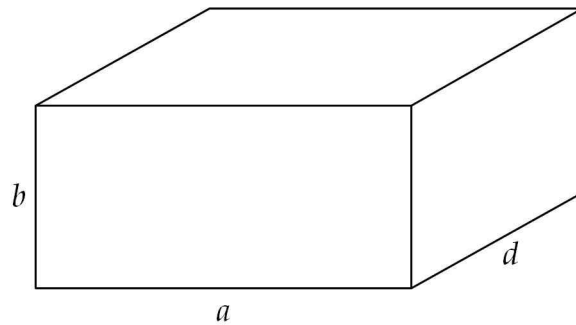


Fig. 3.21. Rectangular resonator.

The fundamental mode of a cavity is TE<sub>101</sub> mode, and its resonant frequency is:

$$f_{TE_{101}} = \frac{c}{2\pi\sqrt{\mu\epsilon}} \sqrt{\left(\frac{\pi}{a}\right)^2 + \left(\frac{\pi}{d}\right)^2} \quad (3.36)$$

It shows that in a cavity, the resonant frequency of the fundamental mode is not related to the height.

### 3.3.3 Irises and Coupling Realization

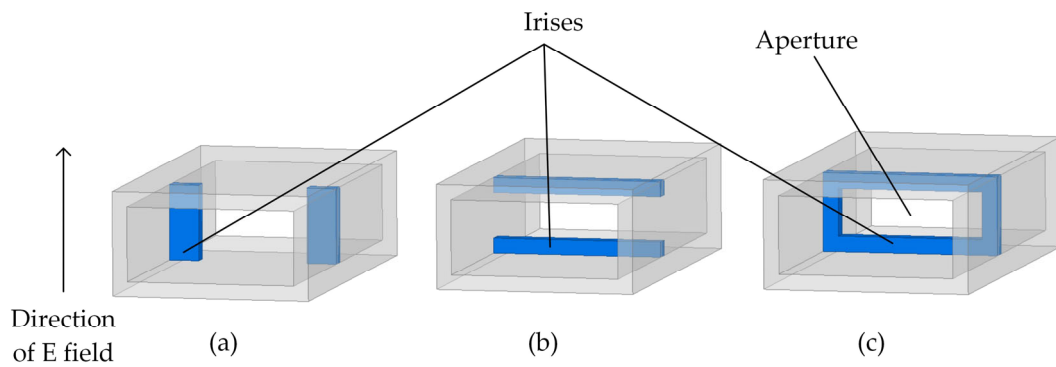


Fig. 3.22. Irises (in blue) in waveguides. (a) inductive iris, (b) capacitive iris and (c) parallel L-C iris. The direction of E field is of the fundamental mode.

Section 3.2 introduced the concept of couplings. The couplings between waveguides/cavities are realized by irises. Irises are obstacles that sit in the waveguide. There is an aperture in the iris. Parasitic elements are introduced when the wave passing through the apertures between the irises. Categorized

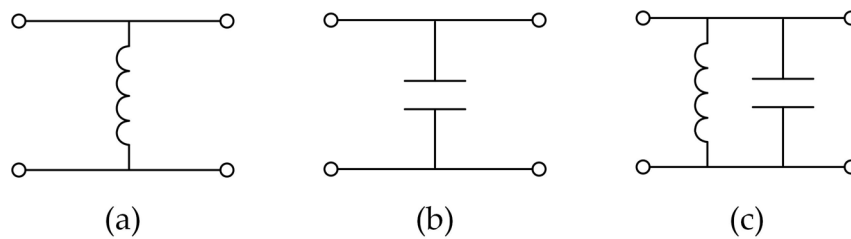


Fig. 3.23. Equivalent circuits of the irises (zero thickness). (a) a shunt inductor introduced by an inductive iris. (b) a shunt capacitor by a capacitive iris and (c) a shunt inductor and capacitor by a parallel L-C iris.



by the parasitic elements they introduced, irises can be divided into three types, that is, inductive iris, capacitive iris and parallel L-C iris, given in Fig. 3.22. The edge of inductive iris is parallel to the direction of the E field of the fundamental mode while the one of capacitive iris is perpendicular to the E field. Parallel L-C iris is the combination. When the thickness of the iris is zero, an inductive iris introduce a shunt inductor, a capacitive iris introduce a shunt capacitor and a parallel L-C iris brings both [8]. This is shown in Fig. 3.23.

Irises between resonators realize the coupling. In filter design, the most used irises are inductive iris and capacitive iris, as given in Fig. 3.24. The blue parts are apertures in the irises. To distinguish the type of coupling (inductive or capacitive) an iris brings, one can look into the resonant frequency of the even

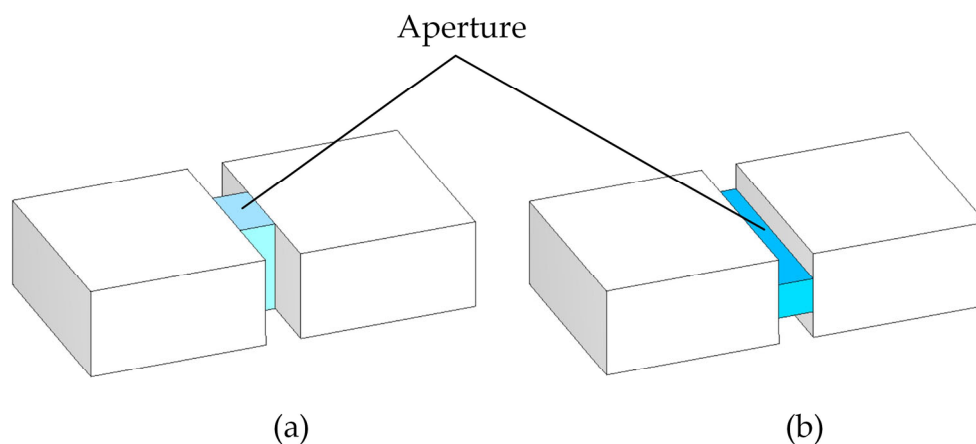


Fig. 3.24. Irises (apertures) between cavities (resonators). (a) Inductive coupling. (b) Capacitive coupling.

and odd modes. Fig. 3.25 gives the simulation model when an inductive coupling is loaded between two resonators. There are two cavities and two ports. The cavities are connected to the ports through weak couplings. With the

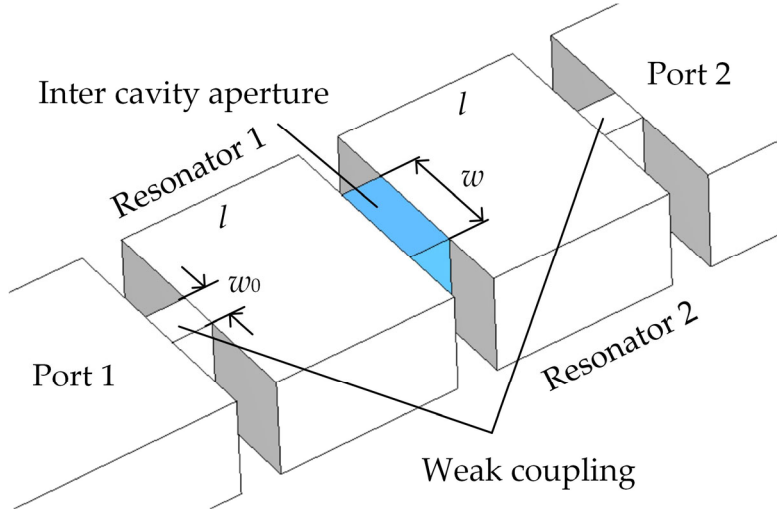


Fig. 3.25. Inter cavity aperture simulation model.

weaking couplings, there are two peaks in the simulation band in the  $|S_{21}|$ , shown in Fig. 3.26. The two peaks are corresponding to the resonant frequencies of even and odd modes. Fig. 3.27 gives the E field patterns of even and odd modes through simulation when  $w = 9.00$ ,  $l = 17.00$ ,  $w_0 = 4.00$  (unit: mm). In inductive coupling, the resonant frequency of the even mode is lower than the one of the odd mode. From 3.27, the resonant frequency of the even

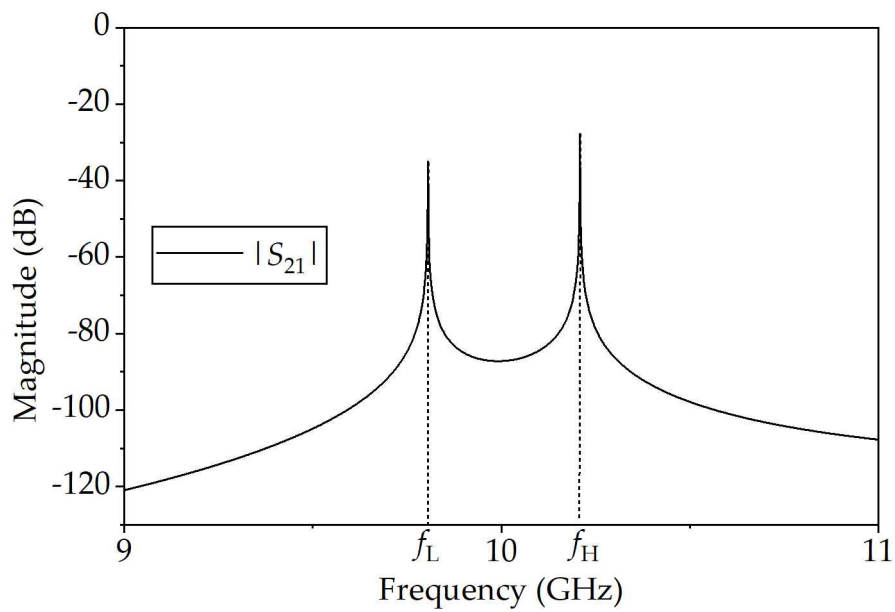


Fig. 3.26. Simulated  $|S_{21}|$  of the model in Fig. 3.25.

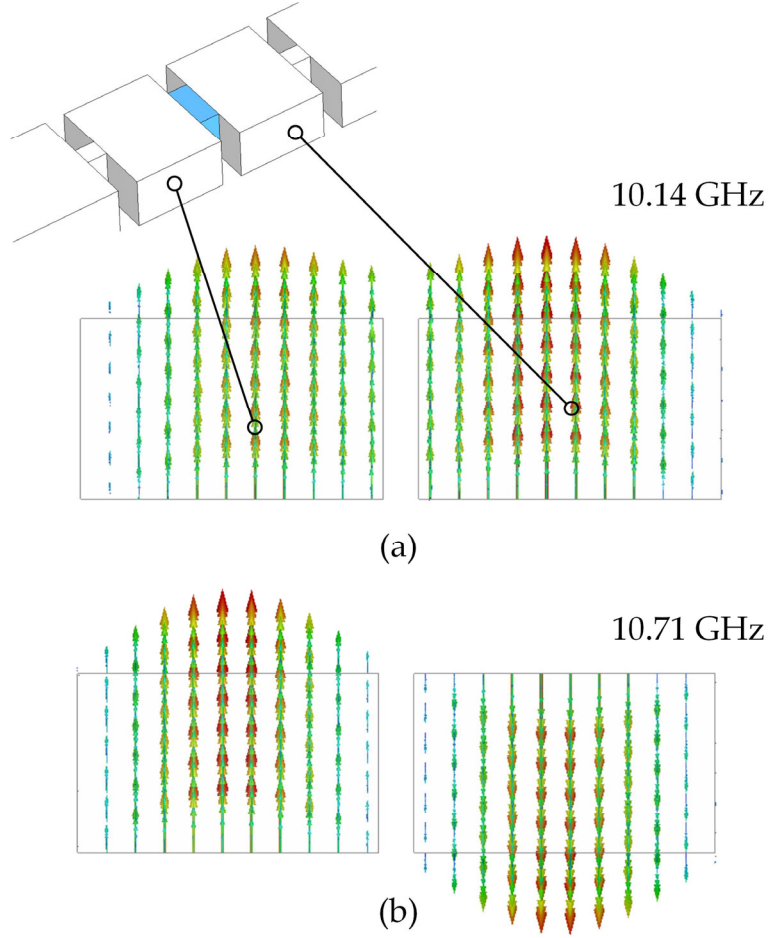


Fig. 3.27. E field patterns of the even mode (10.14 GHz) and odd mode (10.71 GHz) of the two resonators. Note the length of arrows only represents the strength of the E fields, which are confined in the resonators.

mode is 10.14 GHz while the one of the odd mode is 10.71 GHz. For capacitive coupling, the resonant frequency of the even mode is higher than the one of odd mode.

A certain coupling level can be achieved by adjusting the width of the aperture in iris ( $w$ ) and the length of the cavities ( $l$ ). In Fig. 3.26, the frequency points at the two peaks are noted  $f_L$  and  $f_H$ , and the coupling is calculated as [3]:

$$M = \frac{f_H^2 - f_L^2}{f_H^2 + f_L^2} \quad (3.37)$$

Inductive coupling is generally weaker than capacitive coupling, which means

that to achieve the same coupling level, the dimension of the aperture in capacitive iris is normally smaller than the inductive one. This should be noted when designing terahertz devices using cavities, since small dimensions are often beyond the fabrication limitation.

A certain value of external  $Q$  can also be achieved using similar process. Fig. 3.28 gives a model with an aperture (in red) between a port and a cavity to realize a specific external  $Q$ . To calculate the external  $Q$ , there must be another coupling to Port 2, shown in green. The coupling to Port 2 is set weak to limit

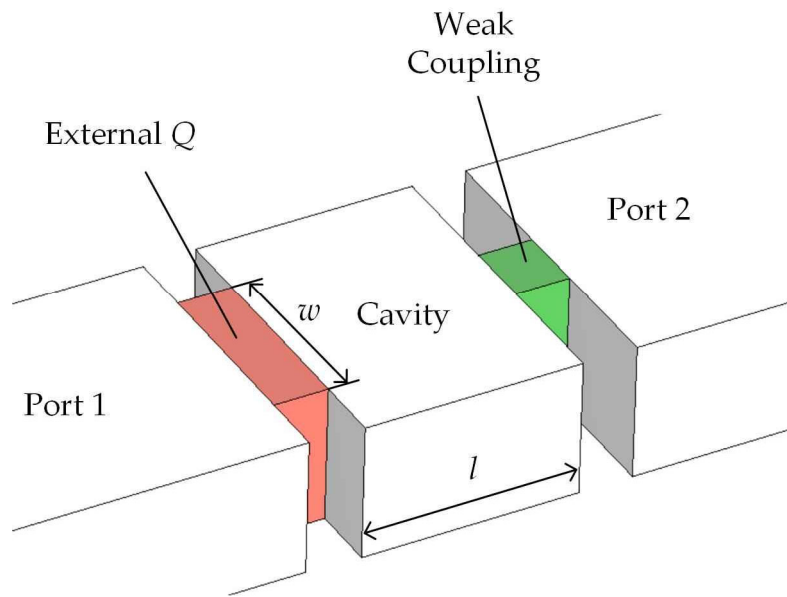


Fig. 3.28. Strong coupling (external  $Q$ ) and weak coupling in a simulation model to obtain the coupling level.

the influence (loading effect) it brings to the calculation. Fig. 3.29 gives a simulation response. The maximum in-band magnitude is -30 dB at frequency  $f_0$ , while the 3-dB bandwidth is noted  $\Delta f$ . The external  $Q$  can be calculated as:

$$Q_{ex} = \frac{f_0}{\Delta f} \quad (3.38)$$

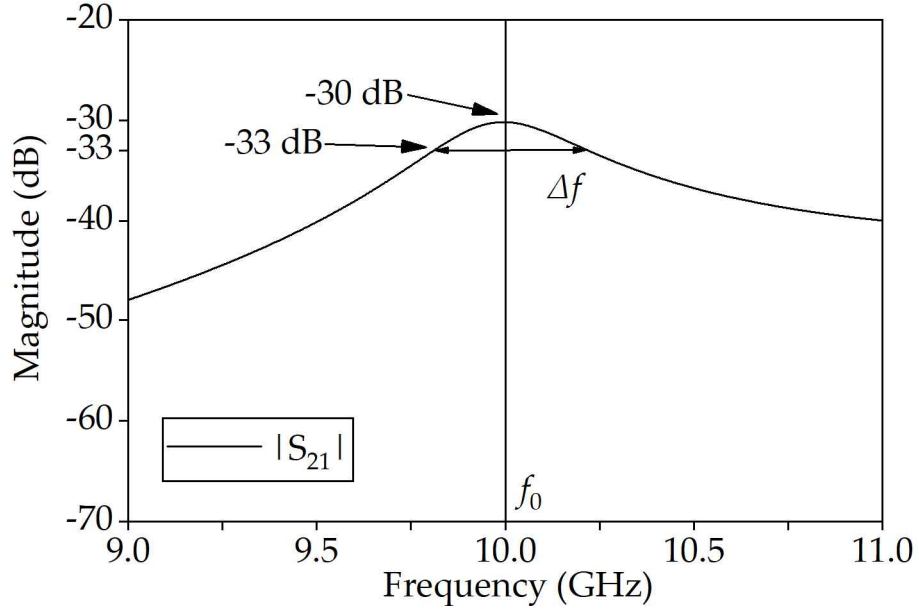


Fig. 3.29. Simulated  $|S_{21}|$  of the model shown in Fig. 3.28.

Note as the peak of the  $|S_{21}|$  is located at 10 GHz in Fig. 3.29, the calculated external  $Q$  is only valid at 10 GHz.

### 3.4 CM of Non-Resonant Circuits

The proposed filtering SPJ (shown in the following chapters) includes resonant parts and non-resonant circuits. The conventional way to realize such circuits is designing them separately and assembling them. This brings unexpected losses due to the mismatch of the corresponding parts by the connection. CM technique is a powerful tool in synthesizing resonant circuits and has been detailed in this chapter. Non-resonant circuits are not supported by conventional CM technique. This section provides a systematic way to extend CM technique to non-resonant circuits, which facilitates the filtering SPJ synthesis and can be used in other filtering circuit designs as well.

An active CM was used in designing an integrated amplifier-filter [9]. The Y-matrix of the amplifier was weaved in the coupling circuit by substituting the entries with corresponding Y parameters. In this way, a CM containing resonant and non-resonant parts was proposed to guide the synthesis of the entire circuit, and the circuit can be optimized as a whole. The non-resonant

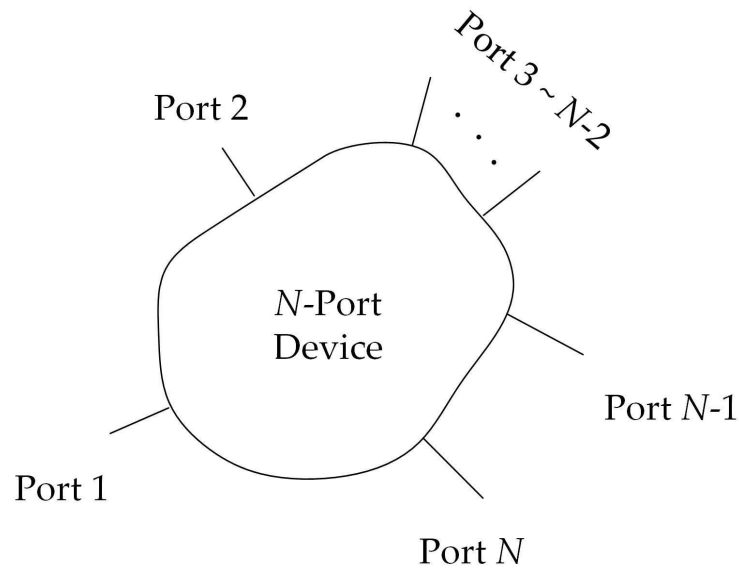


Fig. 3.30. A random  $N$ -port device.

part in [9] contains only two ports (of an amplifier). Inspired by [9], this chapter aims to provide a general method valid for any  $N$ -port non-resonant device.

Consider a device with  $N$ -port as shown in Fig. 3.30. The entries of the Y-matrix of the device are noted  $Y_{ij}$  ( $i = 1$  to  $N$  and  $j = 1$  to  $N$ ). To derive the CM of the device, Fig. 3.30 was redrawn into Fig. 3.31. One  $J$ -inverter was added to each port, and there is a current source at Port 1. The currents in the device are depicted as  $i_N$ , and the voltages are  $v_N$ .  $Y_{p,i}$  ( $i = 1$  to  $N$ ) are the port admittances. Within the Y-matrix of the device, applying Kirchoff's current law, there are:

$$\left\{ \begin{array}{l} Y_{p,1}v_{p,1} - jJ_1v_1 = i_s \\ -jJ_1v_{p,1} + Y_{1,1}v_1 + Y_{1,2}v_2 + \dots + Y_{1,N}v_N = 0 \\ Y_{p,2}v_{p,2} - jJ_2v_2 = 0 \\ -jJ_2v_{p,2} + Y_{2,1}v_1 + Y_{2,2}v_2 + \dots + Y_{2,N}v_N = 0 \\ \vdots \\ Y_{p,N-1}v_{p,N-1} - jJ_{N-1}v_{N-1} = 0 \\ -jJ_{N-1}v_{p,N-1} + Y_{N-1,1}v_1 + Y_{N-1,2}v_2 + \dots + Y_{N-1,N}v_N = 0 \\ Y_{p,N}v_{p,N} - jJ_Nv_N = 0 \\ -jJ_Nv_{p,N} + Y_{N,1}v_1 + Y_{N,2}v_2 + \dots + Y_{N,N}v_N = 0 \end{array} \right. \quad (3.39)$$

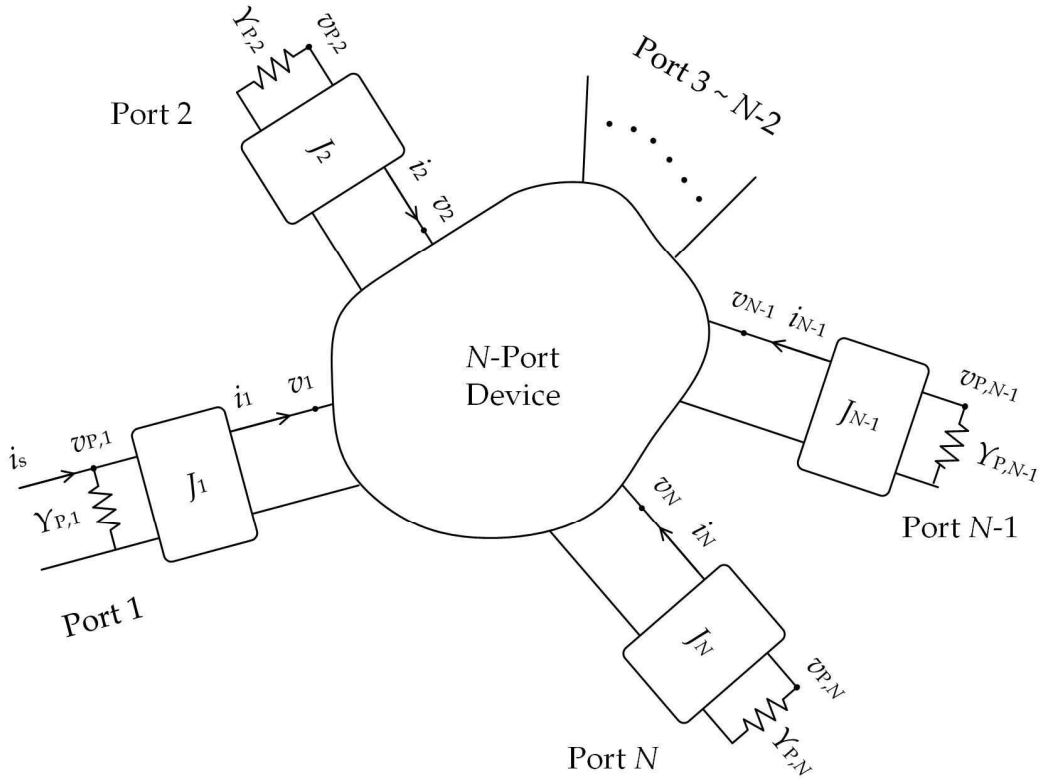


Fig. 3.31. A random  $N$ -port device with  $J$  inverters.

Then the values of  $J$ -inverters are set to be 1, which means the circuits on both sides are connected directly. The admittances of the ports in this device are also normalized to 1 for a perfect match, (3.39) can be re-arranged to:

$$\begin{bmatrix} Y_{1,1} & Y_{1,2} & \cdots & Y_{1,N} & -j & 0 & \cdots & 0 \\ Y_{2,1} & Y_{2,2} & \cdots & Y_{2,N} & 0 & -j & \cdots & 0 \\ \vdots & \vdots & \vdots & \vdots & \vdots & \vdots & \vdots & \vdots \\ Y_{N,1} & Y_{N,2} & \cdots & Y_{N,N} & 0 & 0 & \cdots & -j \\ -j & 0 & \cdots & 0 & 1 & 0 & \cdots & 0 \\ 0 & -j & \cdots & 0 & 0 & 1 & \cdots & 0 \\ \vdots & \vdots & \vdots & \vdots & \vdots & \vdots & \vdots & \vdots \\ 0 & 0 & \cdots & -j & 0 & 0 & \cdots & 1 \end{bmatrix} \begin{bmatrix} v_1 \\ v_2 \\ \vdots \\ v_N \\ v_{p,1} \\ v_{p,2} \\ \vdots \\ v_{p,N} \end{bmatrix} = \begin{bmatrix} 0 \\ 0 \\ \vdots \\ 0 \\ i_s \\ 0 \\ \vdots \\ 0 \end{bmatrix} \quad (3.40)$$

This can be further symbolized by:

$$[A][v] = [i] \quad (3.41)$$

$[A]$  is a  $2N \times 2N$  matrix that can be decomposed to:

$$[A] = [x] + [u] - j[m] \quad (3.42)$$

$[x]$  is a diagonal matrix with entries of  $\{Y_{1,1}, Y_{2,2}, \dots, Y_{N,N}, 1, \dots, 1\}$  ( $N$  sets of 1) and

$[u]$  is a diagonal matrix representing the resonant nodes.  $[u]$  is 0 in this case.

$[m]$  is a  $2N \times 2N$  CM of the  $N$ -port non-resonant structure, which is:

$$[m] = \begin{bmatrix} 0 & jY_{1,2} & \cdots & jY_{1,N} & 1 & 0 & \cdots & 0 \\ jY_{2,1} & 0 & \cdots & jY_{2,N} & 0 & 1 & \cdots & 0 \\ \vdots & \vdots & \vdots & \vdots & \vdots & \vdots & \vdots & \vdots \\ jY_{N,1} & jY_{N,2} & \cdots & 0 & 0 & 0 & \cdots & 1 \\ 1 & 0 & \cdots & 0 & 0 & 0 & \cdots & 0 \\ 0 & 1 & \cdots & 0 & 0 & 0 & \cdots & 0 \\ \vdots & \vdots & \vdots & \vdots & \vdots & \vdots & \vdots & \vdots \\ 0 & 0 & \cdots & 1 & 0 & 0 & \cdots & 0 \end{bmatrix} \quad (3.43)$$

(3.43) represents the  $N$ -port non-resonant device shown in Fig. 3.30 in an  $N$ -port  $N$ -node configuration. The first  $N$  row and  $N$  columns represent the inter couplings, and the entries 1 means the coupling to each port is 1. Fig. 3.30 can be reformed to Fig. 3.32 based on (3.43). There are  $N$  nodes and  $N$  ports in Fig. 3.32, all nodes coupled to each other. The coupling values between the nodes



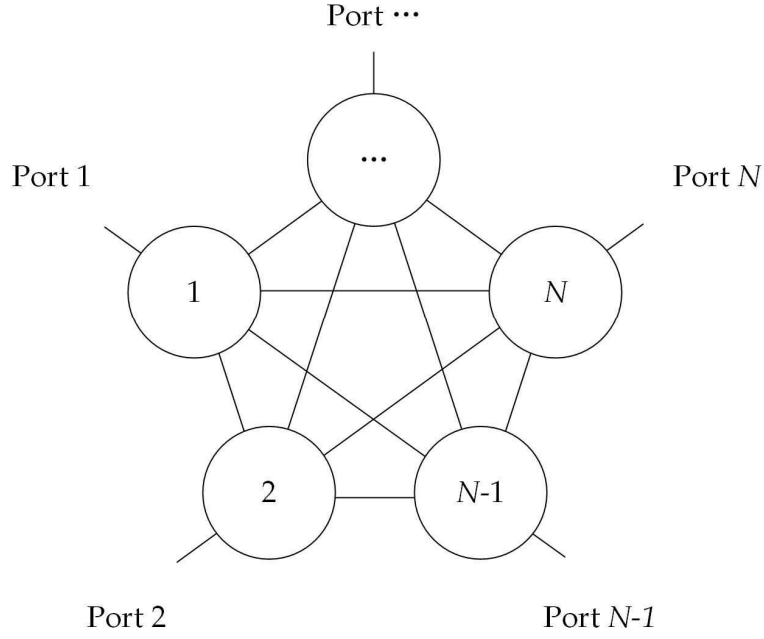


Fig. 3.32. Reformed random  $N$ -port device.

are  $jY_{j,k}$  ( $j, k = 1$  to  $N, j \neq k$ ), and all the normalized external quality factors are 1. Note that the CM of this device has no physical meaning. It only helps the construction of the CM of the filtering SPJ.

### 3.5 Design Procedure

The previous sections provided the background knowledge for filtering-SPJ design. A flowchart is given in Fig. 3.33 showing the design procedure. Following the flowchart, the topology of the filtering SPJ and the corresponding coupling values were defined at first. According to the coupling values, An air model can be built, whose initial dimensions can be deduced using the method in Section 3.3. At the same time, the theoretical response of the model can be obtained by applying the method of CM with NRCs given in Section 3.4. The model will be optimized to make the response close to the theoretical one. The

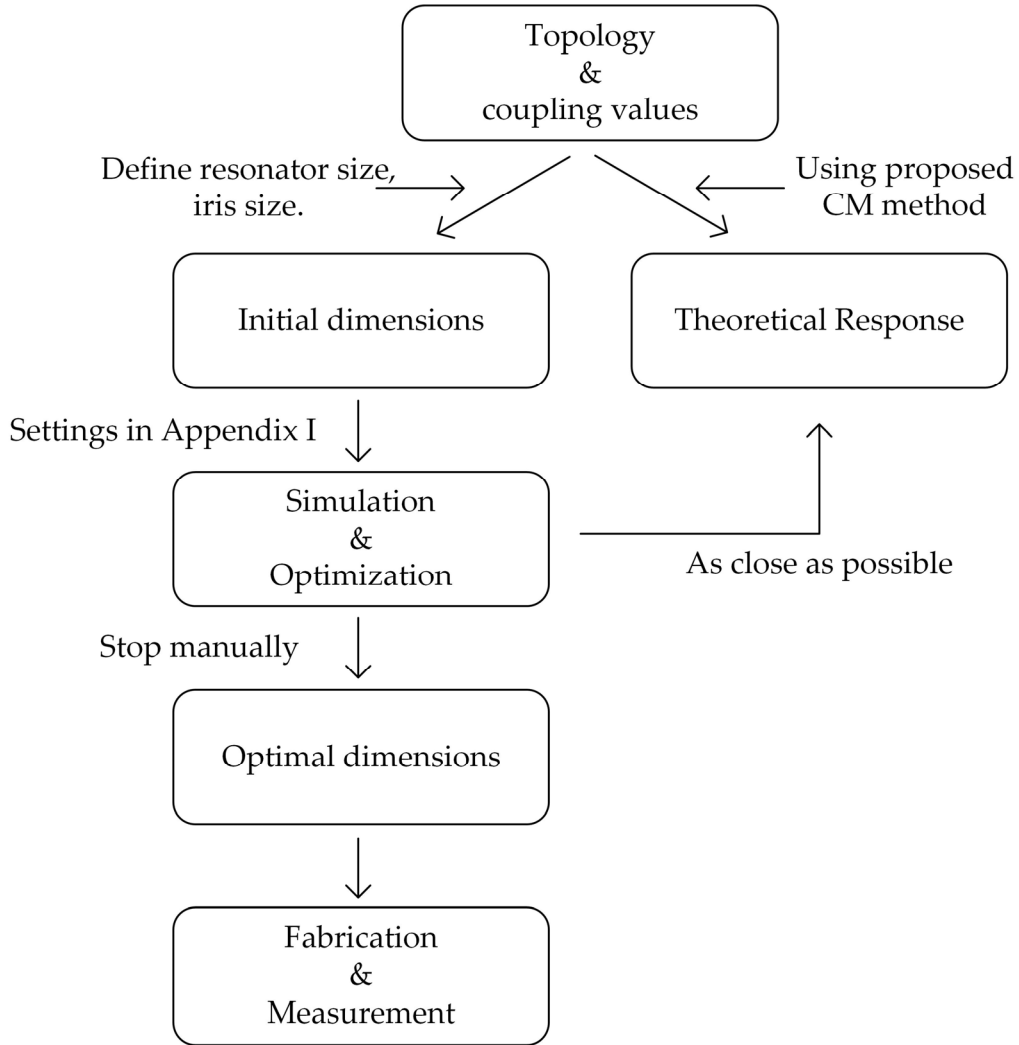


Fig. 3.33. Flowchart for filtering SPJ design.

setting details of the optimization is provided in Appendix I. All the optimization processes in this thesis were stopped manually when there is no certificate change in the response (e.g., The shape of  $|S_{11}|$  remains the same for five rounds). Finally, shell was added to the optimized model for fabrication.

### 3.6 Summary

This chapter gave the theoretical background for filtering SPJ design. It includes the synthesis of cascaded filters, the convention CM technique, the

waveguide structure, the original study of CM with NRCs and a flowchart of design procedure that one can follow. The CM with NRCs helps deduce the theoretical responses of compound circuits containing resonant and non-resonant circuits. This process greatly eases the synthesis procedure. The application of this CM technique will be presented in remaining chapters.

## Reference:

- [1] X. Chen, Y. Wang, T. Skaik, and Q. Zhang, "E-Plane Waveguide Filtering Six-Port Junction," *IEEE Transactions on Microwave Theory and Techniques*, vol. 69, no. 12, pp. 5360-5370, 2021.
- [2] D. M. Pozar, *Microwave engineering*. John wiley & sons, 2011.
- [3] J.-S. G. Hong and M. J. Lancaster, *Microstrip filters for RF/microwave applications*. John Wiley & Sons, 2004.
- [4] A. E. Atia and A. E. Williams, "Narrow-bandpass waveguide filters," *IEEE Transactions on Microwave Theory and Techniques*, vol. 20, no. 4, pp. 258-265, 1972.
- [5] R. J. Cameron, "General coupling matrix synthesis methods for Chebyshev filtering functions," *IEEE transactions on microwave theory and techniques*, vol. 47, no. 4, pp. 433-442, 1999.
- [6] R. J. Cameron, "Advanced coupling matrix synthesis techniques for microwave filters," *IEEE Transactions on Microwave Theory and Techniques*, vol. 51, no. 1, pp. 1-10, 2003.
- [7] P. Zhao and K.-L. Wu, "Model-based vector-fitting method for circuit model extraction of coupled-resonator diplexers," *IEEE Transactions on Microwave Theory and Techniques*, vol. 64, no. 6, pp. 1787-1797, 2016.
- [8] N. Marcuvitz, *Waveguide handbook* (no. 21). Iet, 1951.
- [9] Y. Gao, J. Powell, X. Shang, and M. J. Lancaster, "Coupling matrix-based design of waveguide filter amplifiers," *IEEE Transactions on Microwave Theory and Techniques*, vol. 66, no. 12, pp. 5300-5309, 2018.

## Chapter 4. Amplitude-Balance Enhanced Filtering Coupler

As mentioned in Chapter 1, amplitude imbalance in in-phase and quadrature (I-Q) mixers may lead to extra noise in homodyne receivers. Amplitude imbalance in couplers also influences the magnitude performance of the circuit where they are used, for instance Butler matrix [1-3] and reflective type circuits [4, 5]. This chapter presents an amplitude enhanced filtering coupler (Coupler-A) that is used in the magnetic field (H) plane X-band filtering SPJ in Appendix II. Along with the coupler, the study reveals amplitude balance can be improved by optimizing the physical configuration. This technique for enhancing the amplitude balance has been applied throughout the thesis. To demonstrate the idea, two filtering couplers working in the band from 9.9 to 10.1 GHz were fabricated and measured. A conventionally designed  $180^\circ$  filtering waveguide coupler was used at first to illustrate the inherent amplitude-imbalance problem. Then, a modified  $180^\circ$  filtering waveguide coupler is presented for comparison to show the enhanced amplitude balance. No compromise on isolation, phase balance, or additional circuitry was made. The amplitude balance was improved by adjusting the aperture position to obtain more symmetry in the frequency response. Another key feature of the coupler is the identical outer profile of the resonators. This is realized by loading the resonators with stubs. These stubs serve to adjust the resonant

frequencies without changing the outer dimensions of the resonators and ease the layout. This chapter is based on the published work in [6].

## 4.1 Amplitude Imbalance in Filtering Coupler

There are many reports on filtering couplers. [7] used four resonator groups. Each group has two resonators and possible paths that can realize a  $-90^\circ$  and a  $+90^\circ$  phase shift, respectively. By choosing three  $+90^\circ$  and one  $-90^\circ$  groups, it achieved a  $180^\circ$  filtering coupler. [8] formed a coupler by four microstrip resonators. By involving three positive couplings and one negative coupling, the coupler realized a  $180^\circ$  phase shift. The coupler was further applied in the design of a Butler matrix. The filtering coupler can also be designed with an arbitrary output ratio [9]. The opposite coupling achieved the  $180^\circ$  phase shift, while the arbitrary output ratio was realized by different coupling levels. The principles of resonator-based  $180^\circ$  filtering couplers are the same: four resonators coupled end to end, with one opposite coupling among the four couplings. Fig 4.1 shows the topology. It gives a second-order Chebyshev

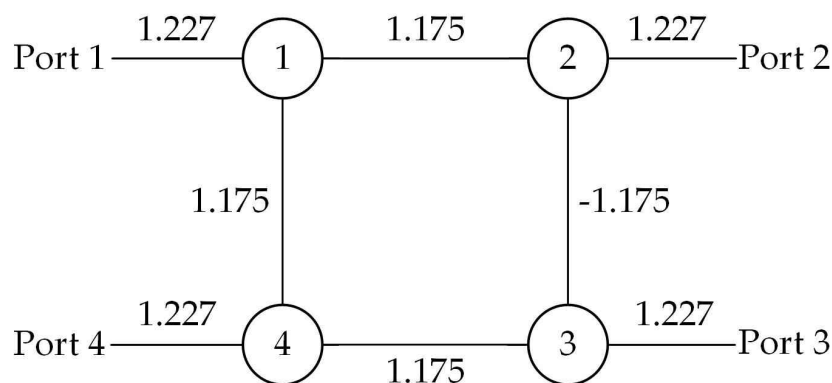


Fig. 4.1. Topology of a second-order filtering coupler with Chebyshev response.

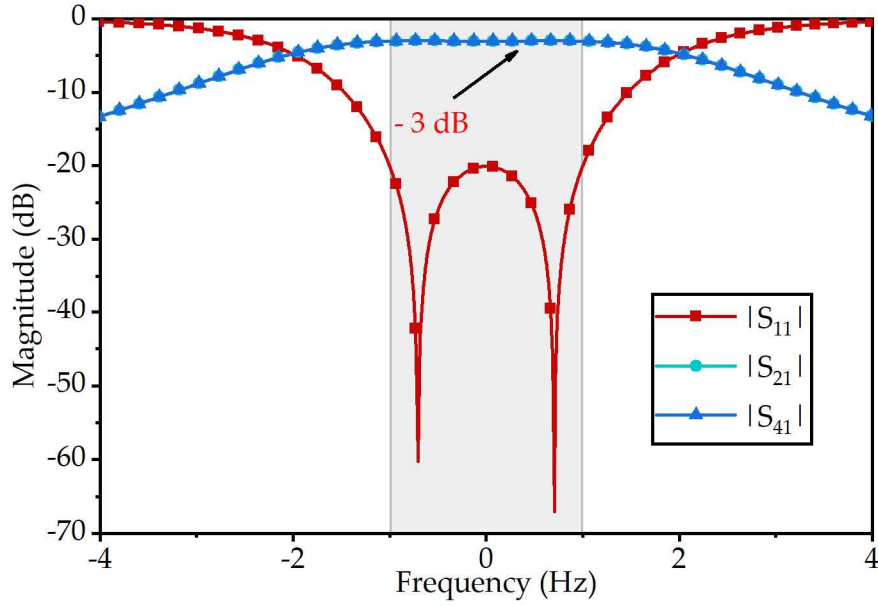


Fig. 4.2. Theoretical magnitude response of the filtering coupler given in Fig. 4.1.

response with the provided coupling values. Note that the coupling between Resonator 2 and 3 is negative while others are positive. The theoretical magnitude response can be found in Fig. 4.2. Port 1 is the input, while Port 2 and Port 4 are two outputs. Theoretically, the isolation is infinity ( $\infty$  dB). Note the two output magnitudes are at the same level at any frequency point.

For the topology in Fig. 4.1, the resonators are placed at four vertices of a square. To ease the layout of the practical coupler, the length of each resonator was set equal to the width, making the resonator also square. A stub was loaded in each resonator for frequency adjusting. The air model of the stub-loaded square resonator is shown in Fig. 4.3(a). The length and the width of the resonator are all 22.86 mm, which is the standard width of an X-band waveguide. A stub is located in the middle of one side, with a 5-mm width. The length of the stub is  $l$ . Fig. 4.3(b) gives the E-field pattern of the fundamental mode of the resonator

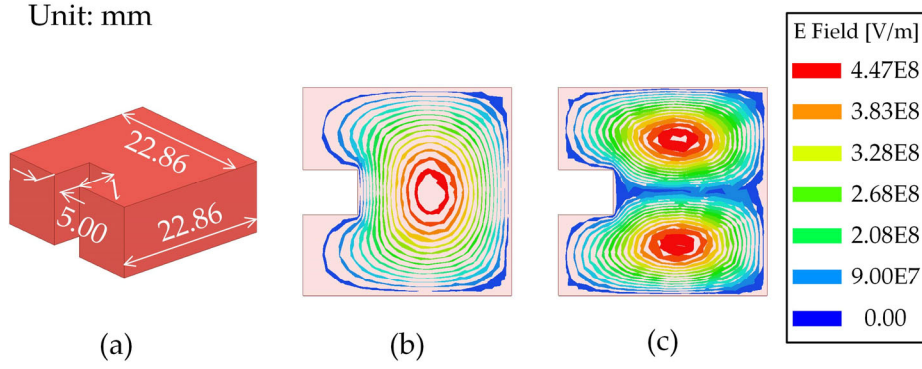


Fig. 4.3. Square resonator with a loaded stub and the resonant E-fields. (a) The overall view of the stub-loaded resonator. (b) The E-field of the fundamental mode. (c) The E-field of the second resonant mode.

when  $l = 6$  mm. The resonant frequency is related to  $l$ . Fig. 4.3(c) gives the second resonant mode.

A plan view of one waveguide implementation of the filtering coupler employing the stub-loaded resonators is shown in Fig. 4.4. The positive and negative couplings can be achieved by inductive and capacitive irises between resonators, respectively. Controlling the depths of stubs in resonators makes it possible to keep all resonators the same square profile when tuning their resonant frequencies. This significantly eases the layout. This model was

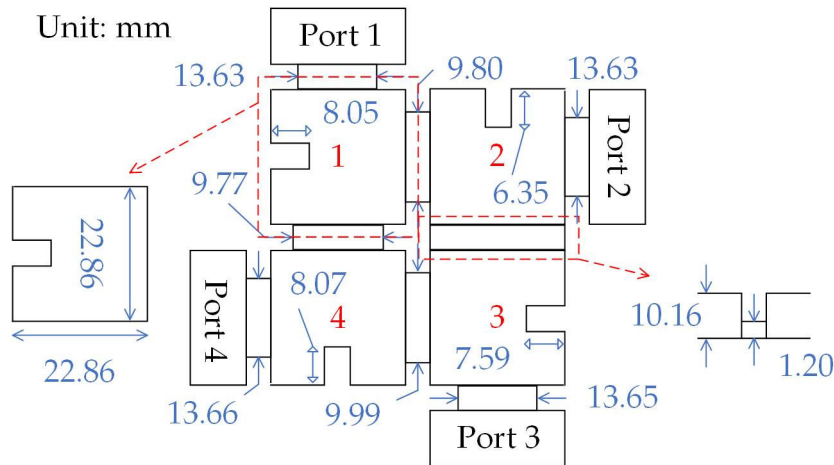


Fig. 4.4. Plan view of the H-plane filtering 180° 3-dB coupler.

optimized using Trust Region Framework method provided in commercial microwave simulator CST (details in Appendix I), which was also used in other model optimizations in this thesis. The optimized magnitude is shown in Fig. 4.5. From the enlarged view over the operation band between 9.9 and 10.1 GHz, it can be noticed that although the filtering coupler functions correctly in the working band, the magnitudes of the two outputs,  $|S_{21}|$  and  $|S_{41}|$ , fluctuate between -2.86 dB and -3.25 dB and cross each other (as opposed to the overlapping curves in the theoretical magnitude response). This implies that the coupler does not retain the amplitude balance in the working band. The following section studies the influence of apertures position on the amplitude balance. It shows that the amplitude balance can be improved dramatically by adjusting the apertures.

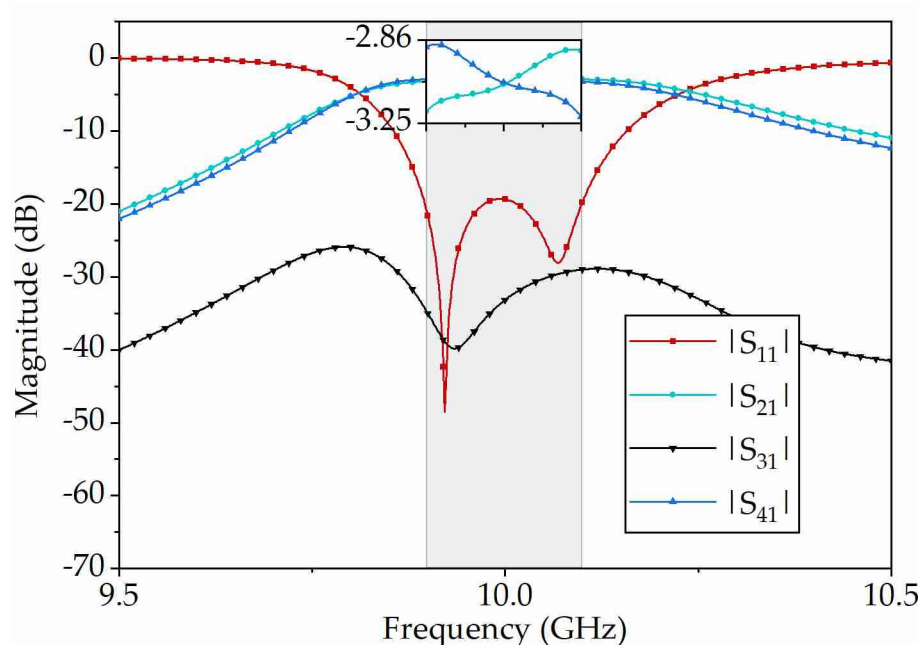


Fig. 4.5. Simulated magnitude response of the coupler in Fig. 4.4.



## 4.2 Effect of Aperture Position on Amplitude Balance

Fundamentally, the amplitude imbalance is intrinsic to the  $180^\circ$  hybrid couplers because of the asymmetric electrical paths of the signals going to the outputs. This is manifested by the uneven couplings between resonators over the operation band. Take one resonator and its three inductive irises as an

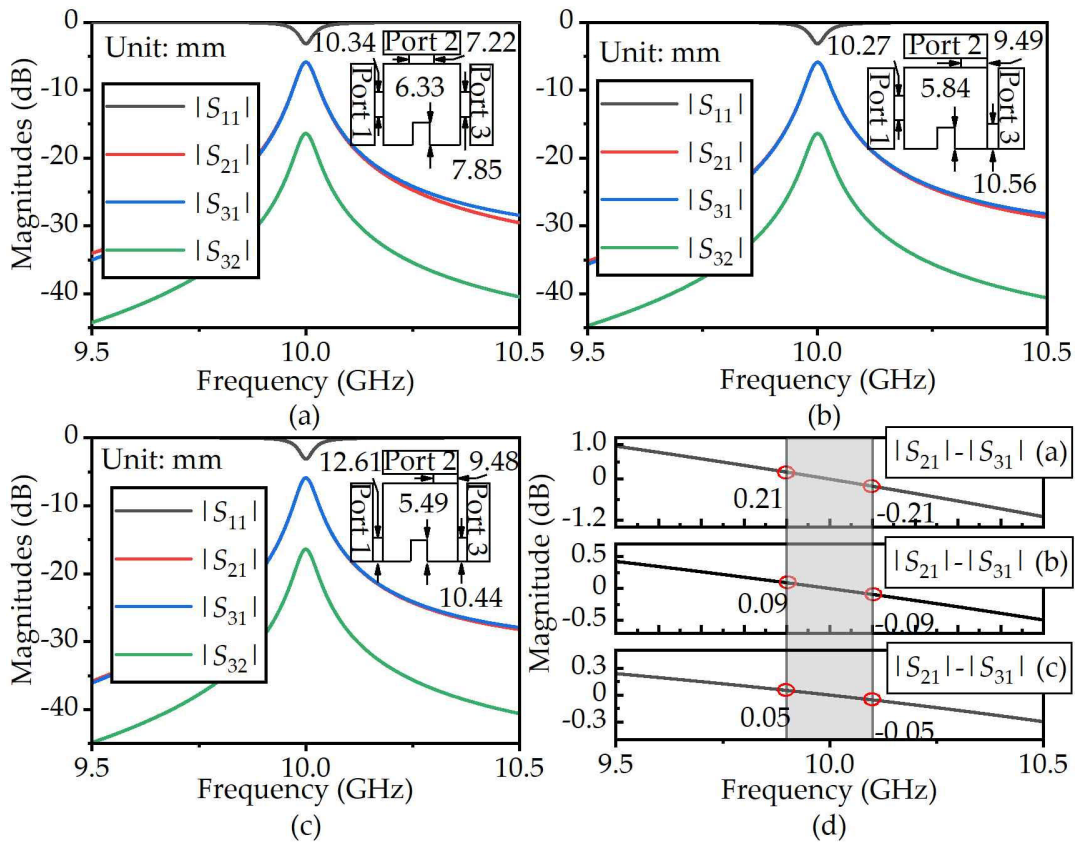


Fig. 4.6. Comparison of the magnitude imbalance in a three-port junction with inductive irises. Port 1 is the input port, Port 2 and Port 3 are output ports: (a) When all three apertures of the iris are at the center. (b) When the apertures to Port 2 and Port 3 are shifted to the edge. (c) When all three apertures are shifted to the edge. (d) The difference between  $|S_{21}|$  and  $|S_{31}|$  in dB in the three situations. The operation band is marked out in light grey in (d).

example, as shown in Fig. 4.6. This is an air model of a three-port power-splitting junction. Three different situations are compared here. Fig. 4.6(a)

shows all the apertures at the centre of the broad wall, shown in the inset. At 10 GHz,  $|S_{21}|$  and  $|S_{31}|$  are the same. Away from it, the difference between them gets larger. As shown in Fig. 4.6(d), this difference is from -1.2 to 1.0 dB over the shown frequency range. In Fig. 4.6(b), Aperture 2 and Aperture 3 are shifted to the edge of the wall. The amplitude imbalance between  $|S_{21}|$  and  $|S_{31}|$  is halved to  $\pm 0.5$  dB. The optimal case is when Aperture 1 is also shifted to the edge of the wall, as in Fig. 4.6(c). The imbalance is reduced to  $\pm 0.3$  dB, as shown in Fig. 4.6(d). Note that the widths of the apertures and the length of the stubs are also changed accordingly to maintain the resonant frequency and the

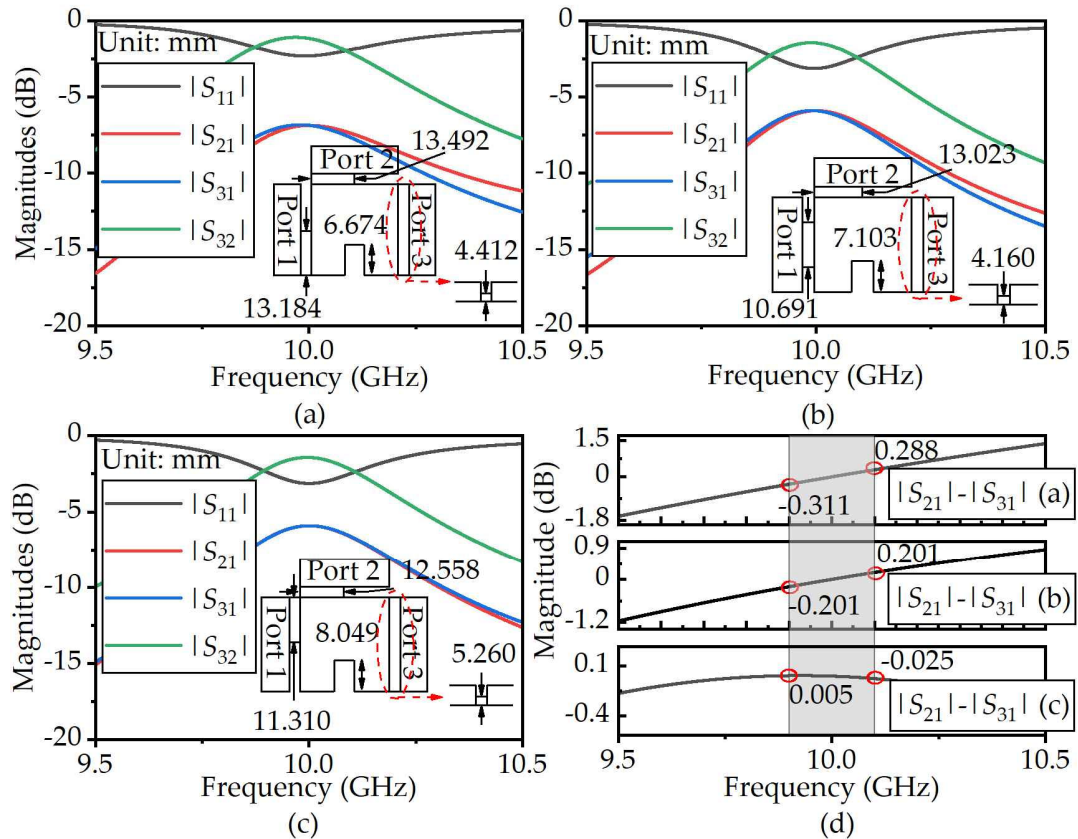


Fig. 4.7. Magnitude imbalance in a junction with capacitive and inductive irises. Port 1 is the input, Port 2 and Port 3 are outputs. (a) to (c) show the configurations and corresponding responses when the aperture to Port 1 shifts from one edge to the other. The magnitude differences can be seen in (d).

overall average output level of the junctions.

Similarly, the situation of mixed inductive and capacitive coupling is illustrated in Fig. 4.7. From Fig. 4.7(a) to (c), the aperture to Port 1 shifts from the bottom to the top, while the positions of the other two apertures keep unchanged. The red circles in Fig. 4.7(d) indicate the imbalance at the edge of the working band. It can be seen clearly that by repositioning the apertures, the amplitude balance can be improved from 1.8 dB to under 0.3 dB across the frequency range.

Both investigations show that the balance of the power split at the three-port junction structures can be effectively improved by adjusting the aperture positions.

### 4.3 Modified Balanced Coupler

A modified H-plane filtering 180° 3-dB coupler with enhanced amplitude balance has been designed to verify the findings. The new structure is shown

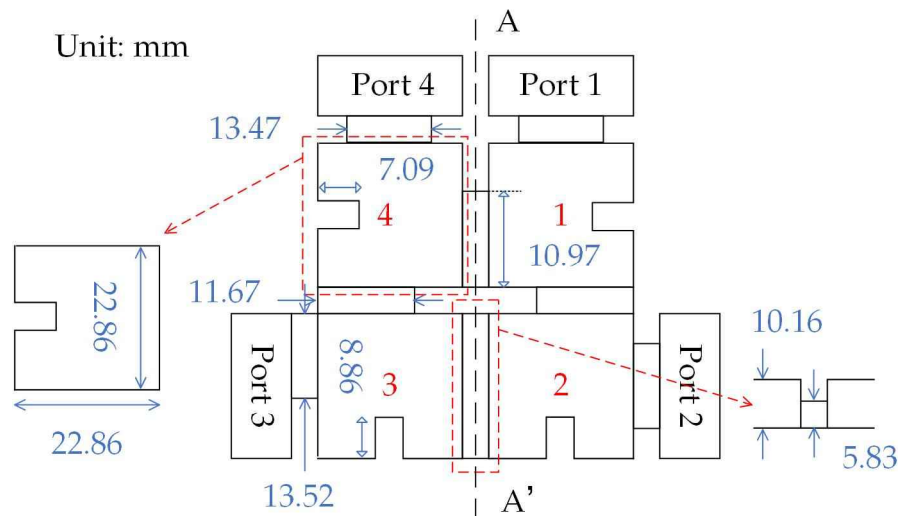


Fig. 4.8. Plan view of the modified H-plane filtering 180° 3-dB coupler.

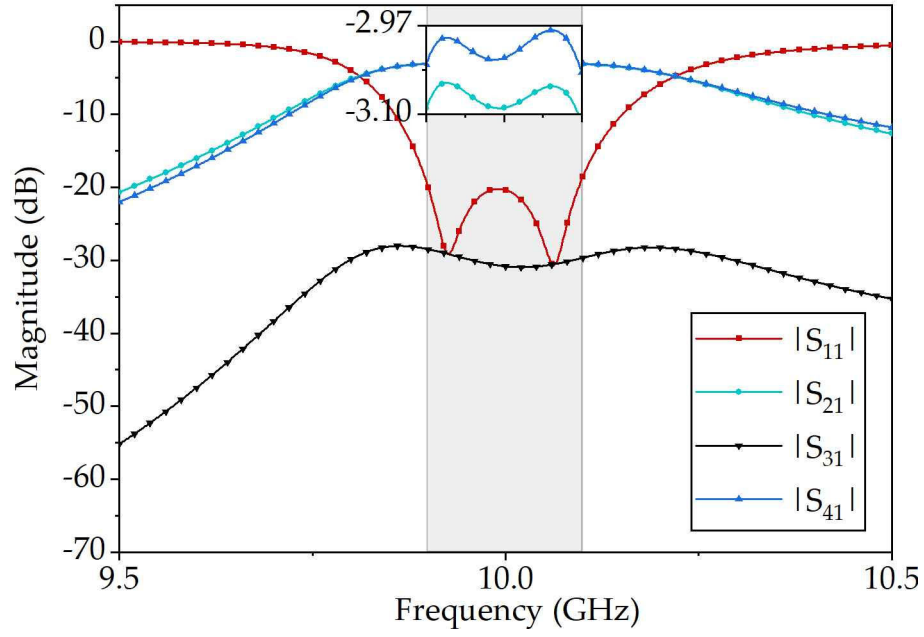


Fig. 4.9. Simulated magnitude response of the coupler in Fig. 4.8.

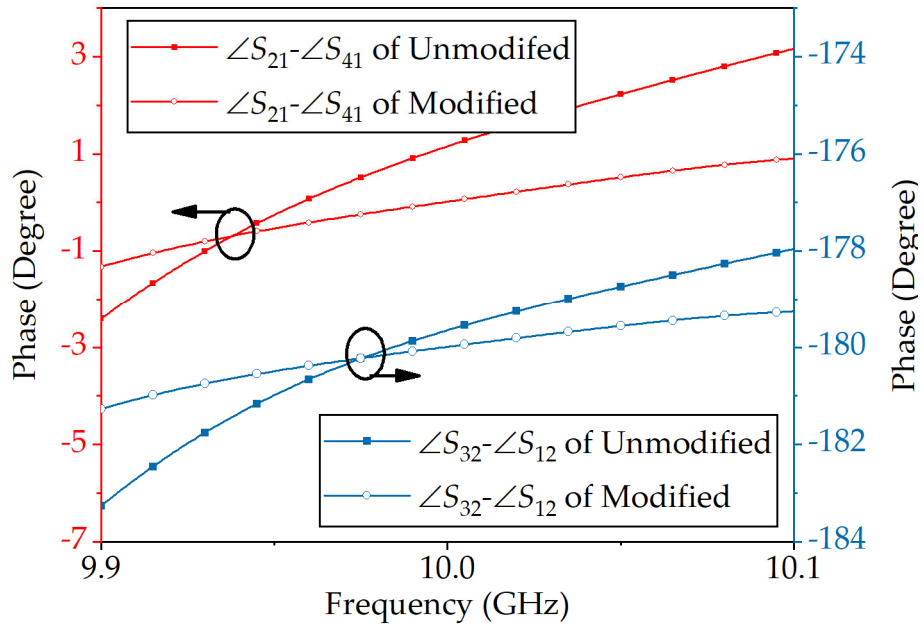


Fig. 4.10. Phase responses of the two filtering couplers.

in Fig. 4.8. The model is symmetrical to the dash line AA'. Between resonators 2 and 3 is the capacitive iris. Other irises are all inductive. The thickness of all the irises is 4 mm. Compared with the unmodified coupler, the aperture positions in irises were adjusted according to the aforementioned method. The

magnitude response from Port 1 is shown together with an enlarged view over the working band in Fig. 4.9. Evidently, different from the response in Fig. 4.5, the magnitudes of the two outputs track each other without crossing and with a very small fluctuation only between -2.97 and -3.10 dB. Note that the in-band return losses/isolations of both couplers are larger than 20/25 dB. The phase error of the modified coupler is also greatly improved, as shown in Fig. 4.10. The maximum error in  $|\angle S_{21} - \angle S_{41}|$  is reduced from  $3^\circ$  to  $1.5^\circ$  (varying between  $-1.5^\circ$  and  $1.0^\circ$ ) in the modified coupler. In  $|\angle S_{32} - \angle S_{12}|$ , this is reduced from  $3.5^\circ$  to  $1.0^\circ$  (varying between  $-181^\circ$  and  $-179^\circ$ ).

## 4.4 Fabrication and Measurement

Both couplers are fabricated using stereolithography (SLA) 3D printing, with a

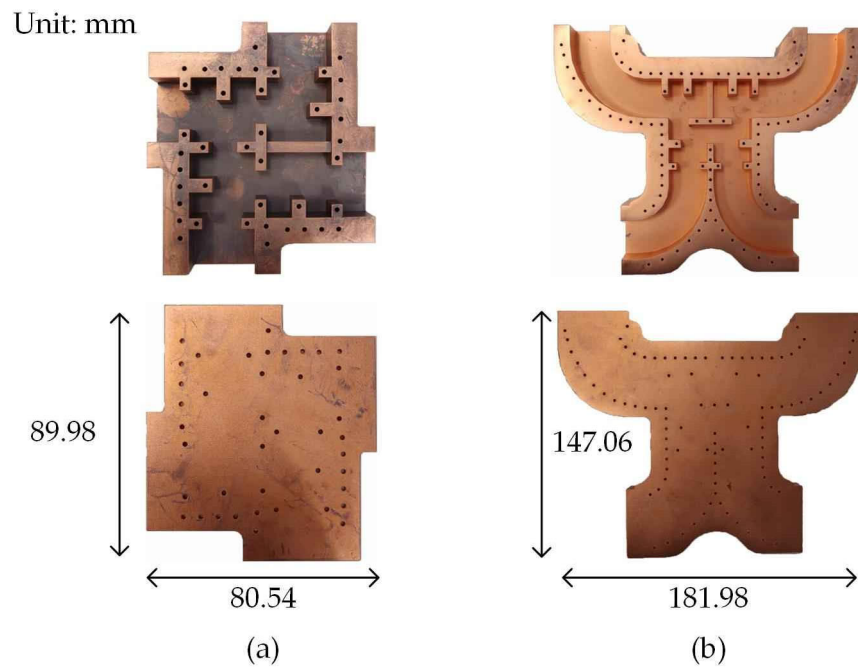


Fig. 4.11. 3D printed (a) Unmodified and (b) modified coupler, and their profile dimensions.

10-um copper coating on the surface. The material used is Somos®PerFORM ceramic resin. Compared with CNC machining, 3D printing features with ease of use, low cost, environmental friendliness and the ability to build a simple hollow sample as whole. However, it lacks accuracy. For lower frequency fabrication (e.g., 10 GHz), 3D printing is an alternative. As the waveguide structure is complex inside and must be coated with conductive metal (copper), the samples were printed separately and assembled after being coated. The two fabricated couplers are shown in Fig. 4.11(a) and (b), with the lengths and widths given. Each port of the modified coupler is extended to make space for

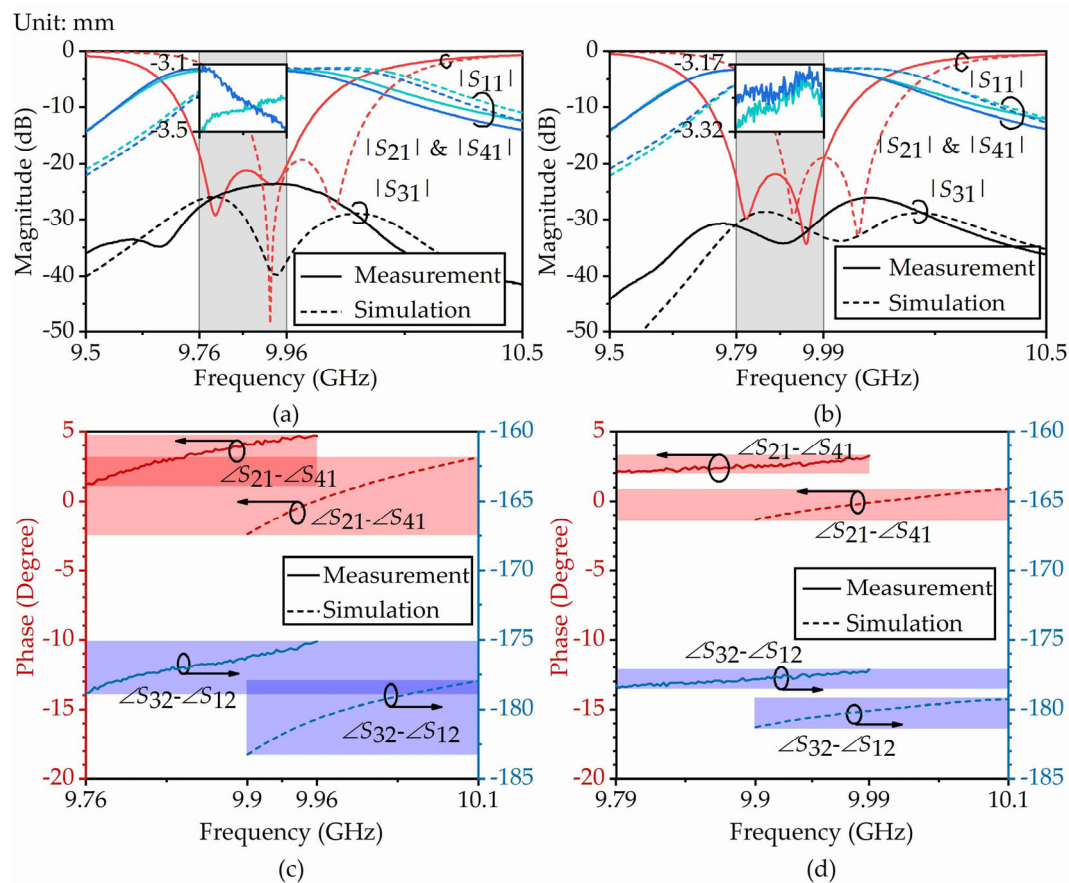


Fig. 4.12. Measured responses in comparison with simulations. (a) and (c) are the magnitude and phase response of the unmodified coupler, respectively. (b) and (d) are the magnitude and phase response of the modified coupler, respectively

flanges. Fig. 4.12 gives the measured magnitude and phase responses compared to simulations. Good magnitude agreement has been achieved with excellent matching, except for a 2% frequency shift. Fig. 4.12(a) shows the unmodified coupler has a 0.24 GHz frequency shift in the measurement, making the operation band 9.76 to 9.96 GHz. The enlarged view shows  $|S_{21}|$  and  $|S_{41}|$  cross each other as in the simulation. The measured magnitude response of modified coupler in Fig. 4.12(b) shows a frequency shift of 0.21 GHz, resulting in a working band of 9.79 to 9.99 GHz. Unlike Fig. 4.12(a), the measured  $|S_{21}|$  and  $|S_{41}|$  have a much smaller imbalance (0.081 dB versus 0.38 dB) and follow each other without crossing. This confirms a much-improved amplitude balance. The phase responses are shown in Fig. 4.12 (c) and (d). As there is a frequency shift in the measurement, only the phase responses in the corresponding measured working band are given. For the unmodified coupler,  $\angle S_{21} - \angle S_{41}$  is from  $2^\circ$  to  $5^\circ$  while  $\angle S_{12} - \angle S_{32}$  is from  $-178^\circ$  to  $-175^\circ$  with  $3^\circ$  variation. For the modified coupler,  $\angle S_{21} - \angle S_{41}$  is from  $2^\circ$  to  $3^\circ$ , while  $\angle S_{12} - \angle S_{32}$  is from  $-183^\circ$  to  $-182^\circ$ , both with only  $1^\circ$  variation. Although there is a notable frequency shift in the measured responses (because of the larger-than-expect dimensions of the 3D printed parts), the balance is still greatly enhanced.

## 4.5 Summary

This chapter presents an amplitude balance enhanced filtering coupler. Along with the coupler design, it investigated how the amplitude balance is affected



by the physical configuration. Two couplers were fabricated and measured for comparison. With the aperture position adjustment, the amplitude imbalance was improved from 0.38 dB to 0.081 dB. This improved filtering coupler (Coupler-A) was later used in the H-plane filtering SPJ working in the X-band, which is given in Appendix II.

## Reference

- [1] M. Bona, L. Manholm, J. Starski, and B. Svensson, "Low-loss compact Butler matrix for a microstrip antenna," *IEEE Transactions on Microwave Theory and Techniques*, vol. 50, no. 9, pp. 2069-2075, 2002.
- [2] G. Tian, J.-P. Yang, and W. Wu, "A novel compact Butler matrix without phase shifter," *IEEE microwave and wireless components letters*, vol. 24, no. 5, pp. 306-308, 2014.
- [3] A. Tajik, A. S. Alavijeh, and M. Fakharzadeh, "Asymmetrical  $4 \times 4$  Butler Matrix and its Application for Single Layer  $8 \times 8$  Butler Matrix," *IEEE Transactions on Antennas and Propagation*, vol. 67, no. 8, pp. 5372-5379, 2019.
- [4] C.-S. Lin, S.-F. Chang, C.-C. Chang, and Y.-H. Shu, "Design of a reflection-type phase shifter with wide relative phase shift and constant insertion loss," *IEEE Transactions on microwave theory and techniques*, vol. 55, no. 9, pp. 1862-1868, 2007.
- [5] J.-C. Wu, T.-Y. Chin, S.-F. Chang, and C.-C. Chang, "2.45-GHz CMOS reflection-type phase-shifter MMICs with minimal loss variation over quadrants of phase-shift range," *IEEE Transactions on Microwave Theory and Techniques*, vol. 56, no. 10, pp. 2180-2189, 2008.
- [6] X. Chen, Y. Wang, and Q. Zhang, "Ring-Shaped D-Band E-Plane Filtering Coupler," *IEEE Microwave and Wireless Components Letters*, vol. 31, no. 8, pp. 953-956, 2021.
- [7] Y.-L. Lu, Y. Wang, C. Hua, and T. Liu, "Design of compact filtering rat-race hybrid with  $\lambda/2$ -resonators," *Electronics letters*, vol. 52, no. 21, pp. 1780-1782, 2016.
- [8] Q. Shao, F.-C. Chen, Q.-X. Chu, and M. J. Lancaster, "Novel Filtering  $180^\circ$  Hybrid Coupler and Its Application to  $2 \times 4$  Filtering Butler Matrix," *IEEE Transactions on Microwave Theory and Techniques*, vol. 66, no. 7, pp. 3288-3296, 2018.
- [9] C.-F. Chen, J.-J. Li, G.-Y. Wang, K.-W. Zhou, and R.-Y. Chen, "Design of compact filtering  $180^\circ$ -degree hybrids with arbitrary power division and filtering response," *IEEE access*, vol. 7, pp. 18521-18530, 2019.



# Chapter 5. E-plane X-band Filtering SPJ

This chapter introduces one E-plane X-band filtering SPJ working in 9.8 to 10.2 GHz, with which to verify: (1) A new SPJ topology involving resonators; (2) The coupling matrix (CM) technique combining nonresonant circuits (NRCs) with resonators. Another application of the CM technique, a hybrid CM is also constructed. It combines simulated and ideal responses in one matrix for a more representative response. Fabrication and measurement of this E-plane SPJ have been done. A desired agreement was obtained. The work of this chapter has been published in [1].

## 5.1 Topology of the SPJ

To integrate the filtering function, the couplers in the conventional SPJs were replaced by filtering couplers, and a new topology of a filtering SPJ is proposed in Fig. 5.1. There are four parts: two identical fourth-order  $180^\circ$  filtering couplers, one  $180^\circ$  branch-line coupler and one  $90^\circ$  branch-line coupler. The two filtering couplers realize the filtering function. There are eight ports in total. While Port 7 and Port 8 belong to two branch-line couplers that function as power dividers, they are supposed to be loaded for matched termination. Port 1 and Port 2 are the two input ports, while Port 3 to 6 are the four outputs. When an input signal goes into resonator 1 of the upper coupler or similarly the lower coupler, it is equally divided with no phase shift between Port 3 and

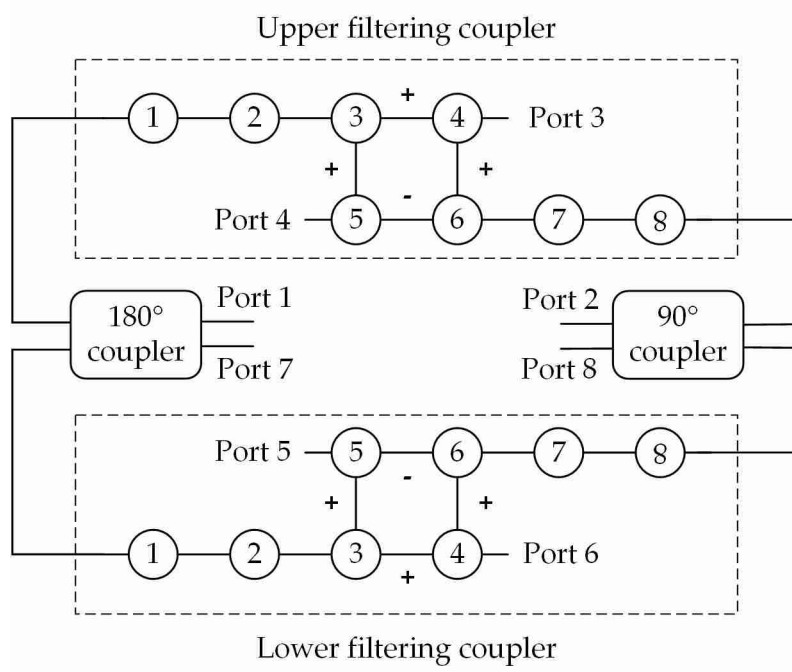


Fig. 5.1. Topology of the filtering SPJ with the fourth-order filtering coupler.

4 of the upper coupler or Port 5 and 6 of the lower coupler. However, when an input signal goes into resonator 8 of either of the filtering couplers, it is split in halves with a  $180^\circ$  phase shift between Port 3 and 4 of the upper coupler, and similarly between Port 5 and 6 for the lower coupler. Furthermore, when two input signals are applied at Port 1 and Port 2, the phase differences at the four output ports are (Note that all the negative values have been added  $360^\circ$  to make them positive):

$$\begin{cases} \angle S_{31} - \angle S_{32} = 0^\circ \\ \angle S_{41} - \angle S_{42} = 180^\circ \\ \angle S_{51} - \angle S_{52} = 90^\circ \\ \angle S_{61} - \angle S_{62} = 270^\circ \end{cases} \quad (5.1)$$

The coupling values of the fourth-order filtering coupler are given in Fig. 5.2. Note that the coupling between resonators 5 and 6 is negative while others are positive. The theoretical magnitude response can be obtained with the coupling values, as shown in Fig. 5.3. Port 1 is the input, Port 2 and Port 3 are outputs, while Port 4 is isolated.

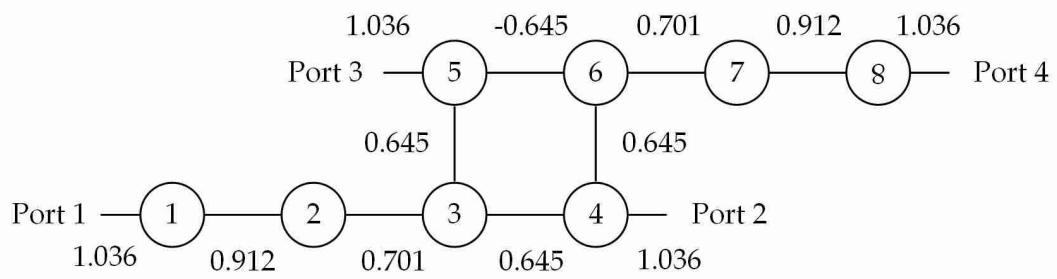


Fig. 5.2. Topology of the fourth-order 180° filtering coupler.

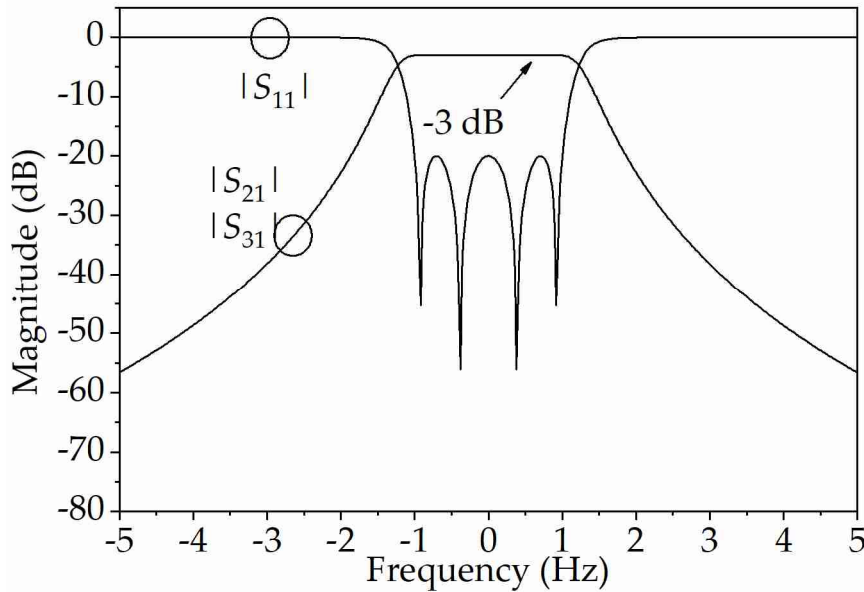


Fig. 5.3. Magnitude response of the fourth-order 180° filtering coupler.

## 5.2 Theoretical response of the SPJ

Chapter 3 gives the CM involving NRCs. To obtain the CM of the topology shown in Fig. 5.1, the two 3-dB branch-line couplers need to be transformed

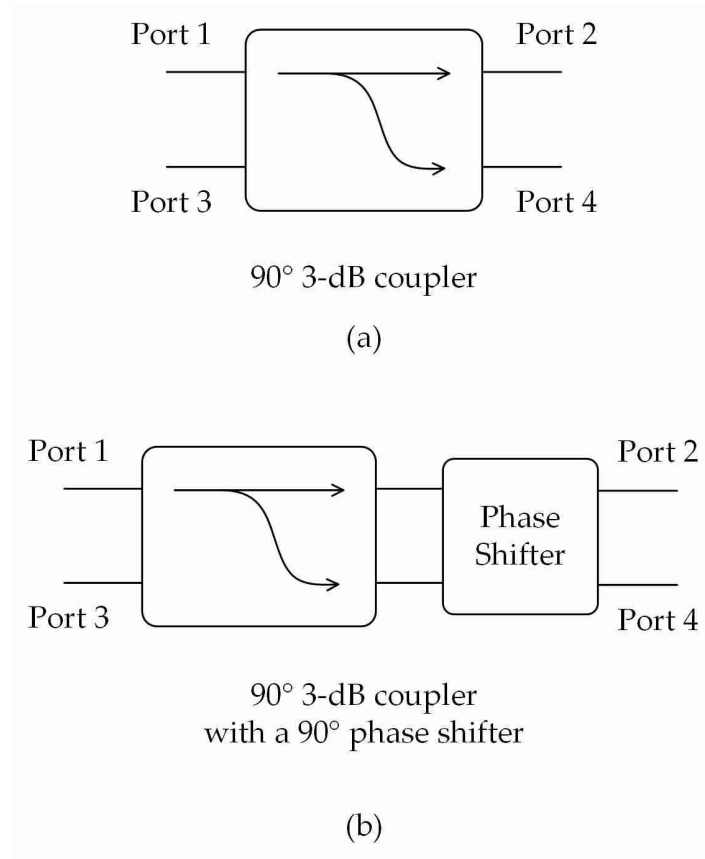


Fig. 5.4. (a)  $90^\circ$  branch-line coupler and (b) the  $180^\circ$  branch-line coupler.

into 'nodes' in the coupling matrix at first. The concept view of the  $90^\circ$  3-dB branch-line coupler and the  $180^\circ$  3-dB branch-line coupler are provided in Fig. 5.4. The  $90^\circ$  3-dB coupler is a conventional 3-dB branch-line coupler, while the  $180^\circ$  3-dB coupler is built upon the conventional  $90^\circ$  3-dB coupler with a  $90^\circ$  phase shifter (four ports, with one reference line). For both couplers, Port 1 is the input port while Port 2 and Port 4 are outputs. Port 3 is isolated. Interconnection lines are inevitable between the waveguide couplers and the filtering couplers. An initial phase  $\theta$  is added to each port to represent these lines. The S-parameters of the  $90^\circ$  hybrid coupler are given by [2]:

$$[S_{90}] = \frac{1}{\sqrt{2}} \begin{bmatrix} 0 & e^{j(\pi/2+\theta)} & 0 & e^{j\theta} \\ e^{j(\pi/2+\theta)} & 0 & e^{j\theta} & 0 \\ 0 & e^{j\theta} & 0 & e^{j(\pi/2+\theta)} \\ e^{j\theta} & 0 & e^{j(\pi/2+\theta)} & 0 \end{bmatrix} \quad (5.2)$$

$$[S_{180}] = \frac{1}{\sqrt{2}} \begin{bmatrix} 0 & e^{j(\pi/2+\theta)} & 0 & e^{j(-\pi/2+\theta)} \\ e^{j(\pi/2+\theta)} & 0 & e^{j\theta} & 0 \\ 0 & e^{j\theta} & 0 & e^{j\theta} \\ e^{j(-\pi/2+\theta)} & 0 & e^{j\theta} & 0 \end{bmatrix} \quad (5.3)$$

Their Y-matrices can be deduced from the S-parameters:

$$[Y_{90}] = j \begin{bmatrix} -\tan 2\theta & -\sqrt{2} \cos \theta \sec 2\theta & \sec 2\theta & \sqrt{2} \sin \theta \sec 2\theta \\ -\sqrt{2} \cos \theta \sec 2\theta & -\tan 2\theta & \sqrt{2} \sin \theta \sec 2\theta & \sec 2\theta \\ \sec 2\theta & \sqrt{2} \sin \theta \sec 2\theta & -\tan 2\theta & -\sqrt{2} \cos \theta \sec 2\theta \\ \sqrt{2} \sin \theta \sec 2\theta & \sec 2\theta & -\sqrt{2} \cos \theta \sec 2\theta & -\tan 2\theta \end{bmatrix} \quad (5.4)$$

$$[Y_{180}] = j \begin{bmatrix} -\tan \theta & -\frac{\sec \theta}{\sqrt{2}} & 0 & \frac{\sec \theta}{\sqrt{2}} \\ -\frac{\sec \theta}{\sqrt{2}} & \cot 2\theta & -\frac{\csc \theta}{\sqrt{2}} & \csc 2\theta \\ 0 & -\frac{\csc \theta}{\sqrt{2}} & \cot \theta & -\frac{\csc \theta}{\sqrt{2}} \\ \frac{\sec \theta}{\sqrt{2}} & \csc 2\theta & -\frac{\csc \theta}{\sqrt{2}} & \cot 2\theta \end{bmatrix} \quad (5.5)$$

According to the discussion around Fig. 3.31, an  $N$ -port device can be represented by an  $N$ -port  $N$ -node network. The CM of the topology in Fig. 5.4 can be deduced, shown in Fig. 5.5. Fig. 5.5(a) gives the node representation of the two branch-line couplers. The two couplers share the same form of node representation and thus the same CM form, which is given in Fig. 5.5(b). However, they have different entries, deduced from the two Y-matrices.

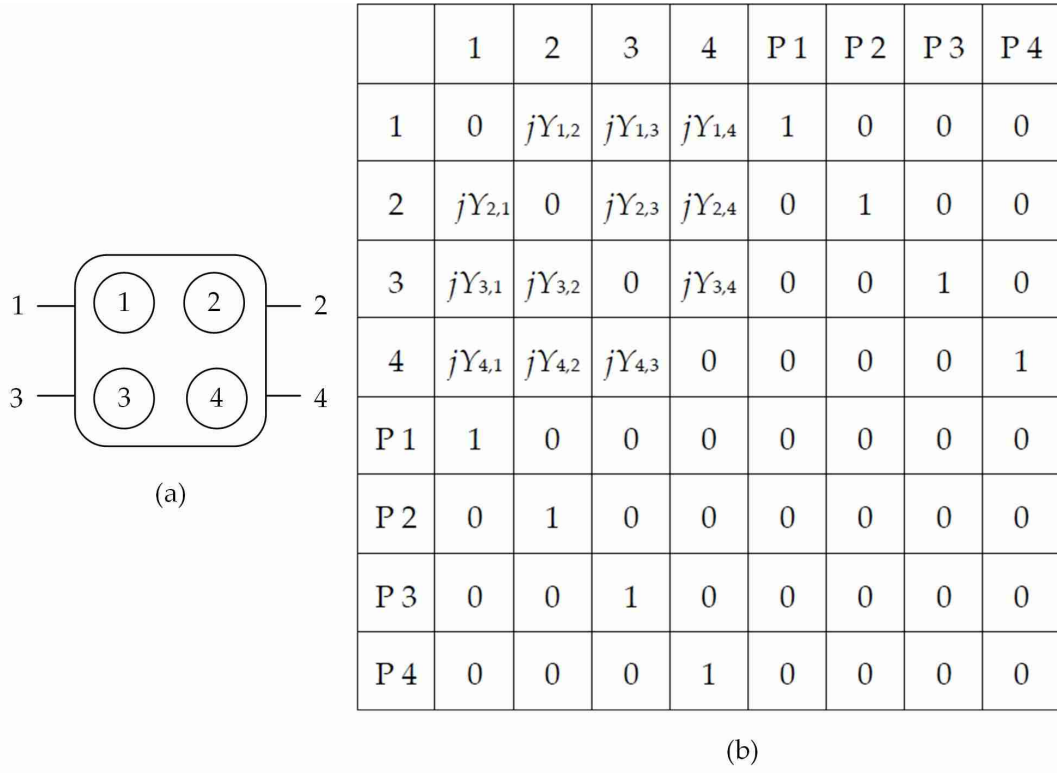


Fig. 5.5. Coupling matrix representation of branch-line couplers. (a) The node representation of the two branch-line couplers. (b) The corresponding CM representation. The two couplers share the same node form.

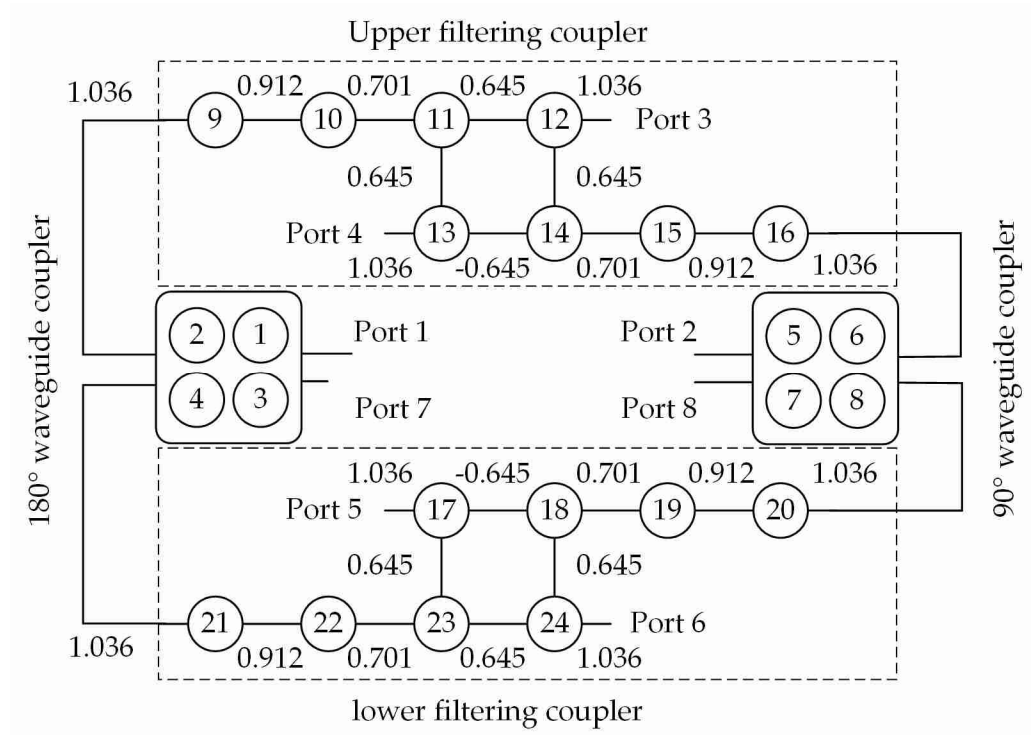


Fig. 5.6. Node representation of the filtering SPJ.

When the two branch-line couplers in Fig. 5.4 were represented by nodes, the

topology of the E-plane X-band filtering SPJ is transformed into Fig. 5.6. Now the filtering SPJ has twenty-four nodes and eight ports. Node 1-4 represents the  $180^\circ$  branch-line coupler while node 5-8 represents the  $90^\circ$  one. The corresponding CM is deduced and given in Fig. 5.7. The grey scatters in the matrix depict the non-zero values. In the CM, the entries in row/column 1 – 4 are for the  $180^\circ$  coupler, the entries in 5 - 9 are for the  $90^\circ$  coupler. The entries in 9 - 16 and 17 - 24 are for the upper and lower fourth-order filtering couplers, respectively. The remaining non-zero entries represent the connection between the couplers and the coupling to ports. These values are also given in (5.6) to

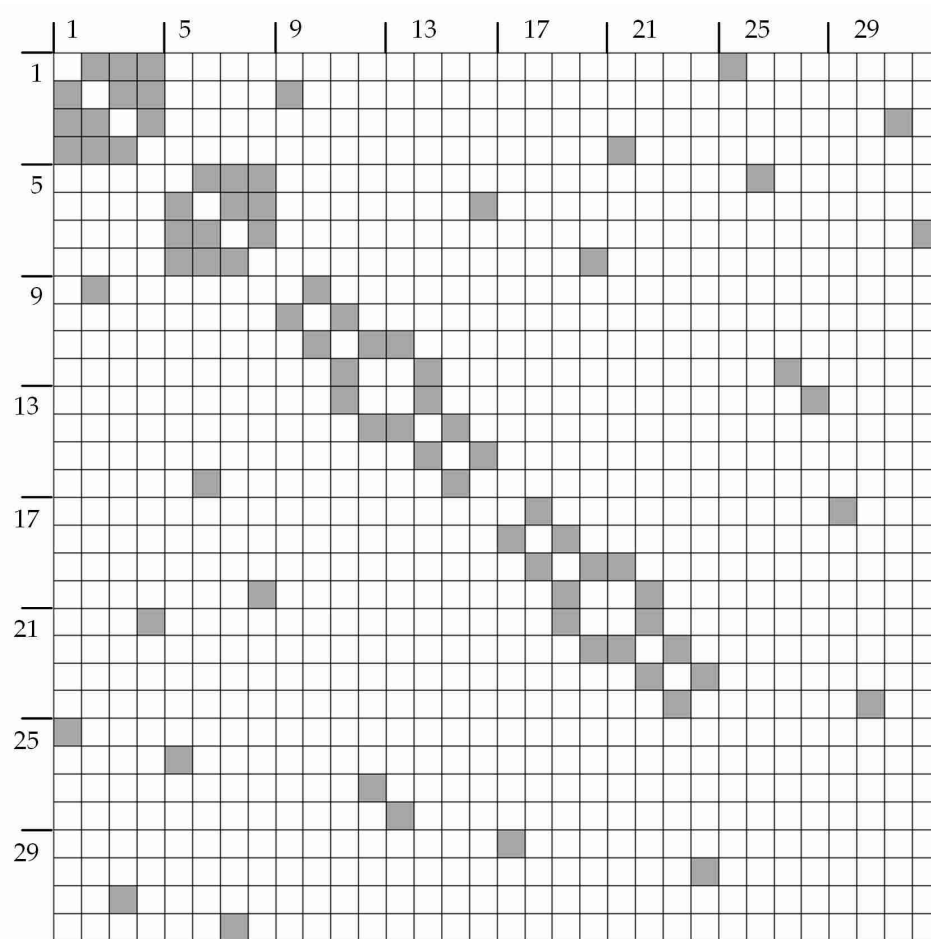


Fig. 5.7. Coupling matrix of the E-plane X-band filtering SPJ.

(5.7).

$$\left\{ \begin{array}{l} m_{1,2} = -\frac{\sec \theta}{\sqrt{2}} \\ m_{1,3} = 0 \\ m_{1,4} = \frac{\sec \theta}{\sqrt{2}} \\ m_{2,3} = -\frac{\csc \theta}{\sqrt{2}} \\ m_{2,4} = -\csc 2\theta \\ m_{3,4} = -\frac{\csc \theta}{\sqrt{2}} \end{array} \right\} \left\{ \begin{array}{l} m_{5,6} = -\sqrt{2} \cos \theta \sec 2\theta \\ m_{5,7} = -\sec 2\theta \\ m_{5,8} = \sqrt{2} \sin \theta \sec 2\theta \\ m_{6,7} = \sqrt{2} \sin \theta \sec 2\theta \\ m_{6,8} = -\sec 2\theta \\ m_{7,8} = -\sqrt{2} \cos \theta \sec 2\theta \end{array} \right. \quad (5.6)$$

$$\left\{ \begin{array}{l} m_{2,9} = m_{4,21} = m_{6,16} = m_{8,20} = 1.036 \\ m_{12,27} = m_{13,28} = m_{17,29} = m_{24,30} = 1.036 \\ m_{9,10} = m_{15,16} = m_{19,20} = m_{21,22} = 0.912 \\ m_{10,11} = m_{14,15} = m_{18,19} = m_{22,23} = 0.701 \\ m_{11,12} = m_{11,13} = m_{12,14} = 0.645 \\ m_{17,23} = m_{18,24} = m_{23,24} = 0.645 \\ m_{13,14} = m_{17,18} = -0.645 \\ m_{1,25} = m_{5,26} = m_{3,31} = m_{7,32} = 1 \end{array} \right. \quad (5.7)$$

$\theta$  represents the connection waveguides between each component. With the

CM, the theoretical magnitude response and phase response can be obtained,

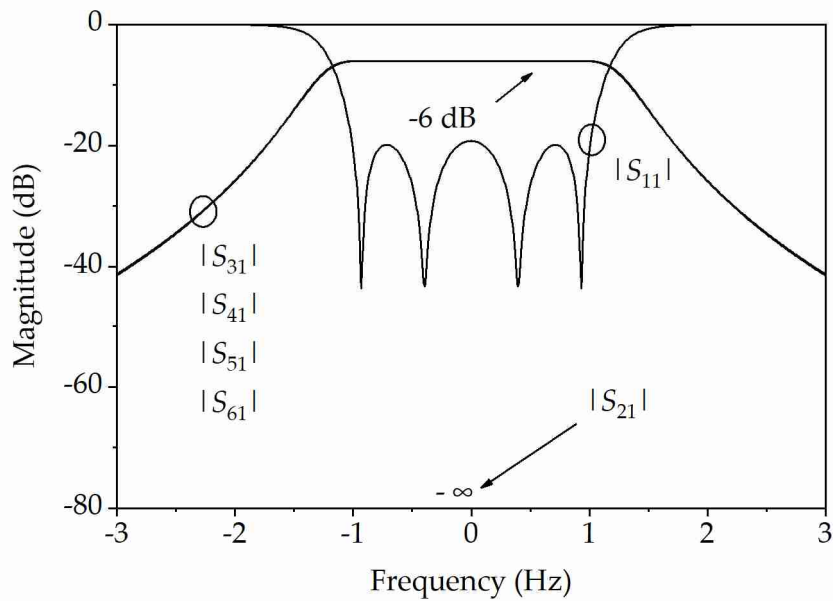


Fig. 5.8. Theoretical magnitude response related to Port 1.



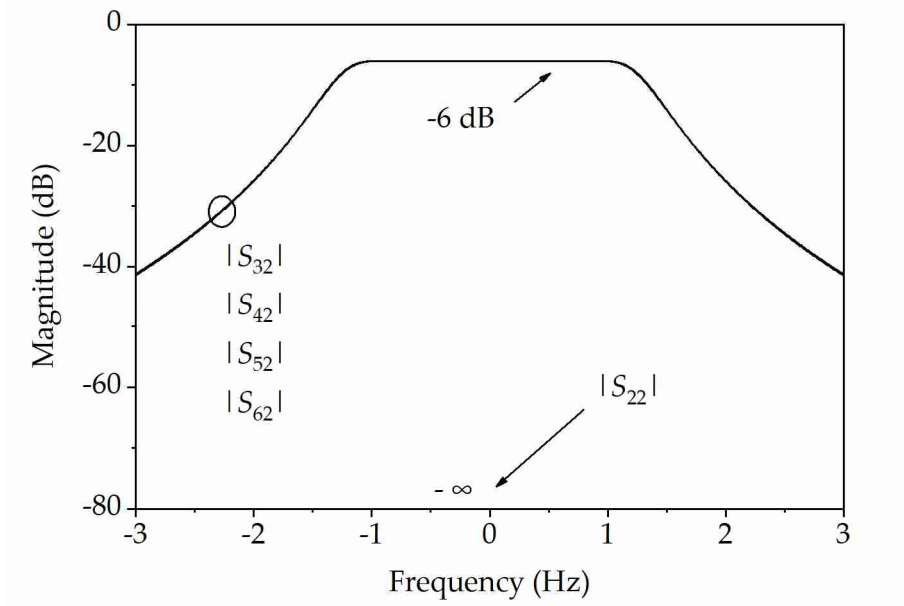


Fig. 5.9. Theoretical magnitude response related to Port 2.

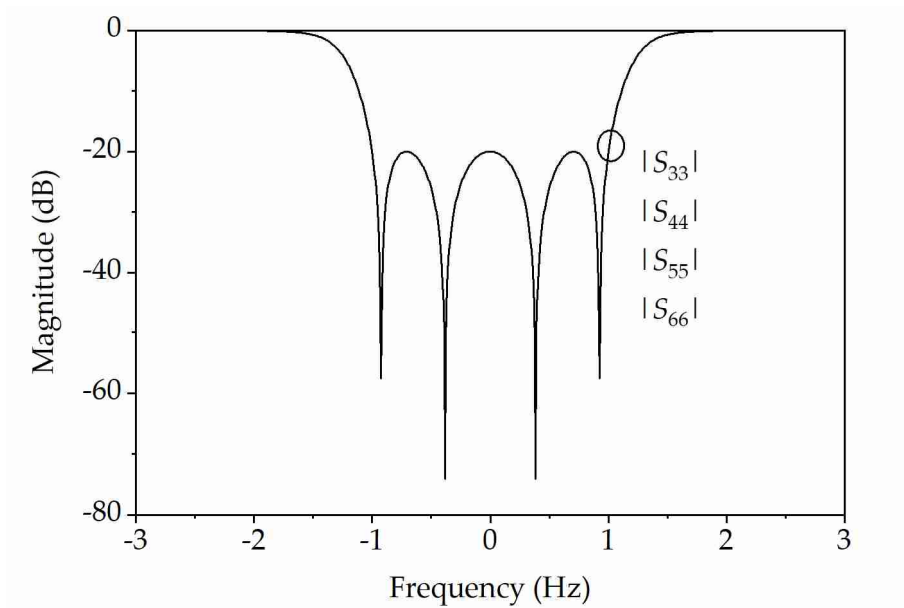


Fig. 5.10. Theoretical magnitude response of the outputs.

given in Fig. 5.8-5.11. Having the fourth-order filtering coupler, the filtering SPJ has a fourth-order Chebyshev response in the working band.  $|S_{21}|$  and  $|S_{22}|$  are both  $-\infty$  theoretically. The theoretical phase response shown in Fig. 5.11 is consistent with those expressed by (5.1).

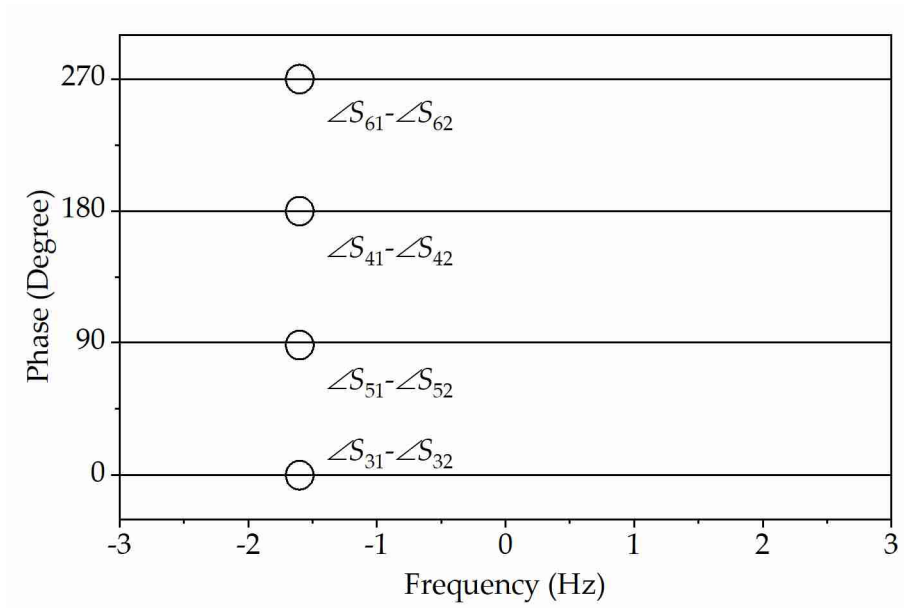


Fig. 5.11. Theoretical phase response of the filtering SPJ.

## 5.3 Implementation of the E-plane SPJ

The SPJ is to be implemented at 10 GHz with 0.4 GHz bandwidth. The constituents of the SPJ can be designed separately. In this section, the two waveguide couplers will be considered first. Then, the simulated responses of the two branch-line couplers will replace corresponding entries of the CM of the SPJ. This makes the CM contain both theoretical and simulated values and can be used to study the behaviour of the filtering SPJ with simulated responses of the constituents, which are more representative.

### 5.3.1 Implementation of the Branch-Line Couplers

The E-plane 90° branch-line coupler working in 9.5-10.5 GHz is shown in Fig. 5.12 with all the critical dimensions given. This 90° coupler has extension lines to connect it to the filtering couplers. Fig. 5.13 gives the simulated magnitude

response and phase response. The working band covers the one of the filtering SPJ, which is 9.8-10.2 GHz. This E-plane  $90^\circ$  branch-line coupler has a desired magnitude balance and low phase error in 9.8 to 10.2 GHz.

The E-plane  $180^\circ$  waveguide coupler is built upon a  $90^\circ$  coupler and a  $90^\circ$  phase

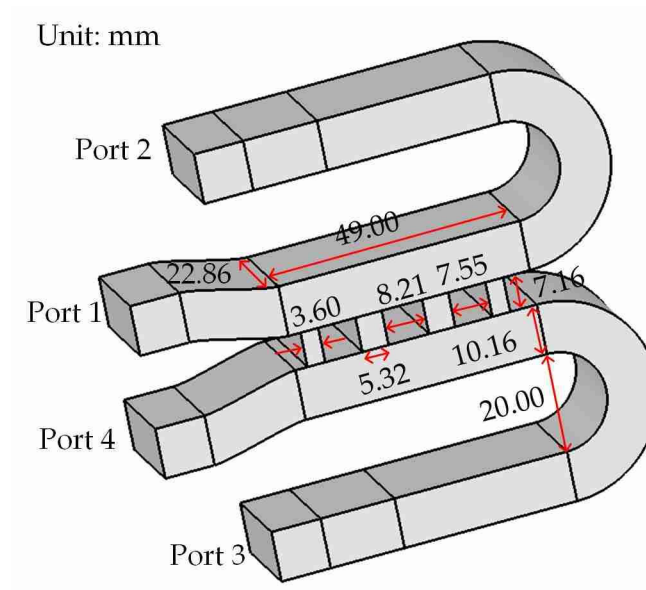


Fig. 5.12. Waveguide-based  $90^\circ$  branch-line coupler model.

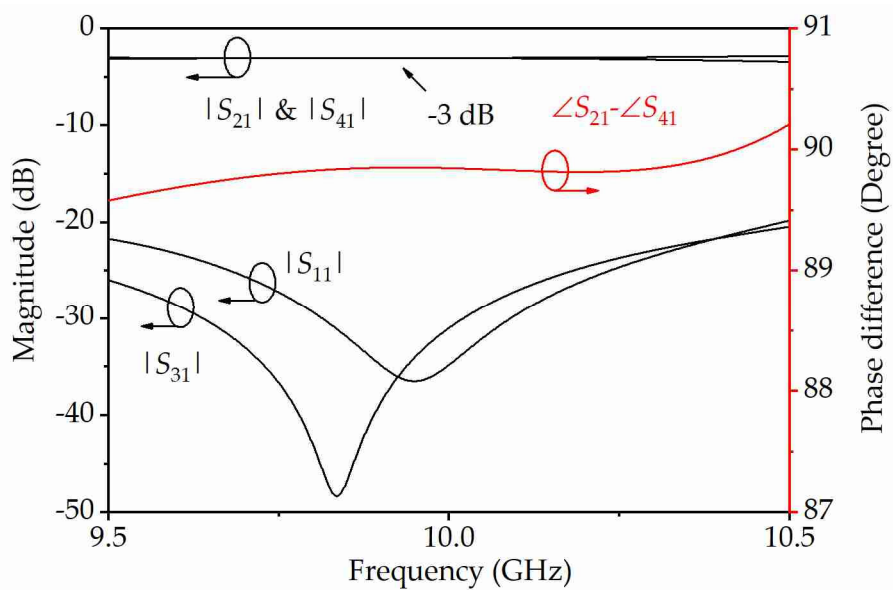


Fig. 5.13. Simulated magnitude and phase response of the waveguide-based  $90^\circ$  branch-line coupler.

Unit: mm

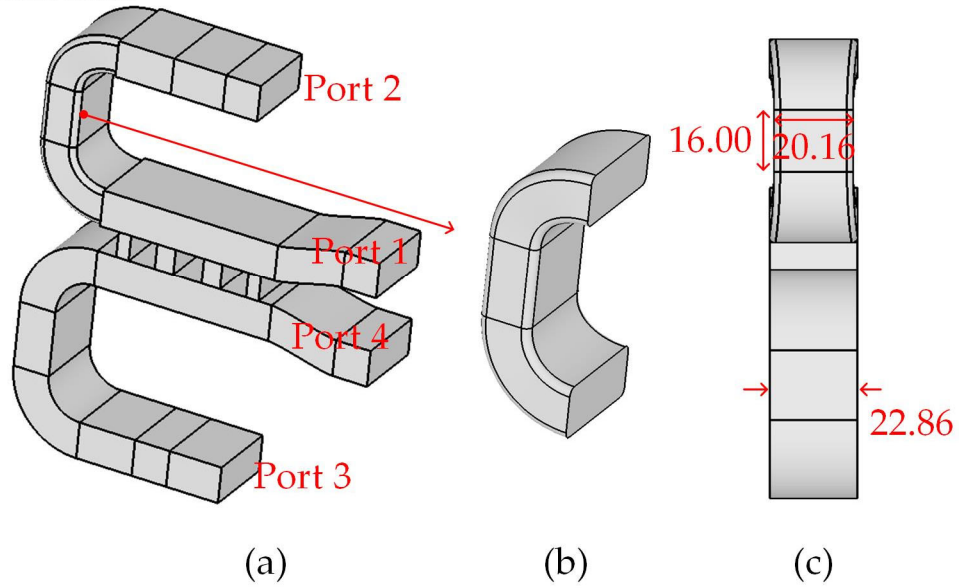


Fig. 5.14. waveguide-based 180° branch-line coupler model. (a) Overall view. (b) Enlarged view of the narrowed waveguide for phase shift purpose. (c) Side view of the coupler.

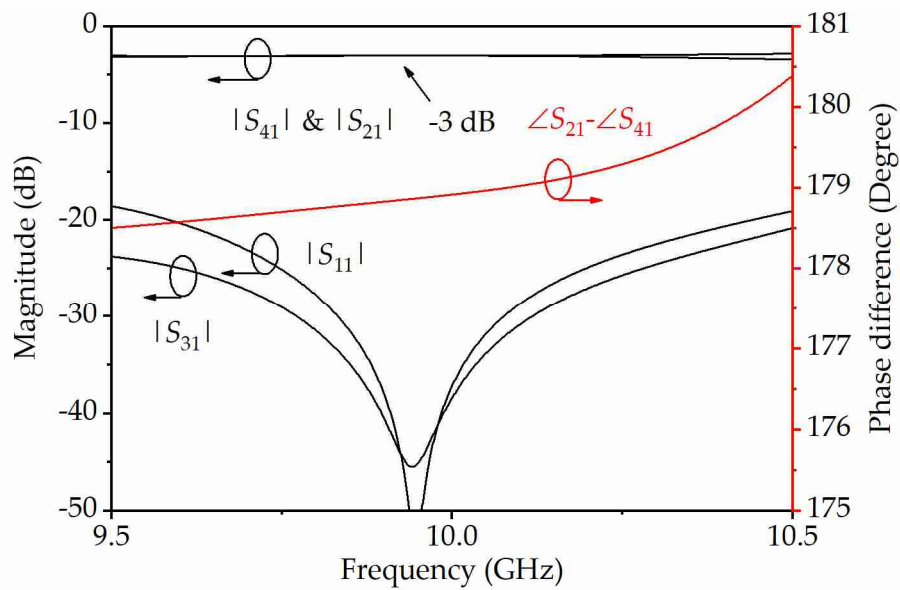


Fig. 5.15. Simulated magnitude and phase response of the waveguide-based 180° branch-line coupler.

shifter, as illustrated in Fig. 5.4(b). The air model of this coupler is provided in Fig. 5.14 with the detail of the phase-shifting waveguide. The fixed phase shift is achieved by adjusting the width of the waveguides, shown in Fig. 5.14(b).

The width of the waveguide connected to Port 2 is reduced to 20.16 mm, while the others are kept the same at 22.86 mm. The edges of the narrowed waveguide are rounded by 1 mm in radius to meet the CNC machining requirements. The narrowed waveguide provides the extra 90° phase shift.

The simulated magnitude and phase responses of the 180° branch-line couplers are shown in Fig. 5.15. The working band of this 180° coupler is also from 9.5 to 10.5 GHz, covering the working band of the filtering coupler, which is 9.8 - 10.2 GHz. The phase error of the coupler is less than 1°.

### **5.3.2 Hybrid CM of the E-plane SPJ**

Two branch-line couplers have been designed and optimized in the previous section. The SPJ was a combination of the components. Chapter 3 discussed the approach of weaving a Y-matrix of a circuit into a CM. This Y-matrix can be ideal or from simulation or even from measurement. The hybrid CM introduced in this section is a CM that combines the response of the simulated branch-line couplers with the one of the ideal filtering couplers. The contribution as well as the influence from the simulated waveguide couplers to the whole SPJ can be investigated in this way. Also, according to the influence brought by the model, the coupling of the ideal filtering couplers can be adjusted in order to optimize the performance of the whole circuit.

Based on the topology shown in Fig. 5.6, the response in Fig. 5.13 is from node 5 - 8, while the one in Fig. 5.15 is from node 1 - 4. The simulated S-parameters

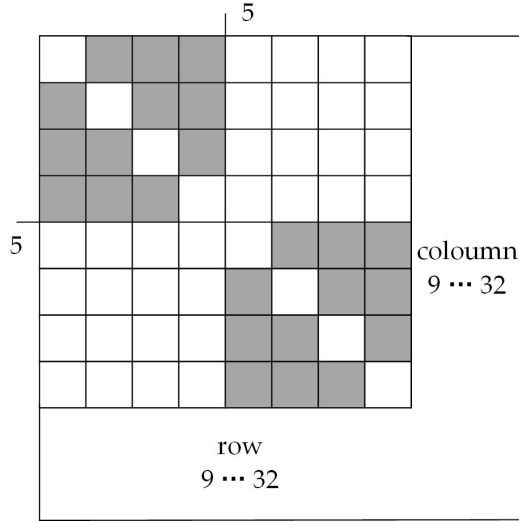


Fig. 5.16. Hybrid CM of the filtering SPJ.

of the two waveguide couplers are firstly transferred into  $Y$ -matrices. A hybrid CM of the SPJ is obtained by substituting the theoretical  $Y$ -matrices of the two filtering couplers with the transformed  $Y$ -matrices based on simulation. This hybrid CM is given in Fig. 5.16. The grey scatters in Fig. 5.16 represent the replaced entries from the original CM while other entries remain the same. The entries were replaced to:

$$\left\{ \begin{array}{l} m_{1,2} = jY_{1,2}^{180} \\ m_{1,3} = jY_{1,3}^{180} \\ m_{1,4} = jY_{1,4}^{180} \\ m_{2,3} = jY_{2,3}^{180} \\ m_{2,4} = jY_{2,4}^{180} \\ m_{3,4} = jY_{3,4}^{180} \end{array} \right\} \left\{ \begin{array}{l} m_{5,6} = jY_{1,2}^{90} \\ m_{5,7} = jY_{1,3}^{90} \\ m_{5,8} = jY_{1,4}^{90} \\ m_{6,7} = jY_{2,3}^{90} \\ m_{6,8} = jY_{2,4}^{90} \\ m_{7,8} = jY_{3,4}^{90} \end{array} \right. \quad (5.8)$$

$Y_{n,m}^{180}$  means the entries of the  $Y$ -matrix of the  $180^\circ$  waveguide coupler while  $Y_{n,m}^{90}$  means the ones of the  $90^\circ$  waveguide coupler. The subscript  $n$  and  $m$  represent the row and column. From the hybrid CM, the responses of the SPJ

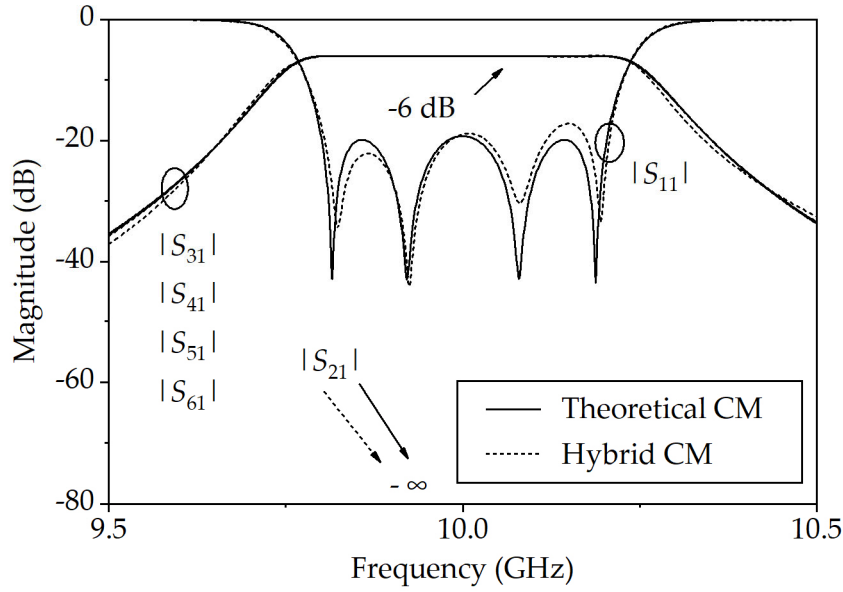


Fig. 5.17. Magnitude response of Port 1 from the hybrid CM of the SPJ. The response is compared with the ideal magnitude response.

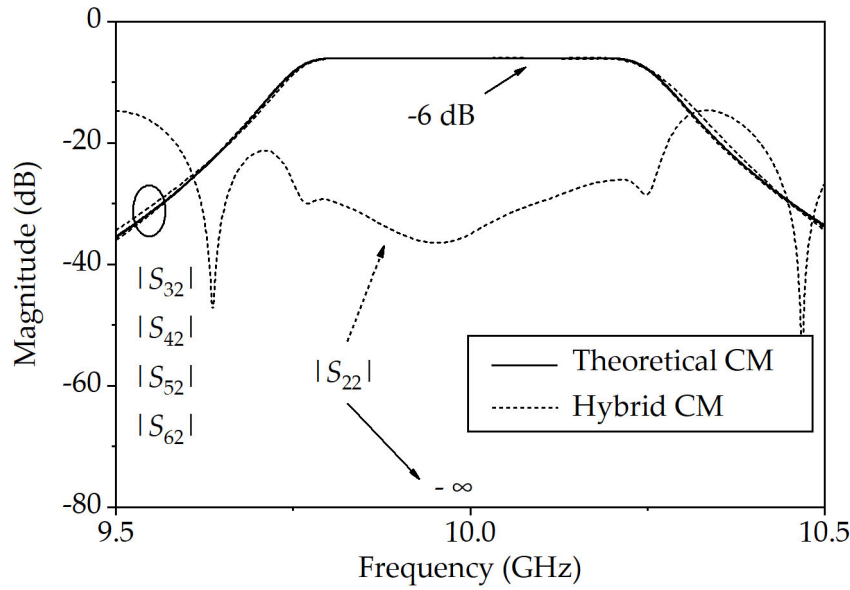


Fig. 5.18. Magnitude response of Port 2 from the hybrid CM of the SPJ.

from 9.5 to 10.5 GHz with two optimized waveguide couplers are derived and shown in Fig.5.17 to 5.19. It can be seen that  $|S_{11}|$  still has the fourth-order Chebyshev response and  $|S_{21}|$  is still  $-\infty$ . Ripples are shown in the  $|S_{22}|$  coming from the hybrid CM. This results from the asymmetrical configuration brought by the two branch-line couplers. Thanks to the decent phase response of the

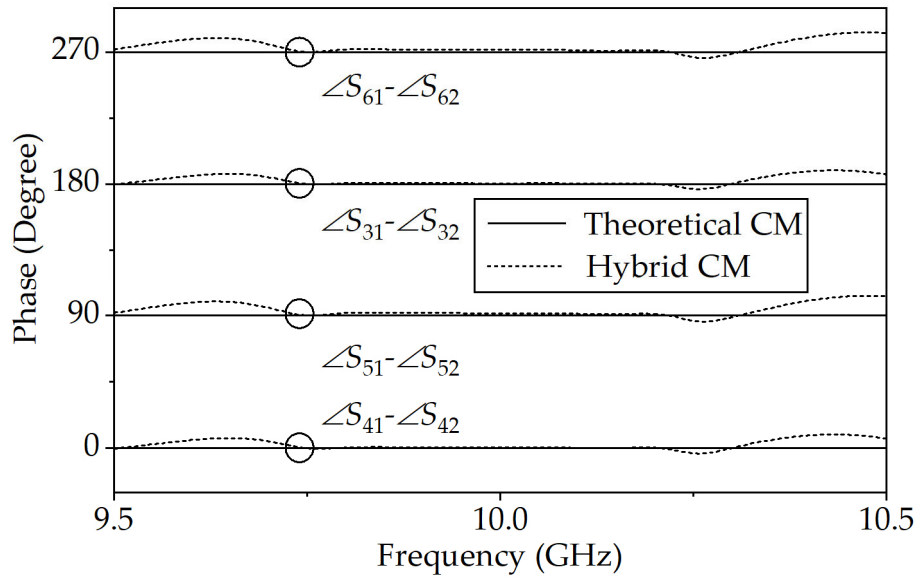


Fig. 5.19. Theoretical phase response of the SPJ from the hybrid CM of the SPJ.

waveguide couplers, the phase response from the hybrid CM is still good in the working band.

### 5.3.3 Design of the E-plane filtering coupler

The filtering function of this SPJ is achieved by the two identical  $180^\circ$  Chebyshev filtering couplers. Their bandwidth determines the bandwidth of

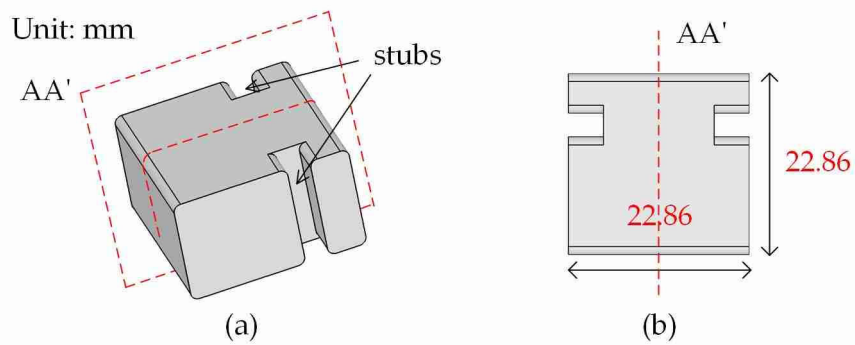


Fig. 5.20. Rectangular resonator with two stubs loaded. (a) The overall view. (b) The top view.

the SPJ, which is 9.8-10.2 GHz. Chapter 4 gives a stub-loaded resonator in designing an amplitude enhanced filtering coupler. This stub-loaded resonator



keeps the outer dimension unchanged while adjusting the resonant frequency, which simplifies the implementation. The stubs can also be applied in the E-plane configuration. But an additional stub must be added to keep the symmetry. Fig. 5.20 shows the model of the rectangular resonator with two stubs loaded, used in the implementation of the E-plane filtering coupler. The resonator is symmetric to the plane AA', shown in red dashed lines. The stub pairs in different resonators have different depths to adjust the resonant frequencies. The outer dimensions of all the resonators are kept the same at  $22.86 \text{ mm} \times 22.86 \text{ mm}$ , as shown in Fig. 5.20(b). The internal edges are rounded to 1 mm in radius to meet the fabrication limit from the milling bits in CNC machining. Fig. 5.21 gives the E-field patterns of the dominant and the second mode. The width of the loaded stubs is 4.00 mm, while the length is 5.00 mm. Under this dimension, the resonator resonates at 10.03 GHz (fundamental

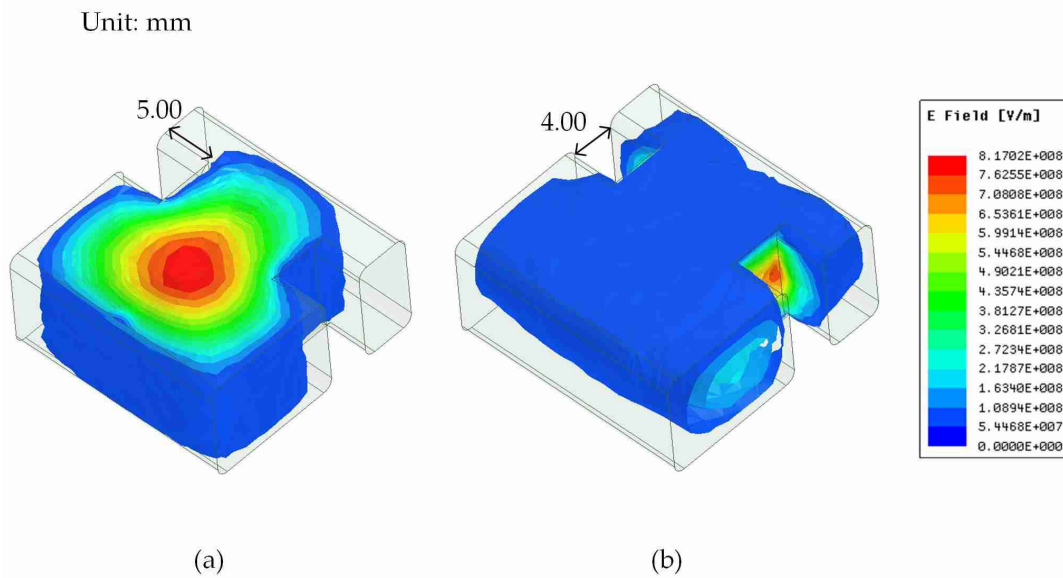


Fig. 5.21. E field patterns of the dominant mode and second mode of the square resonator with two stubs loaded. (a) The E field of the fundamental mode. (b) The E field of the second mode.

mode) and 15.74 GHz (second mode). It can be noticed that for the fundamental mode, the E-plane is the plane AA' in Fig. 5.20.

Based on the topology in Fig. 5.2, with the stub-loaded resonator proposed above, Fig. 5.22(a) shows the filtering coupler working in 9.8-10.2 GHz, with the stub-loaded rectangular resonators. There are eight resonators, all are

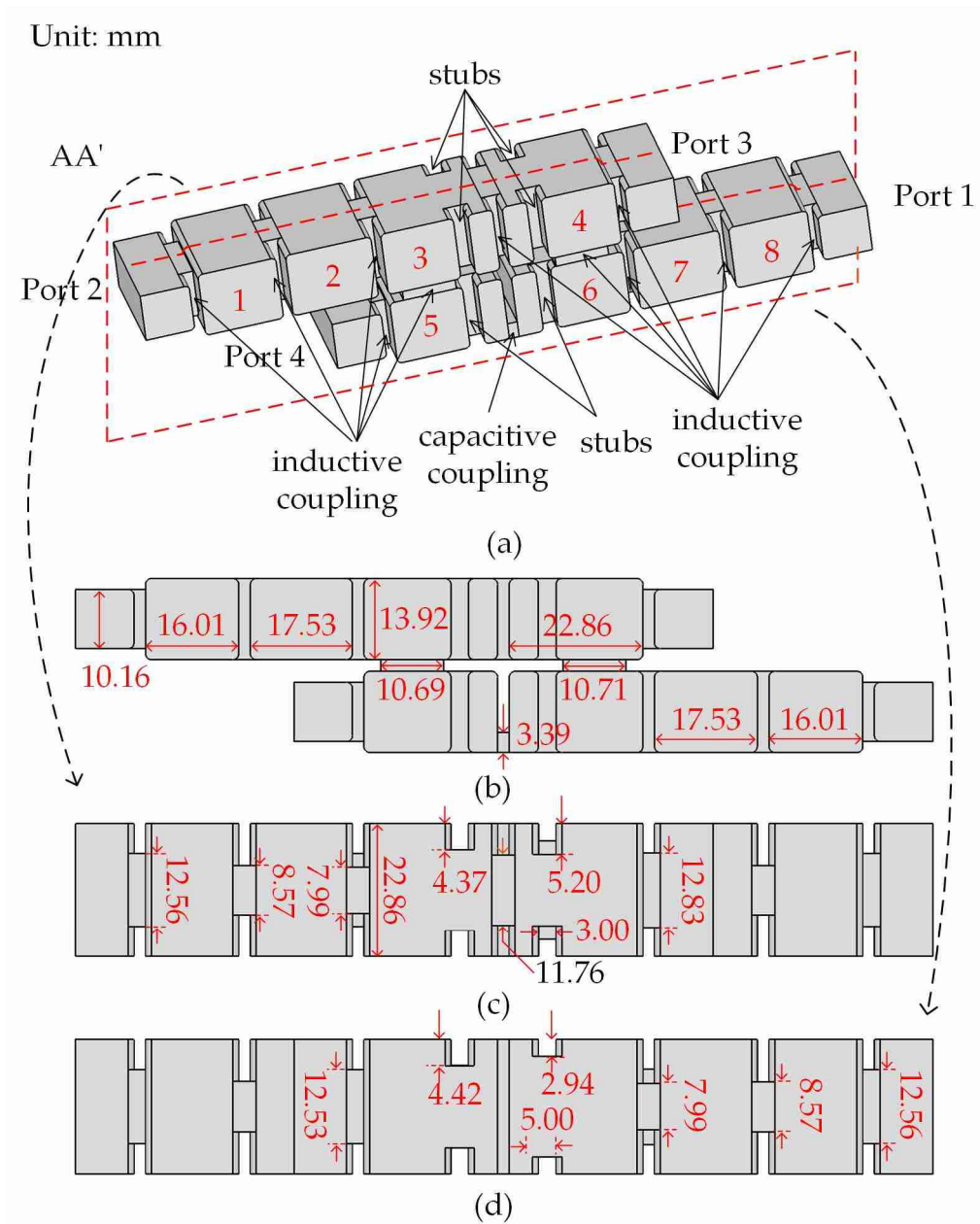


Fig. 5.22. The fourth-order filtering coupler and its dimensions. (a) Overall view; (b) Front view; (c) Top view; (d) Bottom view.

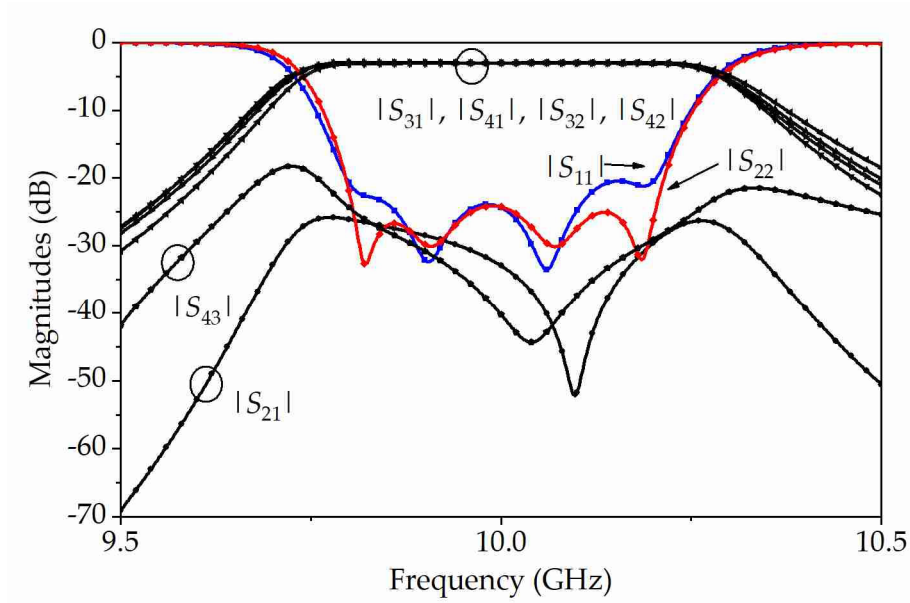


Fig. 5.23. Simulated S-parameters of the 180° filtering coupler in Fig. 6.20.

arranged in the E-plane AA'. The stub-loaded structure was applied in resonators 3, 4, 5, 6. This makes the layout easy to be adjusted. The other resonators are conventional rectangular resonators. Port 1 and Port 2 are isolated from each other, as well as Port 3 and Port 4. Internal edges of all resonators are rounded to 1 mm in radius to meet the CNC machining requirements. Critically, the 180° phase shift is achieved by the capacitive coupling ( $-90^\circ$  phase shift) between resonators 5 and 6 with the inductive couplings ( $+90^\circ$  phase shift) between resonators 3 and 4, 3 and 5, 4 and 6. Chapter 4 indicates the aperture position has influence on amplitude imbalance. The irises (apertures) between resonator 3 and 5, 4 and 6 were also adjusted for improved balance.

The coupler is designed to have the return loss and the isolation of more than 20 dB. The simulated magnitude response is shown in Fig. 5.23. Within the working band (9.8 - 10.2 GHz), the return losses and isolations all meet the

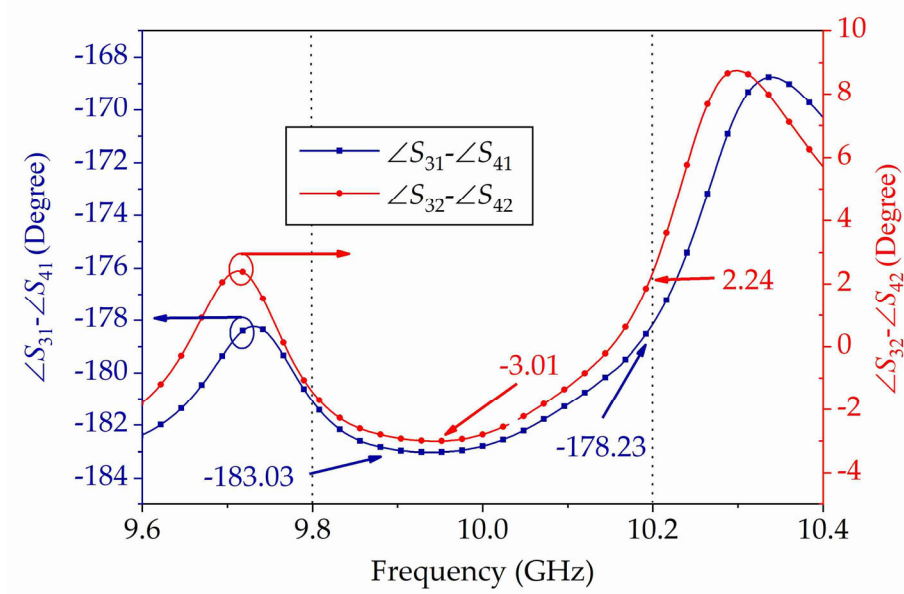


Fig. 5.24. Simulated phase responses of the 180° filtering coupler in Fig. 5.22.

specifications. The passbands are very flat and well-balanced.

The simulated phase responses are shown in Fig. 5.24. Over the working band,  $\angle S_{31} - \angle S_{41}$  varies from  $-183.03^\circ$  to  $-178.23^\circ$ . The phase difference  $\angle S_{32} - \angle S_{42}$  has a maximum of  $2.24^\circ$  and a minimum of  $-3.01^\circ$ . The detailed dimensions of the coupler can be found in Fig. 5.22(b), (c) and (d).

Having designed all the constituent components, the E-plane-cut fourth-order filtering SPJ can now be implemented. Fig. 5.25 shows the SPJ air model. Four ports are inside the circuit, implied by the topology shown in Fig. 5.1. All the ports are bent  $90^\circ$  to spare space for flanges. Fig. 5.25(a) shows the top and side views of the  $90^\circ$  bend. The inner radius is 10.00 mm, and the width of the bend is 22.86 mm. Fig. 5.25(a) also gives the perspective view of the SPJ. Fig. 5.25(b) shows the front and side views of the SPJ. The size of the SPJ air model is 288 mm  $\times$  121 mm  $\times$  26.86 mm. P1 to P8 mark out the ports with P7 and P8 terminated with a load.

Unit: mm

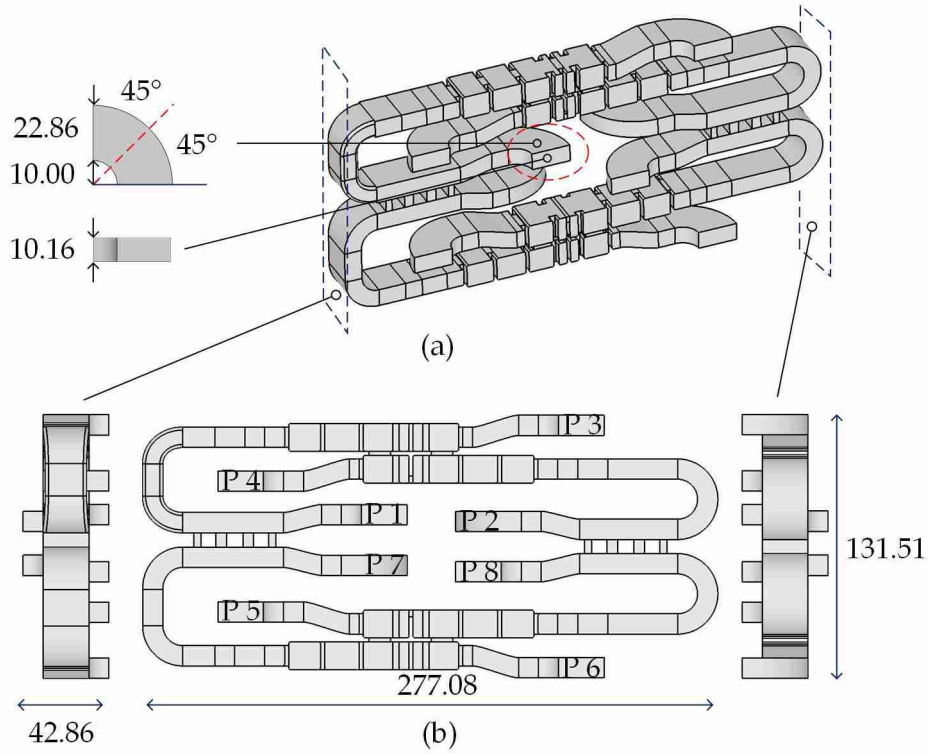


Fig. 5.25. Air model of the filtering SPJ working at 10 GHz. (a) The prospective view. (b) The front and side views.

## 5.4 SPJ Simulation and Measurement

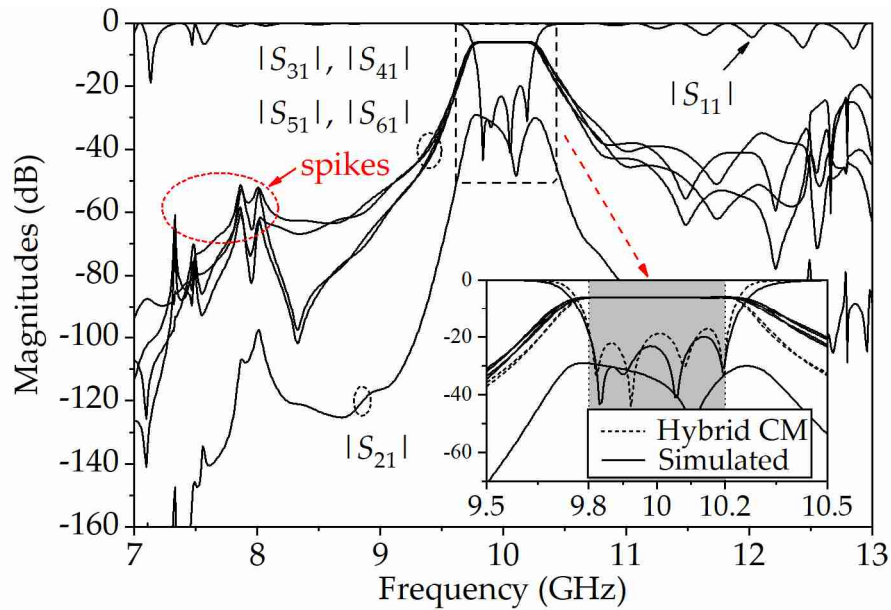


Fig. 5.26. Simulated magnitude responses of the filtering SPJ when input from Port 1. Inset shows the response over 9.5-10.5 GHz.

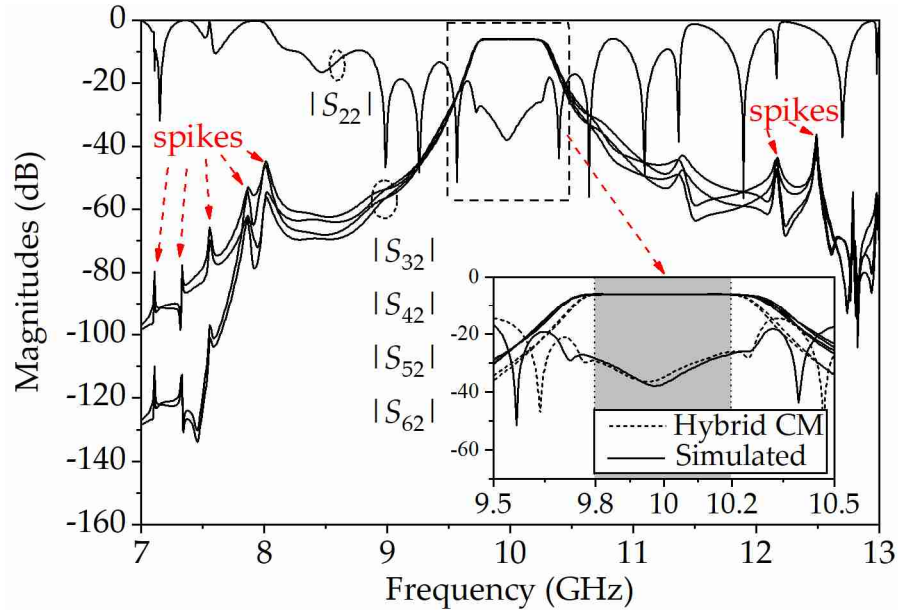


Fig. 5.27. Simulated magnitude responses of the filtering SPJ when input from Port 2. Inset shows the response over 9.5-10.5 GHz.

The simulated magnitude responses are shown in Fig. 5.26 and 5.27. The former is when the input comes from Port 1, and the latter is when input comes from Port 2. It can be seen that the transmissions have a fourth-order filtering characteristic. The insets of Fig. 5.26 and Fig. 5.27 show the magnitude responses from 9.5 to 10.5 GHz, compared with the responses from the hybrid CM. As shown in Fig. 5.26, the isolation between Port 1 and Port 2 is higher than 30 dB. In Fig. 5.27,  $|S_{22}|$  is lower than -20 dB over the same operation band.  $|S_{71}|$  and  $|S_{82}|$  are not shown here because Port 7 and Port 8 are supposed to connect to a load.

From Fig. 5.26 and 5.27, spikes out of the passband can be noticed, which are depicted by red arrows. Ripples in  $|S_{22}|$  are also noticeable in Fig. 5.27. Fig. 5.16 gave a hybrid CM formed from simulated branch-line couplers and idea  $180^\circ$  filtering couplers. The deduced response of Port 2 has been extended to 7 – 13



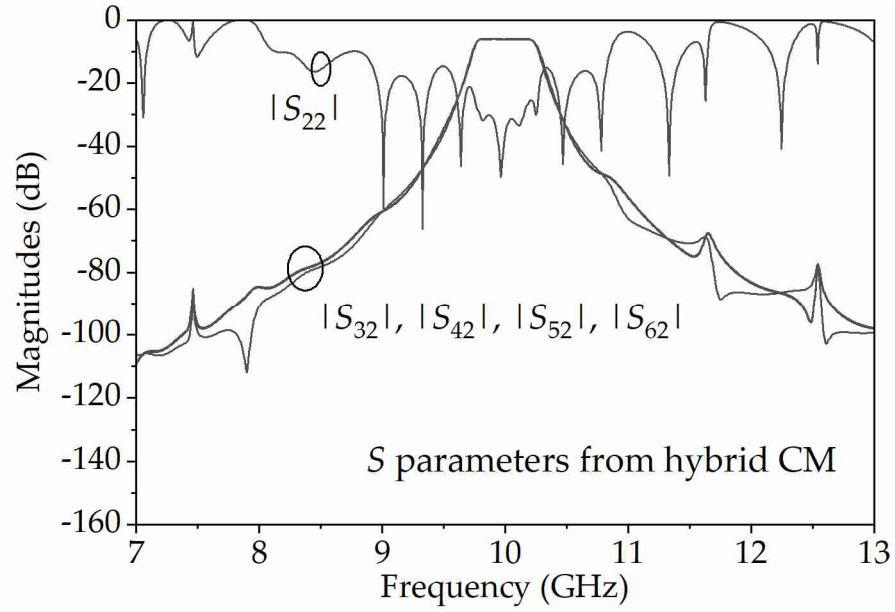


Fig. 5.28. Magnitude response of Port 2 related S-parameters from hybrid CM.

GHz, given in Fig. 5.28. Clearly, the ripples still exist in  $|S_{22}|$ . But, from the hybrid CM, there are no similar spikes in the magnitude response shown. This means the spikes were caused by the modelled filtering couplers. Fig. 5.29 gives the E-field pattern of the resonant part of the SPJ at 8 GHz. It can be noticed there is an unwanted resonant mode in the blue area, which causes the

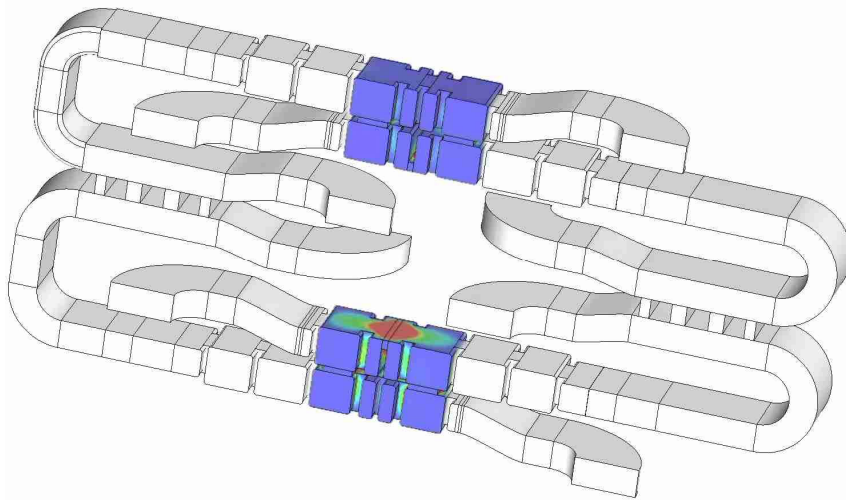


Fig. 5.29. E-field pattern of the resonant part in the SPJ at 8 GHz.

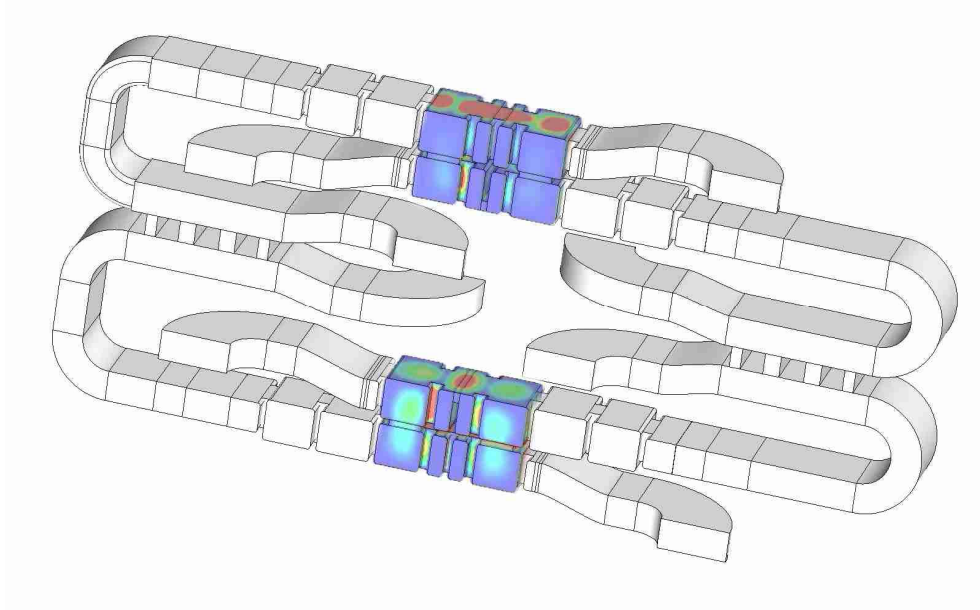


Fig. 5.30. E-field pattern of the resonant part in the SPJ at 12.1 GHz.

corresponding spikes. Other spikes around 12.1 GHz are also caused by the unwanted mode resonating at 12.1 GHz. Fig. 5.30 gives the E-field pattern.

The phase response is the key to an SPJ. Fig. 5.31 shows the simulated phase response of the filtering SPJ from 9.6 to 10.4 GHz. The curves over the working band (9.8 to 10 GHz) have been enlarged for more details. The simulated phase

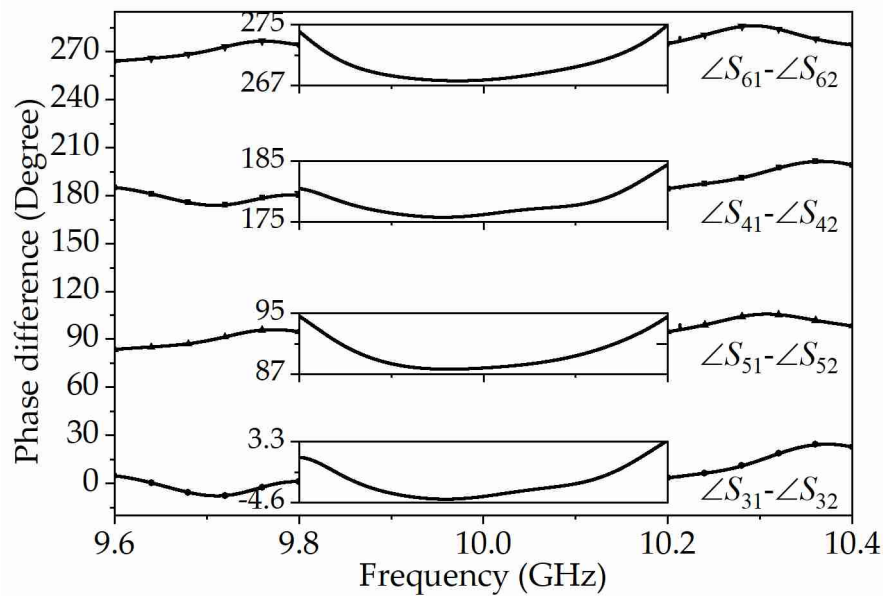


Fig. 5.31. Simulated phase response of the filtering SPJ from 9.6 to 10.4 GHz. The curves are zoomed over the working band (9.8 - 10.2 GHz).



differences agree with those from the theory in (5.1). The largest phase error in simulations is  $5^\circ$ . The SPJ was optimized and fabricated using CNC machining (material: Aluminum). The metal model of the SPJ is given in Fig. 5.32(a). The

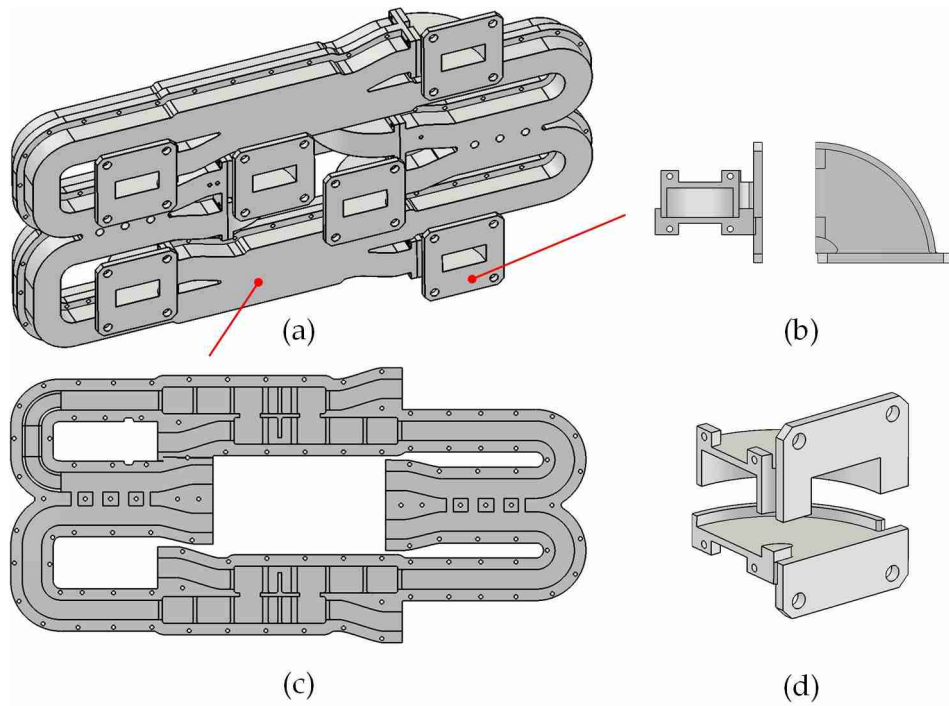


Fig. 5.32. Assembly of the SPJ. (a) Overall view. (b) Side and top view of the bend flange. (c) The main part of the SPJ. (d) Assembly of the bend.

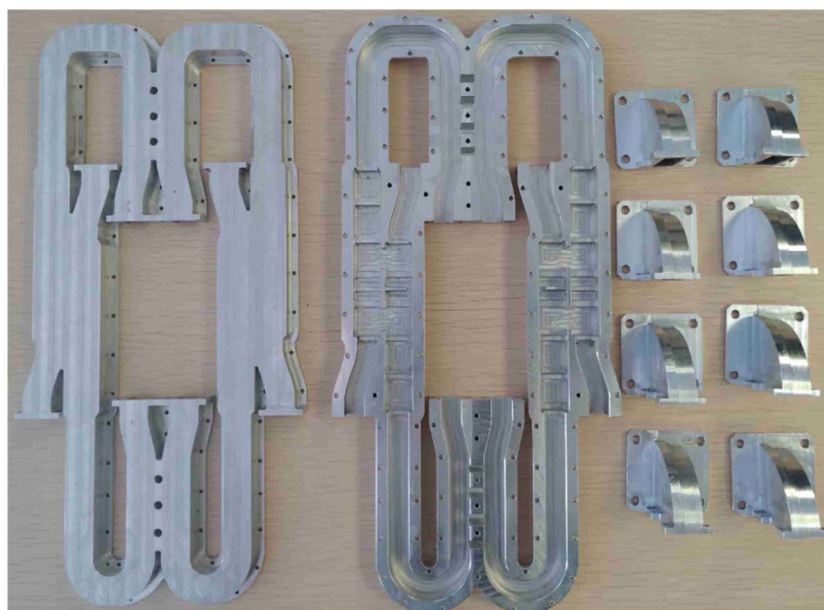


Fig. 5.33. Fabricated SPJ by CNC machining, shown as separate parts.

metal model contains two identical main body blocks and eight flanges with bent waveguides. One of the main body blocks is shown in Fig. 5.32(c). One flange in the SPJ is made by two parts, as shown in Fig. 5.32(d). The two parts were glued together, shown in Fig. 5.32(b). With this model, the SPJ is fabricated and shown in Fig. 5.33.

The measurement setup of the SPJ is shown in Fig. 5.34. There are eight ports

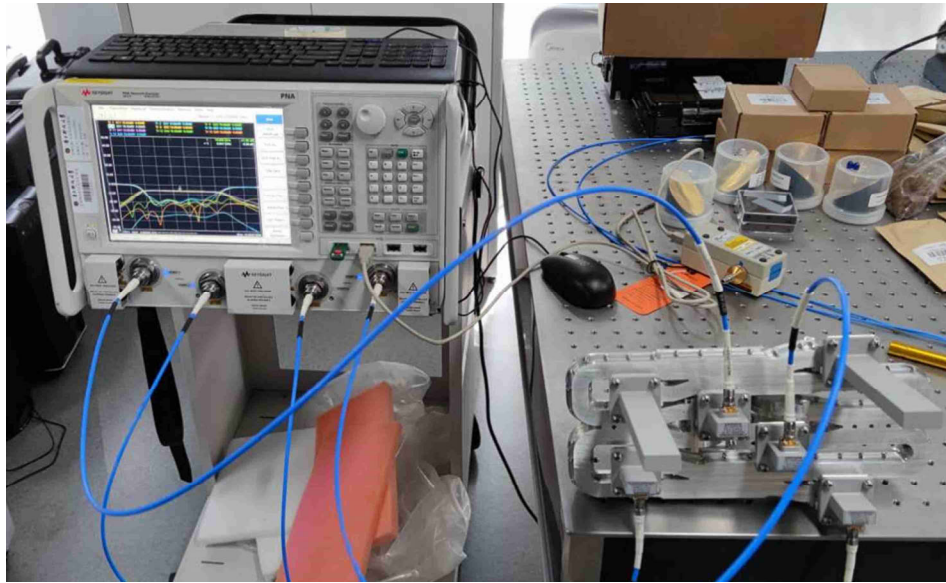


Fig. 5.34. Measurement setup of the SPJ.

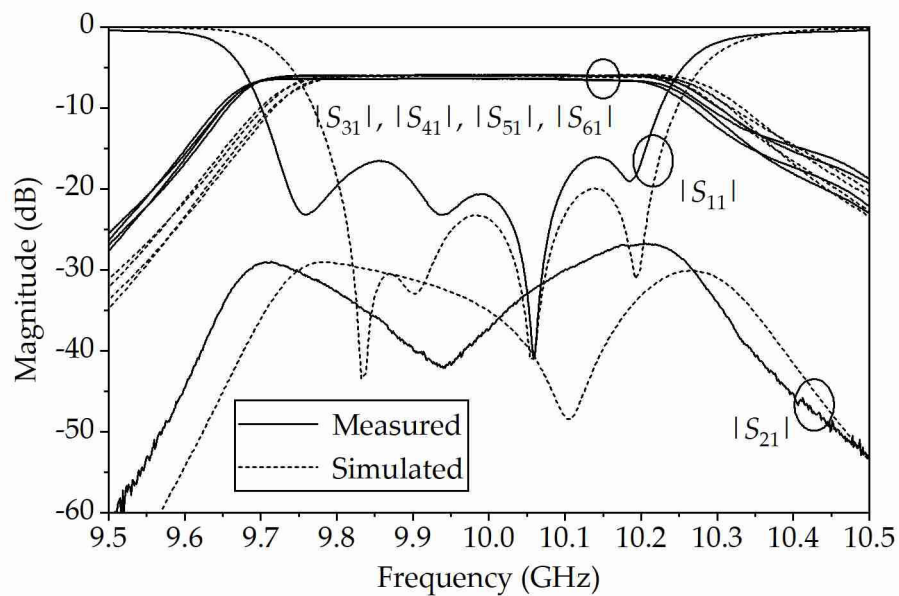


Fig. 5.35. Measured magnitude response of port 1 of the SPJ.

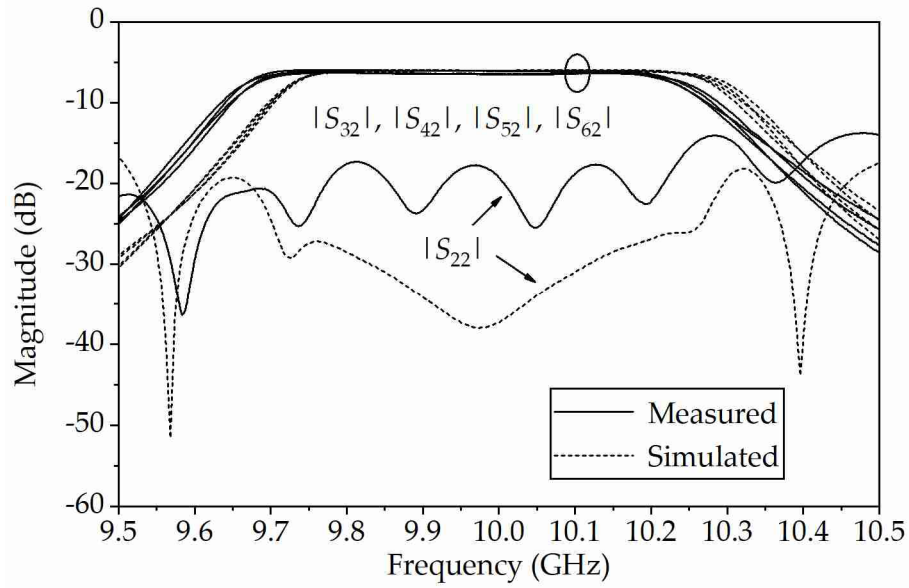


Fig. 5.36. Measured magnitude response of port 2 of the SPJ.

in total, and four of them are connected to loads in each measurement using a four-port vector network analyzer (N5227A). The measured magnitude responses of the SPJ are shown in Fig. 5.35 and Fig. 5.36. It can be noticed that there is a slight frequency shift of about 0.05 GHz. The designed working band is 9.8 to 10.2 GHz while, in the measurement, this is 9.75 to 10.15 GHz. The

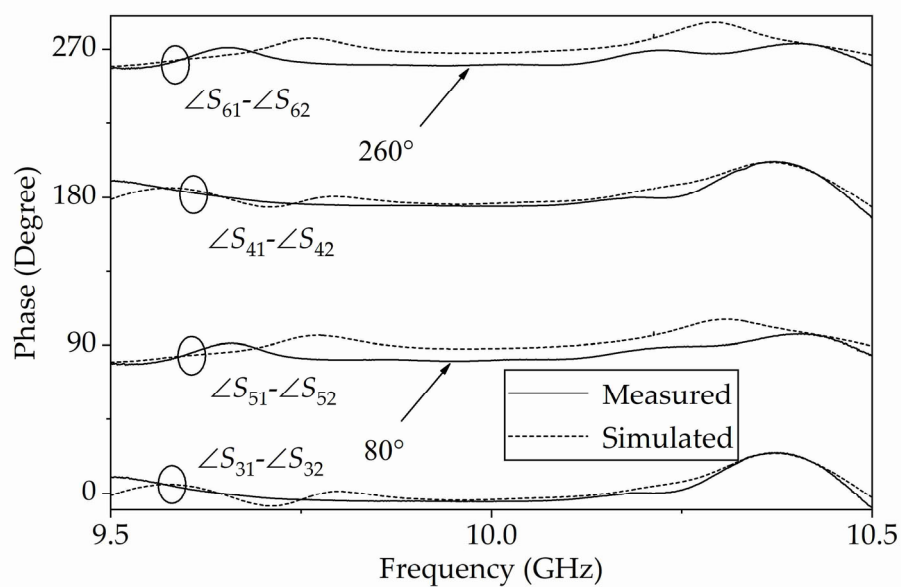


Fig. 5.37. Measured phase response of the SPJ.

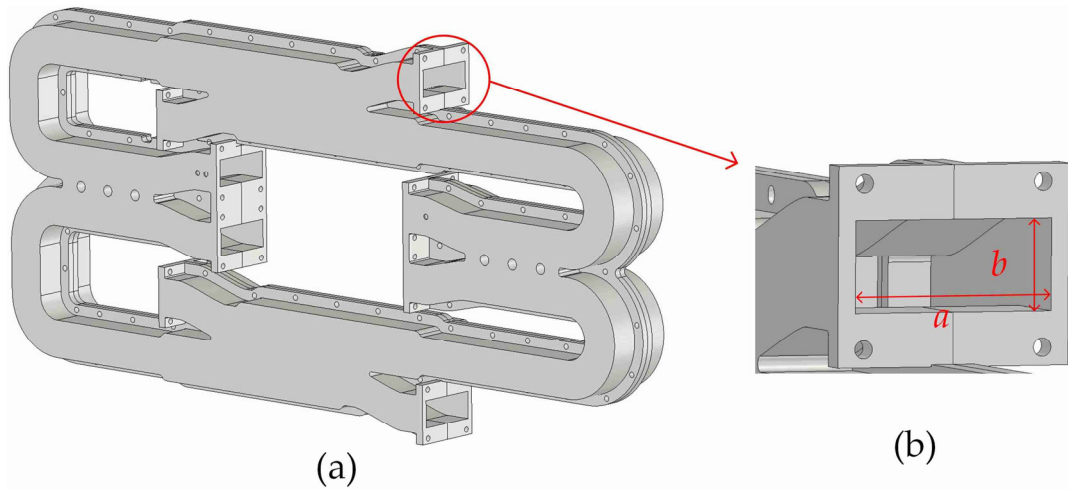


Fig. 5.38. Demonstration of the fabricated metal model. (a) The overall view. (b) is zoomed-in graph for the detail.

measured return loss at Port 1 and 2 in the actual working band is larger than 15 dB. The insertion losses are about 6.4 dB, including 6 dB power division loss in the working band with flat output magnitudes. The four reflection zeros are identifiable in  $|S_{11}|$  response. The phase response of the measurement, compared with the simulation, is shown in Fig. 5.37. The most significant phase error in the measurement is  $10^\circ$ , which is in  $\angle S_{61} - \angle S_{62}$  and  $\angle S_{51} - \angle S_{52}$ . Although there was frequency shift in the measured response, there are still four clear poles in  $|S_{11}|$ . This implies the frequency shift may be brought by a universal error. Fig. 5.38 gives the fabricated model (a) and the detail of the port (b). It is known that the resonant frequency of the fundamental mode in a waveguide is not sensitive to the height  $b$  of the waveguide while the changing of width  $a$  has a direction influence on the resonant frequency. The dimension of the fabricated model was measured using vernier caliper, shown in Fig. 5.38. The measured dimension  $a$  in Fig. 5.38(b) is 23.00 mm while the designed one

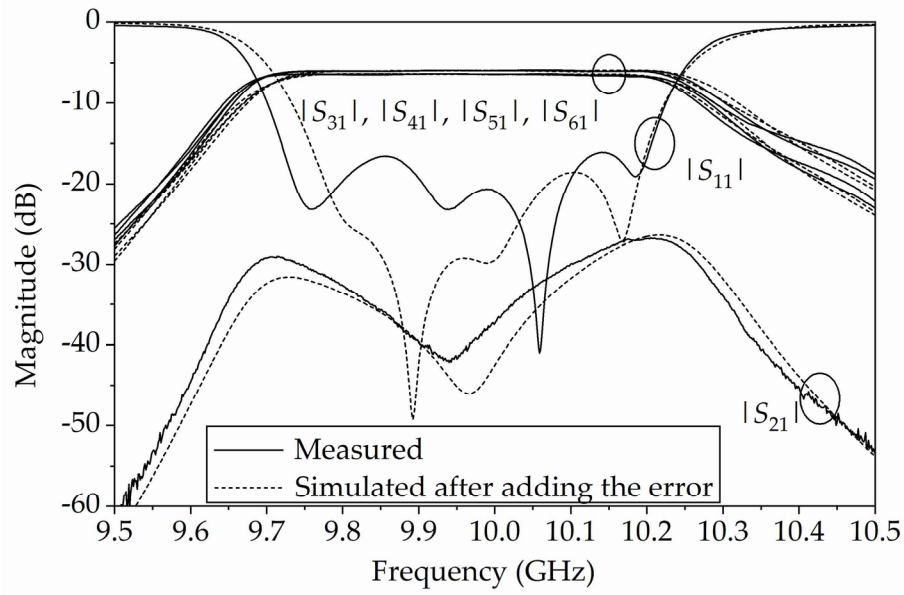


Fig. 5.39. Measured and the re-simulated magnitude responses of Port 1 of the SPJ.

was 22.86 mm. After adding this fabrication error, the re-simulated response was compared with the measurement, given in Fig. 5.39, 5.40 (magnitude responses) and Fig. 5.41 (phase response). It can be noticed after having added the 0.14-mm fabrication error, for magnitude responses, the passband from re-simulation is the same with measurement. For phase response, re-simulation is

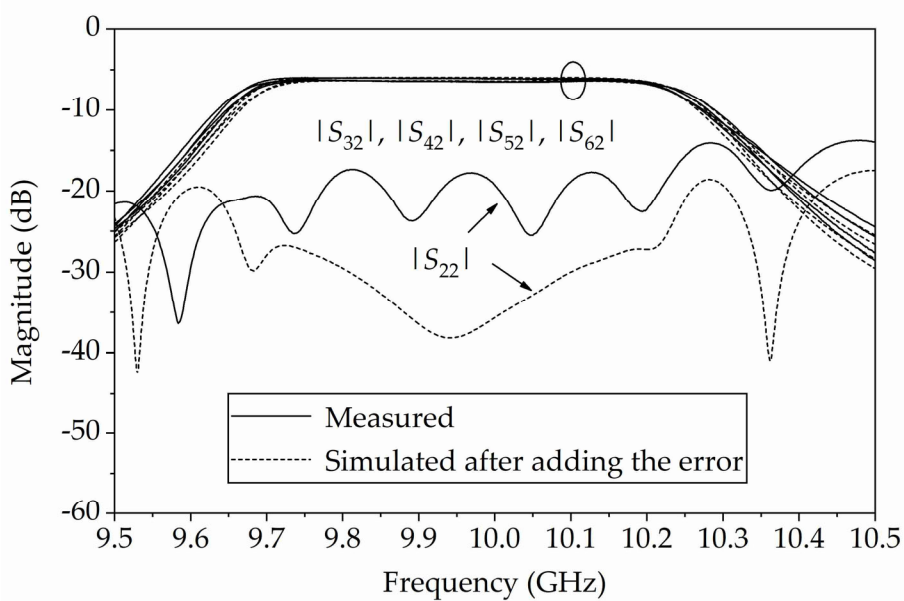


Fig. 5.40. Measured and the re-simulated magnitude responses of Port 2 of the SPJ.

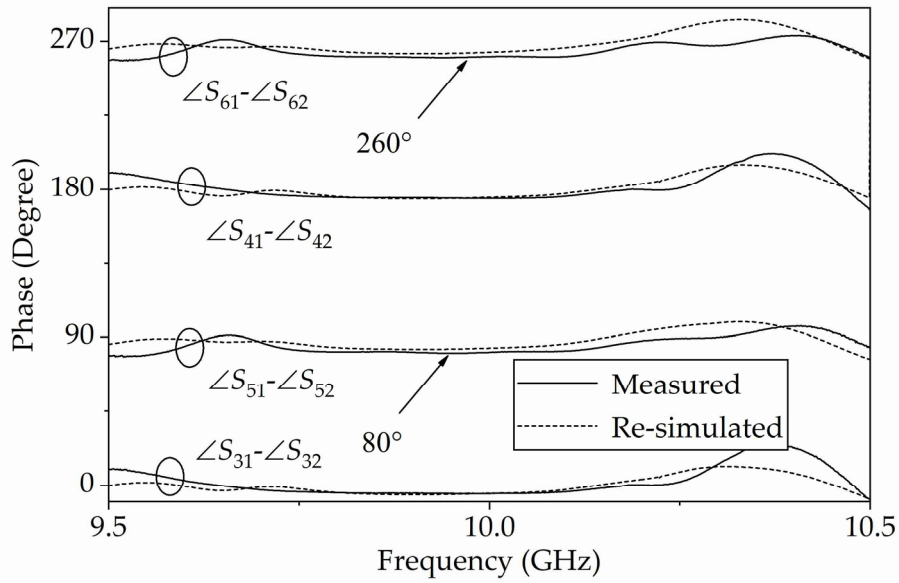


Fig. 5.41. Measured and the re-simulated phase response of the SPJ.

also superimposed with measurement. This result reveals that the 0.14-mm fabrication error brings frequency shift and phase error.

## 5.5 Summary

This chapter presents a filtering SPJ working in 9.8-10.2 GHz. The SPJ was fabricated and assembled. Measurement showed an excellent agreement with the simulation and verified the design approach of the filtering SPJ. A very flat passband with over 15 dB return loss was achieved with the help of the embedded resonators. The phase error was  $10^\circ$  in 9.8 two 10.2 GHz, which was brought by fabrication error. In addition, the CM with NRCs are used not only to give a theoretical response, but a hybrid response. The hybrid response consists of simulated part and ideal part of the circuit. With the help of the hybrid response, the reason for the spurious spikes and ripples in the simulation were easily identified. The procedure in synthesizing the X-band filtering SPJ helps

designing the D-band filtering SPJ in Chapter 7.

## Reference

- [1] X. Chen, Y. Wang, T. Skaik, and Q. Zhang, "E-Plane Waveguide Filtering Six-Port Junction," *IEEE Transactions on Microwave Theory and Techniques*, vol. 69, no. 12, pp. 5360-5370, 2021.
- [2] D. M. Pozar, *Microwave engineering*. John wiley & sons, 2011.



# **Chapter 6. Ring-Shaped D-Band 180° Filtering Coupler**

This chapter presents a ring-shaped D-band 180° filtering coupler at 150 GHz, which is applied in the D-band filtering SPJ later in Chapter 7. The previous chapter introduced a fourth-order 180° filtering coupler working at 10 GHz. The proposed stub-loaded resonator significantly eased the coupler configuration. Although the measurement showed a desired response, it is hard to utilize the same structure in D-band due to the small stubs and apertures in capacitive irises. D-band branch-line couplers have been reported [1-5] under E-plane configuration for minimum radiation loss. This chapter presents a novel fan-shaped resonator, with which a ring-shaped E-plane coupler can be easily achieved. Meanwhile, tiny stubs and capacitive irises, which are difficult to machine at D-band, are also avoided in the design. Inspired by work in Chapter 4, the aperture position was also carefully adjusted to ensure maximum amplitude balance. Through simulation and measurement, a highly desired response was obtained. To the author's knowledge, this is the first report of a filtering 180° coupler working in D-band. The work of this chapter has been published in [6].

## **6.1 Fan-Shaped Resonator**

Fan-shaped resonators were proposed to combine the E-plane configuration



Unit: mm

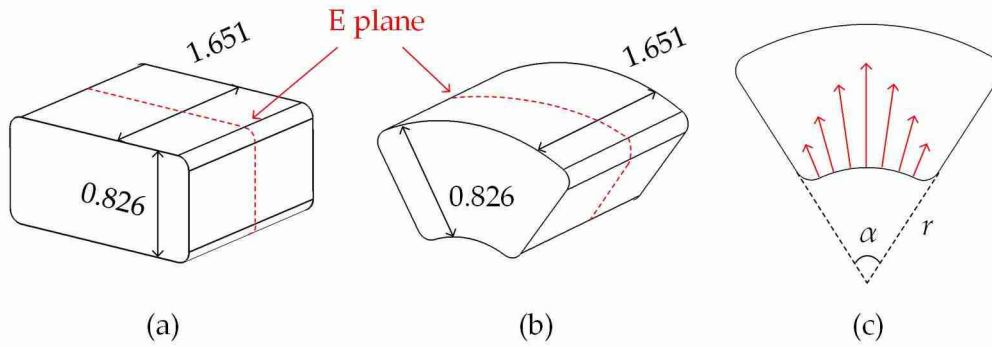


Fig. 6.1. Rectangular resonator versus fan-shape resonator: (a) Original rectangular resonator; (b) Proposed fan-shaped cavity; (c) Projected electric field pattern on the E-plane of the fundant resonant mode.

with waveguide resonators, shown in Fig. 6.1. The conventional rectangular resonators are bent along the length, making fan-shaped resonators, as shown in Fig. 6.1(b). Note that all the internal edges perpendicular to the E-plane (as indicated in the red dash line) are blended with a 0.1-mm radius to meet the fabrication requirement at these high millimetre-wave frequencies. The height and width of the resonators are kept the same as the standard D-band waveguide, which is 0.826 mm  $\times$  1.651 mm. The front view of the bent resonator, is shown in Fig. 6.1(c). The electric field pattern of the fundamental  $TE_{101}$  resonant mode is illustrated in red arrows.  $\alpha$  is the bending angle of the fan-shaped resonator, and  $r$  is the inner radius. Instead of the length, these two values specify the resonators' size and thus the resonant frequency. The E-field patterns of the fundamental mode and the second mode are shown in Fig. 6.2.  $r$  of the fan-shaped resonator is set at 0.8 mm and  $\alpha$  is  $64^\circ$ . The fundamental mode under this dimension resonates at 144.53 GHz, and the second mode

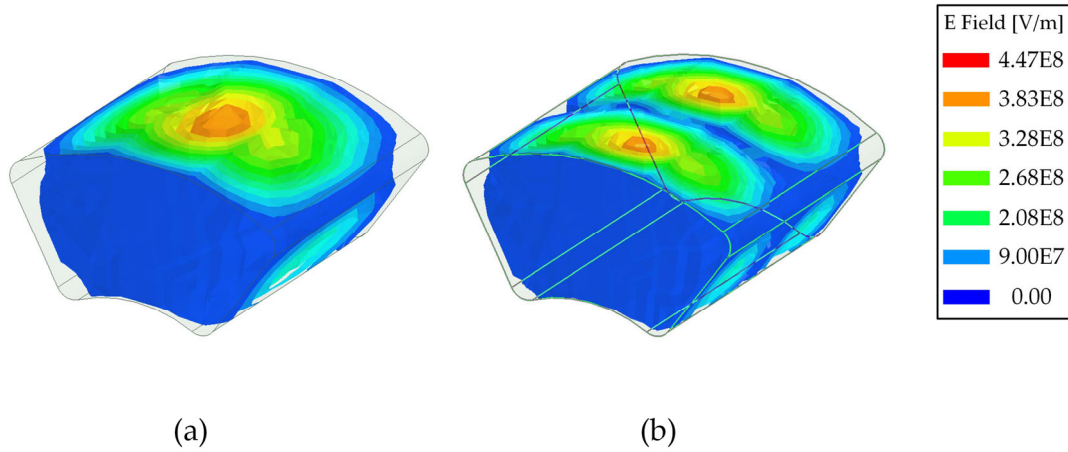


Fig. 6.2. E-field pattern of (a) the fundamental mode and (b) the second mode.

resonates at 213.62 GHz.

The topology of a  $180^\circ$  filtering coupler was initially given in Chapter 4. Capacitive iris was used in that implementation for the X-band filtering couplers. In D-band design, this needs to be avoided because the features are usually too small and too deep to be manufactured with sufficient accuracy. Capacitive couplings are generally stronger than inductive couplings in terms of coupling level. To achieve the same coupling level, the aperture in a capacitive iris is usually much smaller in dimension than in an inductive one. In the 10-GHz filtering coupler shown in Fig. 4.4, the height of the aperture in the capacitive iris is 1.20 mm, which means the height will be around 0.08 mm when the frequency is 150 GHz ( $1.20/15 = 0.08$ ). Thus, limited fabrication capacity may cause a significant error on capacitive irises.

The  $TE_{102}$  mode resonator was adopted to replace the capacitive iris since the mode provides with extra  $180^\circ$  phase shift, as the capacitive iris does. The length of one resonator is doubled to support the  $TE_{102}$  mode while keeping the

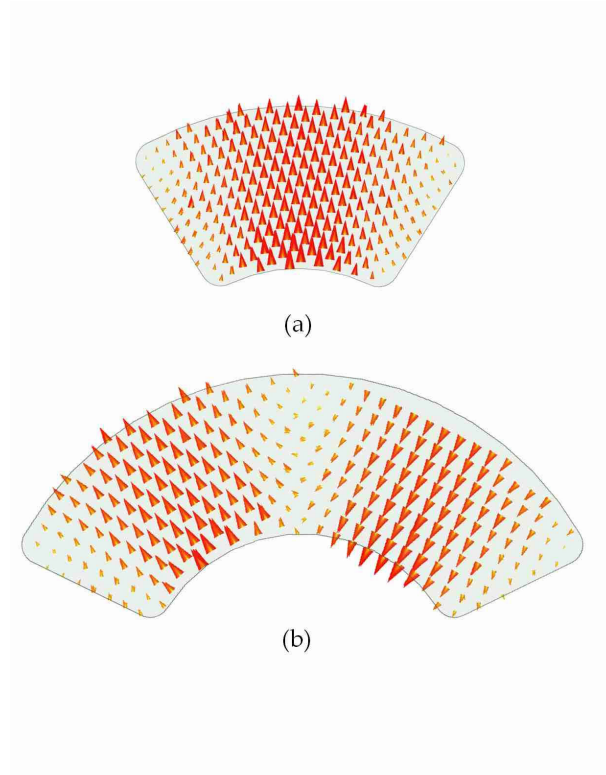


Fig. 6.3. E-field patterns of (a) normal length resonator and (b) doubled length resonator under the same frequency.

working frequency unchanged. Fig. 6.3 gives the E-field patterns of the working modes of one normal size fan-shaped resonator and one double-length (angle) fan-shaped resonator under the same frequency. The angle  $\alpha$  of the  $TE_{101}$ -mode resonator is  $64^\circ$  while it is  $128^\circ$  for the  $TE_{102}$  resonator. Under the same frequency, it can be noticed that the double-length fan-shaped resonator supports  $TE_{102}$  mode. The E-field implies this mode brings an extra  $180^\circ$  phase shift. This feature can be utilized to replace the capacitive iris.

## 6.2 Implementation and Simulation

Fig. 6.4 gives the schematic of an E-plane filtering coupler with this double-length resonator. It supports both  $TE_{101}$  mode and  $TE_{102}$  mode at the working

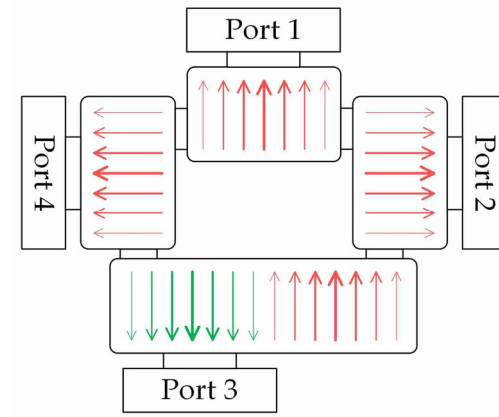


Fig. 6.4. Electric (E) field pattern of the working mode in the schematic diagram of the filtering coupler.

frequency. Contributed by the double-length resonator, the  $TE_{102}$  mode brings a  $180^\circ$  phase shift, replacing a capacitive coupling. All the resonators are coupled through inductive irises. Unlike the H-plane coupler in Chapter 3, the coupler is split along the favourable E-plane. The arrows in Fig. 6.4 indicate the E-field pattern of the standing waves.

The air model of the filtering coupler is shown in Fig. 6.5. The four resonators are laid out in an annular shape to form a compact footprint. Fig. 6.5(a) gives the perspective view of the filtering coupler, and Fig. 6.5(b) gives the side view. Its circumference has been divided into eight parts, four are resonators

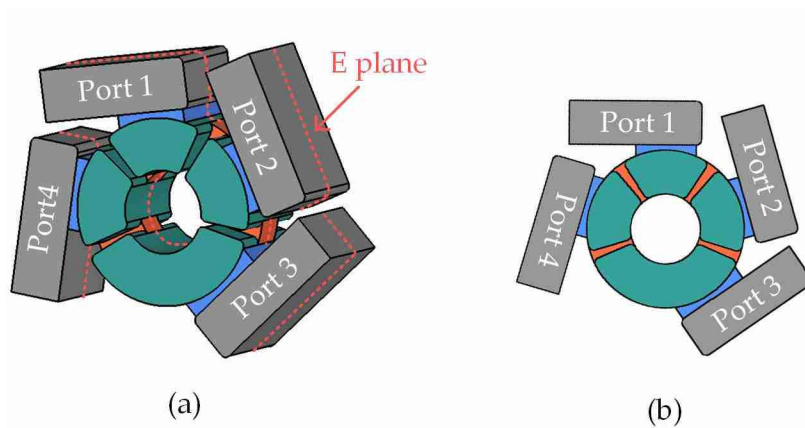


Fig. 6.5. E-plane filtering coupler: (a) The perspective view; (b) The side view.

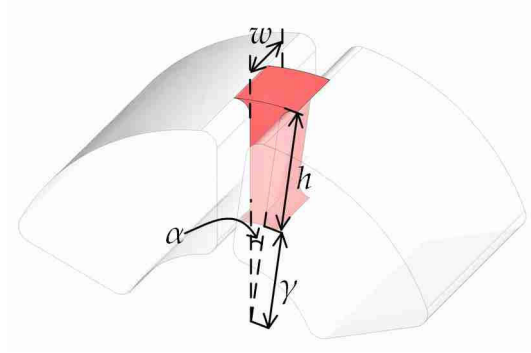


Fig. 6.6. Perspective view of the inter-resonator aperture of an iris in the filtering coupler.

(highlighted in green), and the other four are apertures in irises (orange) between them. The parts in blue are apertures to the ports (grey colour). All the irises are inductive. The detail of the inter-resonator aperture of an iris is shown in Fig. 6.6. There are four parameters related to the coupling level.  $w$  is the width of the aperture,  $h$  is the height,  $\alpha$  is the angle which is  $10^\circ$  initially, and  $\gamma$  is the radius of the fan shape. As the resonators' height is set at 0.826 mm,  $h$  is also 0.826 mm. The irises and resonators form a ring. When the angle of each resonator changes, the angle of the aperture also varies. The only dimension of

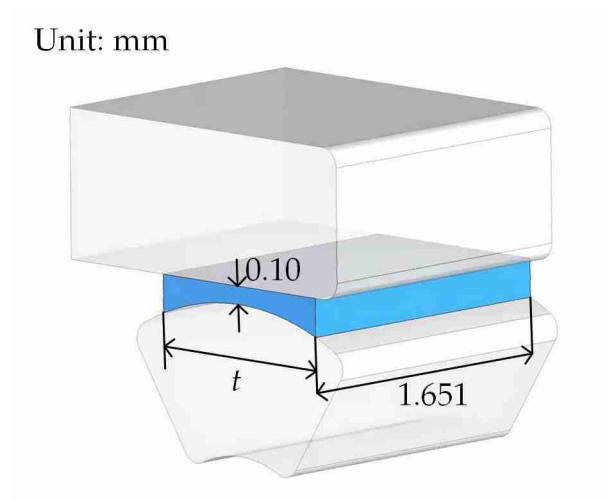


Fig. 6.7. Aperture inter one port and one resonator.

the irises that can be adjusted freely is the width of the aperture. Fig. 6.7 shows the detail of the aperture between resonators and ports. The center height of the aperture is 0.1 mm. the width of the aperture is the same as the resonator, which is 1.651 mm.  $t$  is the only dimension that can be adjusted for a proper coupling level.

In this ring-shaped filtering coupler, angles of fan-shaped resonators replaced the stubs in previous X-band filtering couplers to adjust the resonant frequencies. Before optimization, the angles of the apertures between resonators are all set to be  $10^\circ$ . The default bending angle of the  $TE_{102}$ -mode resonator is  $128^\circ$ , and that of the  $TE_{101}$  mode resonators is  $64^\circ$ . The radius of the coupler is chosen to ensure the resonators work at the proper frequency range. The method mentioned in Chapter 3 was utilized to find the initial width of aperture in each iris. After that, the angle of each resonator and the width of

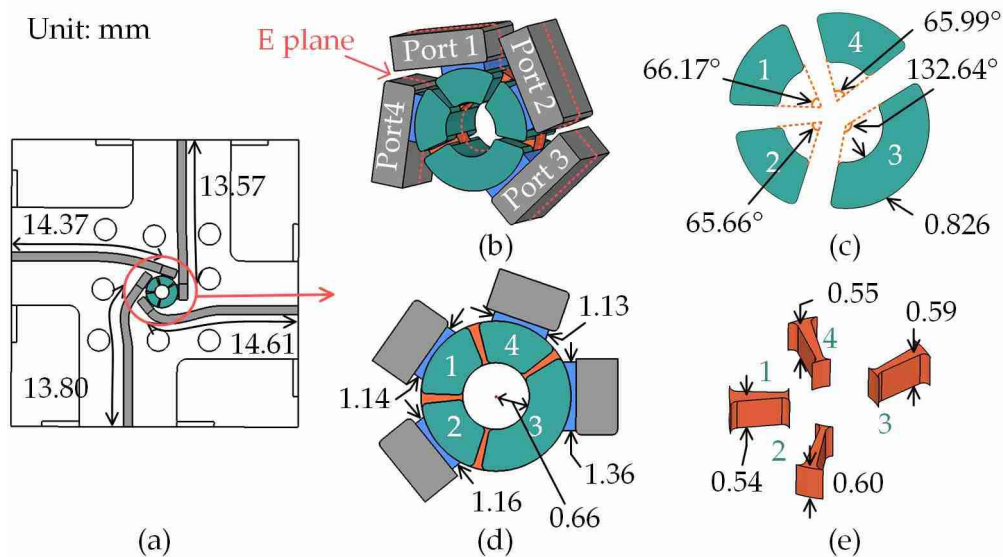


Fig. 6.8. Dimensions of the filtering coupler. (a) Lengths of the extension lines. (b) Width and height of each port and the widths of the irises to ports. (c) Bending angle of each resonator. (d) Width of the port-resonator apertures and (e) Widths of the inter-resonator apertures.

each aperture are left to be optimized. Each aperture shown in Fig. 6.7 locates at the center of the resonator, except the one at the prolonged  $TE_{102}$  resonator. The position of the aperture at this resonator was adjusted for the maximum amplitude balance.

After optimization (manually stopped), the dimensions of the coupler are given in Fig. 6.8. Four extension waveguide sections are added to facilitate the flange connections and measurement, as shown in Fig. 6.8(a). Via holes were surrounding the coupler for tightening screws. The radius of this ring structure is 0.66 mm, as shown in Fig. 6.8(d). The optimal angles of the resonators are given in Fig. 6.8(c). All the angles are larger than the initial ones. The optimized dimensions of the apertures are shown in Fig. 6.8(d) and (e). The widths of the apertures control the couplings. The coupler was split through the E-plane to

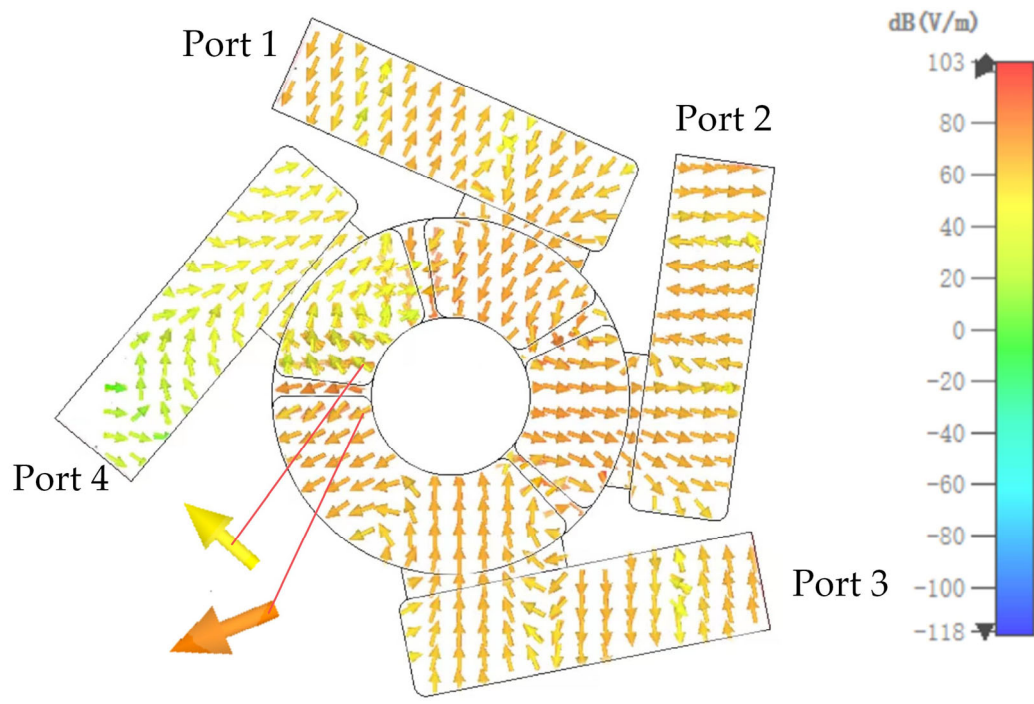


Fig. 6.9. Simulated electric field at 10 GHz of the filtering coupler when input from Port 2. Port 4 is the isolated port.



minimize the leakage due to the imperfect contact between two split blocks.

Fig. 6.9 gives the simulated electric field of the filtering coupler at 10 GHz when input from Port 2. The arrows indicate the direction of the electric field. It can be noticed the inter-resonator apertures change the direction of the electric field, depicted by the two zoomed-in arrows. However, around the port-resonator

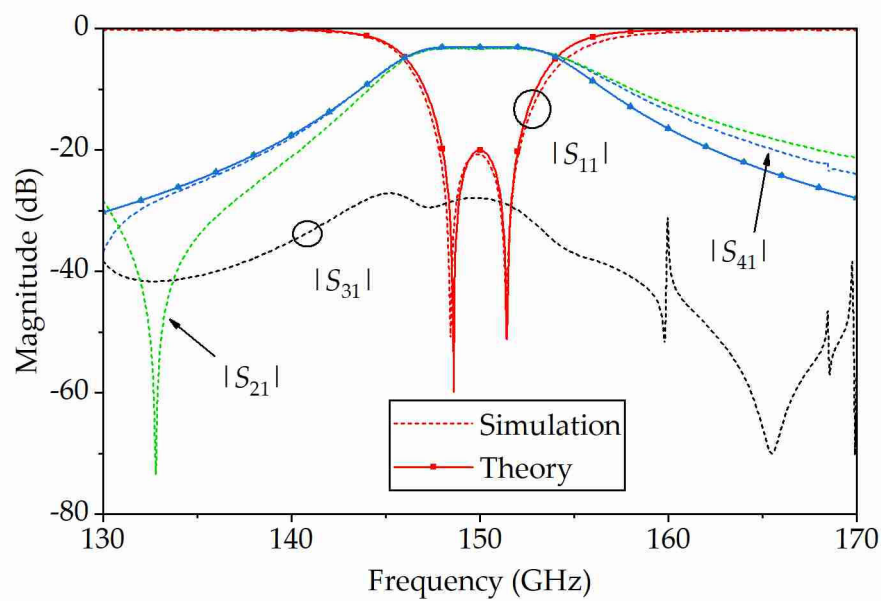


Fig. 6.9. Simulated response in comparison with the theoretical one from the coupling matrix. Note the theoretical  $|S_{31}|$  is  $-\infty$  in dB.

apertures, there is no such a phenomenon. In the  $TE_{102}$  mode resonator, the direction of the electric field has been added with an extra around  $180^\circ$  shift.

The simulated response (gold as the assumed material with a conductivity of  $4.651 \times 10^7$  S/m) at Port 1 is shown in Fig. 6.9, compared with the theoretical response. The simulated insertion-losses of  $S_{21}$  and  $S_{41}$  are 0.31 dB and 0.26 dB at 150 GHz, respectively. Note that there is a transmission zero (TZ) at around 133 GHz. Fig. 6.10 shows the E-field at the TZ when a signal is input from Port 1. As observed, the E-field is reversed in the area 'a'. As a result, the signals



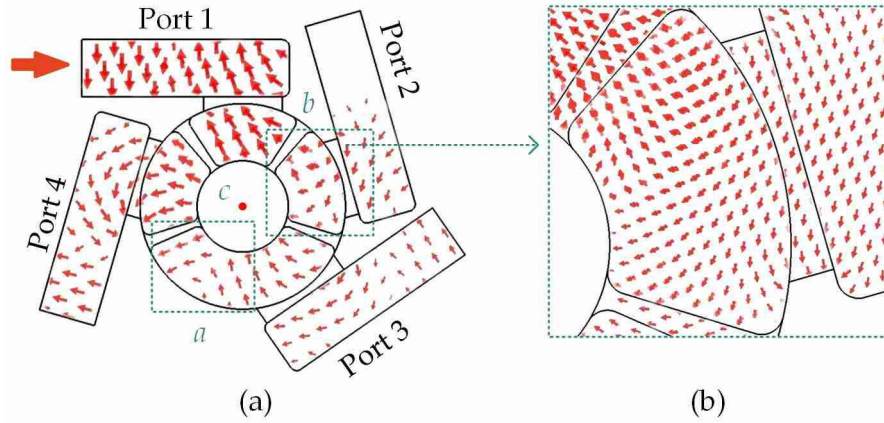


Fig. 6.10. The E-field of the coupler at the TZ of 132.85 GHz when input from Port 1. (a) E field of the whole coupler. (b) E field in the zoomed-in area 'b'.

cancel out in the area 'b' and therefore at Port 2.

There are also three spikes in the simulated  $|S_{31}|$ , around 160 GHz, 168 GHz and 170 GHz. Fig. 6.11 shows the simulated E-field of the coupler at 160 GHz

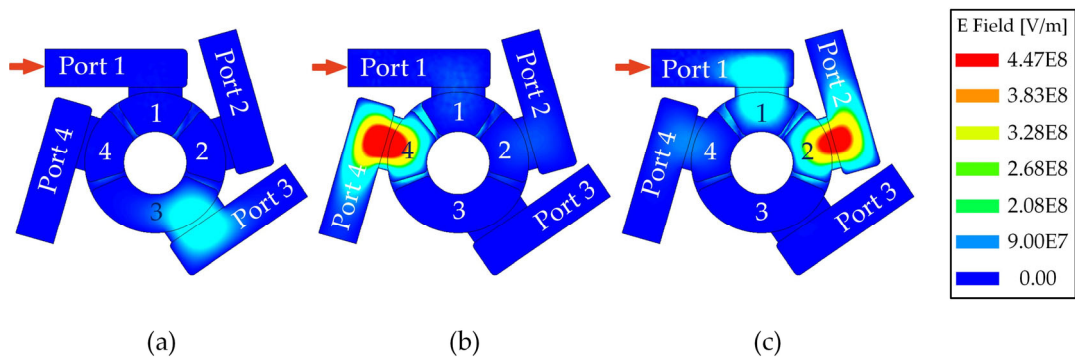


Fig. 6.11. E-field of the coupler when input from Port 1: (a) At 160 GHz; (b) At 168 GHz. (c) At 170 GHz.

in contour form. At 160 GHz, a TM mode resonates between resonator 3 and Port 3. Similar TM-mode resonates between resonator 4 and Port 4 at 168 GHz. At 170 GHz, this happens between resonator 1 and Port 1, resonator 2 and Port 2.

## 6.3 Fabrication and Measurement

The coupler was fabricated using CNC machining. The material is brass and coated with 2- $\mu\text{m}$  gold. Fig. 6.12 shows the fabricated device. Standard UG387 flanges are used. Two low-tolerance press-fit pins help with the location and alignment. The whole block is 27 mm  $\times$  27 mm  $\times$  20 mm in size. The four ports are uniformly positioned on each side. The coupler is designed to work at 150

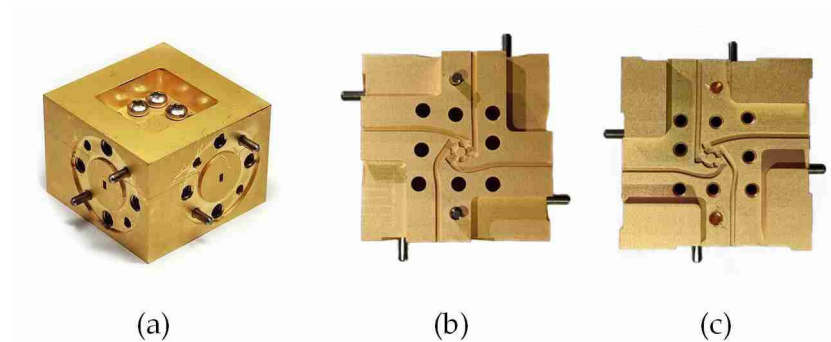


Fig. 6.12. Fabricated filtering coupler. (a) The overall view. (b) The upper part. (c) The lower part.

GHz with 4-GHz bandwidth.

For measurement, the coupler was connected to two vector network analyzer (VNA) extension modules (N5262AW06), as shown in Fig. 6.13. The other two ports were terminated with loads. It has been found that the cables connecting to the LO port significantly influence the phase response. This influence was minimized by using phase-stable cables and keeping them undisturbed. The measured responses are shown in Fig. 6.14. The magnitude responses agree extremely well with the simulation. Within the operation band, the measured return losses of all four ports are higher than 20 dB. The measured insertion-

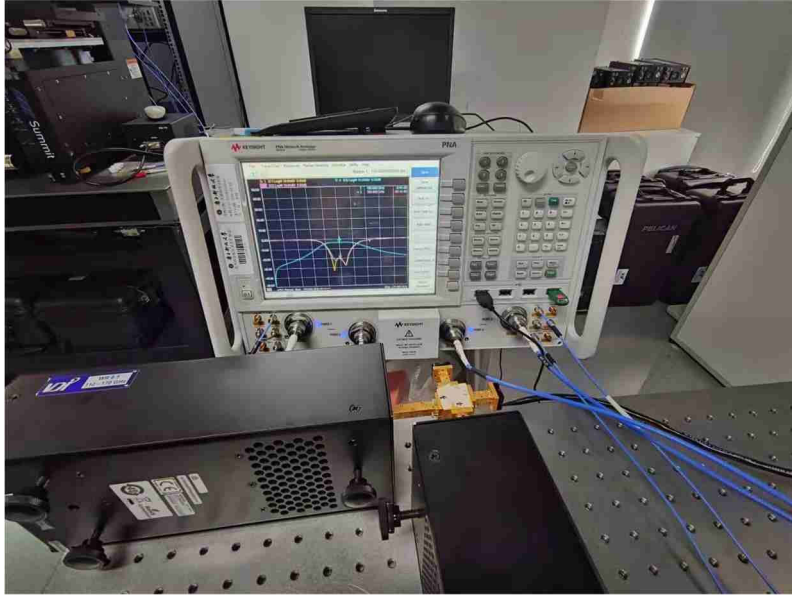


Fig. 6.13. Measurement setup.

losses of  $S_{21}$ ,  $S_{41}$ ,  $S_{32}$  and  $S_{43}$  are 0.46, 0.15, 0.12 and 0.45 dB, respectively. In terms of phase response, the measurement results also follow the simulations very

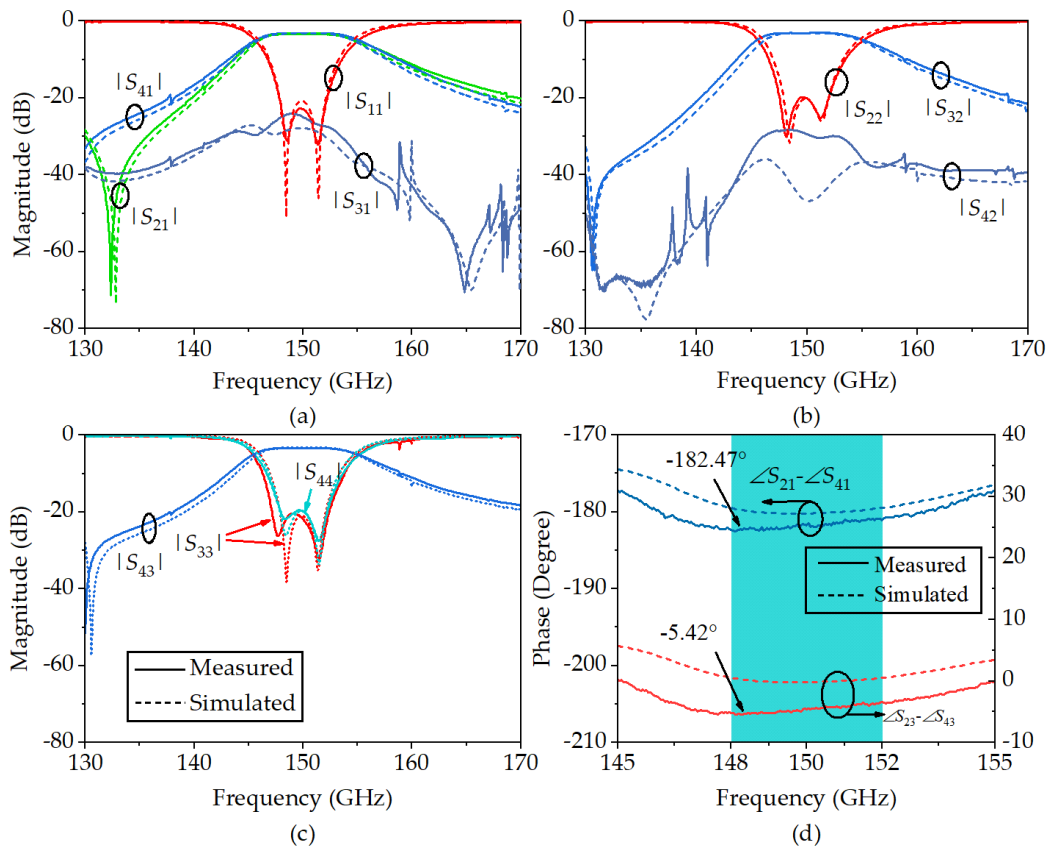


Fig. 6.14. Simulated and measured responses of the filtering coupler. (a)  $|S_{11}|$ ,  $|S_{21}|$ ,  $|S_{31}|$  and  $|S_{41}|$ . (b)  $|S_{22}|$ ,  $|S_{32}|$  and  $|S_{42}|$ . (c)  $|S_{33}|$ ,  $|S_{43}|$ ,  $|S_{44}|$ . (d) Phase imbalance.

TABLE 6.1  
COMPARISON WITH OTHER NON-FILTERING COUPLERS AT AROUND D-BAND

Ref.	RL (dB)	IL (dB)	Iso. (dB)	$\Delta A$ (dB)	$\Delta P$ (Degree)	CF (GHz)
[1]	10-23	1	15-23	0.4	2	170
[2]	16	0.23	16	0.15	2.5	187
[3]	17	0.8	17	0.3	4	195
[4]	16	0.25	16	0.2	4	187.5
This work	20	0.46	20	0.31	5.42	150

RL = return loss, IL = insertion loss, Iso. = Isolation,  $\Delta A$  = amplitude imbalance,  $\Delta P$  = phase imbalance, CF = Center frequency.

well. The maximum measured phase imbalance is  $5.42^\circ$  in  $\angle S_{23} - \angle S_{43}$ . To the authors' best knowledge, there is no filtering coupler working above 100 GHz reported in the literature. The comparison with non-filtering couplers around D-band is shown in Table 6.1. All other couplers are wideband. Apart from the embedded filtering function, this work shows competitive performance overall with excellent matching and isolation. With the narrowband nature considered, the insertion-loss level is also very comparable. The high phase imbalance is believed to be partly due to measurement uncertainty.

## 6.4 Summary

This chapter presents a novel design of an E-plane filtering coupler at 150 GHz. The fan-shaped resonator and annular layout make the coupler not only have the embedded filtering function, but also avoided small stubs and apertures in capacitive irises. The measured response agrees very well with the simulated response with a low insertion loss and excellent matching and isolation. The demonstrated high performance of the D-band device makes this configuration

a capable candidate for filtering SPJ design in D-band.

## Reference

- [1] P. J. Sobis, J. Stake, and A. Emrich, "A 170 GHz 45° Hybrid for Submillimeter Wave Sideband Separating Subharmonic Mixers," *IEEE microwave and wireless components letters*, vol. 18, no. 10, pp. 680-682, 2008.
- [2] H. Rashid, D. Meledin, V. Desmaris, and V. Belitsky, "Novel waveguide 3 dB hybrid with improved amplitude imbalance," *IEEE microwave and wireless components letters*, vol. 24, no. 4, pp. 212-214, 2014.
- [3] H. Rashid, V. Desmaris, V. Belitsky, M. Ruf, T. Bednorz, and A. Henkel, "Design of wideband waveguide hybrid with ultra-low amplitude imbalance," *IEEE transactions on terahertz science and technology*, vol. 6, no. 1, pp. 83-90, 2015.
- [4] Z. Niu *et al.*, "A novel 3-dB waveguide hybrid coupler for terahertz operation," *IEEE Microwave and Wireless Components Letters*, vol. 29, no. 4, pp. 273-275, 2019.
- [5] Z. Niu *et al.*, "Mode analyzing method for fast design of branch waveguide coupler," *IEEE Transactions on Microwave Theory and Techniques*, vol. 67, no. 12, pp. 4733-4740, 2019.
- [6] X. Chen, Y. Wang, and Q. Zhang, "Ring-Shaped D-Band E-Plane Filtering Coupler," *IEEE Microwave and Wireless Components Letters*, vol. 31, no. 8, pp. 953-956, 2021.

## Chapter 7. E-plane D-band Filtering SPJ

The previous chapters introduced one E-plane filtering SPJ, working at X-band. This was designed as a prototype to verify the theories and design. In the filtering SPJ, four of the ports are inside the circuit periphery. Bent flanges were used to link the inner ports to outer devices. However, this configuration becomes unfeasible in the D-band due to the large flange size and difficulties in fabrication. The four inside ports were a result of the  $180^\circ$  filtering couplers. This chapter at first proposes a  $90^\circ$  filtering coupler to replace the  $180^\circ$  filtering coupler to solve the inner-port problem. The challenge and solution are mentioned in the first section. This  $90^\circ$  filtering coupler was then combined with the ring-shaped filtering coupler in the design of the D-band filtering SPJ. The CM technique presented in Chapter 3 was also utilized for the synthesis. In the implementation, physical symmetry was considered for maximum amplitude balance. In addition, termination loads were successfully realized by using low-cost silicon chips for compactness. The simulation reveals a desired response of this SPJ, and reasonable measurement results are obtained. This chapter is organized as follows: At first, the implementation of the  $90^\circ$  filtering coupler will be given. Then, the topology of the SPJ is proposed. This topology is a fusion of the previously proposed coupler techniques. The CM of the topology will be presented for synthesis. This is followed by the air model of the SPJ. In the implementation of the filtering SPJ, silicon chips are used to

match the ports, which will also be detailed. The last section presents the fabrication and measured response. The work of this chapter has been published in [1].

## 7.1 E-Plane D-Band 90° filtering coupler

This section gives the challenge and solution of designing a 90° filtering coupler.

### 7.1.1 Challenge of 90° Filtering Couplers

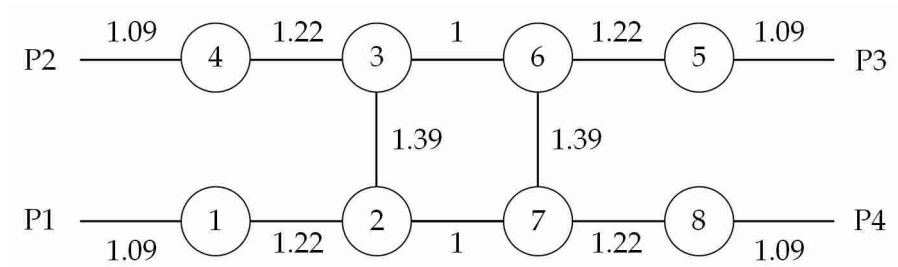


Fig. 7.1 Topology of a 90° filtering coupler.

One paper in the literature realized a 90° filtering coupler using stacked cross coupled-line and loaded cross-stub [2]. This work demonstrated a decent performance and broad out-band rejection. But it is hard to extend this topology to other media and it is a non-resonant structure. Other existing filtering couplers based on resonators can realize 0° or 180° phase shift [3-6]. 180° filtering couplers can be realized by replacing the joints in branch-line couplers with resonators (or replacing transmission lines with couplings). But this is not valid in the 90° filtering coupler design. Fig. 7.1 gives the scenario of

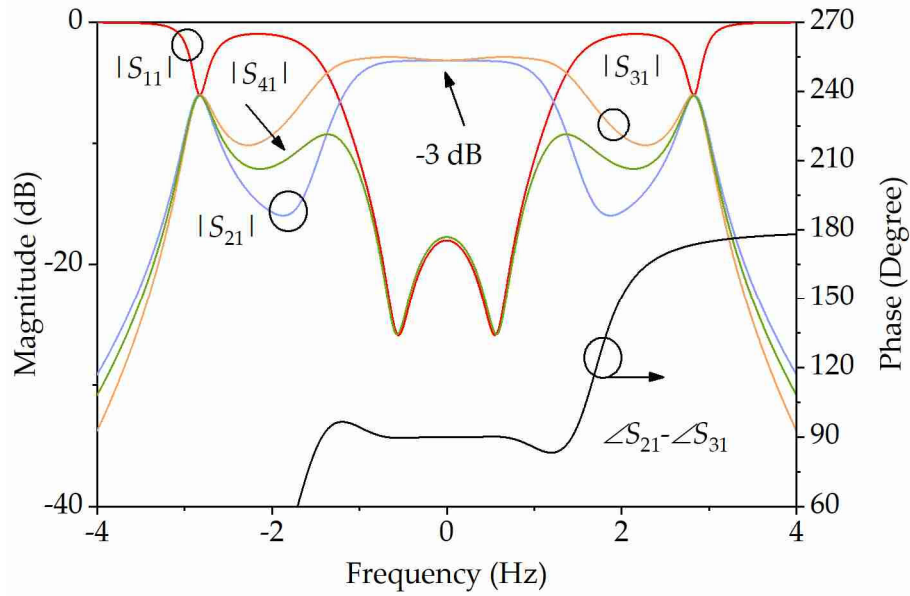


Fig. 7.2. Theoretical magnitude response of the topology in Fig. 7.1.

replacing transmission lines with couplings. There are eight resonators; Port 1 is the input, Port 2 and Port 3 are two outputs, while Port 4 is isolated. The coupling values were optimized to get the 90° coupler response in the passband, also shown in Fig. 7.1. There is a 90° phase shift between P2 and P3 due to the extra coupling in resonators 3 and 6. The number of resonators is different in the two paths of Port 1 to Port 2 and Port 1 to Port 3. This is the fundamental challenge with the 90° coupler. In the path of Port 1 to Port 2, there are resonators 1, 2, 3 and 4, whereas in the path of Port 1 to Port 3, the available resonators are 1, 2, 3, 6 and 5. Different paths cause an different response of  $|S_{21}|$  and  $|S_{31}|$ . The theoretical magnitude and phase responses of the coupler are in Fig. 7.2. It can be noticed that with the given coupling values, the 90° filtering coupler functions properly between -1 to 1 Hz. However, around -3 and 3 Hz, there are two unwanted poles. The poles cannot be moved into the working band nor canceled as this is caused by different paths in terms of



resonator number to the two ports. To solve the problem, the introduction of  $90^\circ$  phase shift must be independent from the resonators. That is to say, resonator 3 and 6 must act as two non-resonant power splitters. Based on this hypothesis, the topology in Fig. 7.1 was modified and will be discussed next.

### 7.1.2 Solution for $90^\circ$ Filtering Coupler

As stated, node 3 and 6 in Fig. 7.1 must be non-resonant. Thus, the resonators following them must be removed to ensure proper filtering functions. Fig. 7.3 shows the new modified topology of the  $90^\circ$  filtering coupler. There are ten resonators in total. The topology is symmetric to line AA'. When input from Port 1, Port 3 and Port 4 are two outputs while Port 2 is isolated. When input from Port 3, Port 1 and Port 2 are two outputs, and Port 4 is the isolation port. Resonator 9 and 10 act as two power splitters in the topology (Resonator 3 and 4 in the original topology), achieved by large values (larger than 5) of  $m_4$ ,  $m_5$  and  $m_{p2}$ . The optimized coupling values for this topology are given in (7.1).

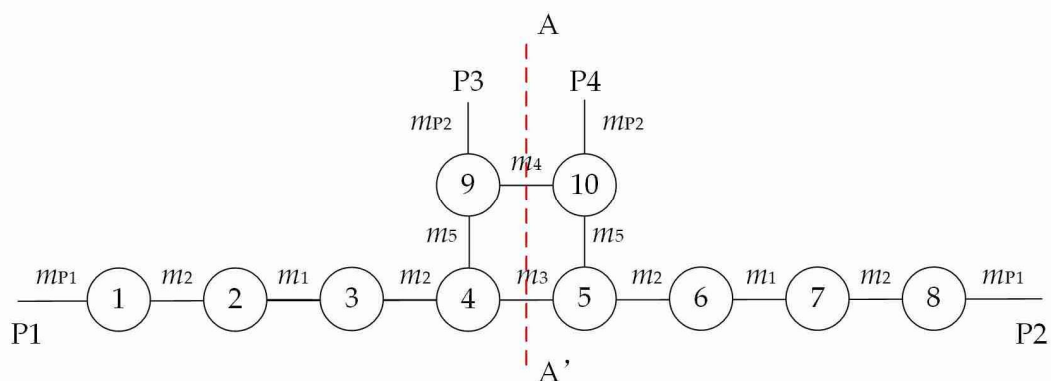


Fig. 7.3. Topology of the proposed  $90^\circ$  filtering coupler.

$$\begin{cases} m_1 = 0.699 \\ m_2 = 0.912 \\ m_3 = 1.080 \\ m_4 = 33.32 \\ m_5 = 8.48 \end{cases} \quad \begin{cases} m_{P1} = 1.038 \\ m_{P2} = 5.755 \end{cases} \quad (7.1)$$

According to (7.1), the theoretical magnitude response of the filtering coupler is given in Fig. 7.4.  $|S_{11}|$  and  $|S_{43}|$  overlap, giving a fourth-order Chebyshev response. Over the passband,  $|S_{33}|$  and  $|S_{21}|$  are both lower than  $-20$  dB. Due to symmetry, input from Port 1/2 or Port 3/4 is split into halves at Port 3 and 4

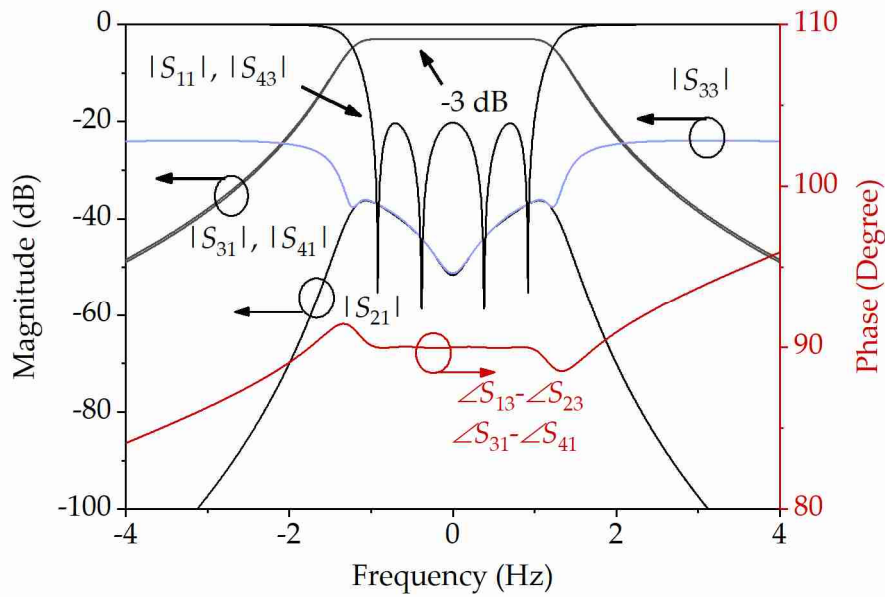


Fig. 7.4. Magnitude and phase response of the proposed filtering coupler from the coupling values given in (7.1).

or Port 1 and 2, respectively. Fig. 7.4 also gives the phase response of the filtering coupler. The phase difference is  $90^\circ$  between the two outputs in the working band.

### 7.1.3 Realization of the $90^\circ$ Filtering Coupler

The aimed working bandwidth is 4 GHz, and the center frequency is 150 GHz.

Thus, the fractional bandwidth is 0.0267. To implement the filtering coupler, converting the couplings and external  $q$  from normalized ones in (7.1) to the real frequency domain, these are:

$$\begin{cases} M_1 = 0.0186 \\ M_2 = 0.0243 \\ M_3 = 0.0287 \\ M_4 = 0.886 \\ M_5 = 0.226 \end{cases} \quad \begin{cases} Q_{ex1} = 34.89 \\ Q_{ex2} = 1.135 \end{cases} \quad (7.2)$$

These couplings are for ideal response, but some of the values are difficult (too large) to achieve in practice. For example, the ideal  $Q_{ex2}$  is 1.135. The method to define the external  $Q$  was introduced around (3.38). Using the provided formula to obtain the ideal  $Q$ , the 3-dB bandwidth of the structure in Fig. 3.28 needs to be near 150 GHz whereas the center frequency is 150 GHz, which is infeasible. To ensure the proper function and feasibility, a compromise on couplings was made and given in (7.3)

$$\begin{cases} M_1^r = 0.0190 \\ M_2^r = 0.0263 \\ M_3^r = 0.0270 \\ M_4^r = 0.0961 \\ M_5^r = 0.0670 \end{cases} \quad \begin{cases} Q_{ex1}^r = 29.49 \\ Q_{ex2}^r = 10.29 \end{cases} \quad (7.3)$$

Based on these couplings, the filtering coupler was realized by rectangular cavity resonators, as shown in Fig. 7.5. To achieve the E-plane structure, resonator 9 and 10 were placed upon resonator 4 and 5. The whole coupler is symmetrical to plane a and b, depicted in red dash lines. Fig. 7.5(b) and Fig. 7.5(c) give the dimensions. The internal corners were rounded by 0.1 mm in radius to meet the requirements of CNC machining. Note that the irises

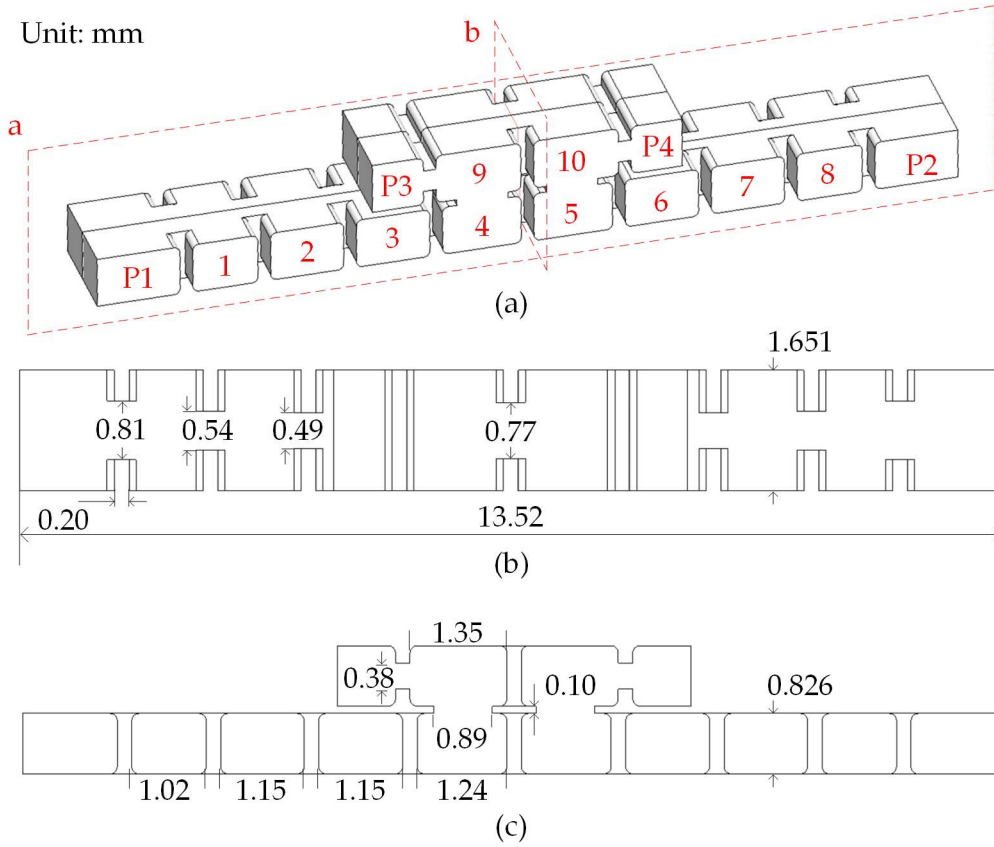


Fig. 7.5. Air model of the E-plane D-band filtering coupler. (a) The overall view. (b) The top view. (c) The front view. The index of resonators and ports are depicted in red.

between resonator 9 and port 3, resonator 10 and port 4 are capacitive to obtain large external coupling  $m_{p2}$ . The large apertures in capacitive irises here do not exceed the fabrication tolerance due to the large coupling values.

The simulated response can be found in Fig. 7.6. In the working band (148 – 152 GHz),  $|S_{11}|$  and  $|S_{43}|$  are lower than -20 dB,  $|S_{33}|$  and  $|S_{21}|$  are lower than -17 dB. The maximum magnitude imbalance in the working band is 0.34 dB, and the maximum phase error is  $2^\circ$ . Within the passband, the simulated performance agrees with the theoretical one from the coupling matrix very well. The simulated  $90^\circ$  filtering coupler model was later used in the filtering SPJ.

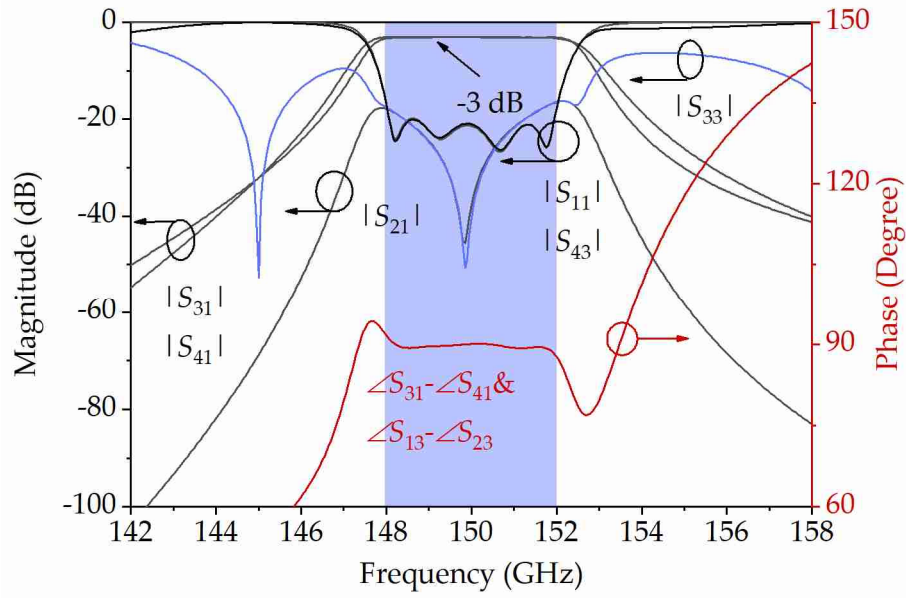


Fig. 7.6. Simulated magnitude response and phase response of the E-plane D-band filtering coupler.

## 7.2 Topology of the Filtering SPJ

Fig. 7.7 gives the topology for E-plane D-band filtering SPJ. There are twenty

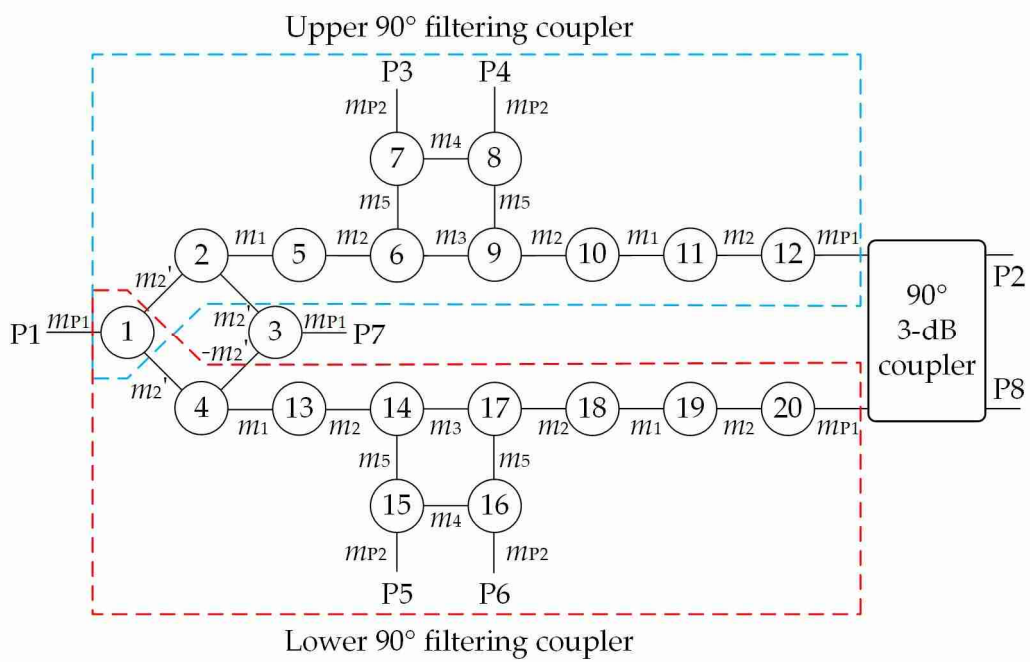


Fig. 7.7. Topology of the proposed filtering SPJ. The resonators with different functions have been depicted by dashed polygons.

resonators in total, with one  $90^\circ$  branch-line coupler. The resonators serve different functions as depicted by dash lines. The blue and red dash polygons mark the upper and lower filtering couplers with a  $90^\circ$  phase shift. This coupler topology was detailed in the preceding section. Resonator 1 to 4 inherit the configuration from Chapter 6, used to merge the two  $90^\circ$  filtering couplers. To achieve the merger, the initial couplings must be converted to:

$$m_2' = m_2 / \sqrt{2} \quad (7.4)$$

In this topology, Port 1 is one input port while Port 2 is the other. Port 3, 4, 5 and 6 are the four outputs. Port 7 and Port 8 are supposed to be terminated by matched loads. Port 7 is still inside the circuit. But this port can be terminated by an absorber made of a silicon chip. When input is from Port 1, the signal is split into two halves to the upper and lower filtering coupler, with no phase shift. Then at Port 3 and Port 4, Port 5 and Port 6, the outputs have a  $90^\circ$  phase shift. When input is from Port 2, the signal is split into two halves but with a  $90^\circ$  phase shift. The theoretical phase shifts at the four outputs are therefore:

$$\begin{cases} \angle S_{31} - \angle S_{32} = 0^\circ \\ \angle S_{41} - \angle S_{42} = 180^\circ \\ \angle S_{51} - \angle S_{52} = 270^\circ \\ \angle S_{61} - \angle S_{62} = 90^\circ \end{cases} \quad (7.5)$$

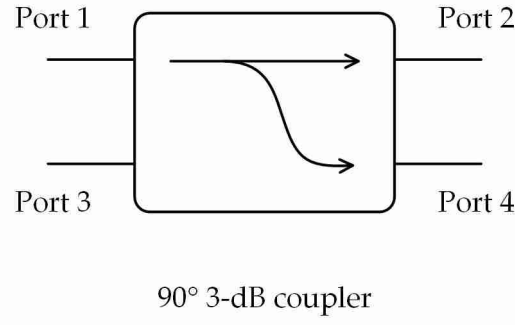


Fig. 7.8. 90° 3-dB coupler.

A method of combining non-resonant components into CM representation was presented in Chapter 3 when the Y-matrices were provided. (7.6) is the Y-matrix of the 90° 3-dB coupler, shown in Fig. 7.8.

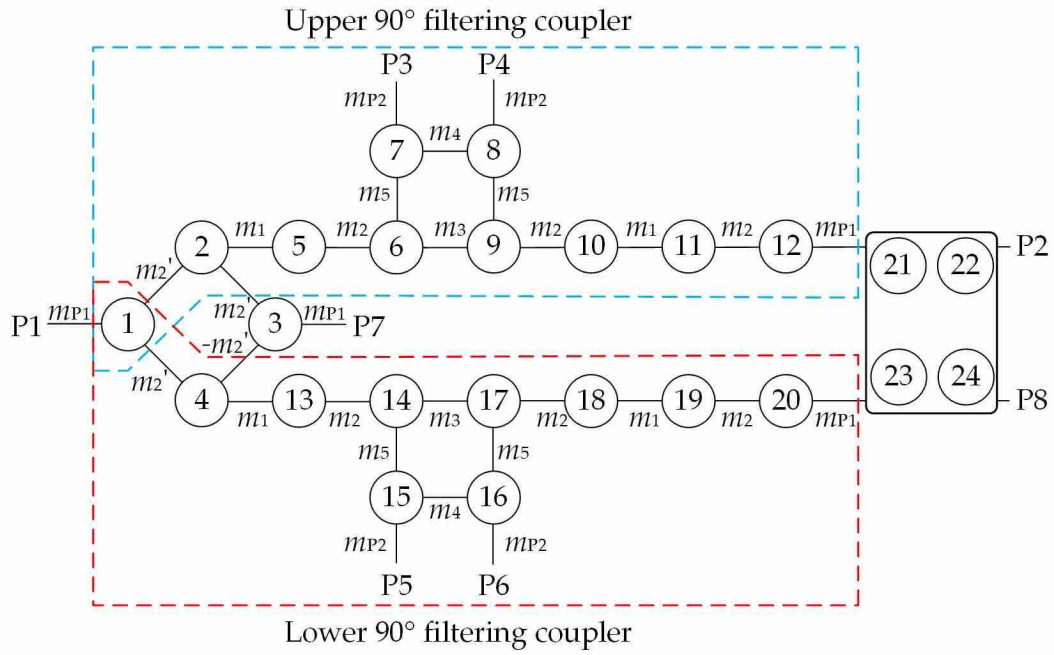


Fig. 7.9. Topology of the proposed filtering SPJ with the 90° 3-dB coupler represented by nodes 21, 22, 23 and 24.

$$[Y_{90}] = j \sec 2\theta \begin{bmatrix} -\sin 2\theta & \sqrt{2} \cos \theta & 1 & -\sqrt{2} \sin \theta \\ \sqrt{2} \cos \theta & -\sin 2\theta & -\sqrt{2} \sin \theta & 1 \\ 1 & -\sqrt{2} \sin \theta & -\sin 2\theta & \sqrt{2} \cos \theta \\ -\sqrt{2} \sin \theta & 1 & \sqrt{2} \cos \theta & -\sin 2\theta \end{bmatrix} \quad (7.6)$$

As mentioned, an  $N$ -port device can be represented by  $N$  nodes with  $N$  ports. Given the  $Y$  matrix, Fig. 7.7 was converted into a node representation in Fig. 7.9, and the corresponding CM is given in Fig. 7.10. The coupling values are given in (7.7).

$$\left\{ \begin{array}{l} m_{p1,1} = m_{p7,3} = m_{12,21} = m_{20,23} = 1.038 \\ m_{p2,22} = m_{p8,24} = 1 \\ m_{p3,7} = m_{p4,8} = m_{p5,15} = m_{p6,16} = 5.755 \\ m_{1,2} = m_{2,3} = -m_{3,4} = m_{1,4} = 0.645 \\ m_{2,5} = m_{4,13} = m_{10,11} = m_{18,19} = 0.699 \\ m_{5,6} = m_{9,10} = m_{11,12} = m_{13,14} = m_{17,18} = m_{19,20} = 0.912 \\ m_{6,9} = m_{14,17} = 1.080 \\ m_{6,7} = m_{8,9} = m_{14,15} = m_{16,17} = 8.48 \\ m_{7,8} = m_{15,16} = 33.32 \\ m_{21,22} = m_{23,24} = j \sec 2\theta \times \sqrt{2} \cos \theta \\ m_{21,23} = m_{22,24} = j \sec 2\theta \\ m_{21,24} = m_{22,23} = -j \sec 2\theta \times \sqrt{2} \sin \theta \end{array} \right. \quad (7.7)$$

The non-zero entries in Fig. 7.10 are shown in grey. The theoretical magnitude responses are deduced from the coupling matrix as shown in Fig. 7.11(a) and (b). Inheriting from the response of the filtering  $90^\circ$  coupler,  $|S_{11}|$  and  $|S_{82}|$  have a fourth-order Chebyshev response. The isolation between the two input ports (Port 1 and Port 2) is higher than 39 dB theoretically.

### 7.3 Simulation of the Filtering SPJ

The filtering SPJ was built in CST as an air model, shown in Fig. 7.12, then fabricated using CNC machining. There are twenty resonators, all labeled with red numbers. The couplings to P3, P4, P5 and P6 are capacitive (to realize large



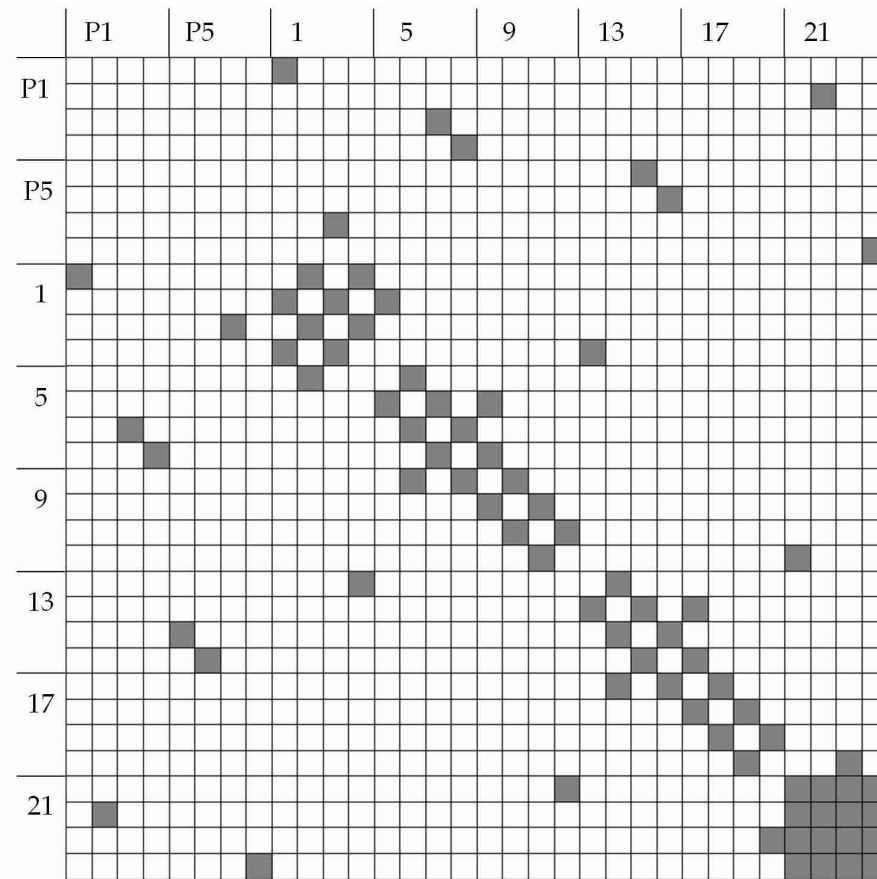


Fig. 7.10. Coupling matrix of the proposed filtering SPJ and the coupling values. Entries painted in grey are non-zero values.

couplings) while others are inductive. Resonator 1 to 4 are bent into a ring to realize the E-plane configuration with no capacitive iris. This technique was provided in the previous section. Resonator 11, 12, 19 and 20 are also bent. Bent resonators make the upper and lower coupler more symmetrical and improve the output amplitude balance. Part B is the E-plane branch-line coupler. P7 and P8 are to be loaded for better isolation and return loss. Fig. 7.13 provides the detail of the dimensions. The extension waveguide at each port was omitted for clarity.

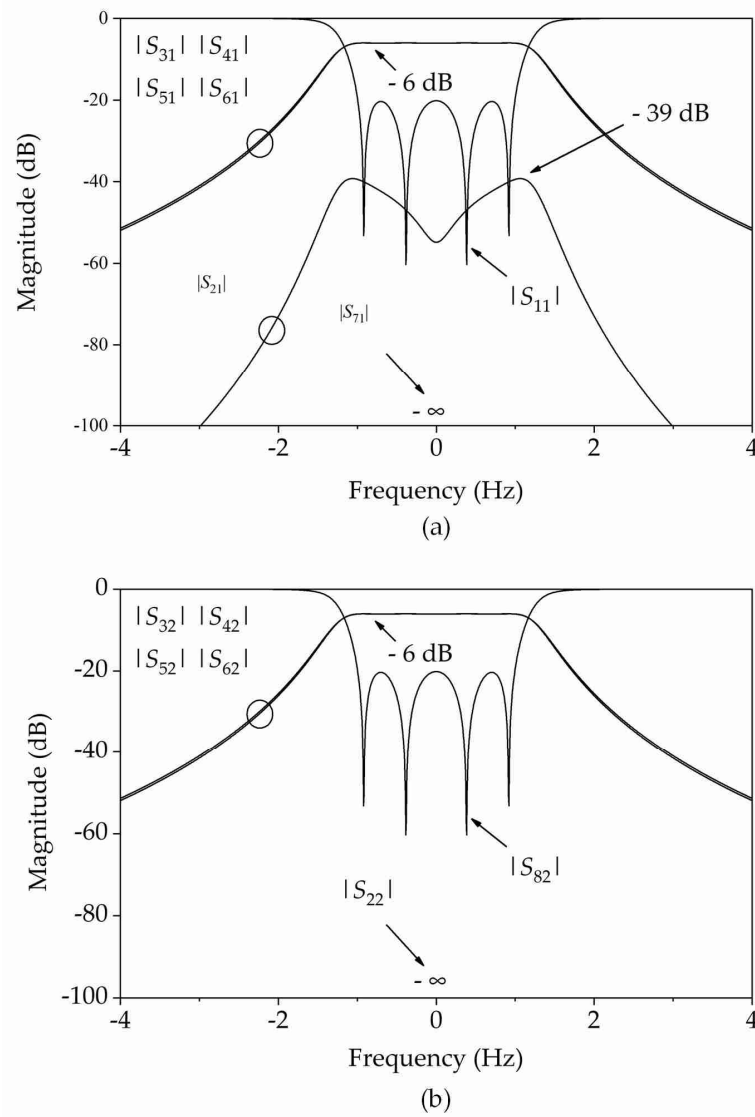


Fig. 7.11. Theoretical magnitude response of the filtering SPJ: (a) The response from Port 1; (b) The response from Port 2.

P7 in the SPJ is inside the circuit periphery, so connecting to a separate waveguide load is difficult in the D-band. We have designed and implemented a compact and straightforward load structure based on low-cost low-resistivity silicon chips. [7] and [8] used silicon as the absorber but with a complex-shaped chip. Fig. 7.14 shows the air model of our silicon chip absorber. It is simply formed of a slanted rectangular silicon substrate attached to the end of the waveguide. Two parameters determine its ability of absorption. One is the

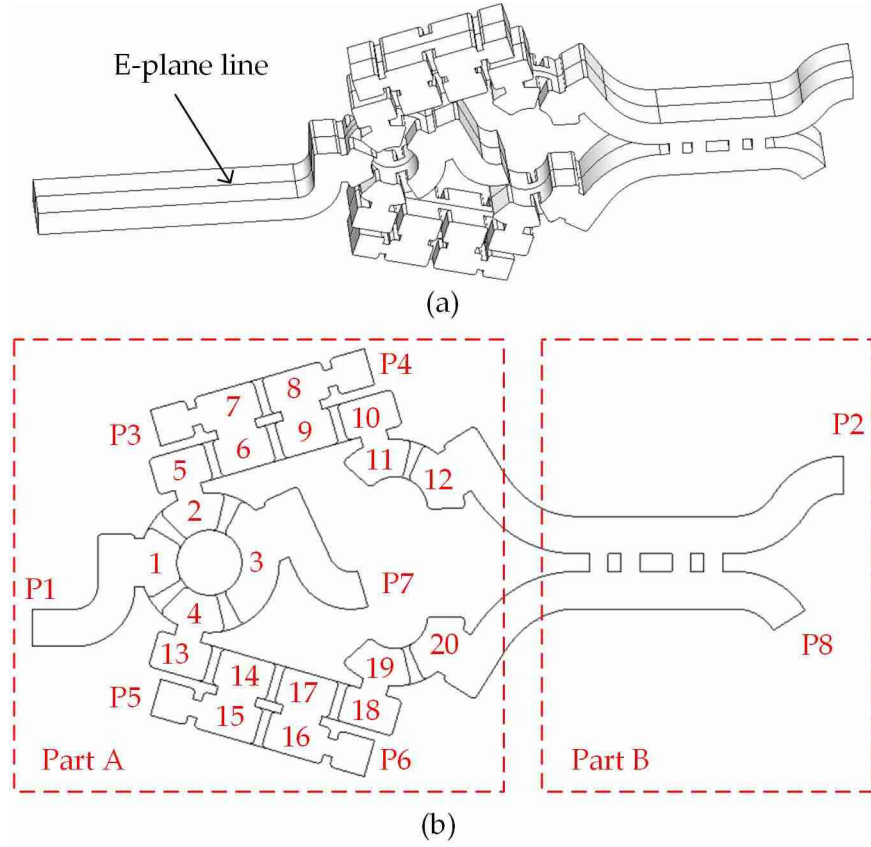


Fig. 7.12. Air model and the plan view of the proposed D-band E-plane filtering SPJ. (a) Overall view of the SPJ. The E-plane line is depicted as shown. (b) Front view. The resonators are numbered in red. Note Port 1 is shortened in (b) to make space for detail.

angle between the waveguide and the silicon chip, which is optimized to be  $19.75^\circ$  in this case. The other is the conductivity of the silicon chip, which is usually provided with a range of values. The estimated conductivity by measurement is around 12 S/m. When the incident wave hits the silicon chip, it will be reflected back to the upper metal wall. Then, the upper metal wall also reflects the wave back to the silicon chip. The wave is absorbed by the silicon chip through multiple reflections. The simulated and measured responses of the absorber are also provided in Fig. 7.14. Simulated  $|S_{11}|$  is lower than  $-30$  dB while measured one is lower than  $-20$  dB in the shown frequency band.

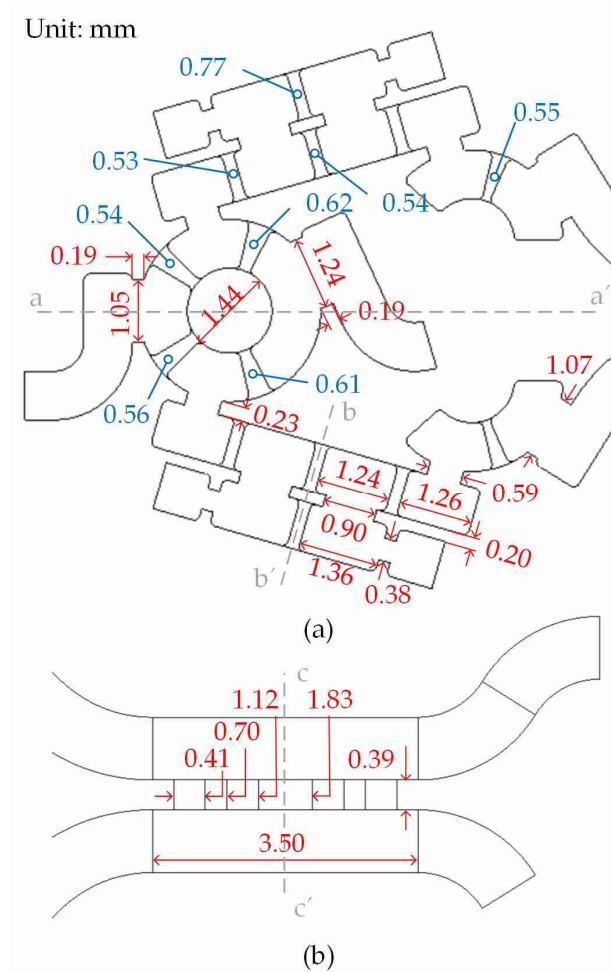


Fig. 7.13. Main dimensions of the SPJ. The dimensions along the E-plane are depicted in red while the ones along the H-planes are in blue. (a) Part A. Line aa' and line bb' are two symmetrical lines. (b) Part B. Line cc' is a symmetrical line.

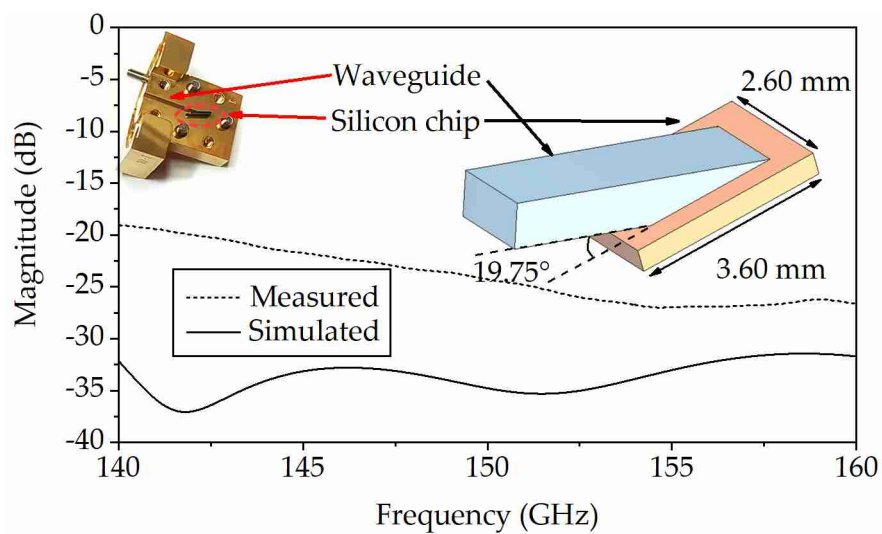


Fig. 7.14. Load made of a silicon chip and its response.

The simulated magnitude responses of the filtering SPJ with silicon absorbers

are given in Fig. 7.15. It can be noticed that the return losses of the two inputs are higher than 20 dB in the working band.  $|S_{21}|$ , the isolation between the two inputs, is larger than 19 dB. Fig. 7.16 gives the simulated phase response of the filtering SPJ after adding the extension lines. The phase values agree with (7.2) in the working band, with a maximum in-band error of  $3.2^\circ$

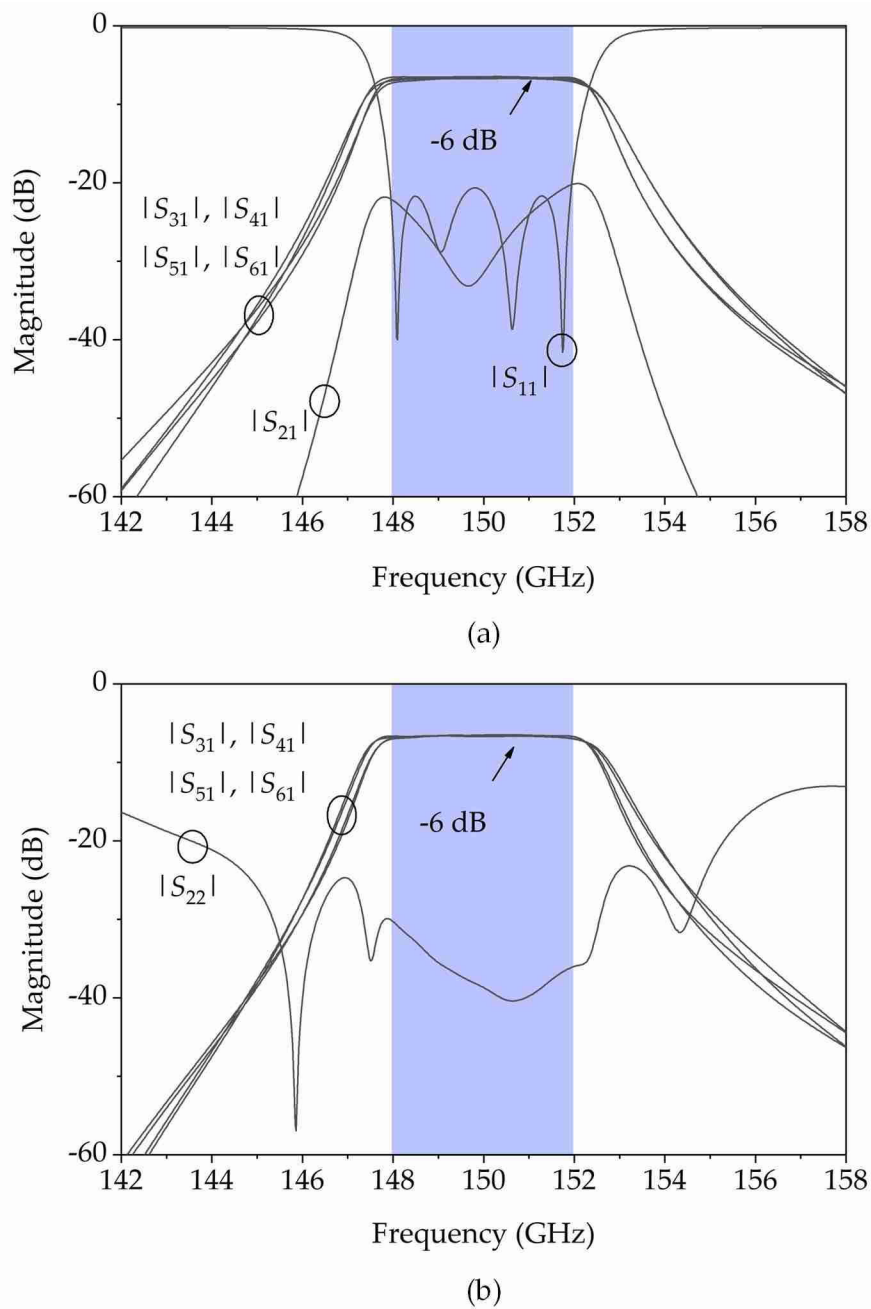


Fig. 7.15. Simulated magnitude response of the SPJ with two absorbers: (a) When input at Port 1; (b) When input at Port 2.

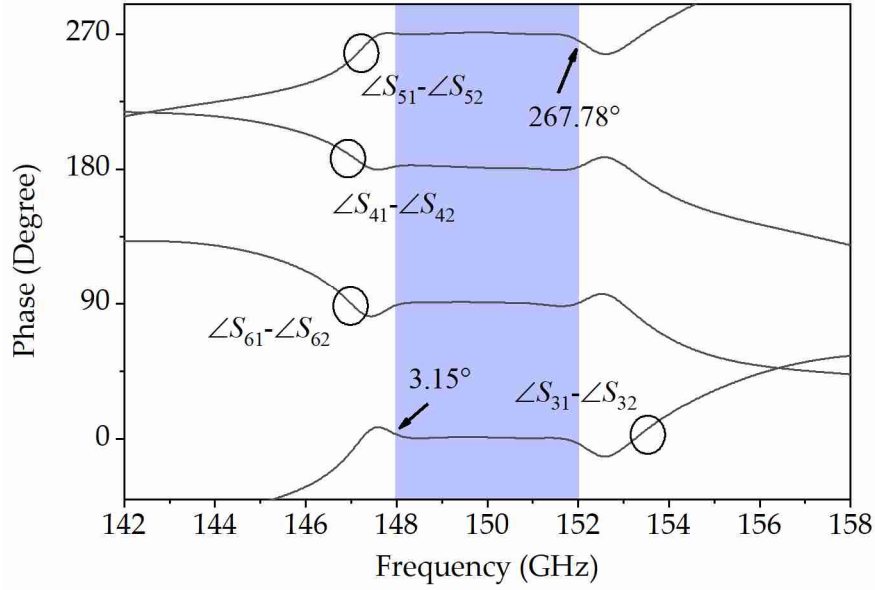


Fig. 7.16. Simulated phase response of the filtering SPJ with two absorbers.

## 7.4 SPJ Fabrication and Measurement

The SPJ with slots for silicon chips (absorbers) was fabricated using CNC machining. The CAD model is given in Fig. 7.17. The device was separated into two pieces along E-plane. Fig. 7.17(a) and (b) are the two parts of the SPJ shell models. The cross-section view is given in Fig. 7.17(c). There are two slots in Fig. 7.17(c) as marked out, reserved for silicon chips. The dimensions of the slots are given on the right side of Fig. 7.17(c). The length is 4.00 mm, and the width is 0.42 mm. The depth of the two slots is 1.30 mm.

The CNC-machined prototype can be found in Fig. 7.18(a). Two silicon chips were loaded in the slots, zoomed-in in Fig. 7.18(b). The material is brass coated with gold. To measure the SPJ, four external matching loads were connected to the model, as shown in Fig. 7.19. Two of them are from the calibration kit and the others are in-house made using silicon chips (Fig. 7.14). The measurement

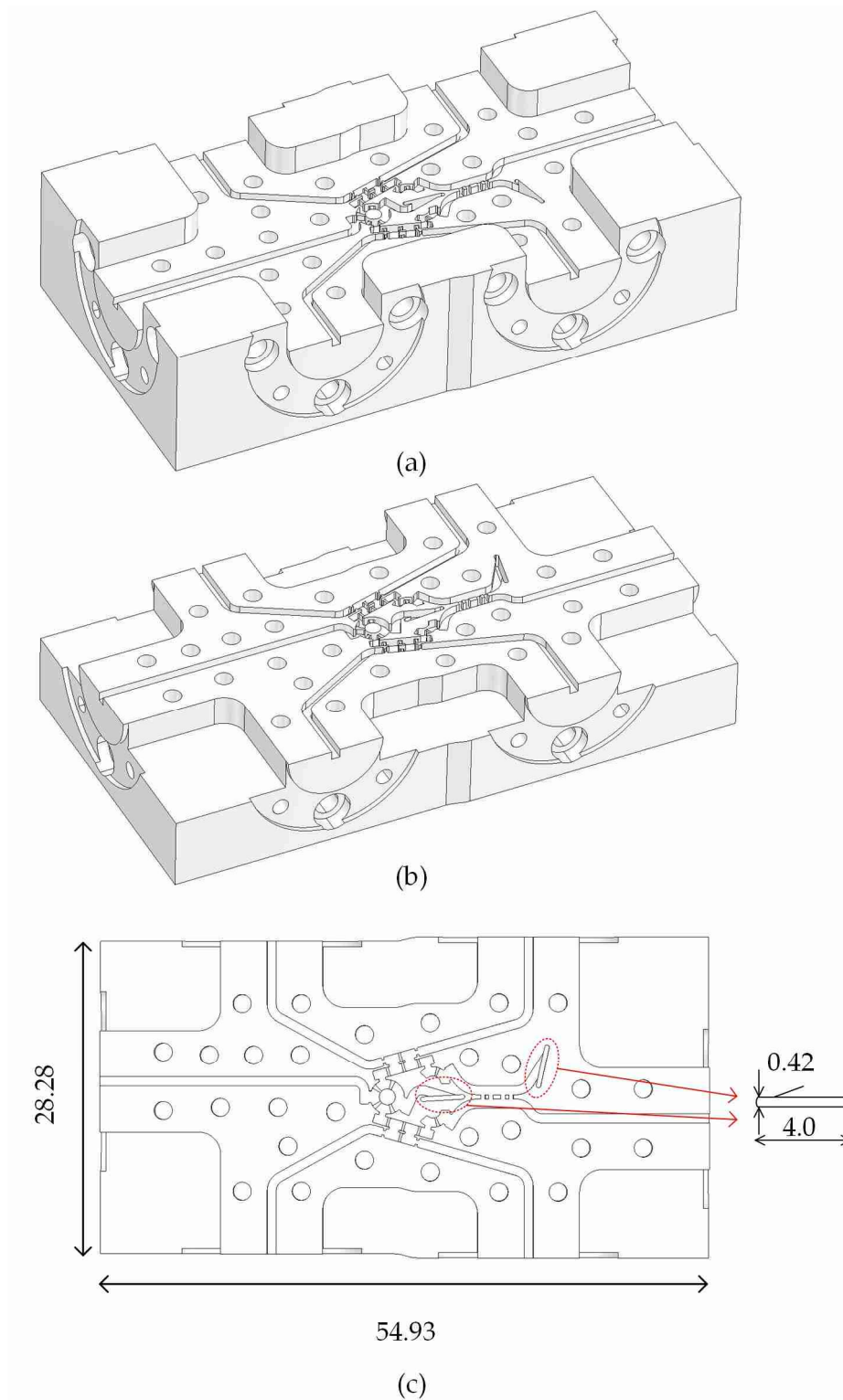


Fig. 7.17. CAD model of the filtering SPJ. (a) and (b) the two parts cut at E-plane. (c) The inside view of the model.

setup can be found in Fig. 7.20. A four-port VNA (N5227A) is connected to two frequency extension modules (N5262AW06). The cables connecting to the LO

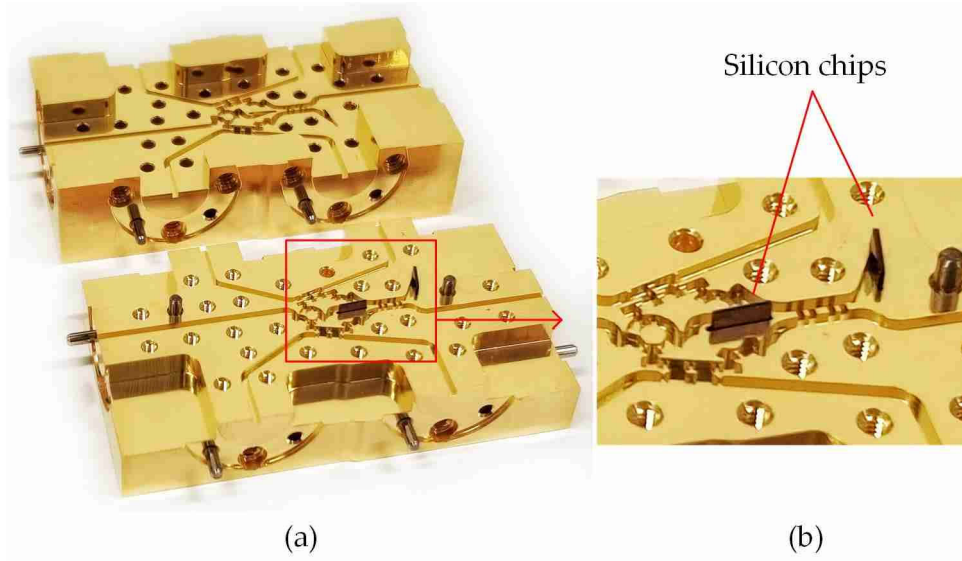


Fig. 7.18. Fabricated prototype of the filtering SPJ. (a) The overall view. (b) The zoomed-in viewgraph of the two silicon absorbers.

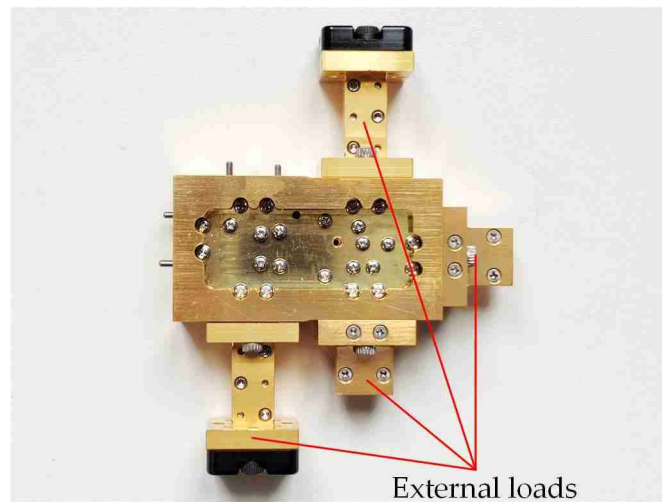


Fig. 7.19. Assembled SPJ with four external loads

port significantly influence the phase response. This influence was minimized by using phase-stable cables and keeping them undisturbed. The measured magnitude and phase responses compared with simulated ones can be found in Fig. 7.21 and Fig. 7.22. The measured  $|S_{11}|$  is lower than -11 dB in the working band. The measured in-band isolation between Port 1 and Port 2 is higher than 17.9 dB. Fig. 7.21(b) shows the measured magnitude response at Port 2.  $|S_{22}|$  is



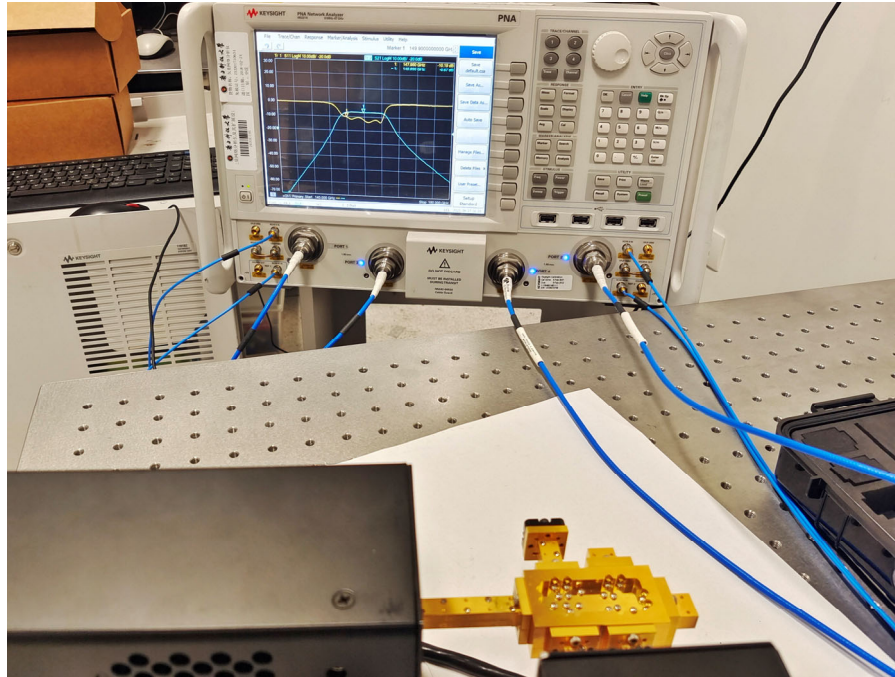
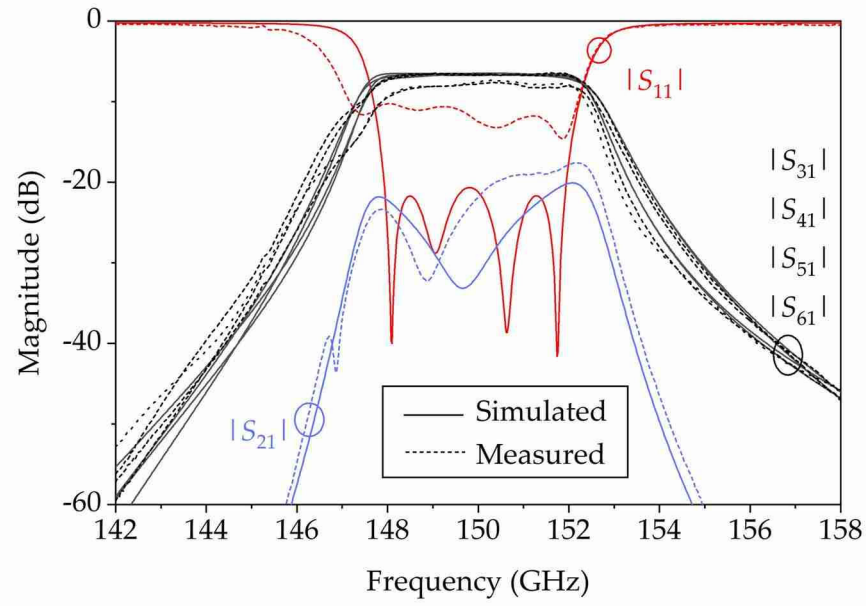
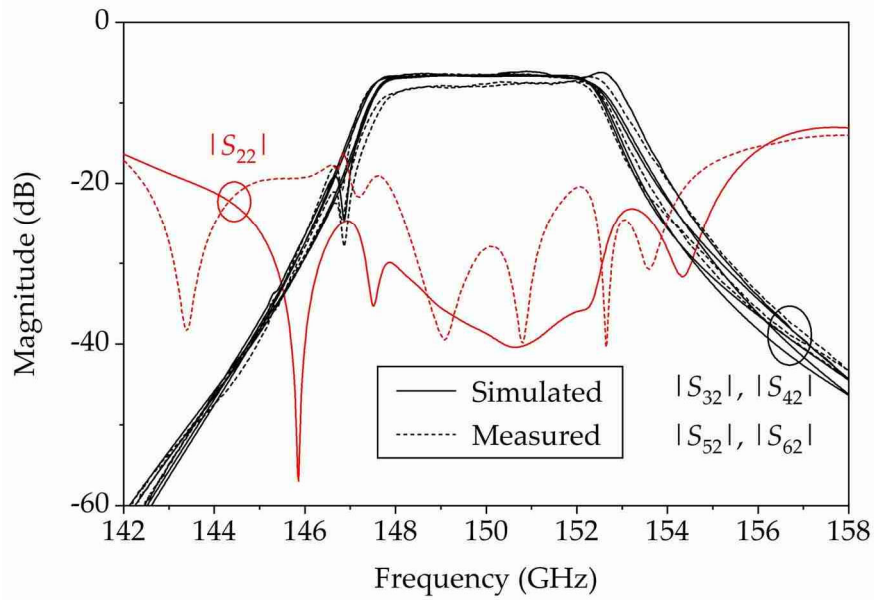


Fig. 7.20. Measurement setup of the SPJ.

below -20 dB in the working band. The maximum measured From measurement, for Port 1 related  $S$ -parameters,  $|S_{31}|$  and  $|S_{51}|$  are with large insertion loss (maximum is 2 dB) while  $|S_{41}|$  and  $|S_{61}|$  are with less insertion loss (0.5 dB maximal). For Port 2 related  $S$ -parameters,  $|S_{42}|$  and  $|S_{62}|$  are with large insertion loss (maximum is 2 dB) while  $|S_{32}|$  and  $|S_{52}|$  are with less insertion loss (0.5 dB maximal). The simulated insertion loss of the four paths is lower than 0.75 dB. This comparison reveals the fabrication error is not distributed throughout the whole circuit but some areas. This is the main reason of the deteriorate  $|S_{11}|$ . This insertion losses are higher than desired but not unexpected for waveguide devices at such a high frequency. The phase response is in Fig. 7.22. The maximum in-band phase error in measurement is



(a)



(b)

Fig. 7.21. Measured magnitude responses of the SPJ compared with simulated ones. (a) The response when input at Port 1. (b) When input at Port 2.

15°. As each output of SPJ can be calibrated separately, the phase error is also acceptable.

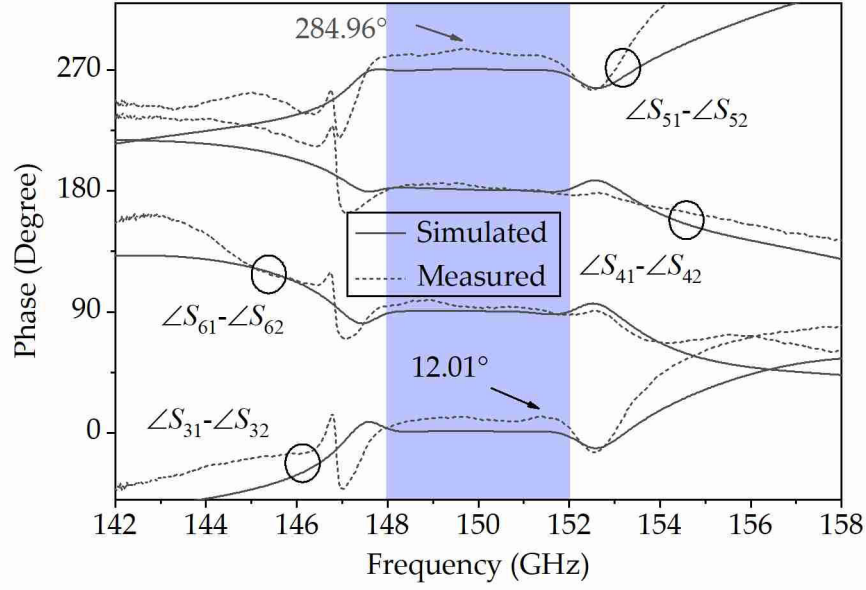


Fig. 7.22. Measured phase response of the filtering SPJ.

## 7.5 Summary

The fan-shaped resonators and the 90° filtering couplers were utilized to design the D-band filtering SPJ. The topology of the filtering SPJ has twenty resonators and one 90° branch-line coupler. Two silicon chips were involved in the SPJ design. The chips with a particular angle and conductivity act as two loads for matched termination. The SPJ was fabricated and also measured. In the working band of 148 to 152 GHz, the measured response gives the minimum 11-dB in-band return-loss and maximum 2-dB insertion-loss. The maximum phase error is 15°.

## Reference

- [1] X. Chen, M. Salek, Q. Zhang, and Y. Wang, "Subterahertz Filtering Six-Port Junction."
- [2] W. Yu, Y. Rao, H. J. Qian, and X. Luo, "Reflectionless filtering 90° coupler using stacked cross coupled-line and loaded cross-stub," *IEEE Microwave and Wireless*

*Components Letters*, vol. 30, no. 5, pp. 481-484, 2020.

- [3] T.-W. Lin, J.-Y. Wu, and J.-T. Kuo, "Filtering rat-race coupler with transmission zeros using compact miniaturized hairpin resonators," in *2015 IEEE International Wireless Symposium (IWS 2015)*, 2015, pp. 1-4: IEEE.
- [4] K. X. Wang, X.-F. Liu, Y. C. Li, L. Z. Lin, and X.-L. Zhao, "LTCC filtering rat-race coupler based on eight-line spatially-symmetrical coupled structure," *IEEE Access*, vol. 6, pp. 262-269, 2017.
- [5] H.-Y. Li, J.-X. Xu, and X. Y. Zhang, "Substrate integrated waveguide filtering rat-race coupler based on orthogonal degenerate modes," *IEEE Transactions on Microwave Theory and Techniques*, vol. 67, no. 1, pp. 140-150, 2018.
- [6] J.-X. Xu, X. Y. Zhang, and H.-Y. Li, "Compact narrowband filtering rat-race coupler using quad-mode dielectric resonator," *IEEE Transactions on Microwave Theory and Techniques*, vol. 66, no. 9, pp. 4029-4039, 2018.
- [7] B. Beuerle, J. Campion, U. Shah, and J. Oberhammer, "Integrated micromachined waveguide absorbers at 220–325 GHz," in *2017 47th European Microwave Conference (EuMC)*, 2017, pp. 695-698: IEEE.
- [8] B. Beuerle, U. Shah, and J. Oberhammer, "Micromachined waveguides with integrated silicon absorbers and attenuators at 220–325 GHz," in *2018 IEEE/MTT-S International Microwave Symposium-IMS*, 2018, pp. 579-582: IEEE.

# Chapter 8. Conclusion and Future Work

This chapter concludes the thesis and outlines the potential future work based on the findings and some new emerging demands.

## 8.1 Summary and conclusion

This thesis reported one method on coupler matrix (CM) with non-resonant circuits (NRCs) and five design cases. The study is presented in Chapter 3 while the five design cases are from Chapter 4 to Chapter 7.

In Chapter 3, a method of constructing a CM with NRCs is presented. This NRC-involved CM helps compound circuits with their theoretical response. Also, by replacing some entries of the CM with Y-parameters of simulated or measured circuits, the influence brought by the circuits can be revealed on the deduced response. This methodology has been successfully applied throughout the thesis.

The five design cases include one X-band amplitude enhanced filtering coupler (Coupler-A), one D-band  $180^\circ$  filtering coupler (Coupler-B), one D-band  $90^\circ$  filtering coupler (Coupler-C), one E-plane X-band filtering SPJ (SPJ-A) and one E-plane D-band filtering SPJ (SPJ-B). The couplers were designed for the implementation of SPJs, and SPJ-B is the ultimate goal of this thesis.

The investigation around Coupler-A suggests the position of apertures in irises significantly influences amplitude balance of a filtering coupler. An effective approach was developed to improve the amplitude balancing. This approach

has been adopted throughout the thesis. Also, it has been demonstrated that symmetrical implementation brings high amplitude balance. This concept was also adopted in SPJ-B.

SPJ-A has fulfilled the function. However, the configuration is impractical when extended to the D-band for their incompatibility with the fabrication capability. Three issues need to be addressed. The first one was the small stubs in the resonators, used to tune the resonance frequency. The second one was the small and deep apertures in capacitive irises that were used to achieve filtering functions. The third one was the four inside-circuit ports. This is brought by  $180^\circ$  filtering couplers. Coupler-B and Coupler-C were proposed to solve the three issues. In Coupler-B, fan-shaped resonators were proposed. This configuration facilitates E-plane filtering coupler without tiny capacitive irises. The resonant frequency is adjustable easily in the fan-shaped resonators without stubs. Coupler-B makes filtering coupler possible in the D-band. Coupler-C achieved  $90^\circ$  phase shift in a filtering coupler. Two resonators in Coupler-C serve as power splitters by introducing large couplings to avoid unwanted poles that the  $90^\circ$  phase shift usually brings.

SPJ-B combined Coupler-B and Coupler-C and have been successfully fabricated and measured. The simulation agrees well with the theory. Measurement also gave acceptable response. It is believed that the response deterioration in measurement was introduced by fabrication error.

## 8.2 Future Works

1. *Approach to lower the insertion loss.* In the measurement of SPJ-B,  $|S_{31}|$  and  $|S_{51}|$  showed a larger insertion loss (maximum of 2 dB) than  $|S_{41}|$  and  $|S_{61}|$  (maximum of 0.5 dB). It implies that the insertion loss of SPJ-B was caused by fabrication error.
2. *A system demonstrator based on SPJ.* SPJs are used in transceiver systems. The Schottky based power detectors are being developed in a parallel activity, which is not the focus of the thesis.
3. *The CM technique involving power detectors.* A general CM technique involving non-resonant parts was introduced in this thesis. When the SPJ is designed with power detectors, the CM technique could also be used to synthesize the whole structure including the detectors.
4. *Wider bandwidth.* Although the SPJs in this thesis achieved filtering functions with balanced amplitude, the bandwidth is limited. For microwave cavities, wide bandwidth is never the focus. To improve the bandwidth, potential methods include using multimode resonators, combining lowpass with highpass, using non-resonant structures and using resonators with lower  $Q$ .
5. *Smart optimization.* In the optimization process, Trust Region Framework (TRF) was used as the optimization algorithm. The optimizations were stopped manually considering the reliability. A more specific algorithm can be devised and used to save time. For example, vector fitting is a method that can be used to extract the coupling matrix (CM) from a practical

resonant model. The extracted CM is used to compare with the theoretical one. The difference will be considered as a guide for the next iteration. This method can be used in the future, making the optimization process more efficient and unattended.



# Appendix I: Simulation and Optimization Settings

This appendix provides the settings in simulation and optimization of the models in this thesis. The software used in model building and simulation was CST Studio Suite 2018. It provides with Time Domain Simulation and Frequency Domain Simulation. Frequency Domain Simulation was used to obtain the  $S$ -parameters. (Time Domain Simulation can also be used to obtain  $S$ -parameters, but this was often adopted in antenna designs to save time). In the setup, it provides an option of “Adaptive tetrahedral mesh refinement”, shown in Fig. I.1, with which the distribution of mesh will be automatically adjusted according to the complexity of the model. This can save some time when a large part of the model is comparatively simple. However, a small change of one dimension may lead to completely different mesh when this option is on, causing sensitivity in the simulated response. For the purpose of

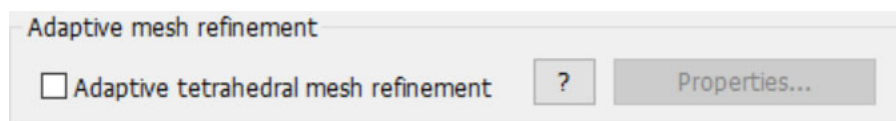


Fig. I.1. Option of Adaptive tetrahedral mesh refinement in simulation setup.

accuracy, this option was off during all the simulations in this thesis. All other settings remained default.

For models working at 10 GHz, the material of the air models was set vacuum and the background was set perfect electric conductor (PEC) to save computation time. For models working at 150 GHz, the priority is accuracy. In

this situation, the material of the air models was air and the background was set as gold, to imitate the real situation in the fabricated models using CNC machining.

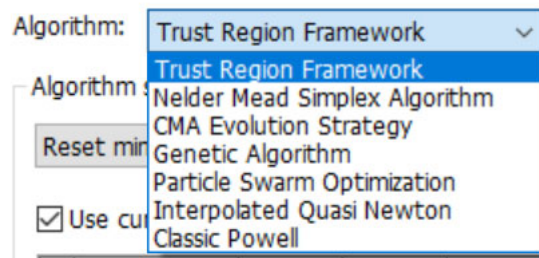


Fig. I.2. Optimization algorithms provided by CST Studio Suite 2018.

CST Studio Suite 2018 provides several optimization algorithms, shown in Fig. I.2. The default algorithm is Trust Region Framework (TRF). Based on the starting data (starting point), this algorithm finds a point in a region where a linear model (built by the algorithm) fits best to the object. If this new point is found, a new trust region will be created and the process will be iterated. The size of the region depends on the distance of the two points. The algorithm

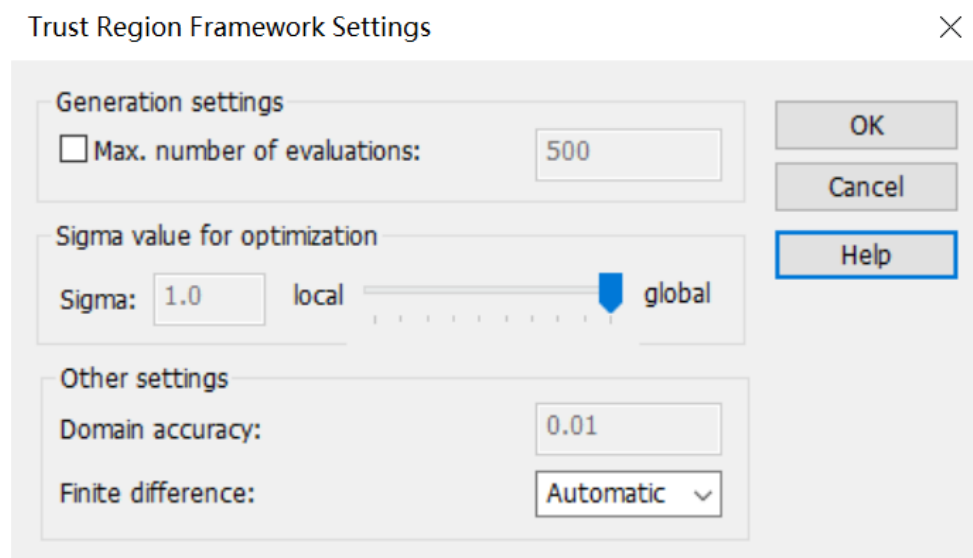


Fig. I.3. Trust Region Framework (TRF) settings.

keeps running until it hits the maximum iteration number or the distance is lower than the specified *domain accuracy*. As an omnipotent and default algorithm, TRF was used in the simulation of all the models in this thesis.

The settings of TRF used in the simulation is provided in Fig. I.3. The maximum number of evaluation was not on, which means the algorithm will not stop until it hits the goal or is stopped manually. The goals for the optimizations were all from the theoretical responses. There were always some difference between the optimal responses and the theoretical ones. Although it is subjective, all the optimization processes in this thesis were stopped manually for the most reliability. The sigma value was set to 1, which means global optimization. Other settings were remained default.

In optimization process, each parameter needs a boundary that defines the upper and lower limits. Chapter 3 provided the methods to find the initial size of irises to achieve desired couplings and external  $Q$  factors. These methods were used in the model building, which provided decent initial parameters. Based on this, the boundary for each parameter to be optimized was set 15% of the initial value, that is to say, the upper limit is 15% larger than the initial value while the lower limit is 15% less.

# Appendix II: H-Plane X-band Filtering SPJ

This appendix gives the simulation result of an H-plane X-band filtering SPJ, using the aforementioned amplitude-balance enhanced filtering coupler in Chapter 4.

## II.1. Topology of the SPJ

To integrate the filtering function, the couplers in the conventional SPJs were replaced by filtering couplers, and a new topology of a filtering SPJ is proposed in Fig. II.1. There are four parts: two identical  $180^\circ$  filtering couplers, one  $180^\circ$  branch-line coupler and one  $90^\circ$  branch-line coupler. The two filtering couplers realize the filtering function. There are eight ports in total. Port 7 and Port 8 are supposed to be loaded for matched termination. Port 1 and Port 2 are the two input ports, while Port 3 to 6 are the four outputs. Given the topology, the phase response can be easily deduced:

$$\left\{ \begin{array}{l} \angle S_{51} - \angle S_{52} = 270^\circ \\ \angle S_{31} - \angle S_{32} = 180^\circ \\ \angle S_{61} - \angle S_{62} = 90^\circ \\ \angle S_{41} - \angle S_{42} = 0^\circ \end{array} \right. \quad (\text{II.1})$$

This phase response satisfies the specification of an SPJ. The theoretical response deduced by CM is given in the following sections.

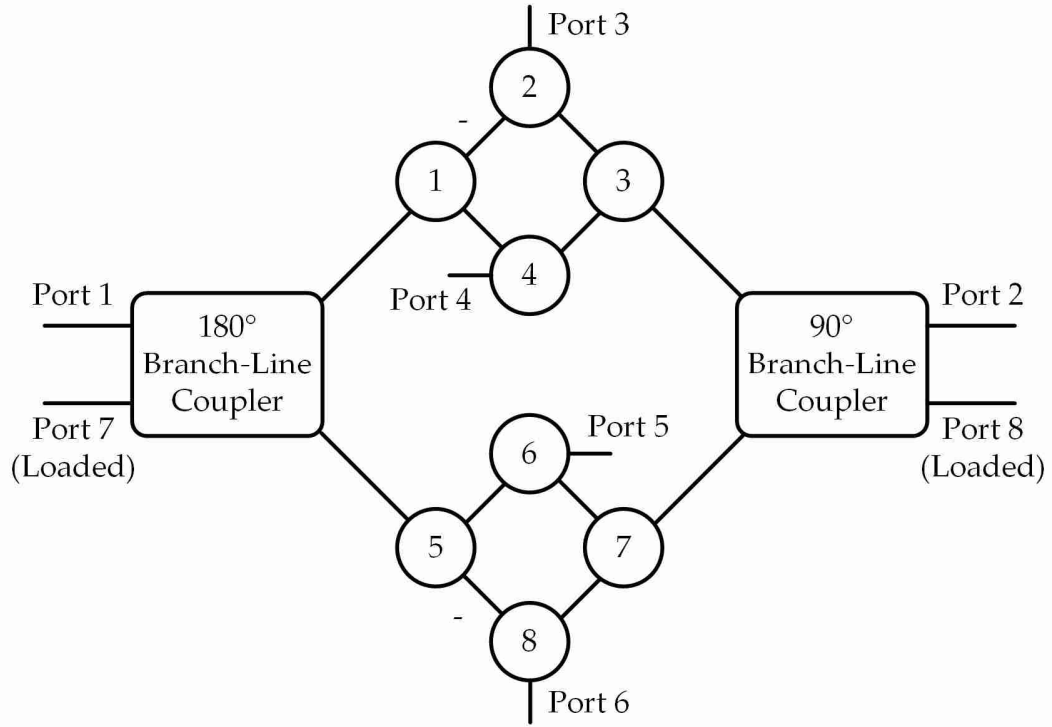


Fig. II.1. Topology of the proposed filtering SPJ consists of two conventional branch-line couplers and two second-order filtering couplers.

## II.2. Theoretical Response of the SPJ

Chapter 3 gives the CM involving NRCs. To obtain the CM of the topology shown in Fig. II.1, the two 3-dB branch-line couplers need to be transformed into 'nodes' in the coupling matrix at first. The concept view of the 90° 3-dB branch-line coupler and the 180° 3-dB branch-line coupler are provided in Fig. II.2. The 90° 3-dB coupler is a conventional 3-dB branch-line coupler, while the 180° 3-dB coupler is built upon the conventional 90° 3-dB coupler with a 90° phase shifter (four ports, with one reference line). For both couplers, Port 1 is the input port while Port 2 and Port 4 are outputs. Port 3 is isolated. Interconnection lines are inevitable between the waveguide couplers and the

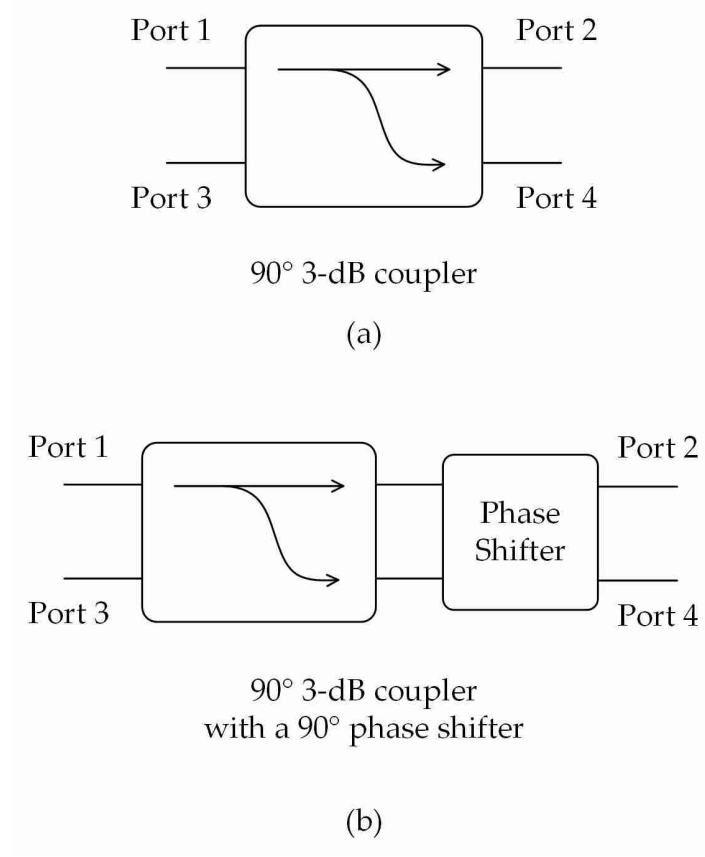


Fig. II.2. (a) 90° branch-line coupler and (b) the 180° branch-line coupler.

filtering couplers. An initial phase  $\theta$  is added to each port to represent these lines. The S-parameters of the 90° hybrid coupler are given by:

$$[S_{90}] = \frac{1}{\sqrt{2}} \begin{bmatrix} 0 & e^{j(\pi/2+\theta)} & 0 & e^{j\theta} \\ e^{j(\pi/2+\theta)} & 0 & e^{j\theta} & 0 \\ 0 & e^{j\theta} & 0 & e^{j(\pi/2+\theta)} \\ e^{j\theta} & 0 & e^{j(\pi/2+\theta)} & 0 \end{bmatrix} \quad (\text{II.2})$$

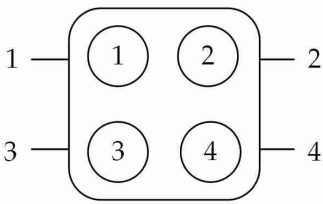
$$[S_{180}] = \frac{1}{\sqrt{2}} \begin{bmatrix} 0 & e^{j(\pi/2+\theta)} & 0 & e^{j(-\pi/2+\theta)} \\ e^{j(\pi/2+\theta)} & 0 & e^{j\theta} & 0 \\ 0 & e^{j\theta} & 0 & e^{j\theta} \\ e^{j(-\pi/2+\theta)} & 0 & e^{j\theta} & 0 \end{bmatrix} \quad (\text{II.3})$$

Their Y-matrices can be deduced from the S-parameters:

$$[Y_{90}] = j \begin{bmatrix} -\tan 2\theta & -\sqrt{2} \cos \theta \sec 2\theta & \sec 2\theta & \sqrt{2} \sin \theta \sec 2\theta \\ -\sqrt{2} \cos \theta \sec 2\theta & -\tan 2\theta & \sqrt{2} \sin \theta \sec 2\theta & \sec 2\theta \\ \sec 2\theta & \sqrt{2} \sin \theta \sec 2\theta & -\tan 2\theta & -\sqrt{2} \cos \theta \sec 2\theta \\ \sqrt{2} \sin \theta \sec 2\theta & \sec 2\theta & -\sqrt{2} \cos \theta \sec 2\theta & -\tan 2\theta \end{bmatrix} \quad (\text{II.4})$$

$$[Y_{180}] = j \begin{bmatrix} -\tan \theta & -\frac{\sec \theta}{\sqrt{2}} & 0 & \frac{\sec \theta}{\sqrt{2}} \\ -\frac{\sec \theta}{\sqrt{2}} & \cot 2\theta & -\frac{\csc \theta}{\sqrt{2}} & \csc 2\theta \\ 0 & -\frac{\csc \theta}{\sqrt{2}} & \cot \theta & -\frac{\csc \theta}{\sqrt{2}} \\ \frac{\sec \theta}{\sqrt{2}} & \csc 2\theta & -\frac{\csc \theta}{\sqrt{2}} & \cot 2\theta \end{bmatrix} \quad (\text{II.5})$$

According to the discussion around Fig. 3.31, an  $N$ -port device can be represented by an  $N$ -port  $N$ -node network. The CM of the topology in Fig. II.2



(a)

	1	2	3	4	P 1	P 2	P 3	P 4
1	0	$jY_{1,2}$	$jY_{1,3}$	$jY_{1,4}$	1	0	0	0
2	$jY_{2,1}$	0	$jY_{2,3}$	$jY_{2,4}$	0	1	0	0
3	$jY_{3,1}$	$jY_{3,2}$	0	$jY_{3,4}$	0	0	1	0
4	$jY_{4,1}$	$jY_{4,2}$	$jY_{4,3}$	0	0	0	0	1
P 1	1	0	0	0	0	0	0	0
P 2	0	1	0	0	0	0	0	0
P 3	0	0	1	0	0	0	0	0
P 4	0	0	0	1	0	0	0	0

(b)

Fig. II.3. Coupling matrix representation of branch-line couplers. (a) The node representation of the two branch-line couplers. (b) The corresponding CM representation. The two couplers share the same node form.

can be deduced, shown in Fig. II.3. Fig. II.3(a) gives the node representation of the two branch-line couplers. The two couplers share the same form of node representation and thus the same CM form, which is given in Fig. II.3(b).

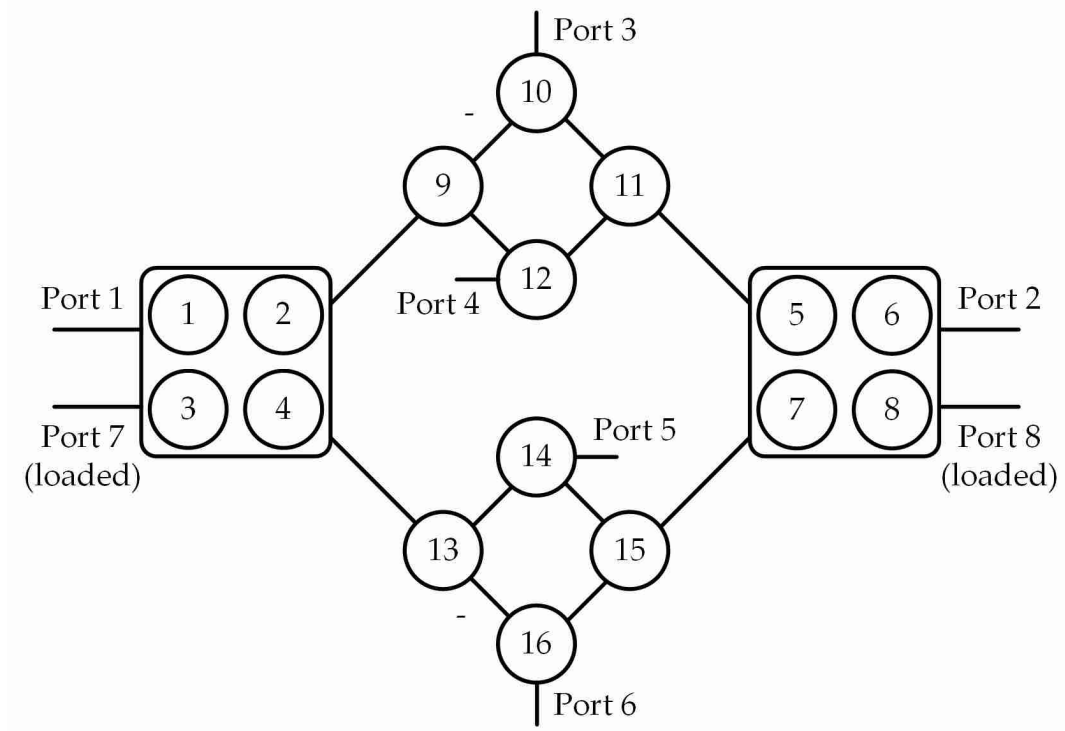


Fig. II.4. Topology of the SPJ in Fig. II.1 when transformed into nodes.

$$\begin{aligned}
 m_{P1,1} &= m_{P2,6} = m_{P7,3} = m_{P8,8} = 1 \\
 m_{P3,10} &= m_{P4,12} = m_{P5,14} = m_{P6,16} = 1.227 \\
 m_{1,2} &= -m_{1,4} = \sec(\theta) / \sqrt{2} \\
 m_{2,3} &= m_{3,4} = -\csc(\theta) / \sqrt{2} \\
 m_{2,4} &= -\csc(2\theta) \\
 m_{2,9} &= m_{4,13} = m_{5,11} = m_{7,15} = 1.227 \\
 m_{5,6} &= m_{7,8} = \sqrt{2} \sec(2\theta) \cot(\theta) \\
 m_{5,7} &= m_{6,8} = -\sec(2\theta) \\
 m_{5,8} &= m_{6,7} = -\sqrt{2} \sec(2\theta) \sin(\theta) \\
 -m_{9,10} &= m_{9,12} = m_{10,11} = m_{11,12} = 1.175 \\
 m_{13,14} &= m_{14,15} = m_{15,16} = -m_{13,16} = 1.175
 \end{aligned}$$

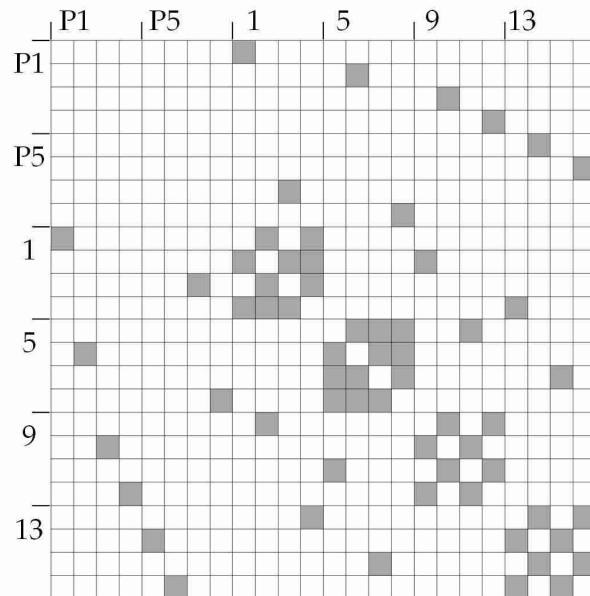


Fig. II.5. CM of the second-order filtering SPJ and the coupling values.



However, they have different entries, deduced from the two Y-matrices.

Having the CMs of the two branch-line couplers, Fig. II.1 is therefore transformed into Fig. II.4, where the  $180^\circ$  branch-line coupler is represented by nodes 1 - 4 and the  $90^\circ$  branch-line coupler is by nodes 5 - 8. Between the two waveguide couplers are two second-order filtering couplers, as introduced in Chapter 4. Now there are sixteen nodes in total with eight ports. The overall 24

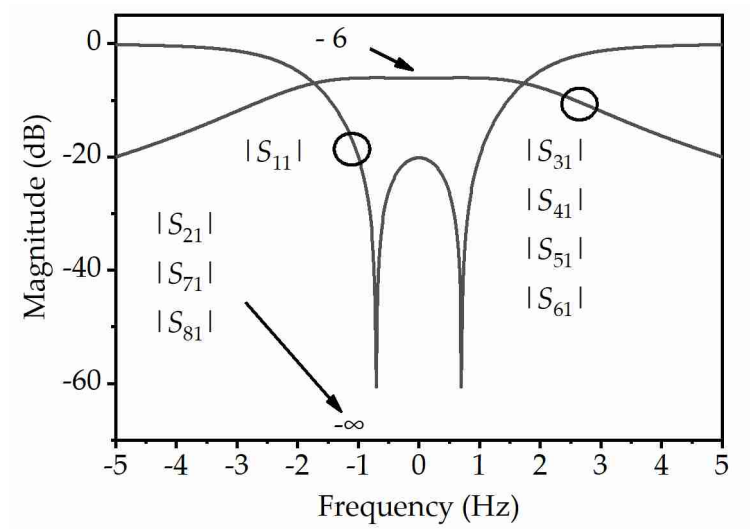


Fig. II.6. Theoretical magnitude response of the second-order filtering SPJ (Port 1 related).

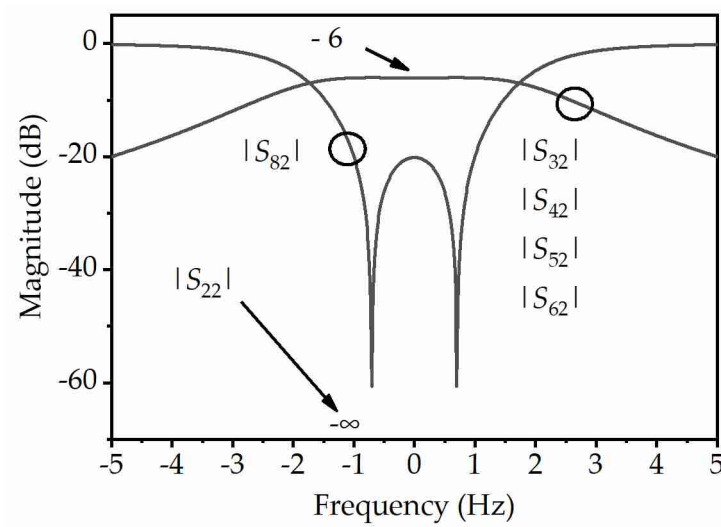


Fig. II.7. Theoretical magnitude response of the second-order filtering SPJ (Port 2 related).

$\times 24$  CM of the SPJ is given in Fig. II.5. The scattered grey entries represent non-zero values. The corresponding coupling values are given on the left. With the CM, the theoretical magnitude and phase responses can be obtained, which are given in Fig. II.6 to Fig. II.9. A second-order Chebyshev response can be found due to the two second-order filtering couplers. The phase response of the SPJ is shown in Fig. II.9. Clearly, the separation between the phase difference is  $\pi/2$ ,

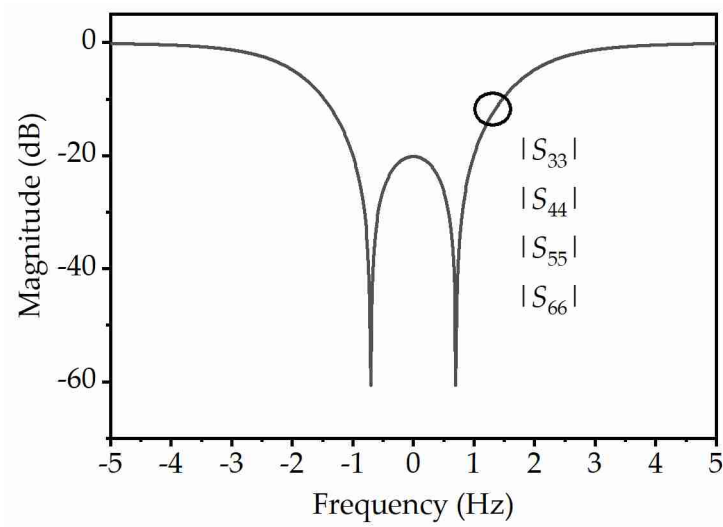


Fig. II.8. Theoretical magnitude response of the second-order filtering SPJ (outputs related).

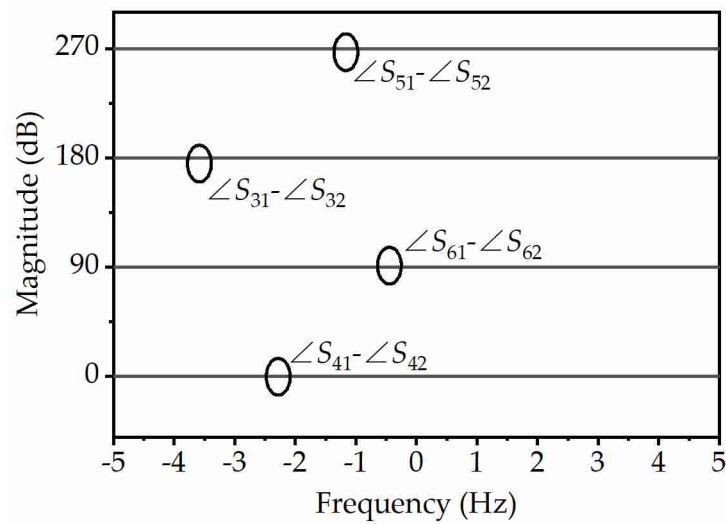


Fig. II.9. Theoretical phase response of the second-order filtering SPJ.

which agrees with (II.1).

### II.3. Implementation of the H-plane SPJ

An H-plane  $90^\circ$  branch-line coupler used in the filtering SPJ was designed and shown in Fig. II.10(a), and the dimensions are given in Fig. II.10(b). The coupler is symmetrical to line  $aa'$  and  $bb'$ . As with Fig. II.2(a), Port 1 is the input, Port 2

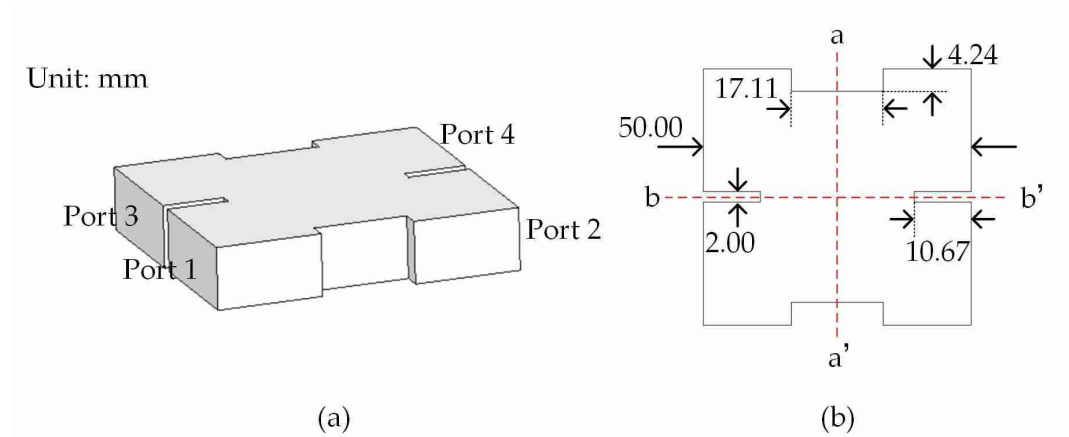


Fig. II.10. Air model of the H-plane  $90^\circ$  branch-line coupler. (a) The perspective view. (b) The dimension detail.

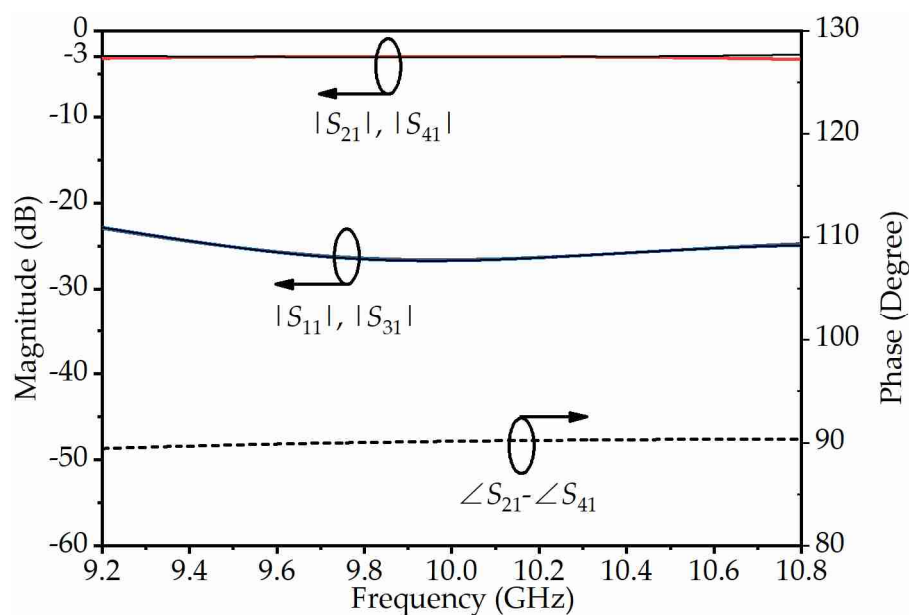


Fig. II.11. Simulated magnitude and phase responses of the  $90^\circ$  branch-line coupler.

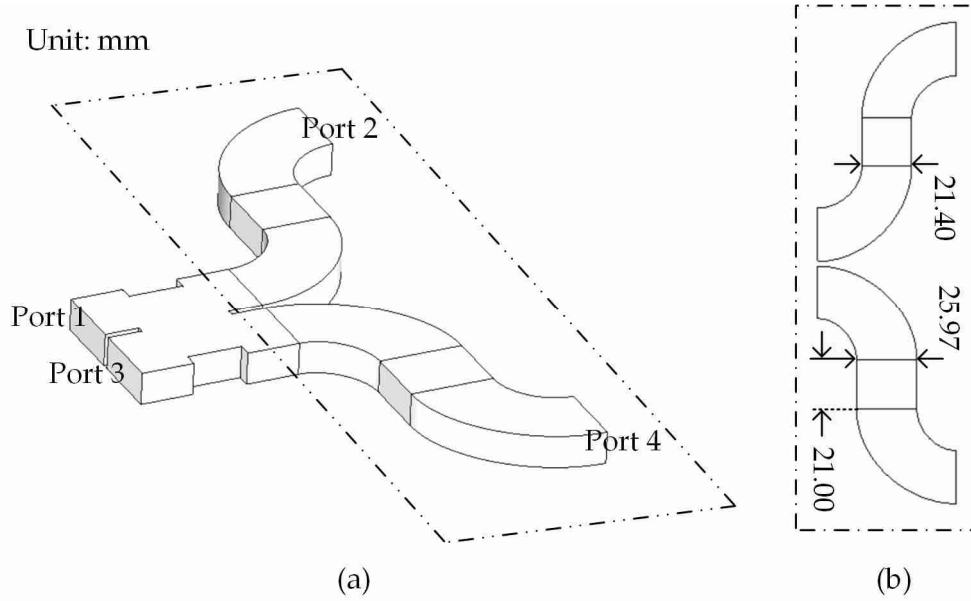


Fig. II.12. Air model of the 180° branch line coupler. (a) The overall view of the model. (b) The detail of the phase shift lines.

and Port 4 are outputs. Port 3 is isolated. The simulated response of this coupler is given in Fig. II.11. The working band of the coupler is 9.2 – 10.8 GHz, covering the designed band of the filtering SPJ (9.9 - 10.1 GHz). The return loss and isolation are higher than 20 dB in the band. The phase response of the coupler

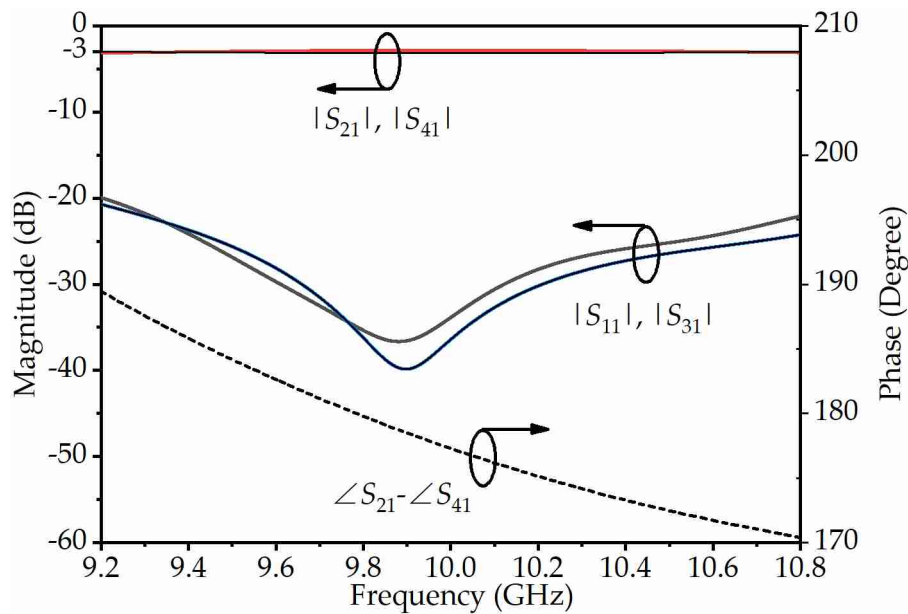


Fig. II.13. Simulated magnitude and phase responses of the 180° branch-line coupler.

is also given in Fig. II.11,  $\angle S_{21} - \angle S_{41}$  is near  $-90^\circ$  over the entire working band. Built upon the  $90^\circ$  branch-line coupler, the  $180^\circ$  branch line coupler was designed by applying the technique mentioned in Chapter 5. The waveguide width is changed to make a phase shift while maintaining the length of the extended waveguide sections to ease layout. The air model is provided in Fig. II.12(a). The  $180^\circ$  coupler consists of one  $90^\circ$  branch line coupler (same as in Fig. II.10(a)) and two additional waveguides. The widths of the waveguides were changed to 21.40 mm and 25.97 mm to introduce the phase shifts, as shown in Fig. II.12(b). The simulated magnitude and phase responses of the coupler are given in Fig. II.13. It can be noticed that, as the  $90^\circ$  branch-line coupler, the power is split into halves at the two outputs. Thanks to the varied waveguide width, the phase difference between the two outputs is around  $180^\circ$  in the working frequency of the SPJ.

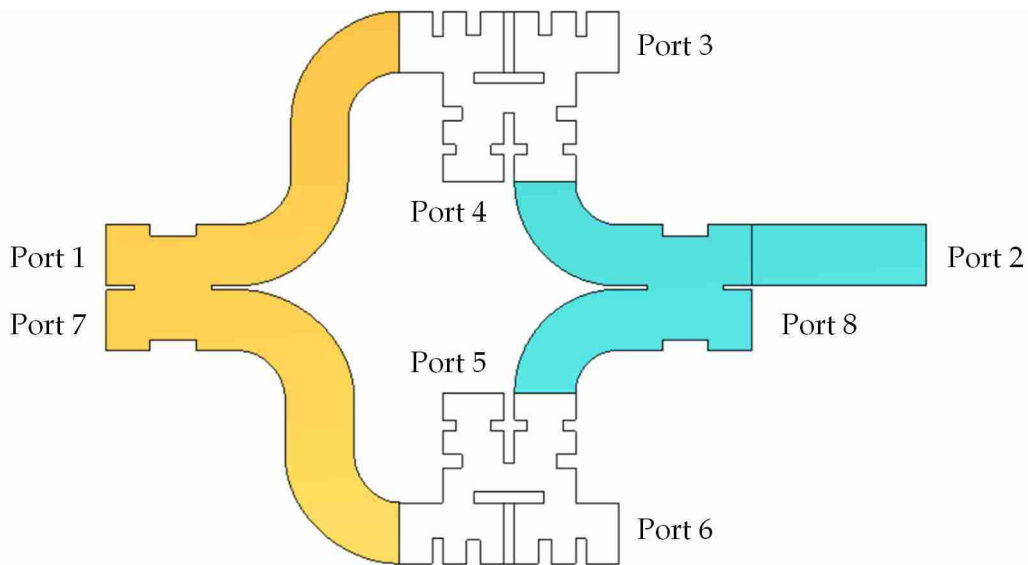


Fig. II.14. Top view of the proposed H-plane filtering SPJ.

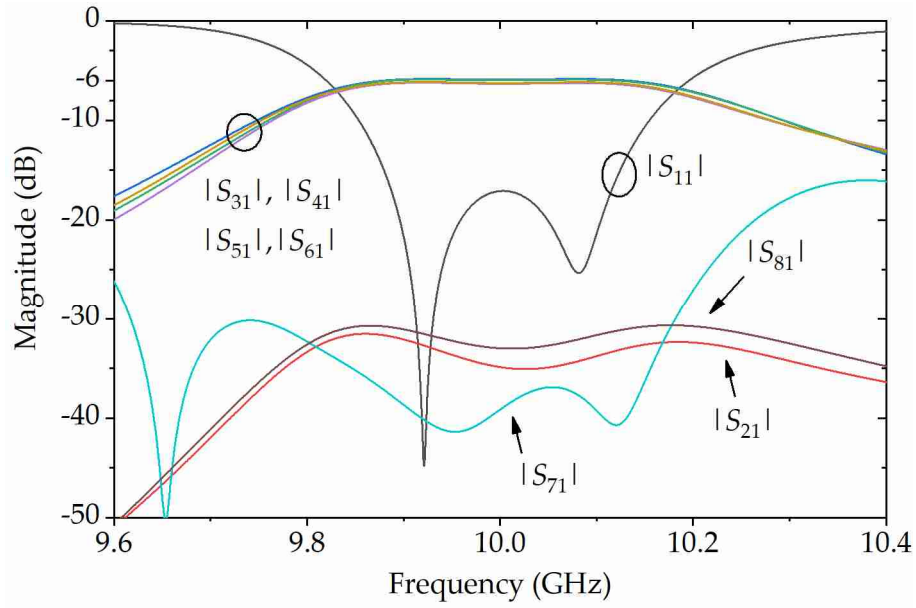


Fig. II.15. Port 1 related magnitude response from the simulation of the SPJ.

The previous chapter discussed the modified filtering coupler (Coupler-A) with balanced amplitude. The  $180^\circ$  filtering coupler in the SPJ topology was implemented with Coupler-A. With the  $90^\circ$  branch-line coupler and the  $180^\circ$  branch-line coupler, now the filtering SPJ can be constructed. The plan view is given in Fig. II.14. There are four parts in the SPJ. The yellow one is the  $180^\circ$

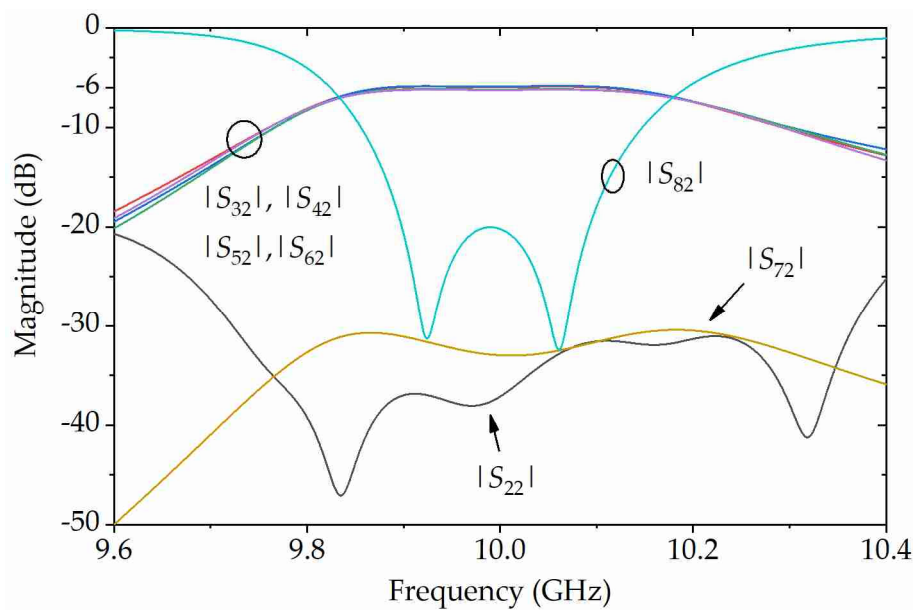


Fig. II.16. Port 2 related magnitude response from the simulation of the SPJ.

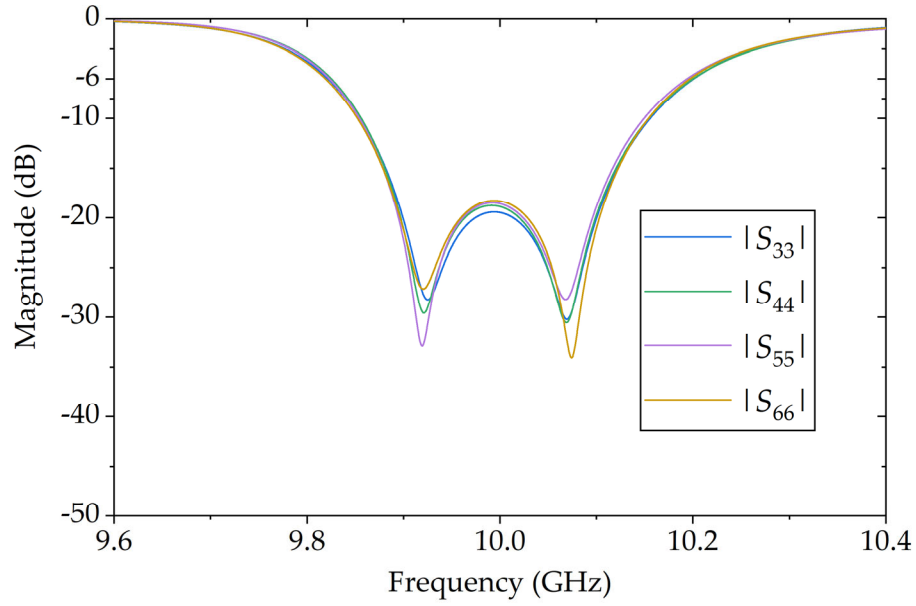


Fig. II.17. Magnitude response of the outputs from the simulation of the SPJ.

branch-line coupler, the two white ones are Coupler-A, and the cyan one is the  $90^\circ$  branch-line coupler with one extension line. The extension line is to make phase compensation. There are eight ports, Port 1 and Port 2 are two input ports, while Port 3 to Port 6 are four outputs. Port 7 and Port 8 are reserved for loads. This model was simulated in the commercial microwave simulator CST. The

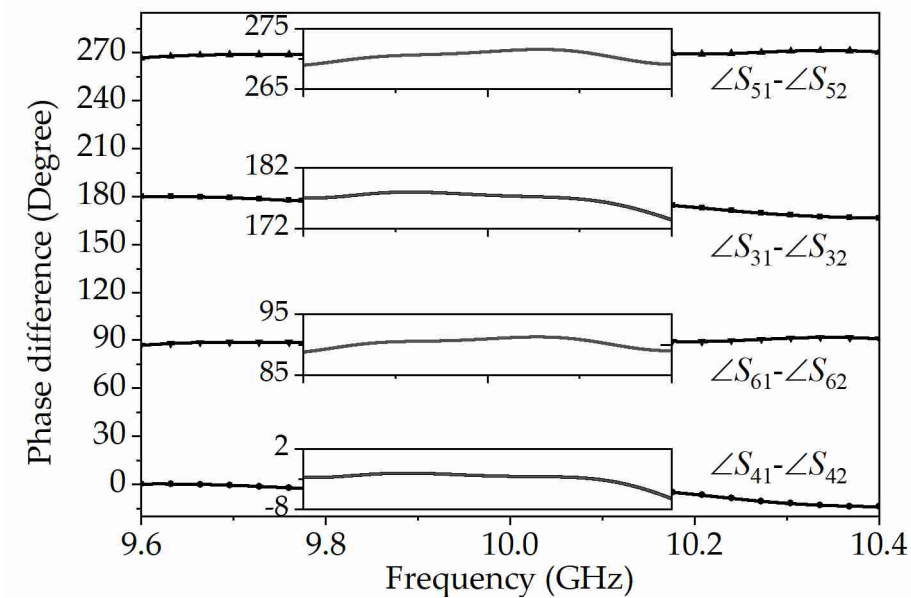


Fig. II.18. Simulated phase response of the filtering SPJ.

simulated responses can be found in Fig. II.15 to Fig. II.18. The two second-order filtering couplers bring the SPJ second-order Chebyshev response, which can be noticed in Fig. II.15 and Fig. II.16. In Fig. II.15,  $|S_{21}|$  indicates the isolation, which is higher than 30 dB in the working band. Besides,  $|S_{11}|$  is lower than -15 dB while in Fig. II.16  $|S_{82}|$  is lower than -20 dB. The return loss of all outputs is more than 18 dB in Fig. II.17. The phase response can be found in Fig. II.18. The phase response agrees with the one in Fig. II.9. With the help of Coupler-A, the simulated amplitude imbalance of this SPJ is less than 0.45 dB.